UNIVERSITEIT GENT

UNIVERSITEIT GENT

DOCTORAL THESIS

Search for heavy neutral leptons in pp collision events with three charged leptons using the CMS detector

Author:
Martina VIT

Supervisors:
Prof. Dr. Didar DOBUR
Prof. Dr. Dirk RYCKBOSCH

GENT, DECEMBER 2021

Supervisors:	prof. Dr. Didar Dobur (UGent) prof. Dr. Dirk Ryckbosch (UGent)
Chairman of the Examination Board:	prof. Dr. Arjen van der Wel (UGent)
Members of the Examination Board:	prof. Dr. Marco Drewes (Université Catholique de Louvain) prof. Dr. Archisman Ghosh (UGent) prof. Dr. Natalie Jachowicz (UGent) prof. Dr. Niki Saoulidou (University of Athens) Dr. Michael Tytgat (UGent)
Date of dissertation:	14.12.2021
Head of the department of Physics and Astronomy:	Prof. Dr. Dimitri Van Neck
Dean of the Faculty of Sciences:	Prof. Dr. Isabel Van Driessche

"*That is fundamentally the only courage which is demanded of us: to be brave in the face of the strangest, most singular and most inexplicable things that can befall us. The fact that human beings have been cowardly in this sense has done endless harm to life; the experiences that are called "apparitions", the whole of the so-called "spirit world", death, all these things that are so closely related to us, have been so crowded out of life by our daily warding them off, that the senses by which we might apprehend them are stunted. To say nothing of God. But fear of the inexplicable has not only impoverished the existence of the solitary man, it has also circumscribed the relationships between human beings, as it were lifted them up from the river bed of infinite possibilities to a fallow spot on the bank, to which nothing happens.*"

Rainer Maria Rilke

UNIVERSITEIT GENT

Summary

Search for heavy neutral leptons in pp collision events with three charged leptons using the CMS detector

Searches for heavy neutral leptons, (N) of Majorana and Dirac natures decaying into a charge lepton and a W boson are presented. The searches target complementary phase spaces in HNL mass (m_{N}) and in $|\mathrm{V}_{\ell\mathrm{N}}|^2$, with $V_{\ell\mathrm{N}}$ the matrix element defining the mixing between N and the Standard Model neutrino of flavor ℓ. The studies focus first on the moderate and high mass searches and then migrates to very low mass search with the introduction of long-lived heavy neutral lepton scenario.

The search for heavy neutral leptons focuses on signatures with three prompt charged leptons in any flavor combination of electrons and muons. This provides a clean experimental signal for probing the production of the N in an extended mass range never investigated before at the LHC: from 1 GeV, and up to 1.2 TeV. The samples of pp collisions at a center-of-mass energy of 13 TeV were collected by the CMS experiment at LHC during 2016 data-taking, amounting to an integrated luminosity of 35.9 fb^{-1}. Organized into two parts, the search is optimized for probing heavy neutral leptons of masses respectively above and below that of the W boson. The data are found to be consistent with the expected Standard Model background. Upper limits at 95% confidence level on the values of $|\mathrm{V}_{\mu\mathrm{N}}|^2$ and $|\mathrm{V}_{\mathrm{eN}}|^2$ are set. These are the first limits obtained at a hadron collider for $m_{\mathrm{N}} < 40$ GeV and the first direct results for $m_{\mathrm{N}} > 500$ GeV.

The search for long-lived heavy neutral leptons targets signatures consisting of one prompt charged lepton and two displaced charged leptons originating from the secondary vertex of the N decay. The data were collected by the CMS experiment during the Run2 period from 2016 to 2018 and corresponds to an integrated luminosity of 137 fb^{-1}. Two interpretations are proposed, considering on the one hand uniquely the N with Dirac nature, on the other hand the N with Majorana nature. No statistically significant deviation from the expected SM background is observed. At 95% confidence level, limits were set on the mixing parameters $|\mathrm{V}_{\mathrm{eN}}|^2$ and $|\mathrm{V}_{\mu\mathrm{N}}|^2$. The excluded values are in the range between 3×10^{-7} and 1×10^{-3} for masses included between 1 GeV $< m_{\mathrm{N}} <$ 15 GeV.

UNIVERSITEIT GENT

Samenvatting

Zoektocht naar zware neutrale leptonen in pp collisies met drie geladen leptonen met de CMS detector

Zoektochten naar zware neutrale leptonen (N), die vervallen naar een geladen lepton en een W boson, worden gepresenteerd. De N kunnen zowel Dirac- als Majorana-fermionen zijn. De analyses focussen op onderling complementaire faseruimtes in de massa van het N, m_{N} en $V_{\ell\mathrm{N}}$, het matrix element dat de koppeling definieert tussen N en neutrino's van het type ℓ in het Standaard Model. De eerste zoektocht focust op gemiddelde en hoge massa's, terwijl de tweede studie naar lagere massa's kijkt, waarbij N langlevend worden.

De eerste zoektocht naar zware neutrale leptonen mikt op vervalscenario's met drie geladen leptonen die allen prompt zijn. De leptonen kunnen elke combinatie van electronen en muonen zijn. Dit vervalkanaal is nog niet eerder onderzocht aan de LHC en laat toe om de productie van N te onderzoeken in enkele grootte-ordes van N massa, namelijk van 1 GeV tot 1.2 TeV. De data, bestaande uit proton-proton botsingen met een totale energie van 13 TeV in het proton-proton massamiddelpunt, is verzameld met de CMS detector aan de LHC. De totale geïntegreerde luminositeit van proton-proton botsingen die gebruikt is, bedraagt 35.9 fb^{-1}. De analyse is onderverdeeld in twee delen, elk deel is geoptimaliseerd om N te herkennen met massa's respectievelijk onder en boven de massa van het W boson. Er zijn geen afwijkingen waargenomen ten opzichte van de voorspellingen van het Standaard Model. Bovenlimieten worden gezet in functie van $|\mathrm{V}_{\mu\mathrm{N}}|^2$ en $|\mathrm{V}_{\mathrm{eN}}|^2$ in een betrouwbaarheidsinterval van 95%. Dit zijn de eerste directe limieten voor $m_{\mathrm{N}} > 500$ GeV en de eerste limieten aan een hadron deeltjesversneller voor $m_{\mathrm{N}} < 40$ GeV.

De tweede, complementaire zoektocht naar langlevende zware neutrale leptonen focust op vervalprocessen met één prompt geladen lepton en 2 verplaatste geladen leptonen die ontstaan in de secundaire vertex van het verplaatste N verval. De data wordt gecollecteerd door het CMS experiment aan de LHC gedurende de periode van 2016 tot 2018 en komt overeen met een geïntegreerde luminositeit van 137 fb^{-1} aan een energie van 13 TeV in het proton-proton massamiddelpunt. Twee mogelijke interpretaties voor de natuur van het N worden gebruikt, namelijk als Majorana- en Dirac-fermionen. Geen statistisch significante afwijkingen van voorspellingen op basis van het Standaard Model zijn waargenomen. In een betrouwbaarheidsinterval van 95% zijn limieten geplaatst op de koppeling parameters $|\mathrm{V}_{\mathrm{eN}}|^2$ en $|\mathrm{V}_{\mu\mathrm{N}}|^2$. De uitgesloten waardes bestrijken een gebied tussen 3×10^{-7} en 1×10^{-3} voor N massa's tussen 1 GeV $< m_{\mathrm{N}} <$ 15 GeV.

Contents

"We have two goals in front of us. One is to explain the story of our universe and why we think it's true, the big picture as we currently understand it. It's a fantastic conception. We humans are blobs of organized mud, which through the impersonal workings of nature's patterns have developed the capacity to contemplate and cherish and engage with the intimidating complexity of the world around us. To understand ourselves, we have to understand the stuff out of which we are made, which means we have to dig deeply into the realm of particles and forces and quantum phenomena, not to mention the spectacular variety of ways that those microscopic pieces can come together to form organized systems capable of feeling and thought.

The other goal is to offer a bit of existential therapy. I want to argue that, though we are part of a universe that runs according to impersonal underlying laws, we nevertheless matter. This isn't a scientific question—there isn't data we can collect by doing experiments that could possibly measure the extent to which a life matters. It's at heart a philosophical problem, one that demands that we discard the way that we've been thinking about our lives and their meaning for thousands of years. By the old way of thinking, human life couldn't possibly be meaningful if we are "just" collections of atoms moving around in accordance with the laws of physics. That's exactly what we are, but it's not the only way of thinking about what we are. We are collections of atoms, operating independently of any immaterial spirits or influences, and we are thinking and feeling people who bring meaning into existence by the way we live our lives.

We are small; the universe is big. It doesn't come with an instruction manual. We have nevertheless figured out an amazing amount about how things actually work. It's a different kind of challenge to accept the world for what it is, to face reality with a smile, and to make our lives into something valuable."

Sean Carroll, 2016 [1]

Preface

"*We do not know what the rules of the game are; all we are allowed to do is to watch the playing. Of course, if we watch long enough, we may eventually catch on to a few of the rules. The rules of the game are what we mean by fundamental physics.*" Richard P. Feynman

This quote brilliantly exemplifies the need for fundamental research. We all want to satisfy our curiosity and science is a process of investigating, keeping on questioning, and trying to uncover the unresolved.
Thus, the need for the construction of huge laboratories where to study the fundamental constituents of matter becomes explicit. CERN's accelerator complex and experiments are the best place to "watch the playing" and "if we watch long enough, we may eventually catch on to a few of the rules".

Since the 1960s, physicists had proposed a collection of what they assumed to be the fundamental particles and the fundamental forces that govern the interaction between particles themselves. This was the start of the development of the Standard Model (SM) of particle physics. At CERN we make use of the world's most potent particle accelerators and experiments to question the predictions and to test limits of the Standard Model. So far, the Standard Model has favorably described and predicted approximately all experimental outcomes till the latest discoveries such as top quark observation (1995) [2] and Higgs boson discovery (2012) [3, 4].

However, cosmological and astronomical observations, together with theoretical considerations allude to physics beyond the Standard Model (BSM). Furthermore, the observation of neutrino flavor oscillations was one of the first definite experimental indications for the presence of new physics not described by the SM theory. Therefore, it felt crucial to investigate the signatures of different BSM models at the LHC experiments to try spotting the mysterious new physics. Above all, comprehending the mechanism that discloses the neutrino mass would be a vital glance into "the rules of the game".

The two results presented in this dissertation cooperate in the arduous attempt of confronting exotic BSM models with the experimental data. The aim is to find new physics that is able to describe the unexplained physics observations not covered by the SM.

This thesis tries to give an overview of all the steps needed to follow to experimentally investigate physics beyond the Standard Model. The reader will encounter respectively the descriptions of: theoretical models and predictions, experimental layout, detector performances, data analysis and unfortunately, at the end not a discovery but exclusion limits on specific exotic models.

After a brief description of the principles of the Standard Model in Chapter 1, a summary of the Large Hadron Collider (LHC) and of the Compact Muon Solenoid (CMS) components and objectives is presented in Chapters 2 and 3.

In Chapter 4 the main topic of the doctoral project is introduced. The focus is on the right-handed (RH) neutrino or heavy neutral lepton (N or HNL) model. In Chapters 1 and 4 the relevance and the interest for the ongoing HNL search program is illustrated, describing first the theory setting and then mentioning the various of experiments and results focusing on HNL.

Two separated searches on HNLs have been performed using the data collected by the CMS detector. The two analyses are the core of this dissertation.
The HNL searches are fully described in Chapters 6 and 7 and they target complementary phase spaces in HNL mass, m_{N} and mixing parameter, $|\mathrm{V}_{\ell\mathrm{N}}|^2$, between heavy neutrinos and standard model neutrinos. The study focuses first on the moderate and high mass search and then drifts to very low mass search with the introduction of a long-lived HNL scenario.

In Chapter 6, the search for heavy neutral leptons with three prompt charged leptons in any flavor combination of electrons and muons is defined. It results in a comprehensive analysis that probes the production of the N in an extended mass range never investigated before at the LHC: from 1 GeV, and up to 1.2 TeV. Organized into two parts, the search is optimized for probing HNLs of masses respectively above and below that of the W boson. Several analysis techniques are introduced.

In Chapter 7, the search for long-lived heavy neutral leptons is presented. The analysis signature consisting of one prompt charged lepton and two displaced charged leptons originating from the secondary vertex of the N decay. Due to its unconventional signature, the whole analysis process has been quite demanding; several challenges are presented (final part of Chapter 5 as well) and the steps taken during the three year course are inspected and described one by one.

In Chapter 8, a short summary is given together with an inclusive outlook overview. The future prospects section tries to give a feeling of the vast landscape where the two CMS HNL searches sit. The idea is to give a sense of the context and of the perspective from which one should look at these results.

Author's contribution

The author contributed to the development and finalization of the searches for heavy neutral leptons in multilepton final states at CMS.
The precise contributions of the author are specified at the end of the two dedicated chapters (6, 7) and are summarized shortly below.

For almost the first two years of the PhD, the author has participated in the search for heavy neutral leptons with three prompt charged leptons in any flavor combination of electrons and muons.
The analysis results were published in Physical Review Letters in early 2018:

- CMS Collaboration, *Search for heavy neutral leptons in events with three charged leptons in proton-proton collisions at* $\sqrt{s}$ *= 13 TeV*. Phys. Rev. Lett., 120(22):221801, 2018.

The results discussed in Chapter 6 were presented by the author at the following conferences:

- (YSF talk) Search for heavy neutral leptons (sterile neutrinos) with the CMS detector, plenary at La Thuile 2018, 25 Feb-3 Mar 2018 (Italy);

- Search for Heavy Neutral Leptons with CMS detector, poster at EPS-HEP2019, 10-17 Jul 2019 (Belgium);
- Search for Heavy Neutral Leptons with CMS detector, poster at LP2019, 5-10 Aug 2019, University of Toronto (Canada);
- HNL experimental overview, plenary at EOS Winter Solstice meeting, 19 Dec 2019, Brussels (Belgium);
- Search for heavy neutral leptons at CMS, parallel at ICHEP2020, 28 Jul-6 Aug 2020 (Virtual World).

The poster presented at EPS-HEP2019 was awarded "poster prize of the EPS High Energy and Particle Physics Division and the EPS HEP 2019 Conference".

In the last three years of PhD the author was the main developer for the long-lived heavy neutral lepton search.
The analysis results have been collected in the Physics Analysis Summaries, PAS which has been made public. The final paper will be submitted by the end of the year to Journal of High Energy Physics (JHEP):

- CMS Collaboration, *Search for long-lived heavy neutral leptons with displaced vertices in pp collisions at* $\sqrt{s}$ *= 13TeV with the CMS detector.* Technical report, CERN, Geneva, 2021.

The results discussed in Chapter 7 were presented by the author at the following conferences and workshops:

- HNL experimental overview, talks Searching for long-lived particles at the LHC: firth workshop of the LHC LLP Community, 27-29 May 2019, CERN (Switzerland);
- HNL experimental overview', plenary at EOS winter Solstice meeting, 19 Dec 2019, Brussels (Belgium);

At the European Physical Society Conference on High Energy Physics (EPS-HEP) in July 2021, the results were for the first time publicly presented by CMS Physics Coordinator in "Highlights from the CMS Experiment" talk.

Part I

Physics introduction

Chapter 1

The Standard Model and Beyond

1.1 Introduction

Starting from the late 19th century and progressing in the first half of the 20th century, the theories and discoveries of thousands of physicists have led to significant insight into the fundamental structure of matter. By the 1960s, physicists had proposed quite a collection of what they assumed to be fundamental particles, basic building blocks of matter that could not be resolved any further into sub-pieces.

In 1964, theorists Murray Gell-Mann [5] and George Zweig [6] theorized that many components of the so-called "particle zoo" were composite particles that consist of even smaller parts, which are now called quarks. Thus the list of fundamental particles was further reduced and the description of the fundamental forces which govern the interaction between particles themselves was added. This was the outset of the development of the Standard Model of particle physics. The first references to the so-called "Standard Model" can be found in papers published in the 1970s [7, 8].

To this day, the Standard Model (SM) has successfully interpreted nearly all experimental results and accurately predicted a wide variety of phenomena, getting even more credit with the latest discoveries such as top quark observation (1995) [2] and Higgs boson discovery (2012) [3, 4].
Even though it is considered the most solid description of the subatomic world, it falls short when trying to address the full picture. Those unexplained physics observations have inspired the big hunt for new physics that has drawn the creation of so many new experiments and that has fed fresh exotic theories.
This thesis cooperates in this attempt by confronting one of those exotic models with the experimental data.

1.2 The Standard Model of Elementary Particles

Figure 1.1 shows the building blocks of the Standard Model. They are either matter particles, everyday matter, or exotic matter created in particle accelerators and in the early universe, or they are the additional force-carrier particles.

In the SM, the elementary particles are grouped into two main categories on the basis of the statistic they obey and consequently of the spin: fermions and bosons.

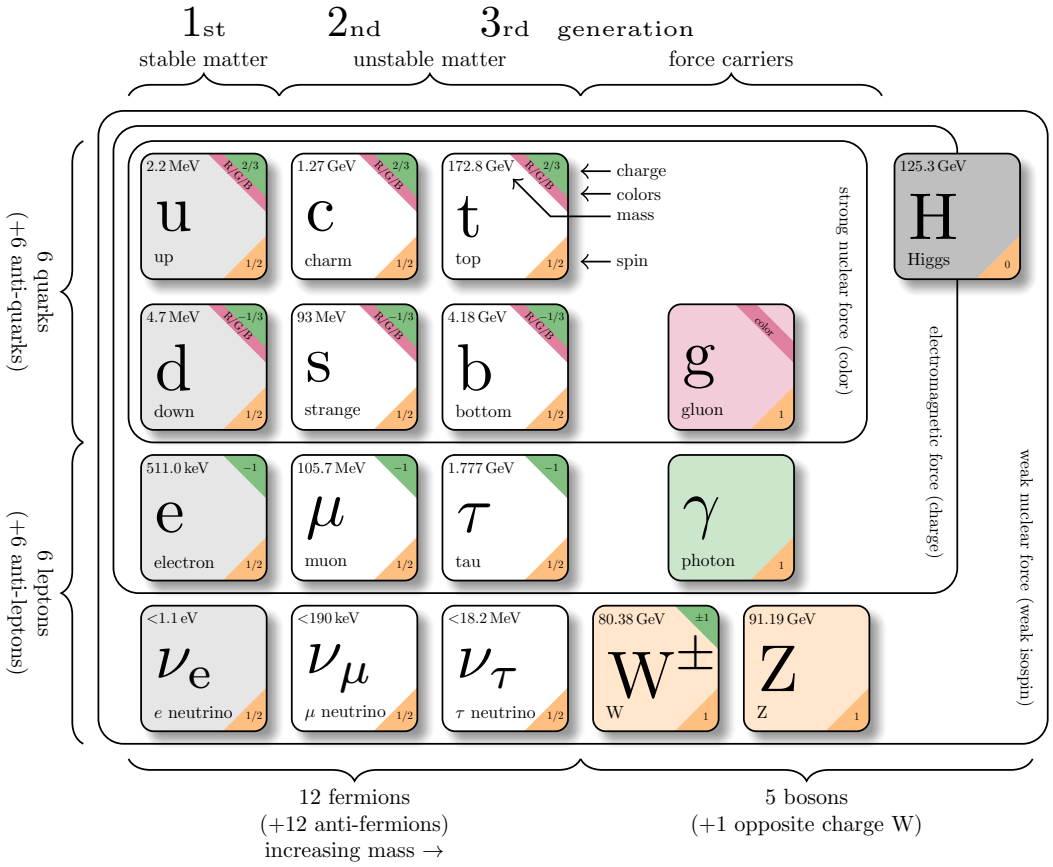

FIGURE 1.1: Elementary particles of the Standard Model (Courtesy of W. Verbeke.)

The fermions are particles that follow Fermi-Dirac statistics and correspondingly have half-odd integer spin (1/2, 3/2, 5/2...). They obey the Pauli exclusion principle and therefore they have different symmetry properties, as opposed to bosons when exchanging two identical particles: the total wave function of a system of two identical fermions is antisymmetric. This leads to the fact that, in a rigorous way, if two identical (in spin and space coordinates) fermions interchange, the total wave function changes its sign. Thus, two or more identical fermions can not simultaneously exist in the same quantum state. On the contrary particles with an integer spin like the bosons which follow Bose-Einstein statistics do not obey the Pauli exclusion principle and can occupy the same quantum state.

In the Standard Model, there are two types of elementary fermions: quarks (which form hadrons such as protons and neutrons) and leptons. Moreover, the fermions are grouped into three generations and each generation has two types of leptons and two quarks. One of the two leptons has one unit electric charge -1, the other one is neutral; the two quarks have charges $-1/3$ (down-type) and $+2/3$ (up-type). Between generations electromagnetic and strong interactions are identical while particles differ by their flavor quantum number and mass. The first generation consists of electrons (e) and electron neutrinos (ν_e) and of *up* and *down* quarks. All the everyday matter is composed by up-down quarks and electrons.

The second generation is made of muons (μ) and muon neutrinos (ν_μ) and of *charm* and *strange* quarks. The third generation is composed by taus (τ) and tau neutrinos (ν_τ) and by *top* and *bottom* quarks. The particles of higher generations have larger masses than the preceding ones, this has the effect that leptons and quarks of the second and third families are more unstable with shorter life-times and can easily decay back to elements from the first generation.
Each of the 12 fermions has an anti-matter particle which presents all the charges with opposite signs.

The fermions interact by exchanging bosons. The elementary bosons are force carriers and each of them is associated with a fundamental force. The photon (γ) is the mediator of the electromagnetic force, it has spin equal to 1, it is neutral and massless. The $W^\pm$ and Z are mediators of the weak force, they have spin 1, the $W^\pm$ have unitary charge (+1 or -1) while Z is neutral; they are heavy ($M_W = 80.379 \pm 0.012$ GeV [9], $M_Z = 91.1876 \pm 0.0021$ GeV [10]) and very short-lived. The quarks possess color charge which means they are subject to the strong interaction mediated by the gluons (g) which themselves carry color charge. Because of a property of the strong interaction known as *color confinement*, quarks can not exist isolated. Therefore quarks and gluons must cluster together to form hadrons that are color neutral (white) and which can exist and propagate freely. The hadrons can be made of either a quark and an anti-quark, *mesons* or three quarks, *baryons*. The mesons are composite bosons (spin 0 or 1) while baryons are composite fermions. Quarks, besides interacting through the strong force, can also transform into quarks of another flavor through the weak interaction by absorbing/emitting a W boson. The strengths/probabilities of the weak interactions between the six quarks do not have all the same magnitude (some are more preferable) and they are described by the values in the Cabibbo–Kobayashi–Maskawa matrix [11].
The massive bosons get their mass thanks to the interaction with the quantum field of the Higgs boson. The so-called Brout–Englert–Higgs (BEH) mechanism refers to the generation of masses for the three weak gauge bosons (W, Z) through electroweak symmetry breaking [12,13]. The mathematical treatment of the Standard Model and of the BEH mechanism is presented in Section 1.3.
The last fundamental force, gravity, is not included in the Standard Model framework.

The leptons are not affected by the strong interaction while they are subject to electromagnetic (only charged leptons) and weak interactions. As already said, the six leptons are organized in three generations, then are arranged in three left-handed weak isospin doublets where charged and neutral leptons share the same left-handed helicity. Each doublet has a different lepton number which has to be conserved during all the interactions implying that leptons and anti-leptons must be created in pairs of a single generation. The only violation of this universal lepton number conservation can be observed in the weak interaction in the neutrino oscillations where transformations between different generations occur. Neutrino oscillation and the obvious consequences are going to be extensively explained in Section 1.4.

1.3 The mathematical formulation of the Standard Model

This section describes the mathematical framework of the Standard Model of particle physics, which is a gauge Quantum Field Theory (QFT). For an extensive discussion and explanation of QFT and of the Standard Model refer to Ref. [14].

1.3.1 Quantum Field Theory and Gauge invariance

In a QFT theory, the fundamental objects are described as quantum fields with specific transformation properties governed by a set of symmetry groups. The fields are: the *fermion* fields ψ, the *electroweak boson* fields W_1, W_2, W_3, and B, the *gluon* field G_a and the Higgs field ϕ.
The description of QFT starts with a Lagrangian density $\mathcal{L}$, which completely determines the dynamics of its quantum fields. It is a function of the fields in the system and their derivatives, and possibly the space-time coordinates; minimizing the action ($\mathcal{S}$), which is the space-time integral of $\mathcal{L}$, the equation of motion can be extracted:

$$\mathcal{S} = \int \mathcal{L}(x)\, d^4x, \tag{1.1}$$

where x is the space-time coordinate.

The complete Standard Model Lagrangian contains specific terms for every one of the fundamental interactions. In the rest of the section, all these elements and the corresponding meanings are going to be illustrated and clarified.

To start, consider the Lagrangian of a free spinor field ψ which contains a kinetic and mass term:

$$\mathcal{L}_{Dirac} = \overline{\psi}(x)\,(i\gamma^\mu\partial_\mu - m)\psi(x) \tag{1.2}$$

where the Einstein notation is used which implies summation over the indices $\mu \in 0, 1, 2, 3$; m is the fermion's mass, γ^μ are the gamma matrices [1] and ∂_μ is the space-time derivative $(\partial/\partial_t, \partial/\partial_x, \partial/\partial_y, \partial/\partial_z)$. The $\psi(x)$ denotes the Dirac fermion field and the anti-fermion field, the adjoint spinor $\overline{\psi}(x)$ is defined as $\psi^\dagger\gamma^0$, with $\psi^\dagger$ the hermitian conjugate of ψ.

The Standard Model is a gauge quantum field theory which means it is based on the hypothesis that some symmetries, i.e. transformations that leave the Lagrangian of the system unchanged, are possible not only globally, but also locally. Most theories of physics are described by Lagrangians which are invariant under certain transformations of the coordinate system performed simultaneously at every point in spacetime: they are therefore said to have global symmetries. A local symmetry is one that keeps a property invariant when a possibly different symmetry transformation is applied at each point of spacetime; specifically, a local symmetry transformation is parameterized by the spacetime coordinates, whereas a global symmetry is not. The concept underlying gauge theories is precisely the postulate that Lagrangians must also possess local symmetries, i.e. gauge symmetries and be gauge invariant.
Going back to Eq. 1.2, this Lagrangian is invariant under a global U(1) phase transformation

[1] $\gamma^\mu\gamma^\nu + \gamma^\nu\gamma^\mu = 2g^{\mu\nu}$ with $g^{\mu\nu}$ the Minkowski metric.

$$\psi(x) \to \psi'(x) = e^{-i\omega}\psi(x), \qquad \overline{\psi}(x) \to \overline{\psi'}(x) = e^{i\omega}\overline{\psi}(x), \tag{1.3}$$

where ω is a constant. Thus, the requirement is for this Lagrangian to be invariant under a local U(1) transformation

$$\psi(x) \to \psi'(x) = e^{-i\omega(x)}\psi(x), \qquad \overline{\psi}(x) \to \overline{\psi'}(x) = e^{i\omega(x)}\overline{\psi}(x), \tag{1.4}$$

where now $\omega(x)$ is a function of the spacetime coordinate x. Considering then that ∂_μ would also act on $\omega(x)$, to make the Lagrangian invariant under this gauge symmetry, a new term, vector field, A_μ has to be introduced in Eq. 1.2:

$$\mathcal{L}_{Dirac} \;=\; \overline{\psi}(i\gamma^\mu(\partial_\mu + igA_\mu) - m)\psi \;\equiv\; \overline{\psi}(i\gamma^\mu\mathcal{D}_\mu - m)\psi \tag{1.5}$$

(the (x) dependence is omitted from the notation).
A_μ is the gauge field which couples to the spinor field ψ with a coupling strength g; $\mathcal{D}_\mu$ is called covariant derivate and it is defined as $\mathcal{D}_\mu = \partial_\mu + igA_\mu$.
The $\mathcal{L}_{Dirac}$ in Eq. 1.5 is invariant under local transformation ($\mathcal{L}_\psi = \mathcal{L}_{\psi'}$) requiring:

$$A_\mu \to A'_\mu = A_\mu + \frac{1}{g}[\partial_\mu\omega(x)] \tag{1.6}$$

This example has made it clear that asking the Lagrangian to be gauge invariant under a certain gauge transformation, gauge fields are naturally introduced in the $\mathcal{L}$ itself. These fields entail the existence of the gauge bosons, spin 1 particles, which couple to the fermions. Defining the field strength tensor $F_{\mu\nu} = \partial_\mu A_\nu - \partial_\nu A_\mu$[2] , the final gauge invariant $\mathcal{L}_{Dirac}$ can be written as

$$\mathcal{L}_{Dirac} \;=\; -\frac{1}{4}F_{\mu\nu}F^{\mu\nu} + \overline{\psi}(i\gamma^\mu(\partial_\mu + igA_\mu) - m)\psi \quad [3] \tag{1.7}$$

The example here was carried out for a U(1) unitary transformation which can be described by one (n^2) degree of freedom (or generator of the gauge group U(1)). U(1) is an Abelian commutative group.
As preface for the next section the general case for a special unitary group of order n, SU(n), is presented here. The special unitary group SU(n) is the Lie group of $n \times n$ matrices with determinant 1. The group is described by a set of $n^2 - 1$ gauge generators, T^a with $a \in (1, 2, ..., n^2 - 1)$. The covariant derivate of SU(n) is then $\mathcal{D}_\mu = \partial_\mu + igT^aA^a_\mu$ and it corresponds to an $n \times n$ matrix. At the same time, there are $n^2 - 1$ gauge bosons which construct the currents and mediate the interaction.
The gauge group can be Abelian, like U(1), or non-Abelian; the latter case means that the generators of the group do not commute. At a different level, it means the field strength tensor and the kinetic term for the gauge fields in the Lagrangian naturally allows for

[2]The field strength tensor is defined as $F^a_{\mu\nu} = \partial_\mu A^a_\nu - \partial_\nu A^a_\mu + gf^{abc}A^b_\mu A^c_\nu$ for the gauge field A_μ with gauge constant g. The structure constant f^{abc} vanishes since U(1), here used, in an Abelian commutative group.

[3]In this equation the mass term is not invariant under local transformations. The boson remain massless up to this point, the concept of spontaneous symmetry breaking is going to be introduced later in Sec 1.3.2.3

self–interactions of the gauge bosons. A theory with a local non-Abelian phase transformation is called a Yang-Mills theory.

1.3.2 The Standard Model gauge group

Three symmetries are identified to be necessary and sufficient in the SM theory to address and describe the experimental results of the particles and of their interactions. The Standard Model is described by a $SU(3) \otimes SU(2) \otimes U(1)$ gauge symmetry group; each subgroup has the corresponding gauge fields.
As it was explained in the previous section, the SM Lagrangian manifests a $U(1)$ local phase invariance. The associated gauge field to this Abelian invariance of the theory is called B_μ. There is then the second invariance, under non-Abelian transformations that build an $SU(2)$ group, which introduces three W_μ^i fields ($i = 1, 2, 3$), one for each of the three generators of $SU(2)$. The last invariance is non-Abelian and it forms an $SU(3)$ group. It leads to the introduction of eight G_μ^a fields ($a = 1, ..., 8$).
The covariant derivative which guarantees the full SM Lagrangian to be invariant under the three transformations described above is:

$$\mathcal{D}_\mu \;=\; \partial_\mu + ig_1\frac{Y}{2}B_\mu - ig_2\frac{\sigma^i}{2}W_\mu^i - ig_s\frac{\lambda^a}{2}G^a s_\mu \tag{1.8}$$

where Y, σ^i and λ^a represent the generators for the $U(1)$ weak hypercharge, the $SU(2)$ weak isospin and the $SU(3)$ color space, respectively. The $SU(2)$ generators in the third term of Eq. 1.8 are the 2×2 Pauli-matrices σ^i and the $SU(3)$ generators, the fourth term in 1.8, are the 3×3 Gell-Man matrices λ^a ($a = 1, ..., 8$).

In the following sections, the distinct terms in the full SM Lagrange are introduced and explained. Starting from the $\mathcal{L}_{Dirac}$ in Eq. 1.5 and using the covariant derivative of Eq. 1.8, the SM Lagrangian becomes then invariant under the three gauge groups transformations. Thus, the fermion behaviors under the gauge transformations and their interactions among all the particles of the SM are described.

1.3.2.1 The Electroweak theory

The Electroweak theory gives a unified description of the electromagnetic and the weak forces, by asking gauge invariance under the $SU(2)_L \otimes U(1)_Y$ gauge symmetry group, with the subscript L referring to the left-handed chiral structure of $SU(2)$.
Introducing the chiral projection operators:

$$P_L = \frac{1}{2}(1 - \gamma^5), \quad P_R = \frac{1}{2}(1 + \gamma^5), \qquad (\text{defining } \gamma^5 = i\gamma^0\gamma^1\gamma^2\gamma^3) \tag{1.9}$$

the Dirac spinors ψ can be projected onto the right-handed (RH) chiral states and the left-handed (LH) chiral states as:

$$\psi = \begin{pmatrix} \psi_L \\ \psi_R \end{pmatrix} \tag{1.10}$$

with ψ_L, ψ_R as left- and right-handed Weyl spinors. Replacing the spinor in the Lagrangian, massless fermions are decoupled into LH and RH particles:

$$\overline{\psi}\gamma^\mu\psi = \overline{\psi}_L\gamma^\mu\psi_L + \overline{\psi}_R\gamma^\mu\psi_R \tag{1.11}$$

where, for massless fermions, their chirality coincides with their helicity. Sustained by clear experimental results for the parity-violating nature of the electroweak theory, the weak-isospin charge appears to be different for particles with different chirality and it looks that the corresponding gauge fields interact only with LH fields. Thus the LH fermions fields are grouped in doublets, for example (e_L, ν_{eL}) or (u_L, d_L), while the RH fermions transform as singlets with zero isospin and as consequence do not interact with the gauge bosons of $SU(2)$. When the RH massless fermions do not couple with any of the interactions, they are called *sterile*. They have not yet been observed, but they are part of extensions of the SM (refer to Chapter 4).
Another important consequence of the chiral nature of the isospin transformations is that the mass term can be written as:

$$m\overline{\psi}\psi = m(\overline{\psi}_R\psi_L + \overline{\psi}_L\psi_R) \tag{1.12}$$

which violates the $SU(2)$ gauge invariance.

The physical gauge fields of the EW theory are the neutral Z boson field Z^0_μ, the two charged W boson fields $W^\pm_\mu$ and the photon field A_μ. Those physically observable gauge fields are the linear superposition of the gauge fields of the $SU(2)_L \otimes U(1)_Y$ gauge group according to:

$$Z^0_\mu = \cos\theta_W W^3_\mu - \sin\theta_W B_\mu \tag{1.13}$$

$$W^\pm_\mu = \sqrt{\frac{1}{2}}(W^1_\mu \mp iW^2_\mu) \tag{1.14}$$

$$A_\mu = \sin\theta_W W^3_\mu + \cos\theta_W B_\mu \tag{1.15}$$

where the θ_W is the Weinberg angle defined as:

$$\tan\theta_W = \frac{g_1}{g_2} \tag{1.16}$$

The relevant quantum numbers related to the $SU(2)_L \otimes U(1)_Y$ gauge group transformations are the weak isospin, T, in particular, the third component of it, T_3 and the weak hypercharge Y. As a convention, the quantum number for left-handed leptons is chosen to be $Y = -1$. All the quantum numbers of the RH and LH fermions can be derived using the following relations: $Y_R = 2Y_L$ and $Y = 2(Q_{EW} - T_3)$.

To summarize, a theory of massless fermions and EW bosons was described. The theory defines electromagnetic interactions between the photon field and the charged fermions; it includes charged and neutral current interactions between the fermions and the W and Z bosons respectively and finally allows self–interactions between the gauge bosons.

1.3.2.2 QCD, Quantum Chromodynamics

The description of the strong nuclear force in the SM is introduced by the theory of Quantum Chromodynamics which defines the interaction between quarks and gluons.
The SM Lagrangian is invariant under $SU(3)_C$ gauge transformations; as previously described, $SU(3)_C$ is a non-abelian group, with eight generators, the 3×3 Gell-Man matrices λ^a $(a = 1, ..., 8)$ and eight massless gauge bosons fields G^a_μ called gluons. The subscript "C" refers to the color quantum number or color charge, therefore the strong interaction only interests color particles, quarks and gluons, while the other fermions and bosons are singlets under this gauge symmetry.
The strong coupling constant (g_s in Eq. 1.8) decreases as the energy of the interaction that is probed increases; this phenomenon is called asymptotic freedom. Because of a property of the strong interaction known as *color confinement*, quarks can neither exist nor be observed as individual asymptotic states, thus they are always clustered in at least a pair or multi-quark particles called hadrons.

1.3.2.3 Electroweak symmetry breaking

As anticipated in section 1.3.2.1, the theory still encloses no mass term for the fermions (Eq. 1.12) since it would not be invariant under gauge transformations. The same issue appears for the mass term $-m^2 A_\mu A^\mu$ in the bosons gauge fields of Eq. 1.13- 1.14. Up to this point, the fermions and bosons are massless.

The mechanism proposed to explain the particle masses and generate in a gauge invariant way is referred to as spontaneous symmetry breaking.
In the SM this mechanism is called the Brout-Englert-Higgs (BEH) mechanism, proposed by Robert Brout, Francois Englert, and Peter Higgs in 1964 [12,13]. It introduces a complex scalar field ϕ, defined as a doublet in $SU(2)_L$ space and with non-zero hypercharge under $U(1)_Y$ and represented as a singlet in $SU(3)_C$ color space:

$$\phi = \begin{pmatrix} \phi^+ \\ \phi^0 \end{pmatrix} \tag{1.17}$$

with ϕ^+ and ϕ^0 complex fields. The Higgs field Lagrangian is:

$$\mathcal{L}_H \;=\; (D^\mu \phi)^\dagger (D_\mu \phi) - V(\phi) \;=\; (D^\mu \phi)^\dagger (D_\mu \phi) - \mu^2 \phi^\dagger \phi - \lambda (\phi^\dagger \phi)^2 \tag{1.18}$$

where $V(\phi)$ is the scalar potential, μ^2 is a mass parameter, $\lambda > 0$ is a dimensionless parameter that quantifies the self-interaction strength of the Higgs field. When $\mu^2 > 0$ the potential $V(\phi)$ has a global minimum for $\phi = 0$, while when $\mu^2 < 0$ the potential, takes the shape of a so-called "Mexican hat potential", and has non-zero degenerate minima at:

$$\phi^\dagger \phi \;=\; -\frac{\mu^2}{2\lambda} \;\equiv\; \frac{v^2}{2} \tag{1.19}$$

with v is the vacuum expectation value (VEV) of the Higgs field. A simplified representation of the two cases can be visualized in Figure. 1.2.

Starting from Eq. 1.19, it can be written $\phi^+ = {}^{(\phi_1 + i\phi_2)}/\sqrt{2}$ and $\phi^0 = {}^{(\phi_3 + i\phi_4)}/\sqrt{2}$ and knowing $2\phi^\dagger \phi = \phi_1^2 + \phi_2^2 + \phi_3^2 + \phi_4^2 = v^2$ it is clear that the minima form a four-dimensional

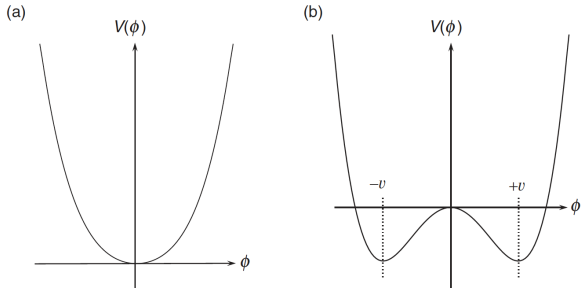

FIGURE 1.2: One dimensional representation [15] of the Higgs potential in case (a) of $\mu^2 > 0$ and minimum for $\phi = 0$ for an unbroken theory and in case (b) for $\mu^2 < 0$ and VEV for a spontaneous symmetry breaking.

sphere.
Furthermore, studying the region of the vacuum and choosing a particular vacuum in the $SU(2)$ space with $\phi_3 = v$ and $\phi_1 = \phi_2 = \phi_4 = 0$, it is possible to expand around the minimum and write:

$$\phi(x) = \frac{1}{\sqrt{2}} \begin{pmatrix} 0 \\ v + h^0 \end{pmatrix} \tag{1.20}$$

where h^0 is a scalar Higgs field. Now combining and replacing 1.8 and 1.20 into the Lagrangian 1.18 it happens that photon field remains massless while the two mass terms for W and Z bosons are naturally obtained:

$$m_W^2 = \frac{g_2^2 v^2}{4} \tag{1.21}$$

$$m_Z^2 = \frac{(g_1^2 + g_2^2)v^2}{4} \tag{1.22}$$

Identifying those terms with the electroweak gauge-bosons allows for the extrapolation of the expectation value $v = \sqrt{\mu^2/\lambda} = 246$ GeV of the Higgs field in the vacuum. The three components ϕ_1, ϕ_2 and ϕ_4 are referred to as massless Goldstone bosons and, as it was shown before, in a specific gauge choice called *unitary gauge* ($\phi_3 = v$ and $\phi_1 = \phi_2 = \phi_4 = 0$) they do vanish. The remaining degree of freedom, the scalar field h^0, is known as the Brout-Englert-Higgs boson. The mass of this SM Higgs boson is equal to $\sqrt{2\lambda}v$, with λ being a free parameter in the SM, and hence, there is no a priori prediction for the Higgs mass. The experimental measurements of the Higgs boson mass state $m_{h^0} = 125.10 \pm 0.14$ GeV [9].

It was observed for the first time by ATLAS [3] and CMS [4] experiments in 2012. About CMS results, they were searches for the Higgs boson in pp collisions at 7 TeV and 8 TeV corresponding to an integrated luminosity of 5.1 fb^{-1} and 5.3 fb^{-1} respectively. The search was carried out in five decay modes, but the most significant excess above the expected background was observed in the two decay modes that provide the best mass resolution: $h^0 \to ZZ$ and $h^0 \to \gamma\gamma$. The final signal and background yields are shown in Figure 1.3. An excess of events with local significance of 5.0σ was found 125 GeV.
From the observed decay modes, it was inferred that the new particle, h^0 is a boson with spin that is not equal to one since it decays into two photons. Finally, h^0 has no electric charge, and it has weak isospin $T_3 = -1/2$ and hypercharge $Y = 1$.

Once the mass problem of the W and Z bosons is fixed, it is necessary to address the

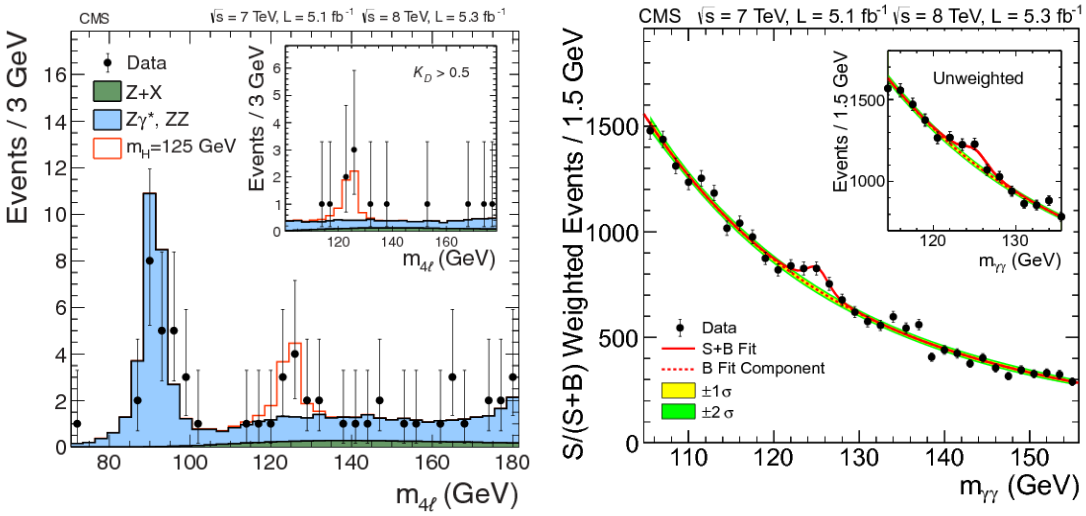

FIGURE 1.3: Left, "distribution of the four-lepton invariant mass for the $ZZ \to 4\ell$ analysis. The points represent the data, the filled histograms represent the background, and the open histogram shows the signal expectation for a Higgs boson of mass , added to the background expectation" [4]. Right, "the diphoton invariant mass distribution with each event weighted by the S/(S + B) value of its category. The lines represent the fitted background and signal, and the colored bands represent the ±1 and ±2 standard deviation uncertainties in the background estimate" [4].

problem of the generation of the mass terms for the SM fermions. Introducing Yukawa interactions between fermions and the scalar field into the SM Lagrangian, the mass terms for SM fermions are fixed:

$$\mathcal{L}_{\text{Yukawa}} = -\lambda_d^{ij} q_L^{-i} \phi d_R^j - \lambda_u^{ij} q_L^{-i} \tilde{\phi} u_R^j - \lambda_\ell^{ij} \bar{\ell}_L^{-i} \phi e_R^j + \text{hermitian conjugate} \quad (1.23)$$

where $\tilde{\phi} = i\sigma\phi^*$, q_L is a LH quark doublet, u_R and d_R are RH up and down quark singlets, ℓ_L is the LH doublet of leptons while e_R is the RH lepton singlet. λ_u^{ij}, λ_d^{ij} and λ_ℓ^{ij} are the up-quark, down-quark and lepton Yukawa coupling strengths (i, j being the generation indices).
In Eq. 1.23, the Yukawa Lagrangian, it is clear the absence of the mass term for the neutrinos; this remark is going to be crucial when the neutrino flavor oscillation observations will be presented.

To conclude, while the boson mass terms are determined by a gauge principle, the fermionic couplings with the Higgs field are not. Consequently, the corresponding Yukawa coupling constants (or the fermionic masses) are free parameters of the theory in contrast with the bosons masses which are established by the couplings of the gauge interactions and the VEV of the Higgs field.

1.4 Beyond the Standard Model

The SM describes exceptionally well nearly all the processes that have been observed in particle physics, and its predictions do agree with an outstanding level of accuracy with the results from numerous precision measurements. Even though the theory has not shown any decisive evidence of where it can fail or where the formulation can be inaccurate, we know by now that SM does not cover the full picture and there are several indications that other fundamental physics remains to be unmasked.

In this section, a few of the open questions in physics are very briefly listed and described trying to show why new physics beyond the SM is to be expected. Furthermore, some simplified explanations of such possible theories or extensions are provided. They will be discussed as either the scenarios with additional particles and symmetries or as the introduction of a more general theory for very high energies while considering the SM as an effective theory at current or lower energy scales.
Taking into account the context of this work, the focus will be heavily steered towards the introduction of RH heavy neutrinos as Beyond the SM theory and solution.

1.4.1 Open questions of the Standard Model

1.4.1.1 Gravity

The Standard Model does not contain a description of gravitational interactions, therefore, being incomplete and failing to incorporate the general relativity theory in the SM theory itself. Proposals to describe gravity as a quantum field theory have included a possible spin-2 boson, called the graviton, as mediator of the gravitational force; however, no experimental evidence has been found up to now.

1.4.1.2 Dark matter and dark energy

It is well known today from several unquestionable cosmological observations that only roughly 5% of all the energy content of the universe consists of the baryonic matter as defined and included in the SM, then so-called *ordinary matter*. In the standard ΛCDM model of cosmology, on top of the ≈ 5% of ordinary matter, about 27% is made up of another kind of matter that appears to be not directly visible (it does not interact with the electromagnetic field) and thus is so-called *Dark Matter* (DM). The residual 68% is called *Dark Energy*. Hence DM is 85% of the total mass and up to now we can fully describe and predict only 5% of the universe. The values are obtained from observation of the CMB (cosmic microwave background) by the Planck satellite and published in this exhaustive review [16].

There are several cosmological observational indications for dark matter. We can cite the calculations of the velocity dispersion and the rotation curves of galaxies, the gravitational lensing measurements, and the distribution of the cosmic microwave background; additionally, there are the astronomical observations of the universe's current structure and the formation and evolution of structures as galaxies and nebulas.

An interesting and very clear example is the one coming from the observation of the *Bullet Cluster* (1E 0657-56) [18] (see Fig. 1.4) which is a transparent proof of DM. The *Bullet Cluster* indicates a smaller sub-cluster (on the right in Fig. 1.4) moving away from a larger

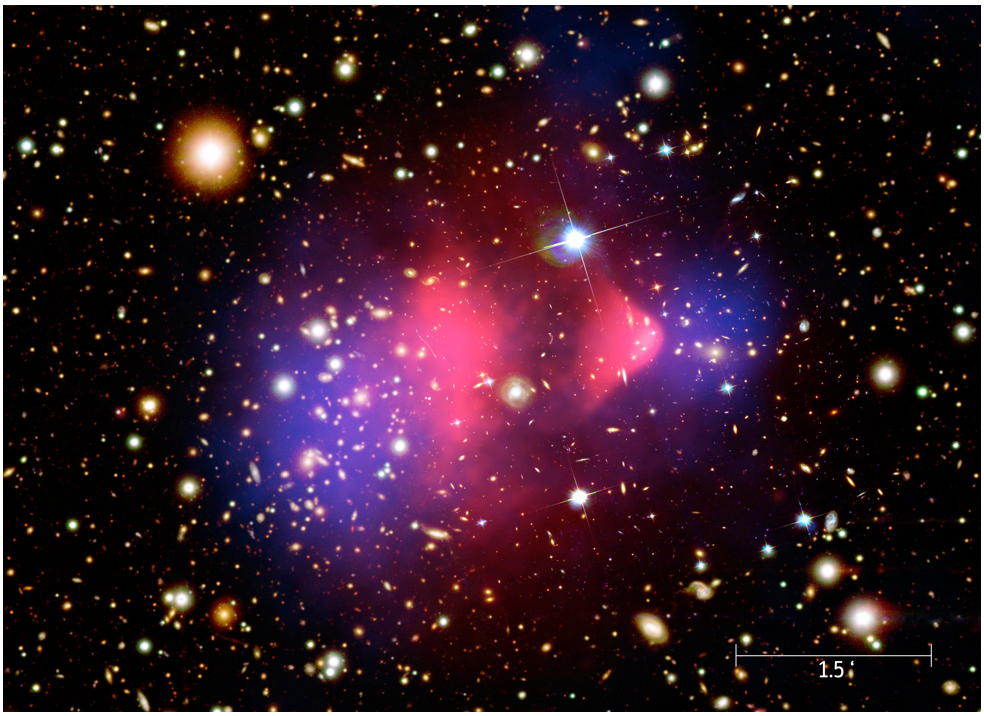

FIGURE 1.4: X-ray image (pink) superimposed over a visible light imagine (galaxies) with the matter distribution (DM plus ordinary matter) calculated from gravitational lensing (blue) [17]

one in a bigger structure consisting of two colliding clusters of galaxies. Comparing the information obtained through X-rays measurements, which quantify the hot gas of baryonic matter, with the total amount of matter (DM plus ordinary matter) detected indirectly by the gravitational lensing of background objects, the Bullet Cluster provides one of the best evidence to date for the existence of dark matter. With a statistical significance of 8σ it was addressed that "spatial offset of the center of the total mass from the center of the baryonic mass peaks cannot be explained with an alteration of the gravitational force law alone and thus proves that the majority of the matter in the system is unseen" [19].

All cosmological evidence of DM relies on its gravitational effects, which is the only type of interaction that, up to now, DM is expected to have with ordinary matter.
Since it is still unknown which is the nature of DM, dark matter searches are one of the hottest and most fascinating topics in both particle physics and theoretical physics. Several experiments have tried to detect DM through either direct detection or indirect detection and via collider experiments where the DM candidate could be produced in the collision of leptonic or hadronic beams. For clear reviews of DM searches at the CMS Experiment see [20, 21].

Many candidates for DM have been proposed, some being part of more structured theories like Supersymmetry or others being completely new exotic particles. To give a simple list of possible solutions, candidates for the non-baryonic dark matter could be particles like axions, weakly interacting massive particles (WIMPs), gravitationally-interacting massive particles (GIMPs), supersymmetric particles, and sterile neutrinos. The latter is very interesting in the scenario of this thesis work too, providing an excellent aspirant as DM [22, 23]. Sterile neutrinos (or neutral leptons) are defined to interact only via gravity and do not

couple with any gauge fields of the SM, hence the name *sterile* to distinguish them from the *active* neutrinos of the SM. In the following references a few interesting models with sterile neutrinos as DM candidate are listed [24–28].

1.4.1.3 Baryon asymmetry and CP violation

The baryon asymmetry problem is also known as the matter-antimatter asymmetry problem and outlines the imbalance between the baryonic matter and the anti-baryonic matter in the observable universe.
At the Big Bang instant, it is believed that same amount of matter and antimatter was produced, but the clear disproportion we observe today and in the early universe suggests that some physical laws must have operated differently for matter and antimatter. As proposed in 1967 by Andrei Sakharov [29], this matter-antimatter asymmetry can only be justified if the theory allows for a violation of charge-conjugation symmetry and of parity symmetry[4]; these simultaneous violations are so-called CP violation.
The first observation of indirect CP violation was provided in 1964 by James Cronin and by Val Fitch with the "the Fitch-Cronin Experiment" [30] where clear evidence was found of CP violation in neutral kaons decays.
For a direct CP violation proof, we needed to wait till 1999 for the results from KTeV experiment [31] at Fermilab and the observation from the NA48 experiment [32] at CERN. The most recent updates come from the LHCb experiment which has announced the discovery of CP violation in neutral D meson decay [33].

The sterile neutrinos, previously mentioned, are seen as possible candidates to address the matter-antimatter asymmetry problem thanks to their different behaviors under CP transformation with respect to active neutrinos. In the following references [34–36] there are a few examples of experimental results interpretations with the sterile neutrinos in the context of CP violation theories.

1.4.1.4 Neutrino masses

In Eq. 1.23, the Yukawa Lagrangian, there are no mass terms for neutrinos. As mentioned and explained in Sec 1.3.2.1 (Eq. 1.11), it is in principle possible to add the mass term as an RH component in the Lagrangian. Nevertheless, up to this day, the RH neutrinos have not been found and it is expected to be very difficult to observe them knowing that the RH fermions do transform as singlets under the entire SM gauge group and consequently they are sterile. It was then accepted for a long time that the neutrinos would be massless particles in nature.

The whole understanding of neutrinos within the boundaries of the SM was shaken and weakened in 1968 with the results from the Brookhaven National Laboratory obtained with the Brookhaven solar neutrino detector [37]. It was observed that the number of electron neutrinos coming from the sun was significantly lower with respect to the expected value using solar-model calculations of the neutrino flux from the decay of ^8B[5] inside the sun.

[4] Parity transformation is the inversion of the sign of one of the spatial coordinates; P-symmetry refers to equations and processes with are invariant under mirror inversions. All the interactions of elementary particles but weak interactions are symmetric under parity.

[5] For the experiment at the Brookhaven National Laboratory, the calculations of the flux of solar neutrino coming from boron-8 decay were used: $^8B \rightarrow {}^8Be + e^+ + \nu_e$. For a simple scheme and explanation see webpage [38].

This was the first hint of the so-called *solar neutrino problem.*
The explanation for this deficiency and for the other observed "neutrino anomalies" during those years was found to be the existence of neutrino flavor oscillations, theoretically predicted in 1957 by Bruno Pontecorvo [39].
The first crucial evidence for these speculations arrived in 1998 with the results from Super-Kamiokande Observatory [40]. The data showed an angularly dependent deficit of muon neutrinos, ν_μ which is not consistent with the expectations based on the calculation of the atmospheric neutrino flux. The difference in angular distribution between neutrinos coming from above the detector and the one coming from below (going through the earth) suggested a higher survival probability for ν_μ traveling a shorter distance.
The first direct observation of the oscillation of the electron neutrino to other flavors was only in 2001 [41] at the Sudbury Neutrino Observatory in Canada. The experiment was designed to detect solar neutrinos from the decay of ^8B via the charged current (CC) reaction on ^2H and by elastic scattering (ES) of electrons; the first reaction (CC) was sensitive only to ν_e, while the ES reaction also to ν_μ and ν_τ. Starting from the assumption that the fusion processes in the sun produce only electron neutrinos, a flux of ν_e equal to the one calculated from ^8B decays was expected. The total flux of electron neutrino was instead found to be much lower than the predictions (as for [37]) but the total rate, $\nu_e + \nu_\mu + \nu_\tau$ was surprisingly in line with the number of neutrinos expected to arrive from the sun. This was the first direct evidence of the neutrino flavor oscillation, i.e. neutrinos change flavor when traveling long distances. The phenomenon in which a neutrino can be created with a specific lepton number and then, after being propagated through space, can be measured to have a different lepton number, is called neutrino oscillation and it can happen only if the neutrinos have a non-zero mass. Then, the main question would be how the neutrino masses arise.

One of the most promising explanations is the addition of the Majorana mass term in Eq. 1.23. This theory, which is the main topic of this thesis, is going to be extensively explored in Chapter 4.

1.5 Summary

In this chapter, the Standard Model of particle physics was presented.
The elementary particles, their properties, and the fundamental forces with their force carriers were introduced. In the Standard Model, the elementary particles are grouped into two main categories on the basis of the statistic they obey: fermions and bosons. The fermions, specifically quarks, charged leptons, and neutral leptons form what we name matter. The fermions interact by exchanging bosons which are force carriers and each of them is associated with a fundamental force: the photon (γ) is the mediator of the electromagnetic force, the $W^{\pm}$ and Z are mediators of the weak force and the gluons are mediators for the strong force. To complete the picture, the Brout–Englert–Higgs (BEH) mechanism was introduced which refers to the generation of masses for the three weak massive gauge bosons (W, Z) through electroweak symmetry breaking.
A short historical walk-through of the Standard Model discoveries and milestones is presented as well as a description of the mathematical framework of the Standard Model of particle physics, the gauge Quantum Field Theory.
Then we selected a few challenges that particle physics encounters: the baryon asymmetry, new physics in the neutrino field, and the inquiry for Dark Matter. All three items are subjects of the two searches presented in the last two chapters of this work. In this thesis, the focus will be steered towards the introduction, the explanation, and then the quest for the heavy neutral leptons.
First, the CMS experiment will be introduced in Chapters 2 and 3, then the heavy neutral leptons model will be explained in Chapter 4 trying to show the reason behind the huge enthusiasm about this topic. In the past $\sim$ 10 years a very active research community has arisen, and an impressive number of papers and several proposals for new experiments were published. Considering that, finally the two searches for heavy neutral leptons at CMS are presented in Chapters 6 and 7 at which the author has firsthand participated during her PhD.

Chapter 2

The CMS experiment at the LHC

This chapter outlines the main features of the Large Hadron Collider (LHC) in Section 2.1 and of the Compact Muon Solenoid (CMS) detector in Section 2.2.

2.1 The Large Hadron Collider

The accelerator structure at CERN is a chain of machines that progressively accelerate particles to higher energies. Before delivering the beam into the next stage in the succession, each machine increments the energy of a beam of particles.
The Large Hadron Collider (LHC) [42] — the last step in this sequence — is a circular particle accelerator located at the CERN laboratories in Geneva operating since 10 September 2008. It is designed to accelerate hadrons (like protons, Lead-ions, Xenon-ions) and to operate at the center-of-mass energies up to 14 TeV. The circular ring is installed in a tunnel of 27 kilometers where the Large Electron-Positron (LEP) collider [43] was previously located. Several other accelerators in the succession have their own experimental areas where beams are used for experiments at lower energies. A graphic representation of the CERN accelerator complex is shown in Figure 2.1.

The LHC consists of accelerating components as well as superconducting magnets to focus the hadrons, keep them on the right trajectory and squeeze them tight together right before the collision point. The protons are accelerated in opposite directions in two distinct accelerator tubes which cross at four interactions points where the protons are made to collide. At the interaction points along the ring, four experiments are located with the aim to reconstruct the sub-atomic particles made at the moment of the high-energy collision. The protons are grouped in bunches which are accelerated in steps using the full accelerator chain consisting of a linear accelerator, boosters, synchrotrons, and, in the end, they are injected into the LHC with energy of 450 GeV. In the LHC ring, a system of superconducting magnets further accelerate them up to 6.5 TeV (7 TeV) [1] to achieve center-of-mass energy of 13 TeV (14 TeV). Every 25 ns collisions between proton bunches occur meaning 40 million bunch crossing per second. At full regime during data taking time period about 2800 bunches travel in the LHC rings and each bunch is made of up to 1.1×10^{11} protons.

The four experiments located at the four interaction points are ALICE [45] (A Large Ion Collider Experiment), ATLAS [46] (A Toroidal LHC ApparatuS), CMS [47] and LHCb [48] (Large Hadron Collider beauty) (refer to Figure 2.1).

[1] 14 TeV is the energy value the LHC was initially designed for. During the last years 2016-to-2018 of data-taking the operational value for the center-of-mass energy was 13 TeV.

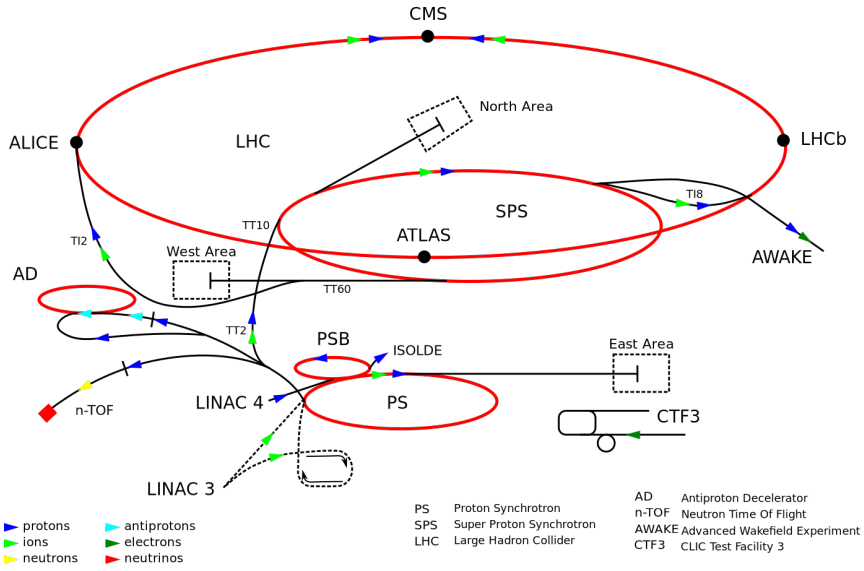

FIGURE 2.1: The LHC is the largest ring (top) in a complex chain of particle accelerators. The smaller machines are used in a chain to help boost the particles to their final energies and provide beams to a whole set of smaller experiments, which also aim to uncover the mysteries of the Universe [44]

ALICE experiment is designed to study the presence and the properties of the hypothetical quark-gluon plasma formed during heavy ions collisions. LHCb is designed to be very sensitive in analyzing the properties of the B and D mesons. The last two, ATLAS and CMS are general-purpose detectors designed to investigate a vast range of physics scenarios starting from the search and discovery of the Higgs boson as far as exotic searches for extra dimensions and dark matter.

There are a few parameters that are accelerator-dependent but worth mentioning because are also very important for the physics analyses. They are the instantaneous and integrated luminosity, the number of simultaneous collisions in the same bunch crossing and the center-of-mass energy of the proton-proton collisions.
The instantaneous luminosity is defined as a time-dependent parameter, $d\mathcal{L}/dt$, which correlates the number of collisions (N) in a certain amount of time (t) and the cross-section of a given process:

$$\frac{dN}{dt} = \frac{d\mathcal{L}}{dt}\sigma \tag{2.1}$$

The unit of the instantaneous luminosity is $b^{-1}s^{-1}$, where 1 barn = 10^{-24} cm^2 and it depends on the number of bunches in the proton beam, on the number of protons per bunch, and on the beam optics.
The integrated luminosity is the integral of the instantaneous luminosity over time, and relates the cross section of a given process to the number of events N of that process:

$$\mathcal{L} = \int \frac{d\mathcal{L}}{dt}dt = \frac{N}{\sigma} \tag{2.2}$$

The LHC was designed to deliver instantaneous luminosity up to $10^{34}cm^{-2}s^{-1}$.

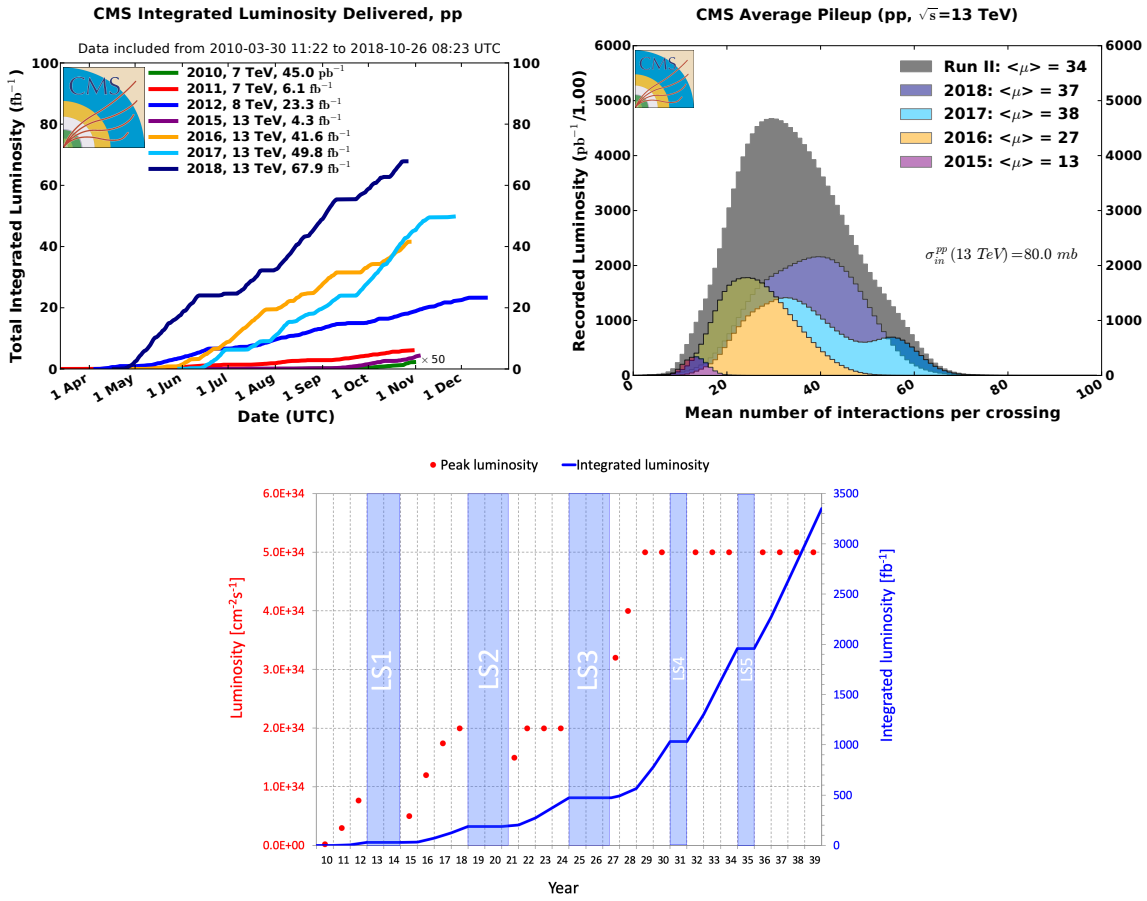

FIGURE 2.2: Top-left: integrated luminosity delivered to the CMS experiment; top-right: distribution of the average number of interactions per crossing (pileup) for pp collisions in 2015 (purple), 2016 (yellow), 2017 (azure), 2018 (periwinkle), and full Run2 (gray), [49]. Bottom: scheduled and projected integrated and instantaneous luminosity at the LHC [50].

Figure 2.2 (top-left and central plots) shows the schedule of the Large Hadron Collider from the start to the following years of operations. The LHC has delivered two outstanding runs of data taking exceeding its design specifications: the first phase, Run1 (2010-2012) at center-of-mass energy of 7 and 8 TeV and total delivered integrated luminosity of 29.4 fb^{-1}; the first three years of data taking proved the physics potentiality of the LHC with, among others, the Higgs boson discovery. The second run, Run2 (2015-2018) started after two years Long Shutdown when the machine and the detectors were consolidated to be able to run at the full capacity with center-of-mass energy of 13 TeV and total delivered integrated luminosity of 162.9 fb^{-1}.

The increase in luminosity over the years was the result of improvements in the beam quality and optics which led to a higher number of pp collisions per bunch crossing. This quantity is referred to as pileup, PU which is shown in the top-right plot in Figure 2.2. The average $\langle PU \rangle$ for Run2 is 34. On one hand this large number of collisions per bunch crossing expands the physics reach of CMS and ATLAS because of the higher probability of an episode of a rare collision; however most of the PU interactions pollute the information of the event being mostly low energy and less interesting to look for new physics models.

Thus it is a challenging task for the detector and for the reconstruction algorithms to be able to disentangle and reconstruct each single pp collision per single bunch crossing.

2.2 The Compact Muon Solenoid

The Compact Muon Solenoid (CMS) detector is located at one of the four collision points along the LHC ring, at LHC P5 in Cessy in France.
CMS is a multi-purpose detector designed to observe any new physics phenomena that could appear at proton-proton collision. CMS behaves like a high-speed camera capturing instant frames of particle collisions up to 40 million times per second. The detector aims to recreate a photograph of the collision by trying to identify the particles created after the collision and measuring their energies and momenta.
The idea behind the design was to create, around the place where the two proton beams cross each other, a structure of concentric cylindrical layers in order to be able to track and measure the path of the particle escaping from the center.

2.2.1 The CMS coordinate system

The coordinate system used by CMS is a right-handed system. It is defined locating its center in the nominal interaction point, the y-axis is vertical pointing upwards, the x-axis is radial pointing inward towards the center of the LHC ring and the z-axis coincides with the direction of the beam (counter-clockwise beam) (refer to Figure 2.3). The azimuthal angle ϕ is defined from the x-axis in the x-y plane and the polar angle θ is measured from the z-axis in the same transverse plane meaning x-y plane.

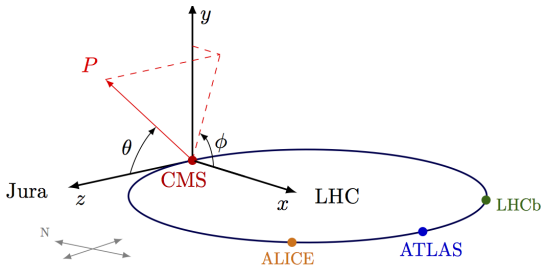

FIGURE 2.3: A scheme of the coordinates system used by CMS [51].

For an object of energy E and momentum $\overrightarrow{p}$, rapidity, y and pseudorapidity, η are defined as:

$$y = \frac{1}{2}\ln\frac{E+p_z}{E-p_z} \approx \eta = \frac{1}{2}\ln\frac{|\overrightarrow{p}|+p_z}{|\overrightarrow{p}|-p_z} = -\ln\tan(\frac{\theta}{2}) \tag{2.3}$$

The approximation of the rapidity with the pseudorapidity is possible for relativistic particles with $p_T \gg m$. The rapidity is used to measure the angular distance between particles, $\Delta R = \sqrt{\Delta y^2 + \Delta\phi^2}$ which is Lorentz invariant under boosts along the beam direction. With the prior approximation, the ΔR quantity is often defined as $\Delta R = \sqrt{\Delta\eta^2 + \Delta\phi^2}$.
Finally, using the x and y components, the transverse variables are defined: the transverse momentum, p_T and the transverse energy, E_T.

The schematic representation of the CMS detector and its parts is shown in Figure 2.4

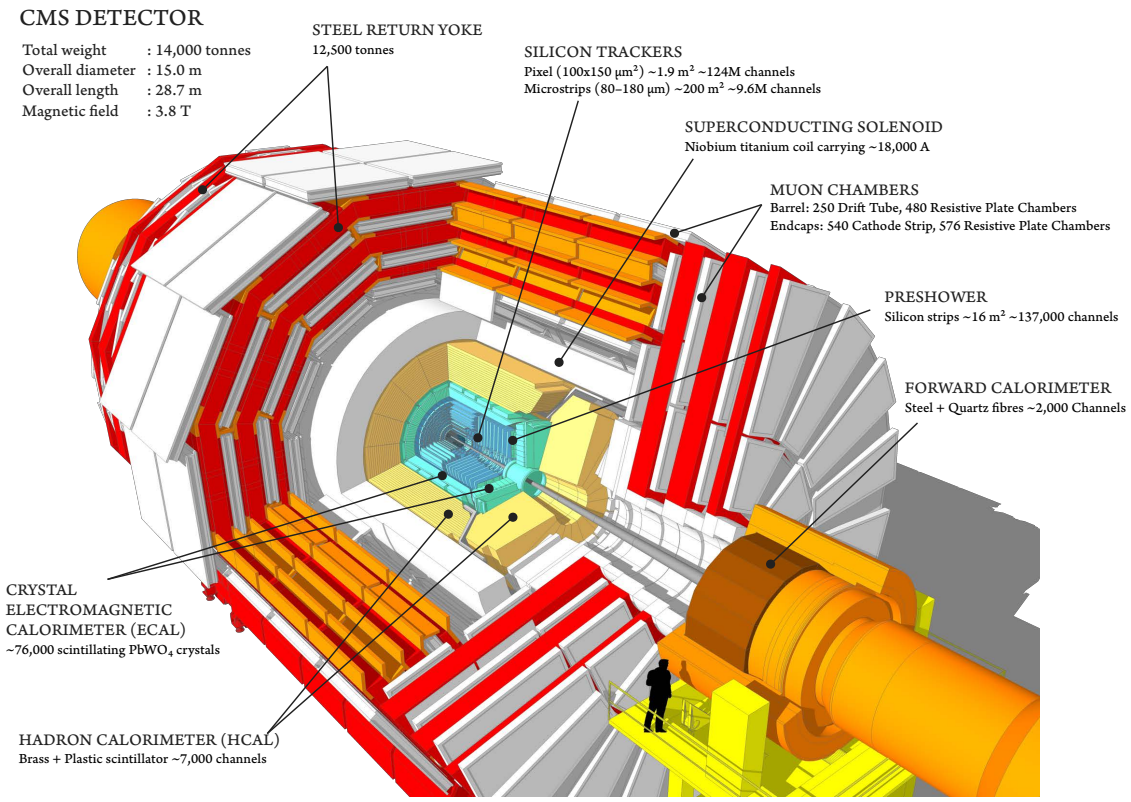

FIGURE 2.4: A scheme of the CMS detector and its parts [52].

2.2.2 CMS detector

With the CMS detector it is possible to detect photons, electrons, muons and hadrons (neutral and charged) by measuring their energies and flight directions. To be able to achieve such results, CMS is made of a system of sub-detectors each of which contributes with measurements of specific properties and quantities of different particles. The overlap and combination of all the information from the sub-detectors allow to identify and measure the properties of the particles produced during the collision [53]. Beginning with the region at the immediate proximity to the interaction point, a charged particle meets first the tracker where its trajectory is measured. This measurement is possible thanks to the presence of the magnetic field, created by the solenoid, which bends the charged particle tracks. Subsequently, there are the electromagnetic (ECAL) and hadronic (HCAL) calorimeters where electrons/photons and hadrons are respectively absorbed and their energies measured. Finally, the muons, getting through the calorimeters, enter into the muon chambers where the whole trajectories are measured [53]. The full reconstruction procedure is explained in the following Chapter 3 in Section 3.1.

The subsystems of the CMS experiment are listed and briefly described in the following paragraphs.

2.2.2.1 The superconducting solenoid

The central element of CMS is a solenoid magnet of 6 m internal diameter which is made of a cylindrical coil of superconducting fibers. It provides a magnetic field of 3.8 T inside the solenoid along the z-axis. The area in the barrel region outside the solenoid feels a magnetic field of about 2 T. In the endcaps, the magnetic flux has an irregular shape and a detailed map is used to delineate the accurate chart.

2.2.2.2 The tracking system

The particle energy measurement is a piece of critical information to build up the full picture of the event happening at the center of the CMS detector. One way to estimate the momentum is to track the particle course through a magnetic field; the more bent the trajectory is, the less momentum the particle has. The CMS tracking system registers the course taken by charged objects passing through by spotting their location at a few fixed points which are the tracker layers. Thus, the system is able to measure the trajectories of muons, electrons and charged hadrons.

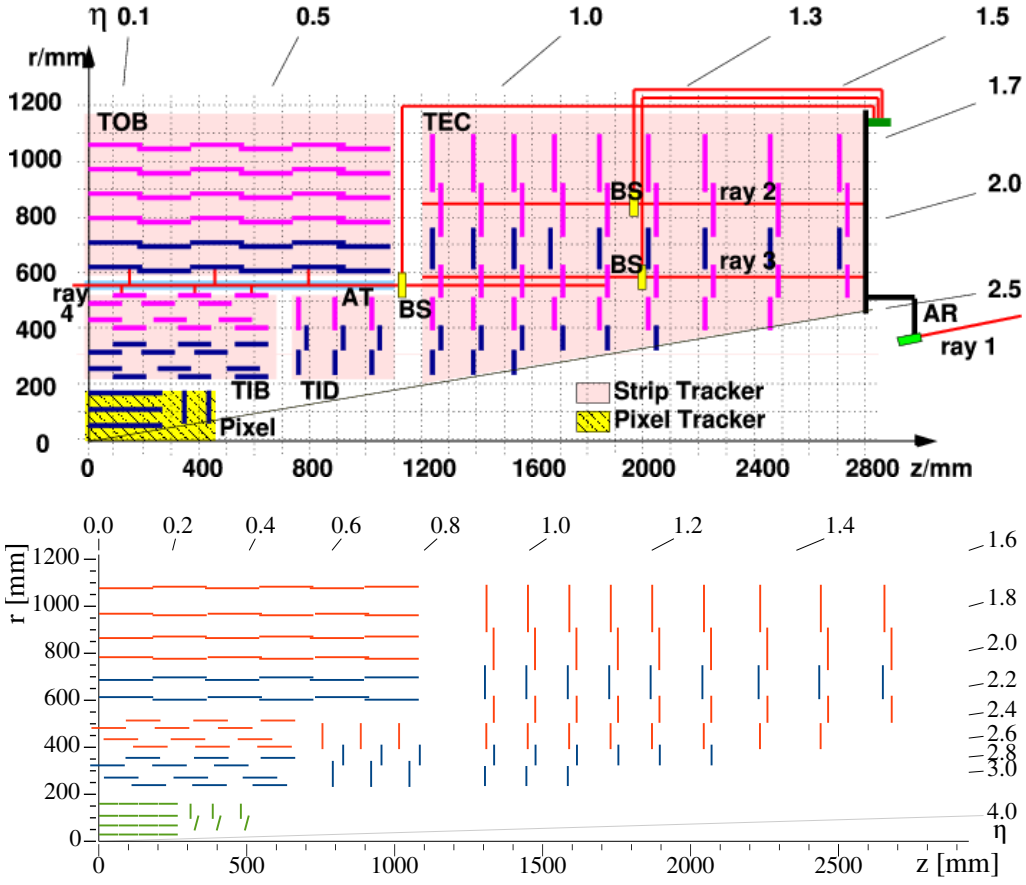

FIGURE 2.5: Top: a quarter of the CMS silicon tracker in an $r - z$ view. The strip tracker comprises several parts: the tracker inner barrel (TIB), the outer barrel (TOB), inner disks (TID), and endcaps (TEC) [54]. Bottom: sketch of one quarter of the current CMS tracking system in r-z view, 2017-2018 data taking. The pixel detector is shown in green with the additional modules [55].

The tracker modules need to have relatively fast responses, good accuracy as well as be lightweight in terms of radiation lengths in order to disturb the particle path as little as possible. Furthermore, the layers closer to the beam pipe receive the largest volume of particles thus the construction materials should have high radiation hardness to resist radiations over time.
Hence the design of the CMS tracking system is optimized to efficiently and precisely measure the trajectories of charged particles and to effectively reconstruct secondary vertices. This latter feature is of particular importance in the context of identifying particles with a relatively long lifetime leading to displaced vertices. This is a very central phenomenon to this thesis work presented in Chapter 7. The vertex position resolution and track reconstruction efficiency play a major role in the analysis acceptance, and thus in the analysis sensitivity. Those parameters are going to be described in detail in Section 3.1.1.
Additionally, the tracking system exhibits high granularity and fast response features to correctly associate each reconstructed track to the respective bunch crossing and to the primary interaction point.

The CMS tracker consists of a pixel detector (pixel Tracker) and a silicon strip detector (strip Tracker), see Figure 2.5. While a particle travels through the tracker the crossed and hit modules create small electric signals which get amplified and detected.
The original pixel detector was made of three barrel layers at radii of 4.4, 7.3, and 10.2 cm and two endcaps modules in the forward region. During the short shutdown between the data-takings 2016 and 2017, an upgraded version of the pixel detector was installed. The detector has currently four barrel layers at radii of 3.0, 6.8, 10.2, and 16.0 cm and three layers in the forward region [56]. The recent innermost modules are positioned closer to the beam pipe in order to improve the precision on the position of the interaction vertices.
The silicon strip detector consists of many parts: the tracker inner and outer barrels (TIB and TOB) making in total ten layers of strip modules in the barrel; the 6 tracker inner disks (TID), three each side; and the nine disks on each side of the tracker endcaps (TEC).
In total the tracking system is 5.8 m long and 2.6 m high, extending the coverage of the tracker up to $|\eta| = 2.5$. The total amount of sensors is 66 million for the pixel and 124 million for the strip detector.

2.2.2.3 The electromagnetic calorimeter

The ECAL detector is a fine-grained and homogeneous calorimeter made up of lead tungstate crystals. Those single crystals are extremely transparent and *scintillate* when photons and electrons pass through them. *Scintillation* occurs when in an excited atom an electron which went to an higher orbit falls back and releases energy in the form of a photon. The electrons, positrons, and photon showers are generated from the interaction between high-energy photons/electrons and dense matter. The showers give

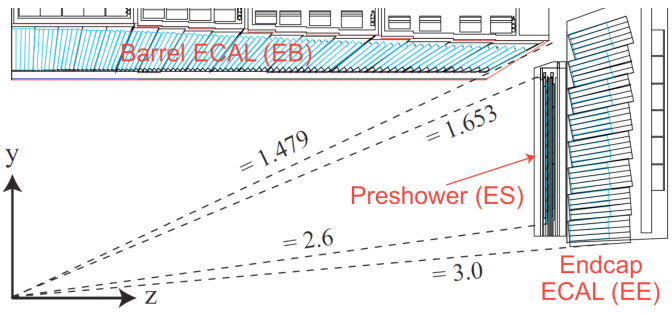

FIGURE 2.6: Geometric view of one quarter of the ECAL [57].

energy to the CMS ECAL's crystals by exciting crystal atoms. Afterwards the crystal atoms "relax" and each excited electron emits energy "falling back" as a photon in the blue light spectrum. The amount of light produced is proportional to the particle's energy allowing a fast and very precise measurement of the momentum property.

The single crystal length in the barrel region is 230 mm (220 mm in endcap) comparable to ∼26 (25) radiation lengths meaning it absorbs more than 98% of the energy deposited by the particle [58].
A scheme of the ECAL is shown in Figure 2.6. ECAL modules are placed in the barrel ($\eta < 1.479$) and the endcap ($1.635 < \eta < 3.0$) regions and a preshower detector is located just before the endcap crystals. The preshower detectors help CMS to distinguish between single high-energy photons and the less interesting pairs of low-energy photons very close to each other, i.e. coming from the decay of a π^0.
For the analyses presented in Chapters 6 and 7 the electron energy correctness is crucial for the proper electron reconstruction and identification.

2.2.2.4 The hadron calorimeter

The HCAL detector is a hermetic sampling calorimeter which means it consists of alternative layers of "absorber" and "scintillator" materials that measure a particle's position, energy, and arrival time. At the moment a hadron collides with an absorber layer (made by brass or steel) an interaction occurs generating several secondary particles. Subsequently, these bunch of particles hit successive layers of absorber interacting again and again and creating particle showers. These showers pass through the layers of scintillators causing them to emit photons in the blue-violet light spectrum. The quantity of light in a given position is summed up over several layers of tiles in depth, called a "tower". The total amount of light is a measure of the particle's energy.
The HCAL is located both inside the solenoid, the main part, and outside it, the outer barrel (HO). Inside the magnet coil, the barrel (HB) and endcap parts (HE) cover respectively the pseudorapidity ranges $\eta < 1.3$ and $1.3 < \eta < 3$. The forward region of pseudorapidity is covered by the forward hadron calorimeter (HF) up to $\eta < 5$. HF is made up of iron radiators and quartz-fiber sensors and it measures both the electromagnetic and the hadronic shower. The outer barrel, HO, ensures no energy leaks out the back of the HB undetected.

2.2.2.5 The muon system

The muon system is constructed to identify muons and to measure their trajectories. Muons can be created in the decays of numerous particles, like Higgs Boson decays ($H \to \mu\mu\mu\mu$) or RH neutrino decays as described in Chapters 5, 6 and 7. For this reason they appear to be one of the clearest and golden signatures for many searches becoming the crucial element of the CMS reconstruction and identification.
Muons can penetrate various meters of the CMS return yoke iron with minimal interactions. Therefore, the modules to detect them are located at the very edge of the detector where they are likely to be the only particles able to register a signal.
The muon system is composed of three different kinds of gaseous particle detectors inserted in the steel yoke. There are the drift tubes modules, DTs, the cathode strip chambers, CSCs, and the resistive plate chambers, RPCs. The four layers of DTs are located in the barrel and they cover up to $\eta < 1.2$ pseudorapidity range in the detector.

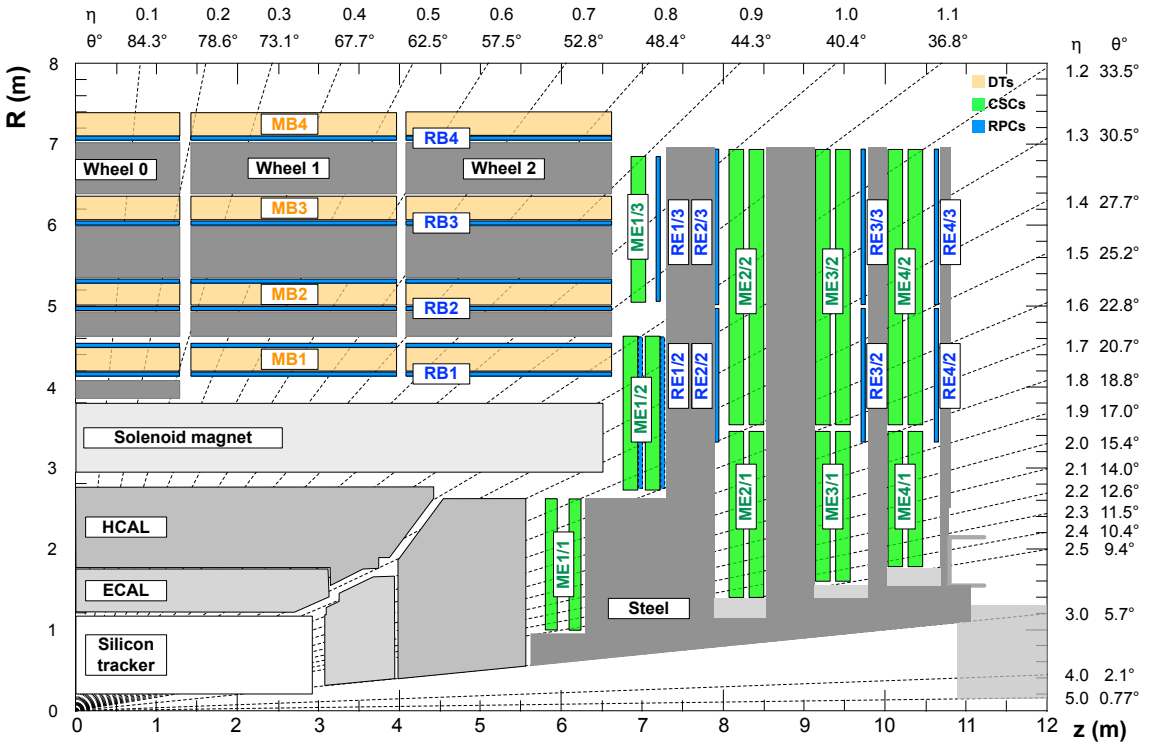

FIGURE 2.7: Geometric view of one quadrant of CMS. The grey areas are tracker, ECAL, and HCAL systems; the colored areas show the muon system and its subsystem. The drift tube, DTs, modules are labeled MB (muon barrel) and the cathode strip chambers, CSCs, are labeled ME (muon endcap). Resistive plate chambers, RPCs, are labeled RB and RE and they are mounted in both the barrel and endcaps of CMS [59].

The rates in the forward region are higher than in the barrel region, so a faster detector is needed there; this is the reason for the CSCs instead of the DTs (shorter drift distance than DTs). The four layers of CSCs are installed in the endcaps covering the pseudorapidity range of $0.9 < \eta < 2.4$.

In addition to an optimal spatial resolution given by combining the measurements from CSCs and DTs, the muon system is required to have a time resolution of the order of 1 ns. This is accomplished by adding the RPCs to the system. The addition grants for almost univocal identification of the proper bunch crossing and for excellent information of the time coincidence of track segments from distinct muon sub-modules (refer to Section 3.1.1). Combining both the great spatial resolution of DTs and CSCs and the high time resolution from the RPCs, the CMS muon system exhibits two complementary and crucial inputs for the trigger system.

The RPCs are positioned both in barrel and endcap parts up to $\eta < 1.6$. The whole pseudorapidity range of the muon system allows to measure muons up to $\eta < 2.4$.

2.2.2.6 The CMS trigger system

At the center of the CMS detector, proton-proton collisions occur every 25 ns which means a frequency of 40 MHz. However not every collision is necessarily of potential interest for the CMS physics program and moreover, there are technical limitations on the rate the collision data can be saved on disk to be analyzed offline. Thus a triggering system is needed to be able to sort between potentially interesting events and the extent of inelastic scattering events. Since the reading and storing time of the collision data is larger than the collision frequency, the viable solution is to store the information in pipelines that hold data from several collisions at the same time. Hence, to distinguish and single out particles from two consecutive pp collisions without mixing them[2], it is required that detectors have a very good time resolution and the signal from the millions of channels of different systems to be synchronized and integrated.

The CMS trigger has a two-stage architecture [60]. The first level, L1 is implemented in custom hardware and uses information from all muon systems and the calorimeters to identify events applying a fast basic identification of measured particles. The first step reduces the event rate to ∼100 kHz. The events sorted by the L1 are further refined by the high-level trigger, HLT. It is a software farm that employs information from all sub-detectors to perform a refined event reconstruction reducing the rate down to a few kHz. The events are then saved for offline analysis. The trigger selection is an irreversible process, what is not selected by it is lost and it can not be recovered [60].

A complete sequence of L1 and HLT selection criteria, including any prescale, is referred to as a trigger path.

In the two analyses presented in Chapters 6 and 7 we make use of specific trigger paths. For the first search we employ single-lepton triggers as well as double- and triple-lepton triggers in any available combination of electron and muons (refer to Table 6.1).
The second search described in Chapter 7 utilizes single-electron and single-muon triggers (refer to Table 7.1).
Among the countless available trigger paths, we picked for both analyses those with prescales equal to 1 and those with the lowest possible p_T thresholds. This choice was driven by the specific signature features characterized by the presence of very low energy leptons.

[2]There is substantial overlap between signals in consecutive events. It is referred to as out-of-time pileup (OOTPU). With in-time pileup, we refer to the number of pp collisions per bunch crossing and it is shown in Figure 2.2.

2.3 Summary

In this chapter, the LHC and the CMS detector were presented.
We briefly introduced the LHC timeline since 2010 and we listed the reached values of instantaneous luminosity and center-of-mass energy over the past years. We illustrated that the CERN accelerator chain produces 6.5 TeV proton beams circulating in the LHC tunnel and colliding in four points one of which is the CMS detector. The data analyzed in this work were collected over a three years period (2016-18) of the LHC data-taking and coincide to an integrated luminosity of 137 fb^{-1}.

We presented the CMS detector with all its sub-components and the trigger system.
We explored the detector subsystems: the tracker made up of pixel and strip parts, the electromagnetic and hadronic calorimeters, and finally the muon system. For each of those, we briefly listed some details on the detection principle, the geometry, and overall performances.

I have personally taken part in the 2017 data-taking while performing shifts as RPC "detector-expert-on-call". This activity gave me the opportunity to comprehend the complexity of the CMS detector in its completeness. In the detector control room located at P5, there is the monitoring center of all detector inputs from the gas-mixtures for the muon-system sub-detectors to the cooling system of the solenoid and the high voltage monitoring for the powered modules. At the same time, the online performances of the different layers are checked as the occupancy of the modules and the dead-time of each detector. Simultaneously from the control room it is possible to oversee the LHC delivered instantaneous luminosity, the related pileup number of vertices, and the L1 and HLT instant rates.
Being at P5 shows firsthand the importance of an attentive data-taking for high data quality. All the electronic signals recorded during each run are going to be stored as raw data and then used for the offline event reconstruction which is the subject of the next chapter.

Chapter 3

Event reconstruction in CMS

This chapter outlines the main features of the CMS event reconstruction. In Section 3.1, an explanation of the reconstruction algorithm, called *Particle flow* is given. Thus the reconstruction performances are discussed. The main focus of Section 3.1 will be on the reconstruction and identification of leptons (i.e. electrons and muons), which are central to this dissertation because of their importance in the multilepton final states of the HNL searches, as discussed in Chapters 6 and 7.

3.1 Event reconstruction

With the term "event reconstruction" we mean the identification of all final state particles which are produced in a proton-proton collision. Particles are classified according to their distinct signatures they leave in the CMS detector, as displayed in Figure 3.1.

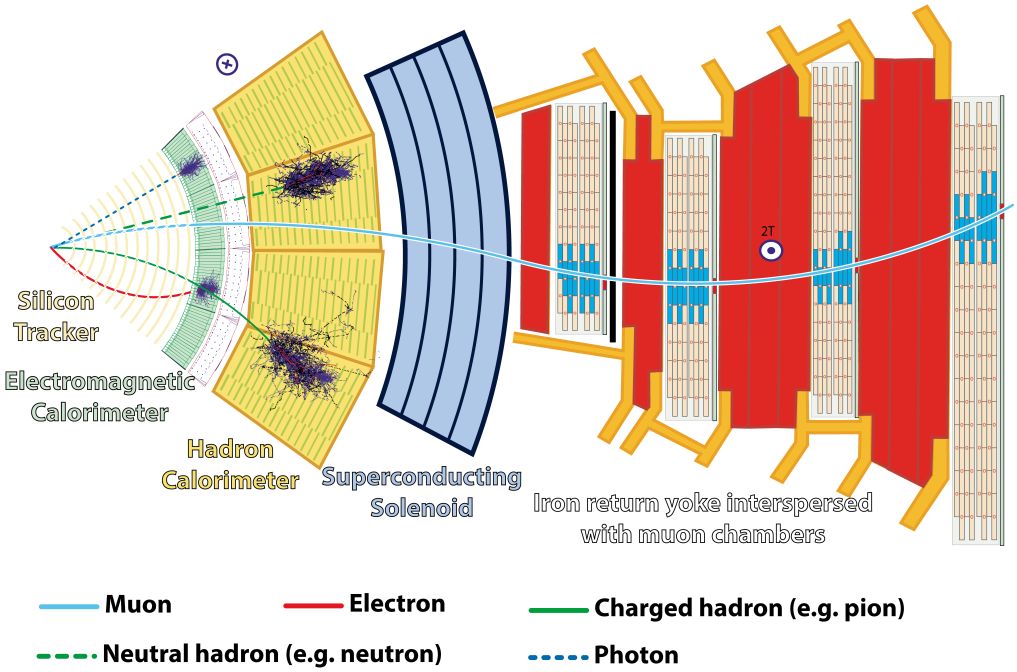

FIGURE 3.1: Geometric view of a transverse slice of the CMS detector showing its sub-detectors and how particles interact with them [61].

The CMS detector is built with the idea of cylindrical detection layers which are wrapped around the beam axis. After the collision, starting from the point where the interaction occurs, particles enter the tracker. In the tracker, the charged-particle trajectories, *tracks* and their origins, *vertices* are reconstructed using the information from electronic signals, *hits*, in the detection layers. Subsequently, electrons and photons are absorbed and stopped in the ECAL, while charged and neutral hadrons are fully absorbed in the HCAL. Finally, muons and neutrinos cross the full detector with little or zero interactions. The muons produce in the muon-system signal hits and their trajectory is finally defined. This simple event-view is graphically displayed in Figure 3.1.

This approach has led to the practice of reconstructing *physics objects* using the signals collected by specific detectors. A crucial improvement on the event description is obtained by correlating (*linking*) the basic *elements* (i.e. tracks and clusters) from all the sub-systems. Therefore, each final-state particle is classified and then the physics-object properties like mass and momentum are reconstructed by combining the information from the sub-systems. This integrated approach is called *particle flow* (PF) *reconstruction* [53] and it is going to be explained later in Section 3.1.2.

This chapter details the concept and the relevant steps of the CMS event reconstruction algorithms, paying particular attention to the aspects pertinent to this thesis (i.e. light leptons). The track and vertex reconstruction is presented in Section 3.1.1 and the particle-flow algorithm is described in Section 3.1.2. Identification and performances of muons and electrons are presented in Sections 3.1.3 and 3.1.4.
Furthermore, some effort is dedicated to the displaced lepton reconstruction in Sections 3.1.3.3 and 3.1.4.3 which is going to be central for the analysis overview presented in Chapter 7.

A topical distinction between the terms *prompt*, *nonprompt* and *displaced* leptons is needed before continuing with this dissertation. With the definition *prompt leptons*, we refer to leptons that originate from the primary interaction vertex of hard scattering collisions and they come from interesting physics phenomena. *Nonprompt leptons* are leptons from heavy-flavor decays, misidentified hadrons, muons from light-mesons that decay in flight, or electrons from unidentified conversions of photons in jets. Both prompt and nonprompt leptons (they will be called also fake leptons) are assumed to be originated in the proximity of the beam spot. Thus, the reconstructed variables that give an estimation of the impact parameters have very small values. *Displaced leptons* are leptons that originate from a separate vertex with respect to the primary interaction vertex. They are the results of the decay of particles that have a lifetime "long" enough to travel from a few mm up to m far from the collision point.

3.1.1 Track and vertex reconstruction

A precise reconstruction of interaction vertices and particle tracks is a crucial element for accurate measurement of charged particle momenta and properties. Moreover, tracks, vertices, and their successive combinations constitute an important input for pileup mitigation (Section 2.1) and for the identification of displaced vertices where long-lived particles decay. Finally, tracks and vertices are fundamental inputs to the particle-flow (PF) algorithm (Section 3.1.2).

The tracking algorithms are devised to maximize the track-finding efficiency while keeping small the contamination of fake tracks, i.e. tracks constructed from uncorrelated hits or including false hits.
The tracks are reconstructed starting from the hits in the pixel and strip tracker. The hit reconstruction follows two steps: the first, indicated as local reconstruction, is a clustering of signals in the tracker sensors. The first estimate of the position of a hit is determined based on the geometry of the single-pixel or strip while taking into consideration the Lorentz drift due to the magnetic field (more detailed info about local reconstruction can be found here: [53]). The second step is a more sophisticated reconstruction that uses the information about the irradiation status of pixel and strip sensors.
The hit efficiency is measured to be above the 99.5%[1] for both pixel and tracker hits [53]. According to the size of the cluster and the angle of incidence of particles, the final resolution in the hit position is measured to be in the range of 20 (10) and 50 μm for the pixel (strip) tracker [53].
Additional input for the track reconstruction is the identification of the LHC beam spot position, i.e. the LHC luminous region's 3D profile, and the position of the collision vertices.

The tracking algorithm used by CMS is called Combinatorial Track Finder (CTF) [62]. To lower the combinatorial complexity, an iterative procedure is applied in distinct successive iterations, each with moderate efficiency and loosened selection requirements on the track quality with respect to the step before. The Kalman filter method [63] is used for the track-finding algorithm. While taking into account the multiple Coulomb scattering on the direction of the track, the Kalman filter makes use of track seeds[2] to extrapolate the track trajectory to the successive detector module. Thus at each layer, new additional consistent hits are integrated into the trajectory and the track parameters are calculated again. The procedure starts again and the new resulting trajectory is extrapolated to the subsequent layer. In the end, tracks that do not fulfill goodness-of-fit requirements are rejected. Tracks that are "easy" to reconstruct, e.g. from particles with large p_T (which means less evident curvature) and produced in proximity to the interaction point, are reconstructed first. Therefore hits associated with these tracks are taken out, making the subsequent iterations less complex. To guarantee high efficiency, track-finding starts with trajectory seeds which are built in the innermost region of the tracker. The reconstruction efficiency for tracks with $p_T > 1$ GeV is measured to be larger than 99% for isolated muons for $|\eta| < 2.5$ and between 80 and 99% for electrons and pions [53]. The track p_T resolution depends on the p_T and η of the tracks, and it is lower than 1% for muons with $p_T \in [1, 10]$ GeV [53].

Vertices are reconstructed using high-quality tracks which are compatible with originating from the beam spot. They are then clustered based on their coordinates along the z-axis. An adaptive vertex fitting [64] developed as an iterative re-weighted Kalman filter

[1] The hit efficiency depends on the $d\mathcal{L}/dt$ and on the trigger rate, in particular in the first layer of the pixel sub-detector where the occupancy is greater.

[2] "*The seeds define the starting trajectory parameters and associated uncertainties of potential tracks. In the quasi-uniform magnetic field of the tracker, charged particles follow helical paths and therefore five parameters are needed to define a trajectory. Extraction of these five parameters requires either three 3-D hits, or two 3-D hits and a constraint on the origin of the trajectory based on the assumption that the particle originated near the beam spot*" [62].

is used to estimate the coordinates of the vertices. To each track, a weight between 0 and 1 is assigned according to the probability for that track to belong to a specific vertex. Thus, vertex weights are appointed to each vertex as the sum of the weights of all the associated tracks, and the vertices with weights inferior with respect to predefined thresholds are rejected. The reconstruction efficiency depends on the number of tracks associated with the vertex and it is estimated to be close to 100% for the cases with more than two tracks and around 98% for vertices with two tracks [53]. The resolutions vary between 10 and 100 μm [53].
Among the multiple vertices that are reconstructed one is selected as the most interesting collision to be analyzed. This so-called primary vertex (PV), is identified as the vertex with the largest p_T^2 sum of all the physics objects associated with it. The other vertices are assigned as pileup vertices.

3.1.2 The particle-flow algorithm

The PF algorithm [53] is devised to cater a global event description by linking and combining information from CMS sub-detectors.

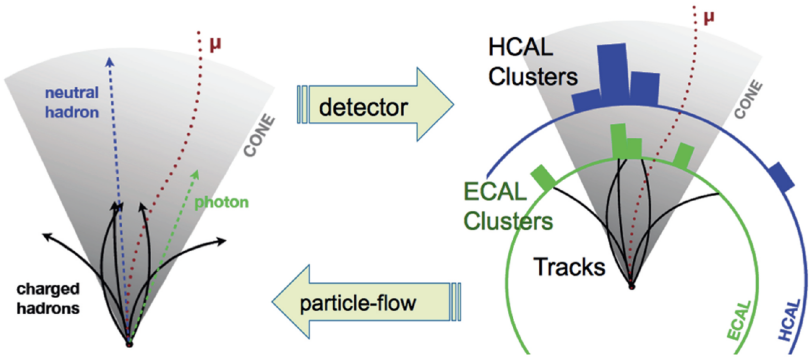

FIGURE 3.2: The output of the PF is a list of candidates like electrons, muons, photons and hadrons. The PF algorithm links information from all the sub-system to give a global description of the collision event [65].

The input of the PF are the *elements* such as tracks, vertices, tracks reconstructed from the muon system, and calorimeter clusters. The output of the PF is a list of candidates like electrons, muons, photons, and charged and neutral hadrons (see Figure 3.2). The identification of leptons, the measurement of the missing transverse energy, and the categorization of the pileup tracks are improved by the usage of the PF algorithm.

3.1.2.1 Jet clustering and reconstruction

As described in Section 1.3.2.2, quarks carrying a color charge can neither exist nor be observed as individual asymptotic states, hence they are always clustered with other colored objects around them to make together colorless objects. The collection of these objects is named jet because the components all tend to fly in the same direction, creating a "jet" of particles. This jet of hadrons originating from quarks and gluons are then identified as PF candidates. To associate these jets of hadrons to the original particles a clustering algorithm is used. Jets reconstruction is performed with a recombination algorithm which is known as

the anti-k_T algorithm (with distance parameter of the cone size of $\Delta R = 0.4$). The detailed description of the anti-k_T algorithm is not discussed in this work but the information can be found in references [66, 67].

In order to reduce the number of jets rising from mis-reconstruction or detector noise, identification requirements are applied depending on the single elements of the jets i.e. the number of particles and the amount of energy of the jet which comes from different types of PF candidates [68]. The jet momentum is set as the vectorial sum of the momenta of the particles constituting the jet. In order to alleviate the effect of pileup contribution in the jet reconstruction, charge hadrons associated to pileup vertices do not enter in the jet clustering. This scheme is known as "charged hadron subtraction" [69] and removes a considerable fraction of charged pileup particles. Subsequently, it is applied a correction to account for the contribution from neutral particles from pileup; the subtraction is based on the average transverse momentum, p_T, per unit area in the pileup jets [70–72].

Corrections on the jet energy are applied in order to correct for the remaining pileup energy contributions and for any discrepancies between jet properties in data and in simulated events. Those corrections are obtained from the ratio between the p_T of a reconstructed jet and its corresponding generated jet and they are measured as a function of p_T and η and applied to data and simulation [73]. The jet p_T resolution is derived both in data and MC and the resolution in the simulation is fixed and smeared to match the one in the data [73].

3.1.2.2 Tagging of jets originating from b quarks

The identification of jets that originate from b quarks, called *b jets*, can be achieved using specific properties and features of heavy quarks inside the jets. This technique usually called *b tagging*, is extremely important to discriminate between signal and background as it will be explained in Chapters 6 and 7.

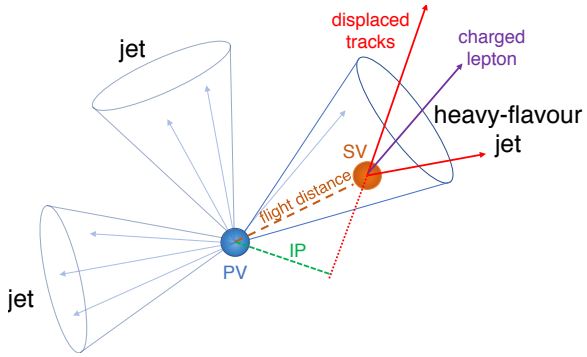

FIGURE 3.3: Schematic view of a b jet with a SV from the decay of a b hadron resulting in tracks which are displaced with respect to the PV, and hence with a large impact parameter (IP) value [74].

The b jets contain b hadron that has a lifetime of the order of 1.5 ps and a mass of about 5 GeV/c^2. Thus the b hadrons can propagate from the PV for a few mm up to one cm before decaying [75]. This results in secondary vertices (SVs) which contain displaced tracks, see Figure 3.3. With respect to light jets (coming from u, d, s quarks or gluons) b jets have larger mass and harder hadronization which means that their decay products have larger momentum and a larger number of tracks related to the jet. These signatures are exploited by the algorithms building variables to separate b jets from light jets. The results

of the b tagging are discriminator values, see Figure 3.4; large discriminator values coincide with a higher probability for the jet to be a jet originating from b hadrons [76, 77].
The b tagging performances are checked in terms of the b jet efficiency (which expresses the fraction of all b jets truly coming from b hadron that are identified as b jets) and of misidentification probability (which expresses the fraction of light jets or jets from c hadrons which are identified as b jets), see Figure 3.4.

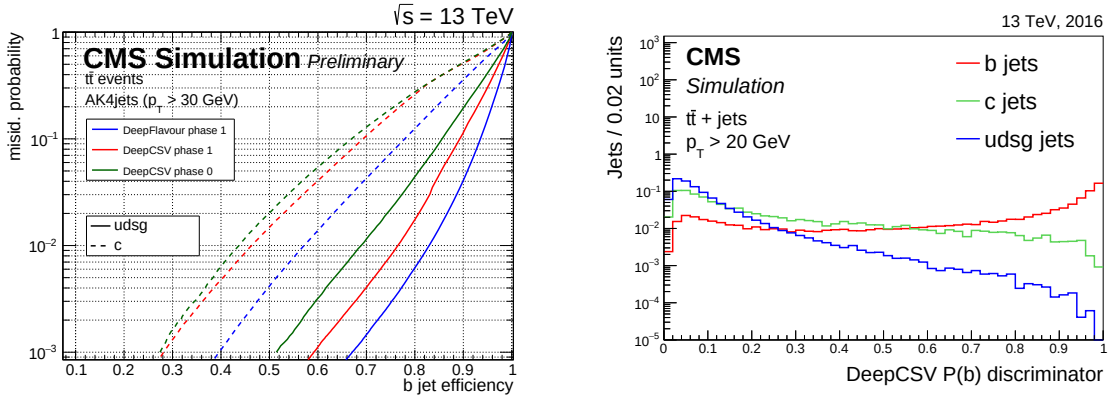

FIGURE 3.4: On the left, "performance of the DeepCSV and DeepFlavour b jet identification algorithms demonstrating the probability for non-b jets to be misidentified as b jet, as a function of the efficiency to correctly identify b jets. For comparison, the performance of DeepCSV with the 2016 detector (Phase 0) are also shown." [77]. On the right, "Distribution of the DeepCSV P(b) discriminator values for jets of different flavors in $t\bar{t}$ events. Jets without a selected track and without a secondary vertex are assigned a discriminator value of 0. The distributions are normalized to unit area" [77].

The two algorithms shown in Figure 3.4 are known as DeepCSV [77] and DeepFlavour [78]. The first is the *deep combined secondary vertex*, DeepCSV, algorithm based on a fully-connected neural network with a fixed set of input variables for preselected tracks and preselected SVs and kinematic features of the jets. The DeepFlavour [78] is an improved version of the DeepCSV. It is based on a deep neural network architecture and it does not require any prior preselections and uses a bigger number of SVs, tracks, and neutral hadrons. Looking at the left plot of Figure 3.4, fixing the misidentification probability the DeepCSV has lower b jet efficiency than DeepFlavour algorithm.
The efficiencies are calculated both in data and MC and the corrections for the discrepancies observed between data and MC are applied to simulated events as per-jet scale factors [77].

3.1.3 Muon reconstruction

This paragraph primarily describes the prompt muon reconstruction (3.1.3.2) and identification (3.1.3.1). A description will follow of the displaced case and of the new improved algorithms which have been designed for these specific scenarios (3.1.3.3, [79]).

3.1.3.1 Muon track reconstruction

Muon tracking [80, 81] makes use of information from both inner tracker and muon system. The inner tracker gives a precise measurement of the muon momentum; the muon system identifies muon objects over a wide acceptance with high efficiency. High purity in muons

is obtained thanks to the upstream ECAL and HCAL which absorb other particles (except neutrinos).
Three kinds of muon candidates are defined according to the tracking algorithms that are used, [81]:

- **standalone muon**. The tracks are built from the information from all the muon sub-detectors, CSC, DT, and RPC. It starts from seeds consisting of groups of DT or CSC segments, and the seeds are used for the pattern recognition in the muon system, to gather all DT, CSC, and RPC hits along a muon trajectory using a Kalman filter technique. The outcome of the fitting is called a *standalone-muon track*.
- **tracker muon**. These tracks are formed "inside-out". They are extrapolated from the inner tracker to the muon system with loose matching to DT and CSC segments. Each inner track that has $p_T > 0.5$ GeV and total momentum > 2.5 GeV is extrapolated to the muon chambers and if at least one muon system segment matches that track then the muon track is defined as *tracker muon track*.
- **global muon**. These tracks are built "outside-in". They are the results of the matching between standalone-muon tracks and tracker tracks. The matching is performed by comparing tracks parameters that are propagated onto a shared surface. Using data from both tracks, the final combined fit is performed with the Kalman filter technique.

About 99% of the muons produced within $\eta < 2.4$ are reconstructed either as a global muon track or as a tracker muon track (or both). In case a global muon and a tracker muon share the same inner track, they are then merged in one single candidate. Global muons reconstruction is meant to be very efficient for muons that penetrate through more than one layer of the muon system. This implicitly requires the muon track p_T to be more than 10 GeV since softer muons easily fail this due to larger multiple scattering in the material of the return yoke; for the cases with $p_T < 10$ GeV, the tracker reconstruction becomes then more efficient. For muons that are not global muons and are matched with the innermost muon station only, the probability for misidentification increases. The possibility for hadron showers to reach the innermost muon station (punch-through) becomes not negligible. In order to mitigate this effect, additional quality criteria on the muons are required at a later stage (described in the following paragraph 3.1.3.2). By using the information from both the inner tracker and the muon system, the p_T resolution, and measurement of global muons is improved in particular for $p_T > 200$ GeV. For the case of standalone-muon tracks, the muons have worse momentum resolution and a higher contamination of cosmic muons than global or tracker muons.

Reconstructed muon tracks are given as input to the PF algorithm which combines then all the information gathered from the different sub-detectors. For the muon case, the PF applies a list of selection criteria to the candidates which have been reconstructed with standalone, track and global muon algorithms.

3.1.3.2 Muon identification

Disparate sources of muons aside from the prompt ones produced in the hard scattering collision can be spotted. Muons can be originated from either decay of heavy-flavor hadrons or cosmic-ray muons going through CMS detector; they can also appear from out-of-time pileup, beam backgrounds, and chamber noise which can compromise the reconstruction.

Implementing a selection based on quality and kinematic parameters is desirable in order to discriminate between different sources and to identify the prompt muons.
According to the desired compromise between efficiency and purity, a set of different variables and selections definitions is defined [81].
This level of details, here described, is going to be recalled and used in Chapters 6 and in particular 7 where a customized and mindful selection is needed for the displaced muon case (specifically Section 7.2.3.2).

Some variables are related to the muon reconstruction itself. We can list the *track fit* χ^2, the number of hits per track (it refers to inner tracker hits, *fraction of valid tracker hits*) and for global muons, the level of *position matching* between the tracker tracks and the standalone muon tracks. Additionally the *muon segment compatibility* is an important parameter that returns values between 0 and 1 with 1 being the highest degree of compatibility. A *kick finder* algorithm is deployed to evaluate a posteriori for each muon track the probability of being a single track or the combination of two separated tracks.
Exploiting these variables, three main identification types of muons are used in CMS physics analyses:

- *Loose muon identification, (Loose ID).* A loose muon is either a tracker muon or a global muon. Loose ID tries to identify muons coming from the PV and from light and heavy flavor decay keeping very high selection efficiency and a rather low misidentification rate of charged hadrons as muons.
- *Medium muon identification, (Medium ID)* [82]. With respect to Loose ID, this selection aims to achieve more rejection of muons from hadron decays in-flight while preserving high selection efficiency. Medium muons are loose muons with tracker tracks that have at least 80% of valid hits in the inner tracker. If the muon is only a tracker muon (not a global muon), the muon segment compatibility has to be larger than 0.451. If the muon is both a tracker muon and a global muon, "the muon segment compatibility need only be greater than 0.303, but then the global fit is required to have goodness-of-fit per degree of freedom (χ^2/dof) less than 3, the position match between the tracker muon and standalone-muon must have $\chi^2 < 12$, and the maximum χ^2 computed by the kink-finding algorithm must be less than 20. The constraints on the segment compatibility were tuned after application of the other constraints to target an overall efficiency of 99.5% for muons from simulated W and Z events." [81].
- *Tight muon identification, (Tight ID).* A tight muon must be reconstructed both as global muon and tracker muon. With respect to the Medium ID, the Tight ID requirements are more stringent on the number of muon stations that have to match with the inner tracker track and on the compatibility between track and PV.

There are other two identification types of muons, *soft muon ID* and *high momentum muon ID* which are not used in the context of this thesis and therefore are not detailed in this section.

Reconstruction and identification efficiencies. The efficiencies of the muon reconstruction and identification are estimated in data and simulation events with a *tag-and-probe* method. The events are selected with two muons whose invariant mass, $M_{\mu\mu}$, is compatible with the Z mass. One of the two muons, the *tag*, is selected with tight requirements. The value of the efficiency for a specific selection (reconstruction or identification variables) is

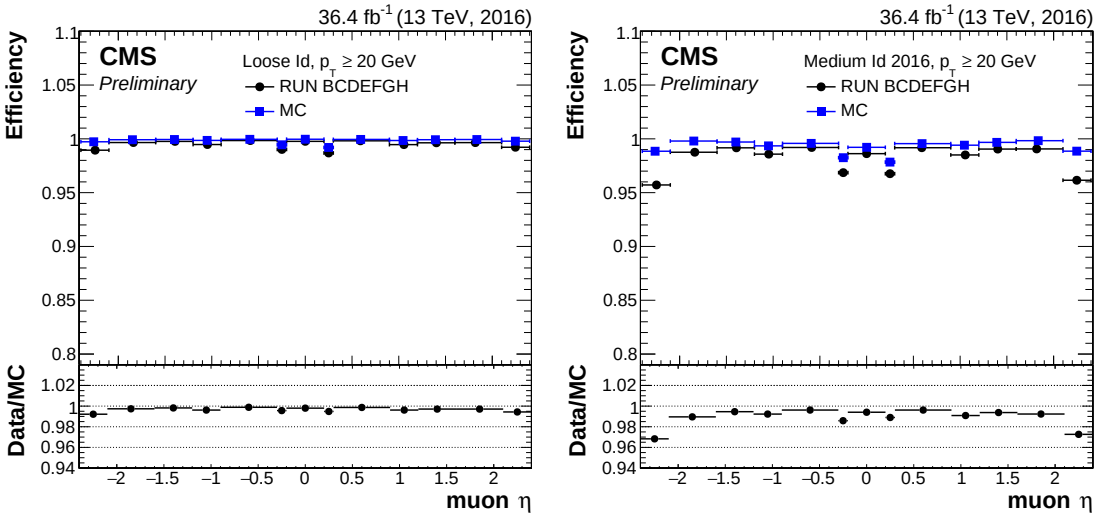

FIGURE 3.5: Tag-and-probe efficiency for muon identification in 2016 data (circle) and simulation (squared). On the left, Loose ID efficiencies as a function of η. On the right, Medium ID efficiencies as a function of η. The denominator contains tracker muons [83].

given by the fraction of the other muons, the *probes*, which pass that specific selection.The differences in efficiencies between data and simulation samples are accounted and then corrected with per-muon scale factors applied to the simulated events [81]. The performances of muon reconstruction and identification in CMS using the data collected in 2016 are shown in Figure 3.5 (details and 2017-2018 results in the reference here: [83, 84]).

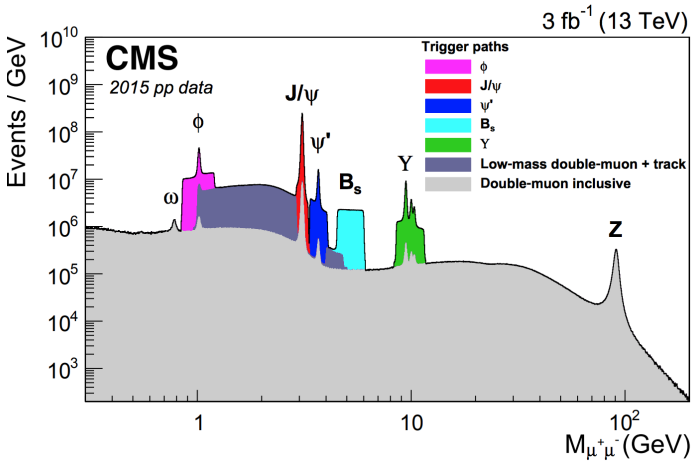

FIGURE 3.6: "The dimuon invariant mass distribution reconstructed by the CMS HLT. Data were collected in 2015 with the inclusive double-muon trigger algorithm (gray), as well as triggers dedicated to selecting resonances at low masses." [81].

Muon isolation To discriminate between prompt muons and muons coming from either the decays of heavy-flavor hadrons or the decay in flight of charged $\pi^{\pm}$s and kaons, the isolation variable appears to be one of the most critical variable to use. The PF isolation of a reconstructed lepton is defined relative to its p_T as the scalar sum of the energy of all the PF candidates emitted around the direction of the muon in the cone, $\Delta R = \sqrt{(\Delta\phi)^2 + (\Delta\eta)^2}$,

surrounding the object. Detailed information on isolation definition and isolation corrections are given in Section 3.3.

Figure 3.6, from reference [81], shows $M_{\mu\mu}$, the invariant mass distribution of dimuon pairs selected by the inclusive trigger on isolated (for isolation definition refer to 3.3) double-muons. Specific triggers for low invariant mass resonances are also included.
The distribution in Figure 3.6 clearly states the CMS capabilities in identifying and triggering on muons, reconstruct the muon properties to unambiguously identify particles that decay into muons over a broad mass range.

3.1.3.3 Displaced muon reconstruction and identification

The search for heavy neutral leptons presented in Chapter 7 includes the long-lived heavy neutrino scenario with displaced leptons, muons and electrons, in the final state. Although CMS detector was initially designed and optimized for prompt object reconstruction and identification, it appears to give promising performances even for displaced lepton reconstruction. Several studies and improvements on displaced physics object reconstruction have been recently delivered, helping in the challenging effort of including long-lived exotic searches in the CMS results ([85–90]).

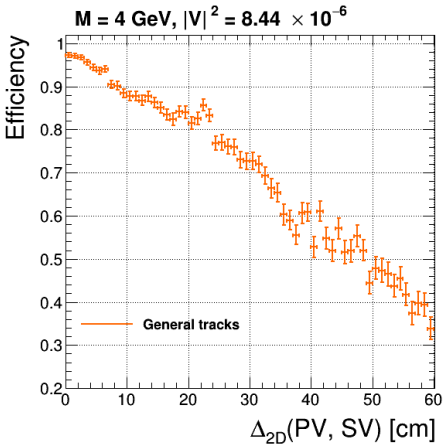

FIGURE 3.7: Efficiency of reconstructed inner tracker tracks with respect to generated muons. A HNL scenario with $(M_N, |V_{\mu N}|^2) = (4GeV, 8.44 \times 10^{-6})$ is used as benchmark. Courtesy of D. Trocino.

The analysis presented in Chapter 7 makes use of the standard reconstruction (explained in Section 3.1.3.1) with dedicated identification selections. In the following, we present the studies of displaced muon reconstruction and identification in the specific context of heavy neutral lepton search (refer to Chapters 4, 5, 6, 7).
These studies are performed with simulated samples containing low p_T displaced muons. The signal samples are characterized by HNLs with an average lifetime of 57 mm ($c\tau$), which corresponds to an average displacement of 633 cm ($\beta\gamma c\tau$).
Figure 3.7 shows the efficiency of reconstructing a muon track in the inner tracker. The efficiency is calculated as pure reconstruction efficiency with respect to the generated tracks. The variable that is used to display the reconstruction performance is the 2-dimensional (2D) distance between the PV and the secondary vertex (SV) and it is a proxy to estimate the flight distance of the displaced muon (details in Section 3.3). The efficiency worsens for muons created towards the external layers of the inner tracker.

Figure. 3.8 shows, on the left, the sequential efficiencies of the plain PF muon requirement, Loose ID, and valid tracker hit fraction requirement (refer to Section 3.1.3.2), with respect to the reconstructed inner-tracker tracks. It is clear that the efficiency of this last selection falls rapidly as the PV-SV distance increases. The valid-hit fraction request is thus removed from the set of requirements of the Medium ID (refer to Section 3.1.3.2).

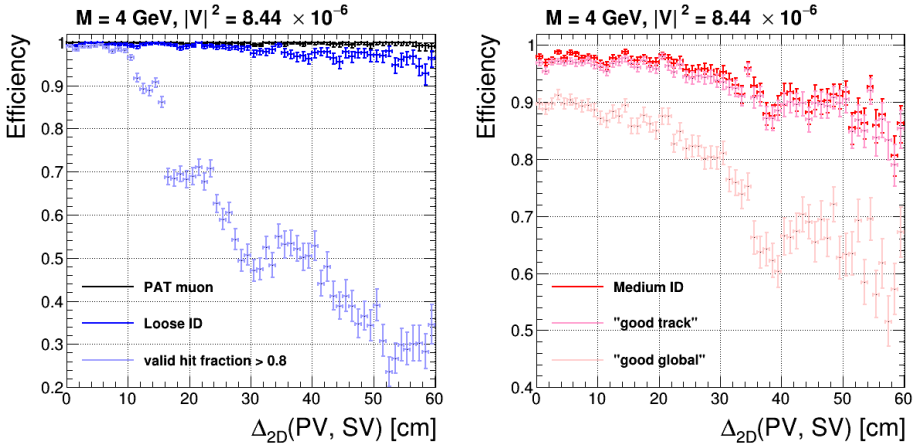

FIGURE 3.8: On the left, the sequential efficiencies of the plain PF Muon requirement, Loose ID, and valid tracker hit fraction requirement are shown. On the right, the efficiency of the tracker-muon only and global-muon only requirements are compared with their logical OR efficiency (using already the customized Medium ID). A HNL scenario with $(M_{\mathrm{N}}, |\mathrm{V}_{\mu\mathrm{N}}|^2) = (4GeV, 8.44 \times 10^{-6})$ is used as benchmark. Courtesy of D. Trocino.

To mitigate the depreciation of the total efficiency for muons not emerging from the primary vertex, the Medium ID is then modified in the context of the analysis presented in Chapter 7. In Figure. 3.8, on the right, the comparison between the efficiencies of the tracker-muon only and global-muon only and their logical OR (i.e., the full customize Medium ID) is shown. The main contribution to the efficiency comes from the tracker-muon selection, while the addition of the global-muon selection only increases the overall efficiency by a few percent.

Finally, Figure 3.9 compares the efficiency of the full customized Medium ID with the efficiencies obtained by removing individual requirements from the global-muon definition. None of these variables appears to hurt the overall efficiency significantly—the larger effect is observed for the segment-compatibility cut of 0.303, and it amounts to 1–2%. Finally, none of the cuts on the global-track variables depends on the displacement.

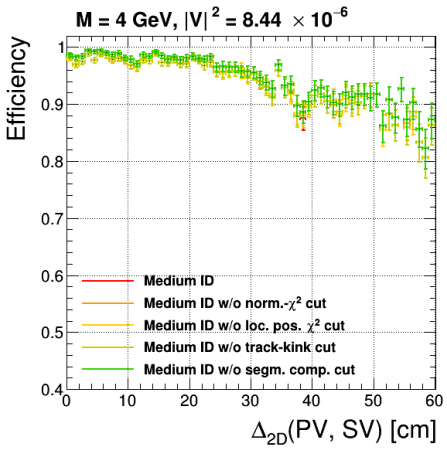

FIGURE 3.9: Efficiency of different Medium-ID selections with respect to tracks for displaced muons. A HNL scenario with $(M_{\mathrm{N}}, |\mathrm{V}_{\mu\mathrm{N}}|^2) = (4GeV, 8.44 \times 10^{-6})$ is used as benchmark. Courtesy of D. Trocino.

As explained in Section 3.1.1, the track reconstruction is done with the clear constraint on the start of the trajectory based on the assumption that the particle is created in the proximity of the beam spot [62]. This requirement places a quite strong limitation on the displaced lepton analysis outlook. As shown in Figure 3.7, the reconstruction efficiency suffers from it and it goes almost to null values at large displacements.

For Run2 data-taking, new reconstruction algorithms have been introduced trying to include

also displaced objects among the PF elements. The most important feature is the removal of constraints on interaction point in muon reconstruction [79, 91].
The two algorithms are the following:

- **Displaced Standalone Muon reconstruction.** Designed for displaced muons produced in decays happening far from the pp collision point, possibly with significant delay with respect to the time of the interaction (*out-of-time or delayed*). The reconstruction procedure uses seeds of groups of segments in the muon system (with similar criteria as the cosmic-ray muon reconstruction). For each seed, a muon track is reconstructed with the same Kalman-filter technique used for prompt muons, but removing any constraint to the interaction point. The Displaced Standalone algorithm has been implemented for the HLT, where it brings a significant improvement to the trigger efficiency for displaced and delayed muons.
- **Displaced Global Muon reconstruction.** Designed for displaced in-time muons produced within the inner-tracker volume, with the muon leaving hits in both the inner tracker and the muon system. The inner tracker tracking is modified with respect to the standard one (3.1.1) and is seeded by the Displaced Standalone Muons and does not use any constraints to the interaction point neither in the pattern recognition nor in the track fit.

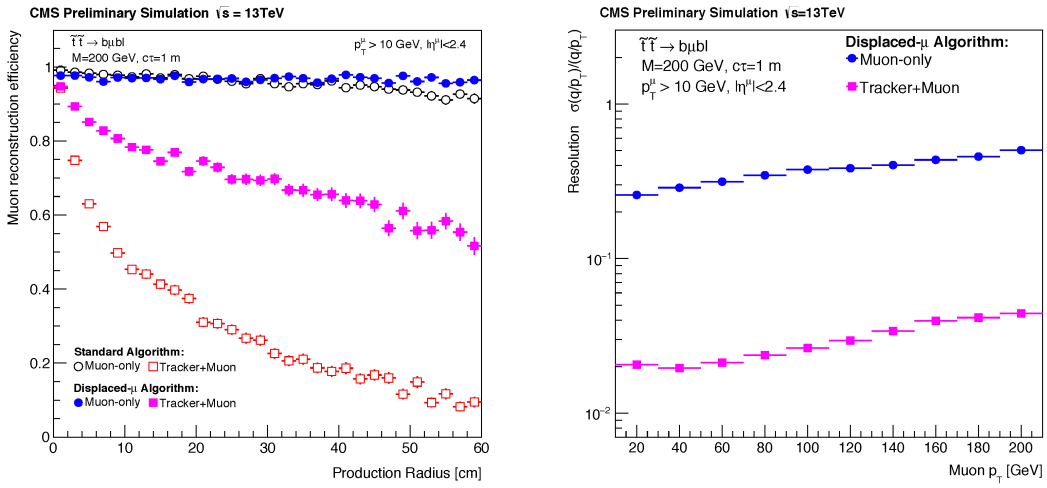

FIGURE 3.10: Left, standard algorithms for muon-only (black) and tracker+muon (red) reconstruction, compared with the new algorithms for displaced-muon reconstruction: Displaced Standalone (blue) and Displaced Global (magenta). Right, the resolution for the Displaced Standalone algorithm (blue) is shown in comparison with that of the Displaced Global algorithm (magenta) [79].

Figure 3.10 (left) shows the muon reconstruction efficiency for the two new algorithms in comparison to the standard ones. The comparison is done in simulated samples [3] with displaced and delayed [4] muons, measuring the efficiency as function of the production radius, for muons from the direct decay $\tilde{t} \to b + \ell$. A noticeable improvement can be appreciated

[3] Simulated signal process: PYTHIA8 stop pair ($\tilde{t}\tilde{t}$) production, $M(\tilde{t}) = 200$ GeV and $c\tau = 1$m. Decay $\tilde{t} \to b + \ell$

[4] Out-of-time or delayed muons indicate muons with significant delay with respect to the time of the interaction.

in the efficiency for displaced muons using the new algorithms. In Figure 3.10 (right) the transverse momentum resolution (q/p_T) is measured as function of the muon p_T for displaced muons from the direct decay $\tilde{t} \to b + \ell$.
The performance plots shown in Figure 3.10 present bright perspectives for the future of long-lived analyses involving displaced muons.

3.1.4 Electron reconstruction

3.1.4.1 Electron track reconstruction

Electron PF objects are reconstructed with the PF algorithm based on the combination of tracker tracks and energy clusters in the ECAL, taking into consideration the sizable fraction of electron energy which is emitted in the form of bremsstrahlung photons while crossing the tracker material [53].
The bremsstrahlung radiation is collected by organizing into a supercluster the ECAL clusters which are reconstructed in a narrow window in η and a wider window in ϕ along the electron direction (azimuthal bending in the magnetic field). For small p_T electrons, the ECAL supercluster approach can give incorrect information regarding the total energy. The soft tracks are significantly bent in the tracker by the magnetic field and the radiated energy is dispersed over an extended area that is not all included in the supercluster. The missed deposits distort the correct position of the supercluster and impede the proper match between supercluster and corresponding hits in the innermost tracker layers. Thus the *tracker-based* electron seeding method [53] is introduced to complement and improve the ECAL-based approach. Figure 3.11 shows the increase in efficiency caused by the tracker-based approach for electrons in b quark jets.

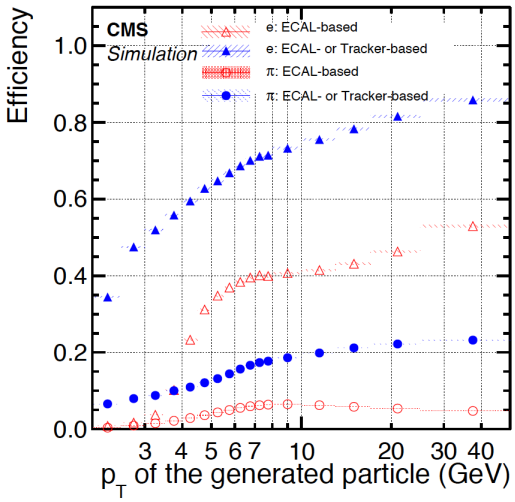

FIGURE 3.11: The electron seeding efficiency for electrons (triangles) and pions (circles) as a function of p_T is shown. Both the efficiencies for ECAL-based seeding only (hollow symbols) and with the tracker-based seeding added (solid symbols) are shown [53].

The final electron tracks are built using the Gaussian Sum Filter (GSF) fitting (details in references [53, 92]) which is more optimal to electrons than the Kalman-filter used in the iterative tracking (refer to Section 3.1.1). The GSF approach gives adequate performances both for large (i.e. soft electrons) and small (i.e. high p_T electrons) amounts of radiated energy in the tracker material.

The tracker-based seeding technique is effective at selecting e^--e^+ coming from γ conversions in the tracker material, for both prompt and bremsstrahlung photons. The possibility to correctly associate the converted bremsstrahlung photons to their parent electrons is key in avoiding energy double counting in the electron PF reconstruction [53]. The proper identification of the electrons from γ conversions in the tracker material becomes crucial for background descriptions. In the analyses presented in Chapters 6 and 7, the so-called "conversion" background has a major contribution and its correct understanding is critical

for good background predictions.

Electrons are reconstructed within the geometrical acceptance of the CMS tracking system, $|\eta| < 2.5$.

3.1.4.2 Electron identification

In CMS detector there are different sources of electrons aside from the prompt ones produced in the collision at the PV. Electrons can be originated from either γ conversions or from the decay of heavy-flavor hadrons, additionally they can also be misidentified jets due to poor reconstruction. It is necessary to implement a selection based on quality and kinematic parameters, in order to discriminate between different sources and to identify the prompt electrons from the hard scattering. Identification criteria are based on the shape of the electromagnetic shower (which is usually smaller than a hadronic shower), on the ratio between the HCAL deposits and the ECAL ones and on a few track properties.
A method to distinguish between prompt and background electrons is the adoption of a multivariate analysis (MVA) classifier. In the MVA approach [93], a single discriminator variable is built; it is computed based on multiple properties of the electron object and it provides the best separation between the signal and backgrounds. The output of the MVA can be used to introduce a sharp cut to reject a portion of electrons or it can be used, as distribution of the values, for a shape-based statistical analysis.
Another possibility is a simple set of criteria that have to be all satisfied. This approach can be called *cut-based* identification (ID) [94]. The average efficiency for MVA ID depends on the chosen discriminator working point, it can be 80% or 90% [93]. For the cut-based ID there are few benchmark selection levels which have efficiency equal to 90% (*loose ID*), 80% (*medium ID*) and 70% (*tight ID*) [94].

The efficiencies of the electron reconstruction and identification are estimated in data and simulation events with a *tag-and-probe* method (refer to 3.1.3.2).

As for the muon case (refer to Section 3.1.3.2), for electrons the relative PF isolation can be evaluated as well. The electron relative isolation is an essential discriminating variable against electrons originating from heavy-flavor hadron decays.

3.1.4.3 Displaced electrons identification

The reconstruction of displaced electron objects is more challenging with respect to the muon one. The main reason is the fact that for electron track reconstruction there is not a corresponding algorithm to the muon standalone track reconstruction. This latter allows a longer lever in the track reconstruction procedure and it expects hits further from the interaction point. The GSF tracks are then less adaptable and optimal for displaced lepton scenarios.

The investigations presented in this paragraph are done in the context of the long-loved heavy neutral lepton analysis presented in Chapter 7. They are circumscribed to this specific scenario and they are not optimized for a more extended implementation.

Displaced electrons are identified using the *cut-based loose ID* but with fewer requirements. Two criteria have been removed because they could affect the efficiency for electrons not emerging from the primary vertex.

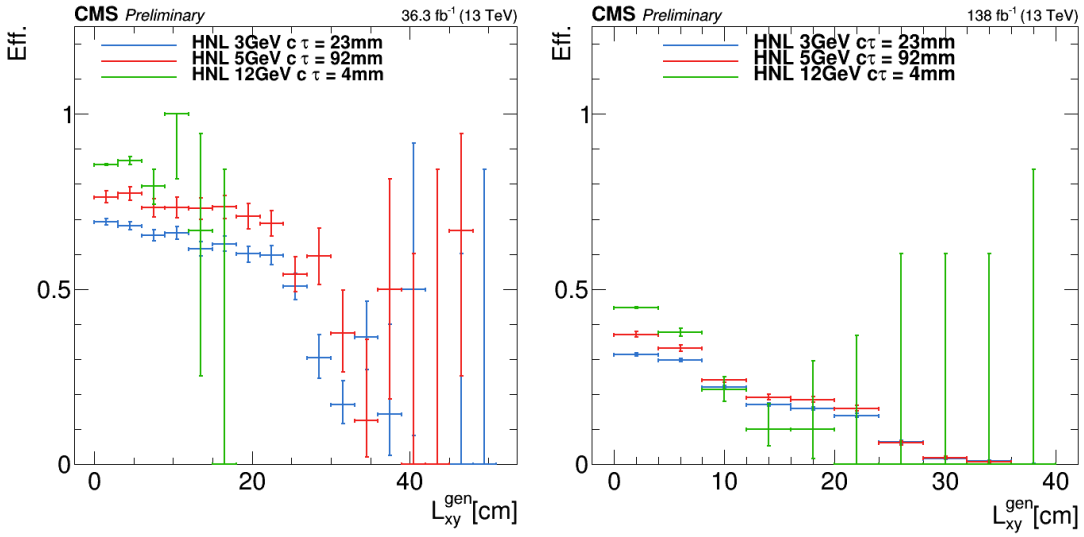

FIGURE 3.12: On the left, the pure ID efficiency with respect to GSF reconstructed tracks is shown. On the right the efficiency of reconstructed and identified electrons with respect to generated electrons is shown. Courtesy of B. Vermassen.

The conversion veto requirement which identifies secondary vertices where e^--e^+ pairs originate from γ conversions in the tracker material is excluded.
Finally, the request on the maximum number of missing inner tracker hits is removed in order to accommodate eventual larger displacements.
In Figure 3.12, on the left, the pure identification efficiency with respect to the reconstructed tracks is shown. It is estimated as a function of the flight distance, L_{xy} of the long-lived particle. In the right figure (3.12), the ID efficiency is convoluted with the reconstruction efficiency of the GSF tracks; hence the values are computed with respect to the number of generated tracks. For this specific case, three heavy neutral lepton benchmark models are used with different neutrino masses (3, 5 and 12 GeV) and different lifetime values.

3.2 Secondary vertex reconstruction

For the search for long-lived HNLs, presented in Chapter 7 supplementary and tailored treatment of the secondary vertex reconstruction and identification is necessary. The SV is the decay vertex of the heavy neutral lepton and it is the point of origin of its decay products.

In this specific case (Section 7.3), exactly two leptons, muon and/or electron, are expected to originate from the SV. The SV reconstruction is done a posteriori after the identification of the two lepton candidates that are believed to be displaced.
The SV is found by fitting the two tracks to a common point with a Kalman-filter approach [63], using the `KalmanVertexFitter` class implemented in the CMS reconstruction software (`CMSSW`). The class returns the least-χ^2 estimator of the two-track vertex position and covariance matrix, along with the χ^2 of the fit, as an indicator of its goodness. Figure 3.13 shows the pulls of the distance of the fitted secondary vertex (SV) from the PV of the interaction projected on the transverse plane (denoted as ρ). The pulls are computed as the difference between the measured distance ρ and its true value from simulation, divided by the uncertainty on the measured value. A standard deviation of about 1.2 is found from a Gaussian fit to the pull distributions, revealing a slight underestimation of the uncertainties.

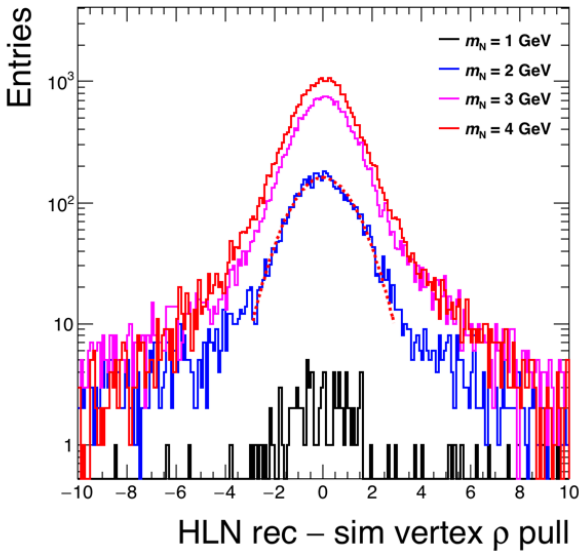

FIGURE 3.13: Pull distributions of the transverse distance of the fitted SV from the PV, for HNL masses from 1 to 4 GeV, all with $|V_{\ell N}|^2 = 10^{-4}$. The red curve overlaid to the blue histogram shows a Gaussian fit. Courtesy of D. Trocino.

To verify the accuracy of the reconstructed SV position, the residuals of the transverse PV–SV distance ρ with respect to the true generated value, $\Delta\rho(\text{gen}, \text{rec})$, and the relative residuals $\Delta\rho(\text{gen}, \text{rec})/\rho(\text{gen})$, are studied as a function of the true ρ. The results are shown in Figure 3.14.
No significant biases are observed and the tails are small: the fraction of events with $\Delta\rho(\text{gen}, \text{rec})/\rho(\text{gen})$ larger than 10%—indicated by the dashed horizontal lines in Figure 3.14 (right)—is about 2.6% for $\rho < 0.5$ cm, and less than 1% for larger displacements.

The quality of the reconstructed SVs is checked with specific variables described in Section 3.3, such as the fit probability and χ^2 of the fit.

The efficiency for this two-track-SV reconstruction is nearly 100%.

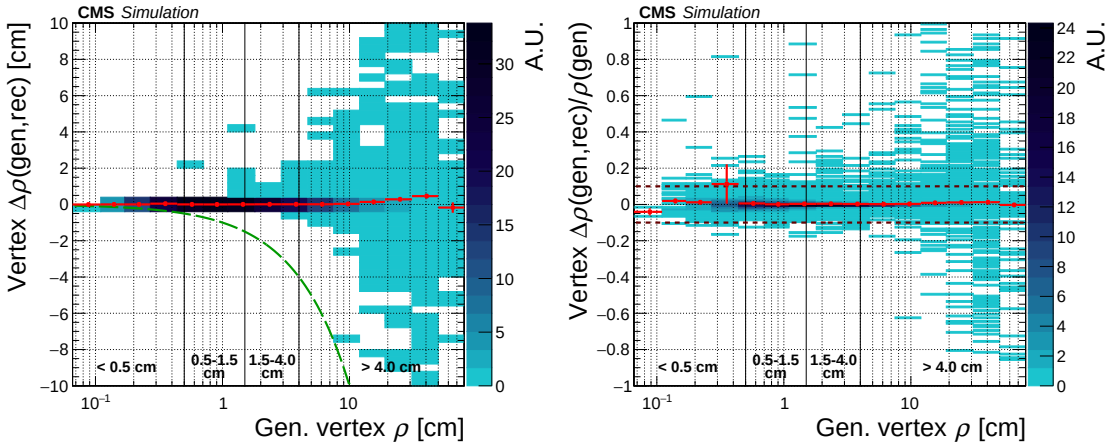

FIGURE 3.14: Residuals (left) and relative residuals (right) of the transverse distance ρ between the fitted secondary vertex and the PV of the interaction, as a function of the true ρ value from simulation. The red graph shows the mean value of the residuals in each ρ bin and the uncertainty on the mean value. The dashed green line in the left plot indicates the distance between the generated primary and secondary vertices: any reconstructed vertex below this line would lie in the "wrong" hemisphere, opposite to the direction of flight of the HNL. The horizontal dashed lines in the right plot delimit the region where $\Delta\rho(\text{gen}, \text{rec})$ is less than 10% of $\rho(\text{gen})$. This region contains more than 99% of the events for $\rho > 0.5$ cm, and about 97.4% for $\rho < 0.5$ cm. Courtesy of D. Trocino.

3.3 PF object and event identification variables

Aside from the variables introduced up to this point, there are additional ones that are worth introducing at this stage of this dissertation. The list of variables presented in the next two sections is contingent on the specification and parameters of the two data analyses presented in Chapters 6 and 7.
There are a number of variables that are referred specifically to as light leptons, electrons, and muons, in particular those that are indicative of the HNL flight distance.
A second set consists of a few event-based observables.

Light lepton identification

Vertices and impact parameter variables. Prompt leptons originate from the PV of the pp collision, hence they are expected to have very modest impact parameters with respect to the PV. On the contrary, displaced leptons have quite considerably large impact parameters due to the decay length of the corresponding parent particles (partons or heavy neutral leptons).

In the context of this thesis work, the following variables are used:

- $\boldsymbol{d_{xy}}$, impact parameter in the $x - y$ plane;
- $\boldsymbol{d_z}$, impact parameter component in the the longitudinal direction, z-axis;
- $\boldsymbol{SIP_{3D}}$, significance of the 3D impact parameter, d_{3D}. It is defined as the ratio between the d_{3D} and its uncertainty;

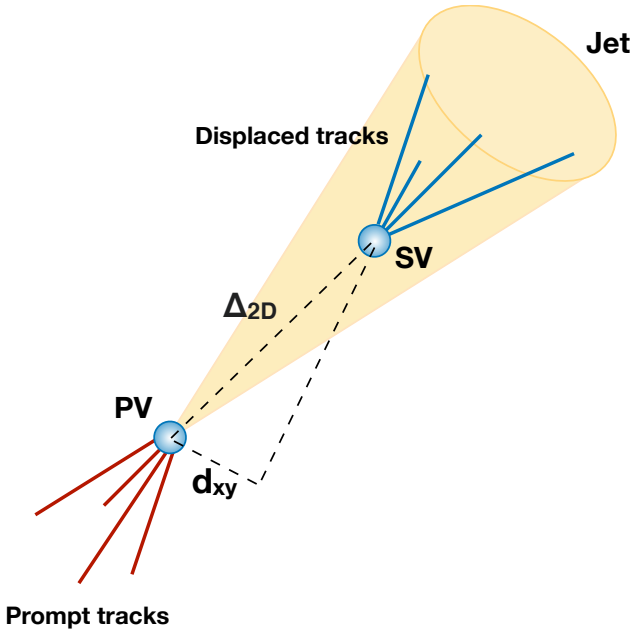

FIGURE 3.15: Schematic representation of the impact parameters variables.

- $\boldsymbol{\Delta_{2D}}$, the 2D distance between the PV and the SV. It is an optimal proxy to estimate the point of origin of the displaced lepton and the heavy neutral lepton decay length. It is computed as $\Delta_{\text{2D}} = \sqrt{(x_{SV} - x_{PV})^2 + (y_{SV} - y_{PV})^2}$;
- $\boldsymbol{S(\Delta_{2D})}$, the significance of the transverse distance between PV and SV, defined as the ratio of the transverse PV-SV distance Δ_{2D} and its uncertainty;
- $\boldsymbol{p_{SV}}$, SV probability. The quality of the reconstructed SV necessarily correlates with the precision on the track parameters of the two leptons in the SV, as well as the spatial separation between their trajectories at the intersection point. The SV quality is estimated as a probability based on the χ^2 fit from the kinematic vertex fitter;
- $\boldsymbol{d}$, displacement. It is used to study the electron reconstruction performance where electrons originate from convert photon. It is computed as: $d = \sqrt{2Rd_{xy} + d_{xy}^2}$ where R is the radius of curvature of the path of the nonprompt electron in magnetic field. This variable represents a suitable proxy to the actual displacement of the converted photon with respect to the PV and is also correlated with the Δ_{2D} variable.

Lepton isolation To discriminate between prompt leptons and leptons coming from either the decays of heavy-flavor hadrons or the decay in flight of charged $\pi^{\pm}$s and kaons, the isolation variable appears to be one of the most critical variable to use. The PF isolation of a reconstructed lepton is defined relative to its p_T as the scalar sum of the energy of all the PF candidates emitted around the direction of the lepton in the cones, $\Delta R = \sqrt{(\Delta\phi)^2 + (\Delta\eta)^2}$,

surrounding the object. It is computed as:

$$I_{\text{rel}} = \frac{1}{p_T^{\ell}} \left(\sum_{ch.hadr.} p_T^{\text{PV}} + \max \left[0, \sum_{neu.hadr.} p_T + \sum_{pho.} p_T - \rho \cdot A_{\text{eff}} \right] \right) \tag{3.1}$$

For the estimation of the PF isolation [53], the sum of the p_T of charged hadrons and the p_T of neutral particles (hadrons and photons) originating from the PV is computed. Typical values used for ΔR are 0.3 and 0.4.
The term $\rho \cdot A_{\text{eff}}$ is used to mitigate the contribution of pileup to the isolation calculation [81]: the average transverse-momentum flow density ρ is calculated in each event using a "jet area" method [70], and the effective area A_{eff} is the geometric area of the isolation cone times an η-dependent correction factor.

General observables

Missing transverse momentum, $\boldsymbol{p_T^{miss}}$. Neutral leptons do not interact with any material of the CMS sub-detectors, thus they leave the detector unseen. Nevertheless, they carry momentum energy which has to be estimated, or else it would create a sizable momentum imbalance in the transverse plane. The transverse momentum of the initial state is zero. Hence, the sum of momenta of all objects in the transverse plane is expected to be zero except for events where undetected particles are created. From this missing balance, it is possible to estimate the energy carried out by the neutrinos.
The p_T^{miss} is obtained as the magnitude of the negative vector sum of the transverse momenta of all reconstructed PF candidates and is further adjusted to account for jet energy corrections applied to the event [95].

$$\overrightarrow{p}_T^{\text{miss}} = \sum \overrightarrow{p}_T, \qquad p_T^{\text{miss}} = |\overrightarrow{p}_T^{\text{miss}}| \tag{3.2}$$

3.4 Summary

In this chapter, the event reconstruction and lepton identification are discussed.
With a clear focus on light leptons, we described the reconstruction of physics objects by using combined information from all the CMS sub-systems. In this context, we described in detail the PF algorithm with its input and output such as leptons.
We addressed the identification and characterization aspects of the reconstructed physics objects. We listed the main identification variables and the related levels of tagging efficiencies. According to the desired compromise between efficiency and purity, for electrons and muons a set of different variables and selections definitions are defined.

In this chapter extensive attention is paid to detail the algorithms and strategies adopted to correctly reconstruct and identify displaced vertices, muons, and electrons.
The CMS centralized displaced object algorithms are described as well as the specific IDs and methods which were developed in the context of this thesis. I have contributed to this latter part. The second year of my PhD was dedicated exclusively to the study, understanding, and identification of displaced objects. In particular, I have contributed to the decision of valuable variables and features to select displaced muons with high efficiency and low misidentification rates. The exotica long-lived working group was the setting for these developments and several improvements were presented and discussed there by myself. The comprehensive insights acquired during the analysis process were crucial during the paper review and helped to formulate the interpretation of the long-lived heavy neutral lepton results.
The displaced object descriptions are going to be central to grasp the scope and the challenges of the analysis presented in Chapter 7.

A list of PF objects and event identification variables are added at the end of this Chapter 3; each of the variables will be found later on in the text.

Part II

Search for heavy neutral leptons

Chapter 4

Heavy Neutral Leptons

In the SM, all the fermions are known to have both left- and right-handed chirality, the only exception comes from the neutrinos.
The recent neutrino oscillation experiments have clearly and definitely shown that neutrinos are massive.
The light masses of the SM neutrinos (ν_{SM}) can be explained by introducing massive right-handed neutrinos (ν_R), often referred to as *heavy neutral leptons* (HNLs), via a seesaw mechanism [96–99]. Another possible endorsement comes from the possibility to consider ν_R as part of the explanation for the baryon asymmetry of the universe; the ν_R mixing violates *CP* symmetry and the ν_R interaction may potentially generate a matter-antimatter asymmetry in the early stage of the formation of the universe [100, 101].

These few examples, which are going to be explored later on, already show the relevance and the interest for the HNL search program and provide strong motivations to investigate the existence of the ν_R. This huge enthusiasm has led in the past $\sim$ 10 years to the creation of a very active community with strong synergy between theorists and experimental collaborations. It had contributed to the publication of an impressive number of papers and the proposal of a considerable number of experiments focused mainly on heavy neutral leptons.

4.1 Neutrino Portal

The *neutrino portal* is defined as the coupling of one or more dark fermions N_I ($I = 1, 2, ... \mathcal{N}$), which are sterile with respect to the SM gauge interactions, to the gauge-invariant operator $\bar{L}_\alpha \cdot \widetilde{\Phi}$; the general form of the neutrino portal could be written as:

$$\mathcal{L} = \mathcal{L}_{SM} + \mathcal{L}_{DS} + \sum F_{\alpha I}(\bar{L}_\alpha \cdot \widetilde{\Phi})N_I + h.c. \tag{4.1}$$

where the summation loops over the flavor of lepton doublets L_α ($\alpha = e,\ \mu,\ \tau$) and the number of available HNLs N_I; $F_{\alpha I}$ are the Yukawa couplings and Φ is the Higgs doublet. The term $\mathcal{L}_{DS}$ is the dark sector Lagrangian which contains the mass term of HNLs which can be either of Majorana or Dirac nature [102]. Fixing the Φ to its vacuum expectation value, $\widetilde{\Phi} = \frac{1}{\sqrt{2}}\binom{v}{0}$, and diagonalizing the mass term of the dark fermions, the last term in Eq. 4.1 brings to the quadratic mixing of the neutrinos ν_α with the N_I; this mixing is parametrized by a matrix V. In the minimal HNL models, the elements of the matrix V control both the production and the decay of the HNLs. If $\mathcal{N} = 3$, there is a right-chiral counterpart for each ν_{SM}, see Figure 4.1. The fermion N_I can have mass M_I, which is

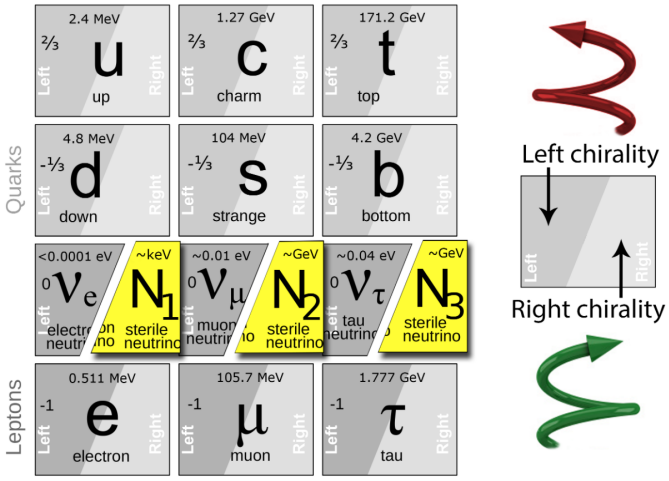

FIGURE 4.1: There are 3 SM neutrinos ν_e, ν_μ, ν_τ which are massless and always left-chiral; 3 right-chiral counterparts are added N_1, N_2, N_3. They are sterile so they do not feel the electric, weak and strong forces. However they can be produced through mixing with the ν_{SM} with the corresponding mixing parameter.

independent of the value of $F_{\alpha I}$.

Many HNL models require the existence of two or more right-handed neutrinos. In experimental searches, however, following a model-independent approach, we can consider the production of a *single* HNL, which is light enough to be kinematically accessible at the accelerator experiments; see the full overview in Ref. [103].

Under this assumption, there are then only two free parameters to be constrained: the mass M_I of the HNL and its mixing parameter with the SM neutrino of flavor α, controlled by the Yukawa coupling $F_{\alpha I}$. The experimental sensitivity is expressed in terms of the coupling $|V_{\alpha I}|^2$ ($= |F_{\alpha I}|^2$) as a function of M_I for a given flavor α. It is frequently assumed that in the matrix V the other mixing elements for the residual flavors are zero; although it does not translate into a valid concrete model, this latter consideration is very useful to evaluate the experimental sensitivity on the single $|V_{\alpha I}|^2$ without involving any model-dependent hierarchy between the different flavor mixings.

4.2 Heavy neutral lepton formalism and extension of the Standard Model

To set up our notation and conventions, we first discuss the formalism for the simplest extension of the SM that includes right-handed singlets. In section 4.3, we will try to contextualize the theory, explained here, summarizing the current constraints on the mass and mixing of a heavy neutrino from various direct detection experiments, accelerator searches, and electroweak precision fits.

4.2.1 Seesaw mechanism

The most general renormalizable Lagrangian for the neutrino masses includes both the Dirac and Majorana mass terms. The SM Lagrangian $\mathcal{L}_{SM}$ is extended adding $\mathcal{N}$ right-handed neutrinos N_I (for notations see Eq. 4.1):

$$\mathcal{L} = \mathcal{L}_{SM} + i\bar{N}_I \partial_\mu \gamma^\mu N_I - \left(F_{\alpha I}\, \bar{L}_\alpha N_I s\tilde{\phi} - \frac{M_I}{2}\, \bar{N}_I^c N_I + h.c. \right) \tag{4.2}$$

As already explained in the section 4.1, these N_I are neutral with respect to all the gauge interactions of the SM, thus are called *sterile neutrinos* or *gauge-singlet fermions*. In the Higgs phase, the term 4.1 contains the $\nu_\alpha - N_I$ mixing. As a result the *charge eigenstates* of $\mathcal{L}_{SM}$ (Eq. 4.2) do not coincide with *mass eigenstates*, which can be extracted by diagonalizing the following matrix:

$$\mathcal{M}_{\nu,N} = \begin{pmatrix} 0 & m_D \\ m_D^T & M_I \end{pmatrix} \tag{4.3}$$

with the matrix elements defined as: $m_D = 3 \times \mathcal{N}$ Dirac mass matrix, $(m_D)_{\alpha I} = F_{\alpha I} v$, $v = \sqrt{2}\langle \Phi \rangle$ and M_I is $\mathcal{N} \times \mathcal{N}$ matrix of Majorana masses.

Considering the relation between M_I and m_D, we could explore two interesting extreme limits:

Pure Majorana neutrino, $m_D \ll M_I$**.** In this limit, the mass matrix gives rise to 3 almost pure right-handed neutrinos with heavy Majorana mass M_I and 3 almost pure left-handed neutrinos with light Majorana mass $m_\nu = -(v m_D)^T M_I^{-1} (v m_D)$ which are the 3 eigenvalues of the matrix $(\mathcal{M}_\nu)_{\alpha\beta}$. This mechanism is then referred to as the *seesaw mechanism*[1] [96] [106] [107]. There are then the other $\mathcal{N}$ eigenstates of the $\mathcal{M}_{\nu,N}$ which

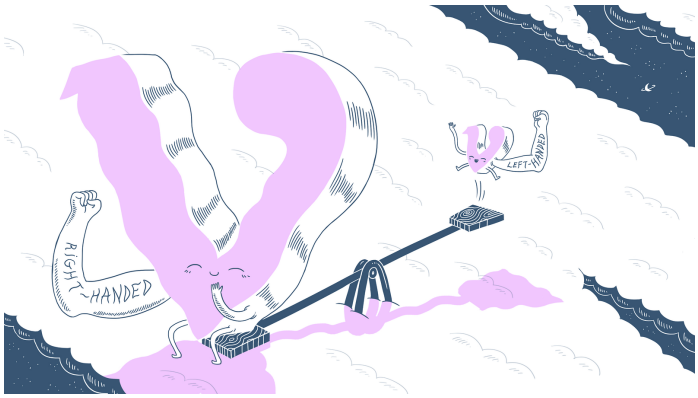

FIGURE 4.2: Silly representation of the *seesaw mechanism* [108]. Note that for a fixed value of m_D, the higher the value of the m_I^R is, the lower m_I^L is and vice-versa, from which we get the *seesaw* name.

almost coincide with the N_I up to a small admixture of ν_α. The magnitude of this mixing is given by the ratio of the Dirac and Majorana masses, giving rise to the mixing angle or

[1] This mechanism is usually called *Type-I seesaw*. *Type-II seesaw* has an extra SU(2) triplet scalar [104]; in *Type-III seesaw* an extra fermion in the adjoint of SU(2) is added to the model [105]

active-sterile mixing:

$$|V_{\alpha I}|^2 \equiv \frac{v^2|F_{\alpha I}|^2}{M_I^2} \ll 1 \tag{4.4}$$

Pure Dirac neutrino, $M_I \ll m_D$. In this limit, the mass matrix gives rise to 3 Dirac neutrinos $\Psi = (\nu_L, \bar{\nu}_R)$ with masses $m_\nu = m_D$. To obtain the observed neutrino masses the coupling needs to be $F_{\alpha I} \sim 10^{-12}$ which is much smaller than the SM Yukawa couplings.

4.2.2 Considerations on Majorana and Dirac neutrinos

The paragraphs below are freely inspired by the overview given by R.D. Kauber in Ref. [109].

4.2.2.1 Distinction between Majorana and Dirac terms.

The term *Majorana* is used to define different properties and features and it is important for the following chapters to clarify the meaning.

In Section 4.2.1 *Majorana* and *Dirac* are used to refer to the mass terms in the Lagrangian of Eq. 4.2. Additional use is related to the type of neutrino. A *Majorana* particle is defined as a particle that is its own antiparticle. A Dirac particle has an antiparticle that is distinctly different from it. Neutrinos are the only particles that can be either *Majorana* or *Dirac*, while all the other known fermions were experimentally found to be of Dirac-type.

4.2.2.2 Lepton Number conservation.

To be clearer and explicit, we write the Dirac mass term as:

$$-m_D(\bar{\nu}_L\nu_R + \bar{\nu}_R\nu_L) \tag{4.5}$$

and the Majorana one:

$$-\frac{1}{2}m_I^L(\bar{\nu}_L\nu_L^c + \bar{\nu}_L^c\nu_L) - \frac{1}{2}m_I^R(\bar{\nu}_R\nu_R^c + \bar{\nu}_R^c\nu_R) \tag{4.6}$$

where R/L labels indicate the left- or right-hand chirality, and the c label the charge conjugation.

Let us consider a HNL produced in the decay of a W boson, and its subsequent leptonic decays, as shown in Figure 4.3. If the HNL is of Majorana nature, then ℓ and l'ℓ' (or ℓ and $\nu_{\ell'}$) can either have the same chirality (Figure 4.3 left) or opposite chirality (Figure 4.3 right). The former decay represents a case of lepton-number violation (LNV), the latter a case of lepton-number conservation (LNC).

In the case of a HNL decay mediated by a W^* boson, an LNV decay (Figure 4.3 top left) can lead to final states with no opposite-sign, same-flavor lepton pairs (no-OSSF), such as $e^\pm e^\pm \mu^\mp$ or $\mu^\pm \mu^\pm e^\mp$. Decays mediated by a Z^* boson (Figure 4.3 bottom) and LNC decays (Figure 4.3 right), instead, are always accompanied by an opposite-sign, same-flavor lepton pair (OSSF).

The HNL can couple exclusively to a single lepton-neutrino family (i.e. only one of $|\mathrm{V_{eN}}|^2$, $|\mathrm{V}_{\mu\mathrm{N}}|^2$, or $|\mathrm{V}_{\tau\mathrm{N}}|^2$ is nonzero) or to multiple families (i.e. at least two of $|\mathrm{V_{eN}}|^2$, $|\mathrm{V}_{\mu\mathrm{N}}|^2$, and $|\mathrm{V}_{\tau\mathrm{N}}|^2$ are nonzero at the same time). In the former case, ℓ and ℓ' (or $\nu_{\ell'}$) always

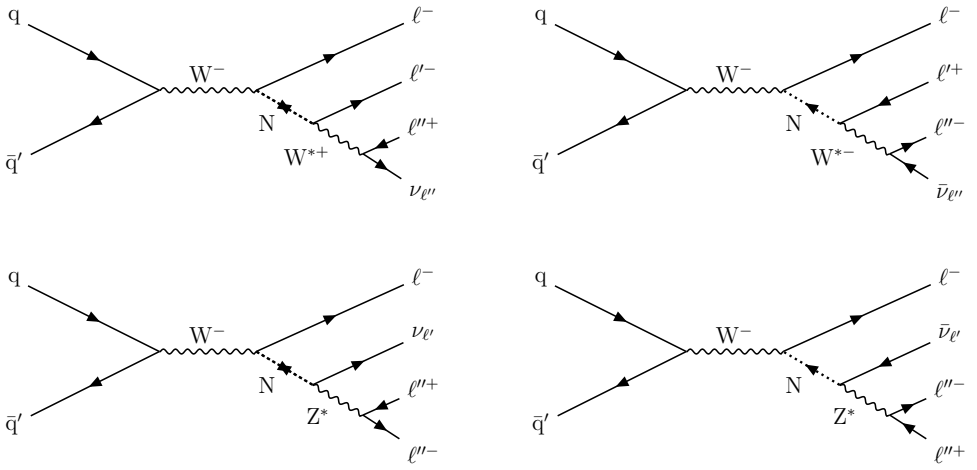

FIGURE 4.3: Typical diagrams for the production of a HNL at the LHC (N) through its mixing with a SM neutrino, leading to a final state with three charged leptons and a neutrino. The HNL decay is mediated by either a W (top row) or a Z (bottom row) boson. In the diagrams on the left, N is assumed to be a Majorana neutrino, thus ℓ and ℓ' in the W^*-mediated diagram (top) can have the same electric charge, with lepton-number violation (LNV). In the diagrams on the right instead, the N decay conserves the lepton number (LNC) and can be either a Majorana or a Dirac particle. Therefore ℓ and ℓ' in the W^*-mediated diagram (top right) have always opposite charge. If N couples exclusively to a single lepton-neutrino generation, then ℓ and ℓ' (or $\nu_{\ell'}$) always belong to the same lepton generation, and the lepton flavor is conserved (LFC). If N couples to multiple lepton families instead, then the lepton flavor can be violated, $\ell \neq \ell'$ (LFV).

belong to the same lepton family, and the lepton flavor is conserved (LFC). If N couples to multiple lepton families instead, then the lepton flavor can be violated, $\ell \neq \ell'$ (LFV). In the LFV case, decay rates to different flavors might not be the same ($|\mathrm{V_{eN}}|^2, |\mathrm{V}_{\mu\mathrm{N}}|^2, |\mathrm{V}_{\tau\mathrm{N}}|^2 > 0$, but $|\mathrm{V_{eN}}|^2 \neq |\mathrm{V}_{\mu\mathrm{N}}|^2 \neq |\mathrm{V}_{\tau\mathrm{N}}|^2$).

4.2.2.3 Decay width and branching ratio

The main consideration and difference between Majorana and Dirac HNL is that in the first case the N particle is defined as a particle that is its own antiparticle. This implies that both $N_I \to W^+\ell^-$, $Z\nu_\ell$, $H\nu_\ell$ and $N_I \to W^-\ell^+$, $Z\bar{\nu}_\ell$, $H\bar{\nu}_\ell$ decay modes are open. Assuming that the partial width of $N_I \to W^+\ell^-$ and $N_I \to W^-\ell^+$ have the same value, the total width for a Majorana neutrino and a Dirac neutrino of same mass are related by:

$$\Gamma_{N_I}^{Tot,\,Majorana} = 2 \times \Gamma_{N_I}^{Tot,\,Dirac} \tag{4.7}$$

This leads to the following relationship between their lifetimes:

$$c\,\tau_{N_I}^{Tot,\,Majorana} = \frac{1}{2} \times c\,\tau_{N_I}^{Tot,\,Dirac} \tag{4.8}$$

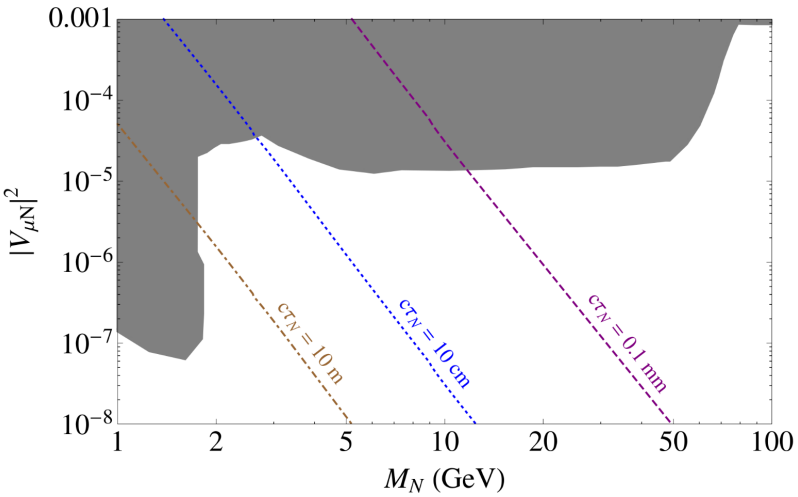

FIGURE 4.4: The calculated lines for $c\tau$ of a HNL are shown as a function of its mass M_{N} and its mixing parameter $|\mathrm{V}_{\ell \mathrm{N}}|^2$ to a single lepton family: the three oblique lines correspond to $c\tau$ values of (from left to right) 10 m, 10 cm, and 0.1 mm. The shaded grey area represents—approximately—the region of the parameter space excluded by previous searches.

4.2.3 Prompt and long-lived HNL

The lifetime of a HNL is strongly dependent on M_{N_I} and $|V_{\alpha I}|^2$, and increases rapidly at small masses and low values of the mixing parameter (see Figure 4.4):

$$c\,\tau_{N_I} \propto \mathrm{M}_{\mathrm{N_I}}^{-5} |\mathrm{V}_{\alpha \mathrm{I}}|^{-2} \tag{4.9}$$

As a consequence, the kinematics and acceptance of HNLs with masses below about 20 GeV are significantly affected by their long lifetimes, and must be accounted for in the signal simulation and in the resulting interpretation. If N has a long lifetime, in particular, its decay products ($\ell^{\pm\prime}$, $\ell^{\mp\prime\prime}$, $\nu_{\ell''}$ or $\nu_{\ell'}$, $\ell^{\pm\prime\prime}$, $\ell^{\mp\prime\prime}$, see Figure 4.3) emerge from a secondary vertex, spatially displaced with respect to the primary vertex of the process, and distinguishable from it.

4.3 Theoretical and experimental constraints

For a complete overview of the theoretical and experimental constraints of sterile neutrinos searches see References [22, 104, 110–113].

Sterile neutrinos mix with ν_{SM}, thus at small mixing the active-neutrino mass states contain a small part of sterile neutrinos.
In principle, in any weak processes where ν_{SM} participate, the HNLs also do so. The strength is suppressed due to the smallness of the $\nu_\alpha - N_I$ mixing angle, but the production of a HNL in the interaction can manifest itself in the kinematic properties of the final decay products because HNLs are much more massive than active neutrinos. Therefore, it is possible to select particular channels and phase spaces that enhance some kinematic features associated with the presence of sterile neutrinos.

These properties are explored and exploited in the direct searches for HNLs.

4.3.1 Direct HNL searches

Considering the wide theoretically accessible mass ranges (MeV-TeV) and taking into account the several production and decay modes, we have a quite rich experimental landscape:

- For M_N values below 1 MeV, HNL can be probed by neutrino-oscillation experiments [114];
- for 10 eV $< M_N <$ 1 MeV, searches for neutrinoless double-beta decay, $0\nu\beta\beta$ and precision measurements of $\beta-$decay energy spectra have constrained the mixing $|\mathrm{V_{eN}}|^2$, only for Majorana cases [104];
- for 1 MeV $< M_N <$ 1 GeV, both $|\mathrm{V_{eN}}|^2$ and $|\mathrm{V_{\mu N}}|^2$ have been constrained by peak searches using leptonic decays of pions and kaons like $K \to \mu(e)N$, $\pi \to \mu(e)N$ [115];
- for HNL in the MeV-GeV mass ranges, many searches through sterile neutrino decay products have been performed at beam-dump experiments [116];
- for HNL in the GeV-TeV mass ranges, we enter the domain of the particle colliders.

Quite often the HNL bounds are shown in the 2D $V_{\alpha N} - M_N$ plane for a specific mixing parameter V, under the assumption that all the other mixing angles are zero.

To have a clear overview of the current experimental (and theoretical) limits we can refer to Figures. 4.5, 4.6 and 4.7. Filled colored areas show the existing limits. For HNL masses below the charm mass, the limits are driven by the results from beam-dump experiments (PS191 and CHARM); for masses above the charm mass, the most stringent limits are those coming from LEP experiments (especially DELPHI), from Belle, and, more recently, from CMS and ATLAS.

A brief experiment-focused overview follows:

- **PS191** (CERN, PS beam 1983) [119]: the PS191 experiment was specifically designed to look for neutrino decays in low-energy neutrino beams. It was a detector composed of a 12 m long decay volume followed by a fine-grain calorimeter. No sterile neutrino candidates were observed but the analysis of neutrino interactions in the calorimeter shows a possible excess of events with electrons [120].
- **CHARM** (CERN, SPS beam 1985) [116]: a search for HNL decays was performed by the CHARM Collaboration using a neutrino beam produced by dumping 400 GeV protons on a thick copper target and looking for possible visible decays. It was assumed that the sterile neutrino is produced in charmed D meson decays, i.e. $c \to sW^*$ with $W^* \to \ell\mathrm{N}$. The following decays were considered, $\mathrm{N} \to e^+e^-\nu_e$, $\to \mu^+e^-\nu_\mu$ and $\to \mu^+\mu^-\nu_\mu$ and the limits were set on $|\mathrm{V_{eN}}|^2$ and $|\mathrm{V_{\mu N}}|^2 < 10^{-7}$ for N masses around 1.5 GeV.
- **Belle** (KEK, asymmetric-energy e^+e^- collider, 2012) [115]: the Belle Collaboration performed a search for heavy neutral leptons in B-meson decays. The data sample contained 772×10^6 $B\overline{B}$ pairs collected at the $\Upsilon(4S)$ resonance. The limits on the mixing parameter were obtained by analyzing the $B\overline{B}$ pairs events using the leptonic and semileptonic B meson decay, $B \to X\ell\nu_R$, where $\ell = e$, μ and the X was either a charmed D meson, a light meson (π, ρ, η) or nothing (leptonic decay). Upper limits were set on $|\mathrm{V_{eN}}|^2$ and $|\mathrm{V_{\mu N}}|^2$ in the mass range 0.5–5.0 GeV.

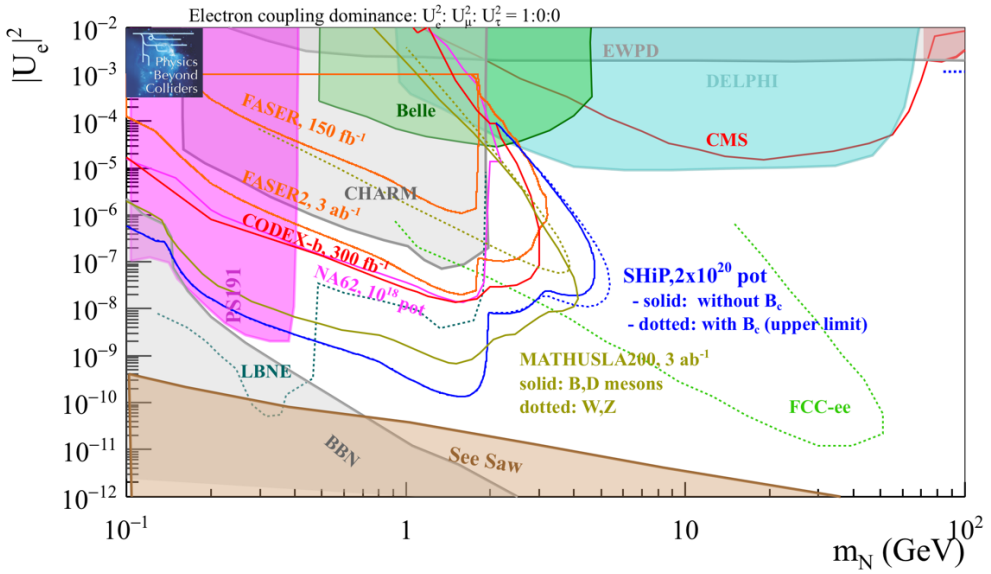

FIGURE 4.5: Sensitivity to HNL with coupling to ν_e only. Current bounds (filled areas) and 10-15 years prospects for projects (SHiP, MATHUSLA200, CODEX-b and FASER2) (solid lines). Projections for a LBNE near detector with 5×10^{21} protons-on-target and from FCC-ee with 10^{12} Z_0 decays are also shown. The gray contour named "BBN" corresponds to a HNL lifetime > 1sec, which is disfavored by BBN [117]. The brown line labeled "seesaw" represents the scale of mixing in general expected in the canonical seesaw. The very light gray at the top labeled as "EWPD" is the 90% C.L. exclusion limit from the electroweak precision data [118]. The other solid contours are explained in the text.

- **DELPHI** (CERN, lepton collider LEP, 1997) [121]: up to the publication of the results presented in this thesis, the most stringent limits between 1 GeV and 10 GeV have been those published by the DELPHI Collaboration. HNL searches were performed using the data collected by DELPHI, corresponding to 3.3×10^6 hadronic Z_0 decays at LEP1. This set of results is, up to this day, one of the most complete, including both the short-lived HNL and the long-lived HNL scenarios and all three lepton flavor couplings. According to the mass and lifetime ranges of the HNL, four separate searches were performed, two for short-lived N production giving monojet or acollinear jet topologies, and two for long-lived N looking for detectable secondary vertices or calorimeter clusters.
  Upper limits were set for the branching ratio $BR(\ Z_0 \rightarrow \mathrm{N})$ of about 1.3×10^{-6} at 95% C.L. for N masses between 1 and 80 GeV. An additional combination of the short and long-lived HNL searches was performed providing the upper limits on $|\mathrm{V}_{\ell \mathrm{N}}|^2$ for N masses between 3.5 and 50 GeV.

- **CMS and ATLAS** (CERN, LHC proton beam, 2016): there have been several searches for HNLs using both CMS and ATLAS detectors. The ATLAS experiment recently reported on a search for HNLs using events with three charged leptons [122] using pp collisions data corresponding to integrated luminosities of 32.9 and of 36.1 fb^{-1}. The search is performed in channels with three muons or two muons plus one electron—providing sensitivity to $|\mathrm{V}_{\mu \mathrm{N}}|^2$ only—, where the displaced decay vertex of the HNL was exploited. CMS performed searches for HNLs only using

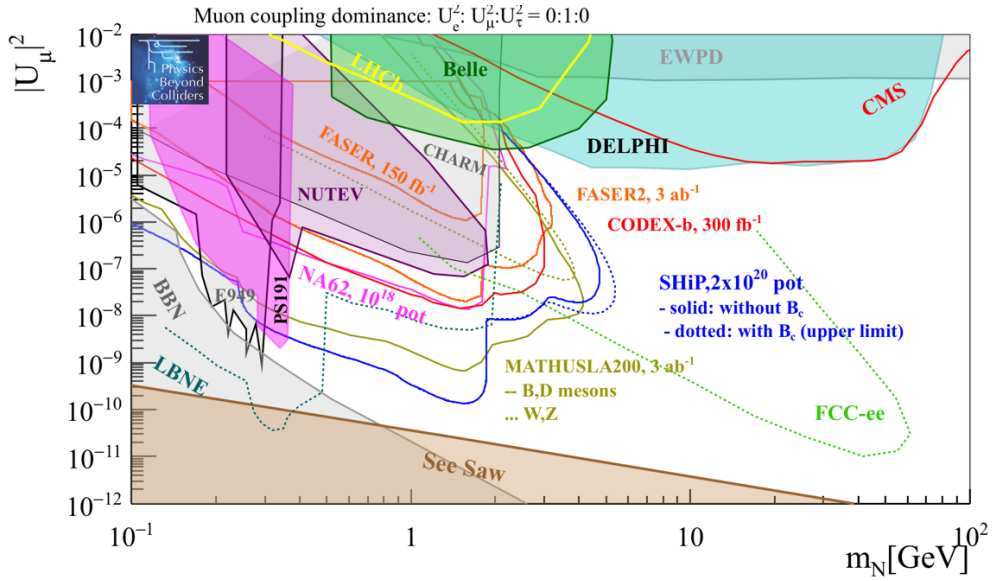

FIGURE 4.6: Sensitivity to HNL with coupling to ν_μ only. Current bounds (filled areas) and 10-15 years prospects for projects (SHiP, MATHUSLA200, CODEX-b and FASER2) (solid lines). Projections for an LBNE near detector with 5×10^{21} protons-on-target and from FCC-ee with 10^{12} Z_0 decays are also shown. The gray contour named "BBN" corresponds to a HNL lifetime > 1sec, which is disfavored by BBN [117]. The brown line labeled "seesaw" represents the scale of mixing in general expected in the canonical seesaw. The very light gray at the top labeled as "EWPD" is the 90% C.L. exclusion limit from the electroweak precision data [118]. The other solid contours are explained in the text.

prompt leptons, either in final states with two same-charge leptons and one or two jets ($W^{\pm(*)} \to \ell^\pm \mathrm{N} \to \ell^\pm \ell'^\pm q\bar{q}'$) [123], or in final states with three prompt leptons and p_T^{miss} in a mass range of 20 GeV to 1.7 TeV. CMS searches with three charged leptons in the final state using the leptonic W decay are going to be extensively discussed in this dissertation.

4.3.2 Constraints on HNL

In the following list, we tried so summarize the current constraints coming from theoretical predictions and from the most recent results (Figs. 4.5, 4.6 and 4.7.)

- **Searches for Charged Lepton Flavor Violation**. If we consider a HNL with a mass close to the EW scale and with large off-diagonal Yukawa couplings, then this can lead to LFV in decays of charged leptons. Thus, testing LFV in multi-lepton searches could be an indirect way to probe the existence of HNL. Searches for such processes have placed 90% C.L. upper limits on decay branching rates, i.e. $BR(\mu^+ \to e^+\gamma) < 4.2 \times 10^{-13}$, $BR(\mu^+ \to e^+e^+e^-) < 1.0 \times 10^{-12}$ and $BR(\tau^- \to e^-\mu^+\mu^-) < 2.7 \times 10^{-8}$. For a complete summary and references see [124].

- **Cosmological constraints on light neutrino masses**. The Planck Satellite's measurements of the large scale structures in the universe, combined with the WMAP + highL + BAO data, have set the upper limits on the sum of all the light neutrinos [125].

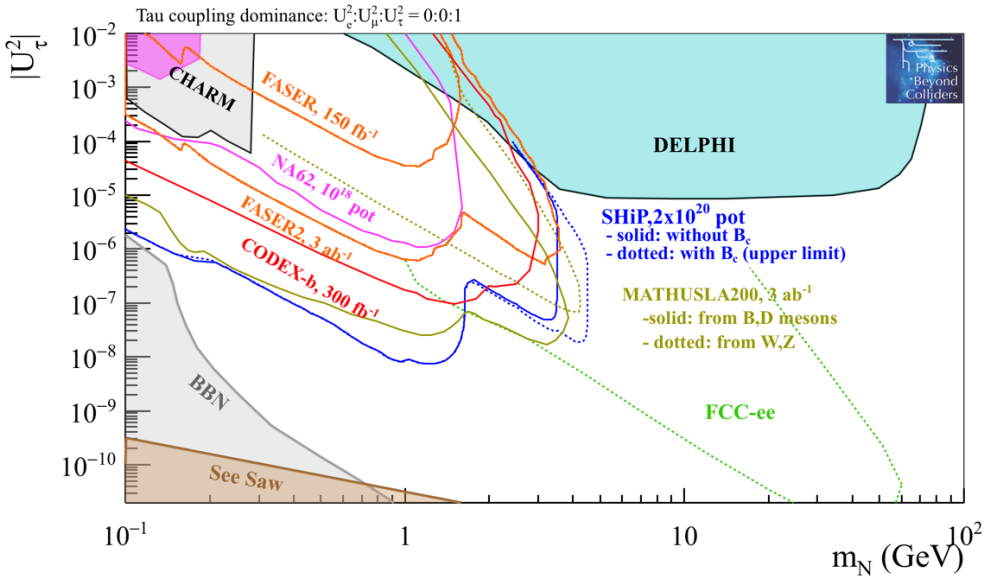

FIGURE 4.7: Sensitivity to HNLs with coupling to ν_τ only. Current bounds (filled areas) and 10-15 years prospects for projects (SHiP, MATHUSLA200, CODEX-b and FASER2) (solid lines). Projections from FCC-ee with 10^{12} Z_0 decays are also shown.

$$\sum_m m_{\nu_m} < 0.12\, eV, \quad at\ 95\%\ C.L. \tag{4.10}$$

This upper limit on the active neutrino masses is directly connected with the possibility of the existence of HNLs and with the predicted numbers of N, $\mathcal{N}$. If the seesaw mechanism is assumed to be responsible for the origin of neutrino masses, one RH neutrino is necessary per observed nonzero light neutrino mass [102]. To conclude, the interpretation of direct search experiments limits and cosmological constraint both strongly depend on $\mathcal{N}$ and the ν_{SM} mass [22, 126]. To clarify, for $\mathcal{N} = 3$, if the lightest neutrino is massless, no lower bound on the mixing parameter $|V_{\ell N}|^2$ can be set. On the other hand, if it is the case like in Eq. 4.10, then there is a lower bound on $|V_{\ell N}|^2$ [22].

- **BBN constraints**. Observing Figs. 4.5, 4.6 and 4.7, a HNL that falls on the left of the Big Bang Nucleosynthesis line would live long enough in the early universe to cause an overproduction of primordial Helium-4 [117].

- **Seesaw limit**. Below the line of the seesaw limit, the mixing of the sterile neutrinos with the active ones becomes too weak to be able to produce the pattern of neutrino flavor oscillations that have been observed [127].

4.4 Summary

In this chapter, we illustrate the relevance and the enthusiasm in the current HNL search program, describing first the theory setting of RH neutrinos and then reporting the rich plethora of experiments and results focusing on HNLs.
In the SM, all fermions are known to have both left- and right-handed chirality, the only exception comes from neutrinos. One argument in favor of the introduction of massive RH neutrinos is that they give an answer to the SM problem of the neutrino masses via the seesaw mechanism. The neutrino mass problem is one of the open questions in physics that indicates that other fundamental physics remains to be unmasked.

When we hypothesize RH neutrinos, N_I, as new particles of the SM we are interested in their properties like the mass M_I and their mixing parameter, $|V_{\alpha I}|^2$, with the SM neutrino of flavor α, controlled by the Yukawa coupling $F_{\alpha I}$. The values of $|V_{\alpha I}|^2$ are unknown and usually the experimental sensitivity is expressed in terms of the coupling $|V_{\alpha I}|^2$ as a function of M_I for a given flavor α.

A list of direct HNL search results are presented; we give an overview of the experimental current and past landscape describing the different decay modes and the mass range that are targeted by each experimental setup. The strategies in direct HNL searches depend greatly on the coupling and mass of the HNLs. For $M_I > 5$ GeV, HNL can be produced uniquely at either LHC or at similar energy colliders, via a few mechanisms (vector boson fusion, s-channel exchange of virtual W-bosons or in real gauge boson decays, refer to Section 5.3) according to the production energy and N mass. A more extensive explanation is given in the following Chapter 5. For $M_I < 5$ GeV, we turn to b-factories or fixed-target experiments.
In this chapter, special attention is paid to the lepton and the hadron collider searches. The LEP results from DELPHI happen to be the best results at low mass from collider experiments up to the publication of the results of this dissertation. For the author, the outstanding sensitivity at low mass from e^+e^- data was surely a good motivation to invest a quite important effort to extend the low mass sensitivity of the CMS experiment. Chronologically we have focused first on the moderate and high mass search to then migrate to the very low mass search which necessarily requires the inclusion of displaced scenarios.

Finally, an overview of the theoretical HNL constraints is presented.
Taking into account the current experimental and theoretical limits on the HNL mass, we discussed the allowed mass window and phase spaces. This clearly necessitates to adopt a comprehensive and vast approach in seeking for HNL. The very wide range of masses, energies and models expects to explore the complementary reach of the current and future experiments.

Chapter 5

Data and simulated datasets

Nearly all of the new physics signals which can be studied at CMS are expected to have their potential backgrounds in which SM processes sporadically have fluctuations that make them appear more exotic than they truly are, or backgrounds arising from detector noise or mis-measurements. For example, an isolated high p_T electron can be a "smoking gun" for a few rare new physics processes. At the same time, an electron contained in a b jet is hardly ever isolated, but since the total b jet cross-section is extremely large, even a small portion can be critical. It becomes crucial to have a sort of "litmus test" to cross-check the observed outcomes with the expected features and the predicted amount of events. The idea is to validate the observed information by comparing it to generated events. For this reason, collision events are simulated for several physics processes as they are predicted from theory. The detector simulation response is taken into account.
In a simplistic way, we can summarize a number of applications of event generators as follows: to give analyzers a sense of the type of events to expect and at which rates; to help in planning new experiment designs hence detector performances are optimal for the desired physics search; to help in drafting analysis strategies which can be applied to data but that have been optimized a priori without any possible unconscious bias; to estimate detector calibrations and acceptance corrections; and to have an appropriate framework inside which to interpret the meaning of observed physics phenomena in the optics of a fundamental underlying theory (SM).

5.1 Simulation of pp collision events

The event simulation is based on the Monte Carlo (MC) method [128]. The simulated events are grouped in a specific sample for each physics process and they are called MC samples. The full simulation chain is divided into separate generation stages:

- **Matrix element (ME) calculation.** The ME calculation makes use of a list of PDFs (Parton Distribution Function) for the initial state depiction; an MC generator is used for the computation of the partonic interaction. For the signal samples produced specifically for this thesis and for most SM processes here presented, the software `MadGraph5_aMC@NLO` [129] is used. For a few other background processes the `POWHEG` [130] software is used. Both softwares have LO and NLO accuracy in QCD. For proton PDFs, in both generators, the NNPDF3.0 [131] and NNPDF3.1 [132] PDFs are used as input.

- **Parton shower simulation.** The simulation is done with the `PYTHIA 8` [133, 134] software. The parton shower step is necessary to address some aspects of the collision with regards to the evolution of quarks and gluons into jets of hadrons, so-called *hadronization*. The hadronization is simulated starting from an energy scale of 1 GeV, adopting phenomenological models tuned to experimental results [135–137].
- **Detector simulation.** The detector simulation is done with `GEANT4` [138] software. The simulation is based on an accurate geometrical model of the CMS detector, hence it includes all the material budget and it tracks the authentic sub-detector responses. Particle interactions with matter are simulated and their energy deposit is reproduced according to the energy and the mass of the particle and the material that it goes through. Data collected by CMS are used to parametrize the real detector response of every single sub-detector. Furthermore, the trigger system and the readout system are mimicked.

While analyzing the simulated samples the kinematics and all properties of the produced primary particles are available in addition to the detector signals just like in real collision data. This possibility makes the simulations a cornerstone of the detector and algorithm performance studies.
Furthermore, there are single year campaigns for each year of data-taking which correspond to different detector conditions for each period.

5.2 Standard Model processes

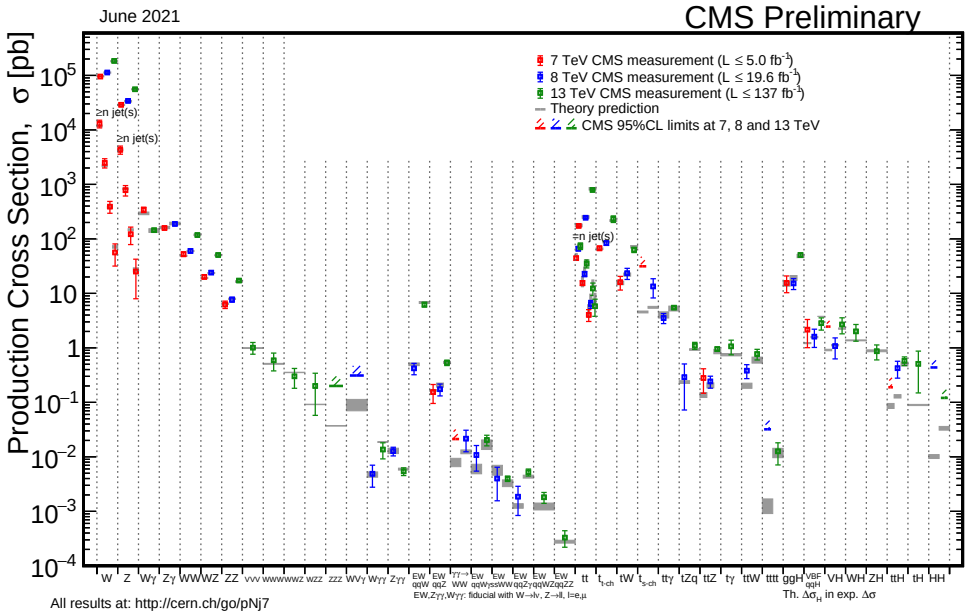

FIGURE 5.1: Summaries of cross sections measurements by CMS [139] for different center-of-mass energies compared to the theory predictions (gray). The plot gives hints about the amount of events we could expect from each single process and the relative rates with respect the signal expected yields.

In this section, we give an overview of the SM processes that form sizable backgrounds to the HNL searches performed in this thesis. The focus is specifically on processes that can lead to three light lepton final states, which is the signature given by HNL decaying either into Z or into W where the bosons decay leptonically; this final state is presented in Chapters 6 and 7.

In Figure 5.1 a summary of cross sections measurements by CMS is presented. The measured values are compared with the theory predictions showing outstanding agreements.

Almost all of the backgrounds are estimated from simulation using the MC samples. The nonprompt lepton background is the only exception and it is discussed for each analysis separately in Sections 6.4.1 and 7.4.2.

In the next paragraphs the SM processes that contribute the most as backgrounds to the HNL searches are listed and explained.

WZ and ZZ production In case both bosons decay leptonically, the associated production of WZ bosons produces three prompt leptons ($Z \to \ell^+\ell^-$, $W \to \ell\nu$) and p_T^{miss}. Its clear signature is an opposite sign same flavor (OSSF) pair with invariant mass compatible with Z mass. The events are characterized by having a few jets or none, and zero b jets. WZ events constitute a dominant background in the three prompt leptons HNL analysis presented in Chapter 6.

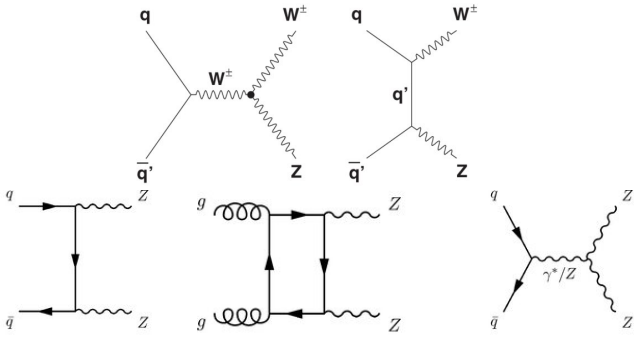

FIGURE 5.2: WZ associated production diagrams (top), ZZ associated production diagrams (bottom) [140].

The associated production of two Z bosons can enter as background in the three lepton final states when one of the leptons fails reconstruction or identification requirements. The events present low p_T^{miss} values and they have just a few jets and zero b jets.

W/Z and photon radiation. In an event, real or virtual photons can appear due to initial state radiation (ISR) or final state radiation (FSR). In the first case, partons in the incoming protons emit low energy/collinear radiation prior to the hard scattering process. For FSR, collinear photons are emitted by the final states particles.
Events (Figure 5.3) presenting either a W or a Z boson in association with a real or virtual photon from ISR or FSR can extensively contribute to the background in three lepton final states.
This is the case when a virtual photon decays (internal conversion) or in which a real photon converts into leptons by interacting with the detector material (external conversion). The photon can undergo an asymmetric internal or external conversion in which one of the

leptons has very low p_T. This soft lepton has a high probability of failing the selection criteria of the analysis, leading to a reconstructed two- (in case of a W boson) or three-lepton (in case of a Z boson) final state. This background mostly contributes to categories with an OSSF pair.
For the displaced lepton analysis presented in Chapter 7 the external conversion is a "nasty" background because it can mimic a HNL decay vertex where e^+e^- is produced. In order to reduce this background either requirements on the kinematic properties of the event or a material veto can be applied. The latter helps in rejecting all the SVs which are located in proximity either of a detector layer or of inert material.

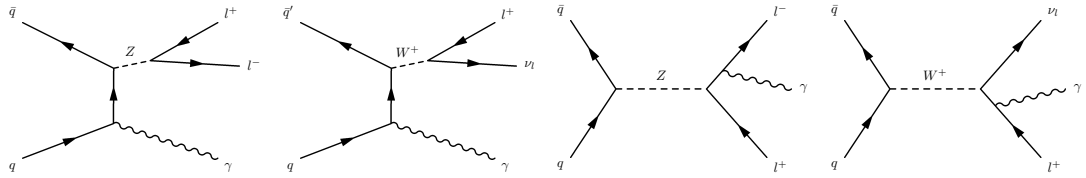

FIGURE 5.3: W or Z plus γ production diagrams. The two diagrams on the left represent an initial state radiation event in association with W/Z production. The two on the right show an final state radiation subsequent to W/Z production [140].

Drell-Yan production. The Drell-Yan process happens when a quark from one of the initial protons annihilates with an anti-quark from the other proton leading to a virtual photon, γ^* or to a Z boson, which then decays into two leptons.

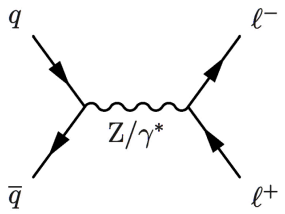

FIGURE 5.4: Drell–Yan dilepton production [140].

Drell-Yan events contribute to three prompt leptons final states when associated with a jet production (DY plus jets) or when one nonprompt lepton is reconstructed and passes the analysis selection. The Drell-Yan production cross-section is so large with respect to the other three leptons processes that even a modest misidentification probability can lead to a large background contribution.

Top quark production. In both the analysis presented in the following two chapters, the background from top quark production ($t\bar{t}$) is among the dominant ones.
In this case, the three leptons come from $t\bar{t}$ production where they originate from semi-leptonic b quark decay and lepton W decay.

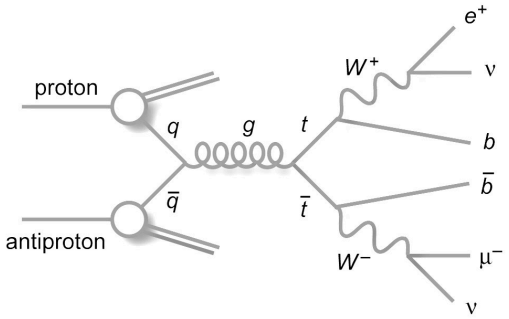

FIGURE 5.5: Diagram for $t\bar{t}$ production. [140]

5.2.1 Long-lived particles

Long-lived HNL search looks for displaced vertices and displaced leptons produced relatively far from the PV. This kind of signature happens to be very different with respect to the very well known SM processes. Along these lines, the backgrounds are not the conventional ones and therefore special care has to be used in understanding them.

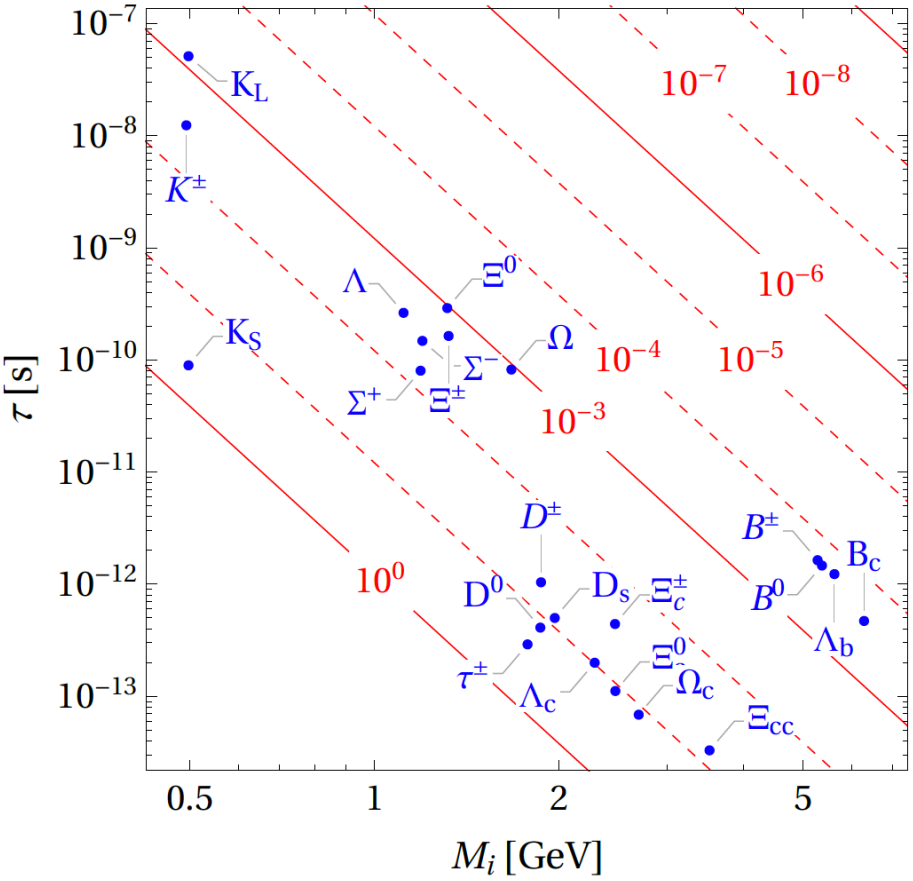

FIGURE 5.6: HNL $|V_{\ell N}|^2$ (red lines) superimposed with potentially important SM backgrounds (blue dots) as function of HNL mass and life time [141].

In Figure 5.6 the phase space of long-lived HNLs is superimposed with potentially important backgrounds coming from long-lived meson and baryon decays. The figure shows the crowded area as a function of HNL mass and lifetime.
It is clear from Figure 5.6 that the resonance backgrounds can be rejected with proper criteria according to the phase space we are investigating. The top-right corner of Figure 5.6 is background-free because it marks a region with very displaced particles with relatively high masses; in this region, we will not need to implement any selection to remove B and D meson contribution. In the central region of Figure 5.6, $m_{\mathrm{N}} \sim 1$ GeV, we find several baryons with relative small lifetimes. In these cases, implementing a veto on a narrow mass window only for those events with small displacement could help in rejecting them. The same mass veto is redundant for events with larger displacement in the same mass region. This strategy will be presented in Chapter 7 where carefully selected mass windows are removed to avoid background contamination.

5.3 Heavy Neutrino signal event Generation

This section is strictly relevant to the signal model used in Chapters 6 and 7. The model is circumscribed to the CMS results only and it is not adopted for ATLAS's results ([122]) which are often used for comparison purposes with the CMS results.

5.3.1 Signal simulation

Signal samples are generated using the `MadGraph5_aMC@NLO` [129] software. The generator is used with next-to-leading order (NLO) precision in perturbative quantum chromodynamics (QCD) for the prompt HNL model, and at leading-order (LO) precision for the long-lived model. The generation is based on the `heavyN` model described in Ref. [142], which is available in Universal FeynRules Output (UFO) by Ref. [143–145]. This model extends the SM with up to three RH neutrinos, which are singlets under the SM gauge symmetry. The mass and mixing parameters of the HNL can be defined for each scenario to probe.

The HNL production via charged current (CC) Drell-Yan process, 5.7(a), via gluon fusion, 5.7(b), and via $W\gamma$ fusion, 5.7(c) is simulated.

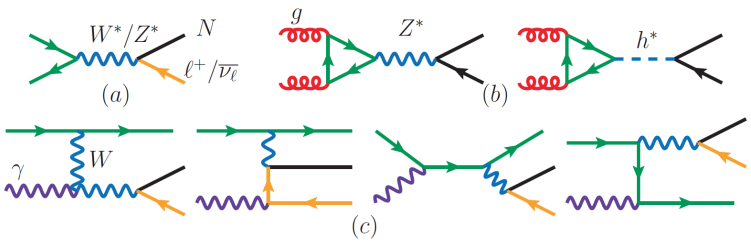

FIGURE 5.7: Diagrams for heavy neutrino production mechanisms at LHC [124]. Each color corresponds to a different particle: black = N, yellow = leptons/neutrinos, green = quarks, blue = bosons, purble = photons and red = gluons.

The production mechanisms via gluon and vector-boson fusion are crucial because at the LHC energies and at high N mass, the CC DY process is no longer the only viable way for producing heavy neutrinos. Vector boson fusion $W\gamma \rightarrow N\ell^{\pm}$ [143, 144, 146] is the dominant production mechanism at the LHC energies for HNLs with very large masses (TeV energy scale) [124, 143, 144] and for lighter HNLs it enhances the inclusive production rate. Neutral current processes [147,148], which involve gluon fusion, $gg \rightarrow Z^*/H^* \rightarrow N\nu\ell$ can even surpass the CC DY cross section for large HNL masses [124,149]. See Figure 5.8 for reference.

For the high mass HNL samples used in the search described in Chapter 6, both gluon fusion and $W\gamma$ fusion are added as production mechanisms. The first two employ the

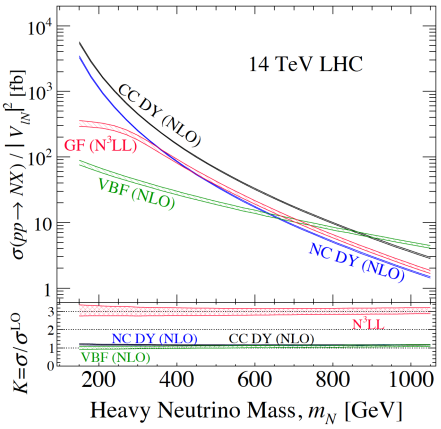

FIGURE 5.8: "HNL production cross section, divided by $|V_{\ell N}|^2$, via charged (CC) and neutral (NC) current DY, $W\gamma$ fusion (VBF), and gluon fusion (GF) at $\sqrt{s} \sim 14$ TeV" [124].

NNPDF3.0 NLO PDFs set [131], while $W\gamma$ fusion uses the LUXqed plus PDF4LHC15 NNLO 100 PDF set [150].
For all the signal MC samples the parton showering and hadronization are simulated with PYTHIA.

Samples with HNL masses from $M_{\mathrm{N}} = 1$ GeV to $M_{\mathrm{N}} = 1.2$ TeV are produced for signal modeling. The simulated HNLs couple exclusively to one of the three SM neutrino families at a time with mixing probabilities typically in a range $|\mathrm{V}_{\ell\mathrm{N}}|^2 = 10^{-6} - 1$, depending on the mass. For this thesis work only the mixing processes between ν_e–N and ν_μ–N are considered and they are assumed to be different from zero while the ν_τ–N is set to zero. The mixing parameters are:

$$\mathbf{V}_{\mathrm{N}\ell} = \begin{pmatrix} \mathrm{V}_{\mathrm{N}e} & 0 & 0 \\ 0 & 0 & 0 \\ 0 & 0 & 0 \end{pmatrix}, \qquad \mathbf{V}_{\mathrm{N}\ell} = \begin{pmatrix} 0 & 0 & 0 \\ \mathrm{V}_{\mathrm{N}\mu} & 0 & 0 \\ 0 & 0 & 0 \end{pmatrix}, \tag{5.1}$$

where $\mathbf{V}_{\mathrm{N}\ell}$ represents the active-sterile neutrino mixing matrix:

$$\begin{pmatrix} \nu_e \\ \nu_\mu \\ \nu_\tau \end{pmatrix} = \mathbf{V}_{\mathrm{N}\ell} \cdot \begin{pmatrix} \mathrm{N}_1 \\ \mathrm{N}_2 \\ \mathrm{N}_3 \end{pmatrix}. \tag{5.2}$$

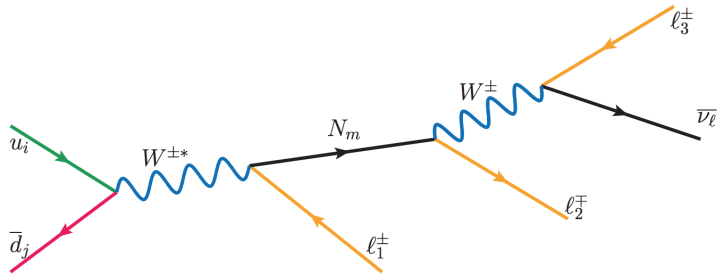

FIGURE 5.9: HNL production and decay. Only the leptonic decay of the W is considered [124].

5.3.1.1 Long-lived HNL samples

For the long-lived HNL, the width Γ_{N} is computed automatically by the generator, and the mean lifetime $\tau_{\mathrm{N}} = \hbar/\Gamma_{\mathrm{N}}$ is used to extract the HNL lifetime in each simulated event, according to a decay probability distribution

$$\frac{dN(t)}{dt} = \frac{1}{\tau_{\mathrm{N}}} e^{-t/\tau_{\mathrm{N}}} \tag{5.3}$$

where t is the *proper* lifetime, measured in the HNL rest frame.
As explained in Section 4.2.3, the values of M_{N} and $|\mathrm{V}_{\ell\mathrm{N}}|^2$ do not only determine the HNL production cross section, but also its mean lifetime and, consequently, its kinematics, acceptance, and reconstruction efficiency. For a fixed value of M_{N}, therefore, a simple cross-section rescaling is not sufficient to correctly reproduce the behavior of other HNLs with the same mass and different $|\mathrm{V}_{\ell\mathrm{N}}|^2$.

The simple and naive approach with endless computing power would be an iterative one. For a M_{N} and $|\mathrm{V}_{\ell\mathrm{N}}|^2$ scenario, first, compute the limits by evaluating parameters of interest as the overall *signal strength* (number of signal events / number of expected signal events); when computing the fit between signal, data, and background yields, by default the signal strength is left floating in the fit so that the measurement is independent of the presence or absence of a signal. Depending on the value of the signal strength there are two options. If the signal strength is below 1 it means that the M_{N}–$|\mathrm{V}_{\ell\mathrm{N}}|^2$ case is excluded and a new sample with the same M_{N} but smaller $|\mathrm{V}_{\ell\mathrm{N}}|^2$ has to be simulated. If the signal strength is above 1 it means that the analysis is not sensitive to that M_{N}–$|\mathrm{V}_{\ell\mathrm{N}}|^2$ case and a new sample with the same M_{N} but larger $|\mathrm{V}_{\ell\mathrm{N}}|^2$ has to be simulated. This iteration can be repeated with steps smaller and smaller until the signal strength is exactly 1 which means we found the exclusion limits. It is clear that this kind of approach is not sustainable due to the limited computing time and available computing power. A smarter correction procedure is needed.
To this purpose, a per-event re-weighting technique based on the HNL lifetime is used instead, which properly accounts for all the variations in kinematics and acceptance.
First, it is noticed that the average kinematics of a HNL decay is entirely defined by the HNL mass M_{N}, its momentum $p_{\mathrm{N}} = \beta\gamma M_{\mathrm{N}}$, and its decay length, independently of its mean lifetime τ_{N}. Therefore, given a simulated HNL sample of mass M_{N} and mean lifetime τ_0, we can reproduce the kinematic distributions of any target HNL scenario with the same mass and different lifetime, $(M_{\mathrm{N}}, \tau_{\mathrm{T}})$. An event with proper decay time t taken from the simulated sample of mean lifetime τ_0 is re-weighted by the ratio of probabilities to obtain t from τ_{T} or from τ_0:

$$W(t; \tau_0 \to \tau_{\mathrm{T}}) \;=\; \frac{dN_{\mathrm{T}}(t)/dt}{dN_0(t)/dt} \;=\; \frac{\tau_0}{\tau_{\mathrm{T}}} \exp\left[-t\left(\frac{1}{\tau_{\mathrm{T}}} - \frac{1}{\tau_0}\right)\right]. \tag{5.4}$$

Taking it a step further, a whole set of multiple HNL samples with different lifetimes $\{\tau_i\}$ can be used to emulate the τ_{T} scenario. In this case the decay time distributions must include the correct normalization factors for each sample, N_i/τ_i, where N_i is the number of simulated events for the sample with mean lifetime τ_i and $N_{\mathrm{tot}} = \sum_i N_i$:

$$W(t; \{\tau_i\} \to \tau_{\mathrm{T}}) \;=\; \frac{dN_{\mathrm{T}}(t)/dt}{\sum_i dN_i(t)/dt} \;=\; \frac{\frac{N_{\mathrm{tot}}}{\tau_{\mathrm{T}}} \exp\left(-t/\tau_{\mathrm{T}}\right)}{\sum_i \frac{N_i}{\tau_i} \exp\left(-t/\tau_i\right)}.$$

If σ_{T} is the production cross section for $(M_{\mathrm{N}}, \tau_{\mathrm{T}})$ and $\mathcal{L}$ is the integrated luminosity, the complete event weight is

$$w(t; \{\tau_i\} \to \tau_{\mathrm{T}}) \;=\; \frac{\sigma_{\mathrm{T}}\mathcal{L}}{N_{\mathrm{tot}}} W(t; \{\tau_i\} \to \tau_{\mathrm{T}}) \;=\; \frac{\frac{\sigma_{\mathrm{T}}\mathcal{L}}{\tau_{\mathrm{T}}} \exp\left(-t/\tau_{\mathrm{T}}\right)}{\sum_i \frac{N_i}{\tau_i} \exp\left(-t/\tau_i\right)}. \tag{5.5}$$

Figure 5.10 compares the proper decay length (ct) distributions for three samples of $M_{\mathrm{N}} = 4$ GeV with different mean lifetimes, and the corresponding models built from the sum of the three samples by re-weighting with Eq. 5.5. An excellent agreement is observed, with the re-weighted summed sample exhibiting less statistical fluctuations than the individual samples. Figure 5.11 shows distributions of the reconstructed dilepton mass ($M(\ell_2, \ell_3)$) and secondary-vertex transverse displacement ($\Delta_{2\mathrm{D}}$ (3.3)) for a HNL scenario with $M_{\mathrm{N}} = 4$ GeV

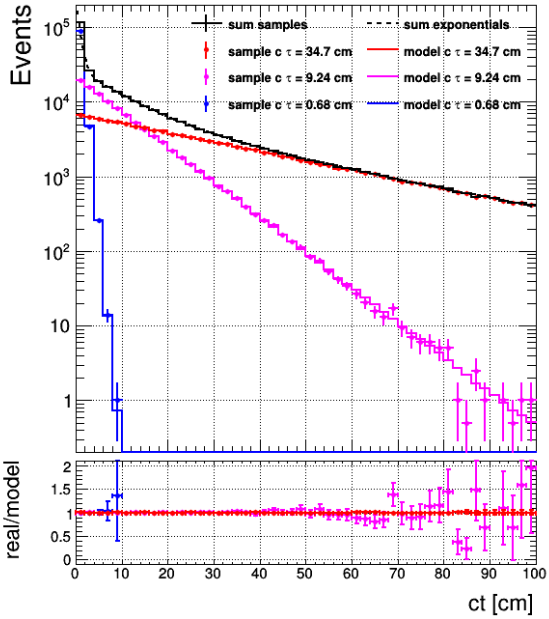

FIGURE 5.10: Distribution of the proper decay length ct for three HNL samples of $M_N = 4GeV$ and different mean lifetimes (points withs error bars), and the corresponding models built from the sum of the three samples by re-weighting with Eq. 5.5 (continuous histograms). The black, continuous histogram shows the sum of the three samples, while the black, dashed line is the sum of the three exponential functions that describe the proper decay length of the three samples. Courtesy of D. Trocino.

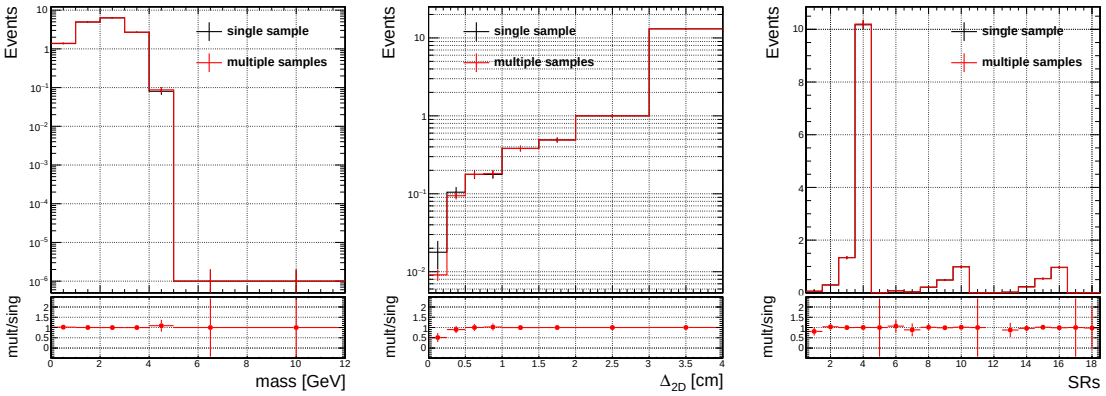

FIGURE 5.11: Distributions of the reconstructed dilepton mass $M(\ell_2, \ell_3)$ (left), secondary-vertex transverse displacement Δ_{2D} (middle), and final signal-region yields described in Section 7.3.2 (right), for a HNL scenario with $M_N = 4GeV$ and $|V_{\mu N}|^2 = 6.31 \cdot 10^{-6}$ in the 2018 simulation. The black histograms are modeled using a single sample with the re-weighting of Eq. 5.4, while the red histograms use the sum of three samples with different $|V_{\mu N}|^2$ values and the re-weighting of Eq. 5.5. Courtesy of D. Trocino.

and $|V_{\mu N}|^2 = 6.31 \cdot 10^{-6}$ in 2018, modeled using either a single sample with the re-weighting of Eq. 5.4 (black histograms), or the sum of three samples with different $|V_{\mu N}|^2$ values and the re-weighting of Eq. 5.5 (red histograms). The two models are compatible.
The histograms presented in Figure 5.11 are filled with events that pass the event selection

specifically designed for the long-lived HNL analysis presented in Chapter 7, for details refer to Section 7.3.

Figure 5.12 shows the total number of HNL signal events available for each $(M_N, |V_{\mu N}|^2)$ point, which were generated specifically for the long-live HNL search. For each HNL mass, all the samples produced with different lifetimes $\{\tau_i\}$ have been used to emulate the τ_T scenario.

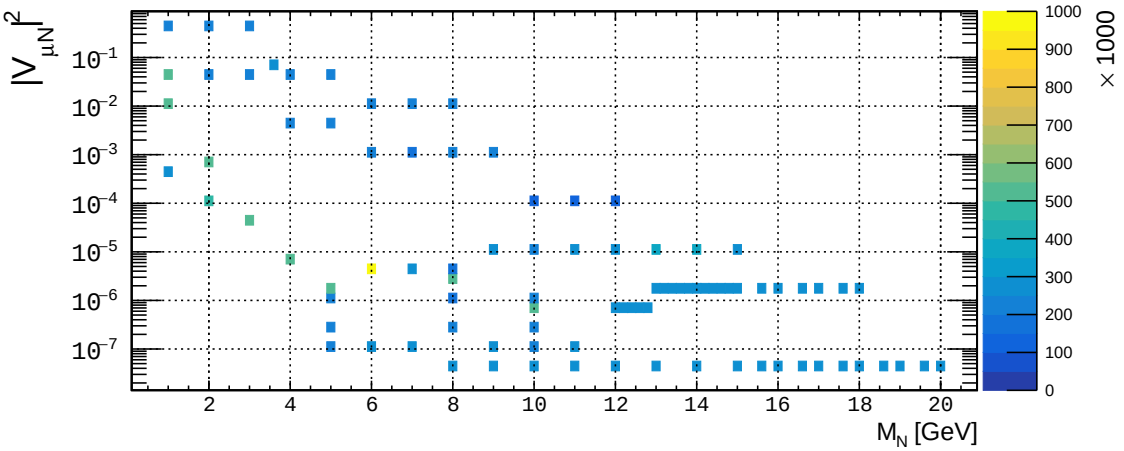

FIGURE 5.12: Total number of signal MC events available for each $(M_N, |V_{\mu N}|^2)$ point, considering both private and central CMS productions. The number of events can be read with color code using the palette on the right; the range is from 100 to 1000 events. The picture can be mirrored for $(M_N, |V_{eN}|^2)$ scenario.

5.3.1.2 Dirac HNL signal emulation

The HNL production cross-section is fixed by the M_N and $|V_{\ell N}|^2$ values [144, 145], and it is the same for Dirac and Majorana HNLs. The resonance width for a Majorana HNL, on the other hand, is exactly twice the width of a Dirac HNL with same M_N–$|V_{\ell N}|^2$ values, due to the additional charge-conjugated (LNV) decay channels (refer to Figure 5.13). As a consequence, the average lifetime of a Dirac HNL is twice that of a Majorana HNL with same $(M_N, |V_{\ell N}|^2)$. Refer to Section 4.2.2.

For the HNL analysis with three prompt leptons (Chapter 6) there is no need to produce distinct Dirac and Majorana MC samples since there is no difference between them except the final state combinations. For the long-lived scenario, separate samples are necessary.

After the lessons learned with the emulation procedure described above, a similar idea and strategy was also adopted for obtaining HNL signal sample for the scenario where HNL has a Dirac nature using the sample where HNL is a Majorana particle.
To optimize computing resources and in the interest of time, high-statistics MC samples were produced on a large scale for Majorana HNL scenarios only. Dirac HNL scenarios for any $(M_N, |V_{\ell N}|^2)$ point were emulated starting from the corresponding Majorana HNL samples, following these steps:

- from a Majorana HNL sample, select only the LNC events by looking at the unique identity number of the generated particles;

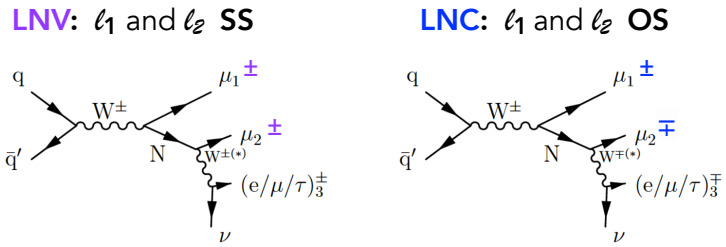

FIGURE 5.13: Visualization of the LNV and LVC cases. HNL with a Majorana nature contributes to both diagrams, while Dirac type HNL can only lead to right side diagram. These diagrams show the specific case when N mixes with ν_μ only resulting in having μ_1 and μ_2. The same diagrams can be made for e_1 and e_2 as well.

- re-weight each LNC event to emulate the correct lifetime of the Dirac HNL, by using Eq. 5.4 with $\tau_T = 2\tau_0$;
- since only half the events of the original Majorana sample are used (while the cross-section is the same for Majorana and Dirac scenarios), add a factor 2 to the event weight to restore the correct normalization.

This method provides good modeling of the Dirac HNL signal, but uses only half the events from the Majorana HNL MC samples. With a simple extra assumption, it is possible to make use of the full statistical power of our MC production.
As explained in Section 7.7, the signal selection is the same for LNC and LNV events. Just in the final stage of the analysis, events are split into same-lepton-charge and opposite-lepton-charge categories to distinguish LNV and LNC events for the physics interpretation. If we assume that the lepton efficiency and the acceptance are the same for positively and negatively charged leptons (i.e., same reconstruction and identification efficiency, the same momentum scale and resolution, etc.), then we can use both LNC and LNV events from the Majorana HNL samples to emulate the Dirac scenarios, and simply classify all of them as opposite-charge events. In fact, any difference in the performance of positive and negative leptons is expected to be negligible, certainly well below the systematic uncertainties assigned to the displaced leptons (see Section 7.5.3). This approach allows us to use all the available events from the Majorana HNL samples in the Dirac HNL interpretation.
Figure 5.14 shows a comparison between Dirac HNL samples and Majorana HNL samples corrected to emulate Dirac scenarios, employing both strategies outlined above. As can be seen, differences are small across the most relevant observables for defining the search strategy.

5.3.1.3 Uncertainty on LL-signal MC cross section

The `heavyN` model used for the generation of long-lived HNL events does not allow for NLO QCD calculations. The simulation of HNL events happens therefore at LO, resulting in large theoretical uncertainties on the cross-section (up to 15%) that have to cover the effect of the missing higher-order QCD corrections and PDF uncertainties.

Instead of relying on these LO uncertainties, a general correction factor for the cross-section from LO to NNLO can be derived based on the SM production of $W \to \ell\,\bar{\nu}$. In HNL

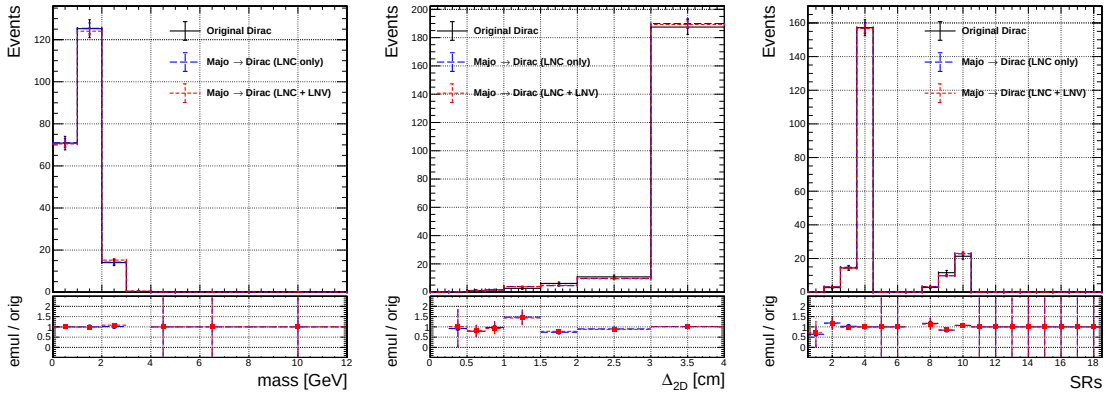

FIGURE 5.14: Distributions of the reconstructed dilepton mass $M(\ell_2, \ell_3)$ (left), of the transverse displacement of the reconstructed HNL decay vertex Δ_{2D} (middle), and event yields in the different analysis categories (right) for a Dirac HNL with $M_N = 2$ GeV and $|V_{\mu N}|^2 = 2.47 \times 10^{-4}$ in 2018 simulation, using three models: a Dirac HNL sample (black), or a set of Majorana HNL samples with $M_N = 2$ GeV and various $|V_{\mu N}|^2$ values, re-weighted to emulate the Dirac scenario with $|V_{\mu N}|^2 = 2.47 \times 10^{-4}$, using LNC events only (blue) or all events (red). Courtesy of D. Trocino.

production, the only difference from this SM process is the exchange of the SM neutrino by a HNL. The effect of the mass and coupling of the HNL can be factorized in the calculation of the HNL cross-section and is not affected by the PDF and scale variations. The dominant effect of these uncertainties appears at the production of the W boson, therefore it can be studied in the SM process $W \to \ell\ \bar{\nu}$, for which recommended values for the cross-section at NNLO exist with their corresponding theory uncertainties. Our approach is to get a LO cross-section for $W \to \ell\ \bar{\nu}$ calculated with Madgraph using the same exact conditions as the HNL MC production. A correction factor from LO to NNLO can be derived based on this and can then be applied to HNL MC. The PDF and scale uncertainties at NNLO are applied as flat systematic uncertainties to cover the remaining uncertainty on the MC cross-section.

It has been checked and verified that the generator conditions are similar between our MC production and the centrally produced W+jets samples, from which the recommended NNLO cross-section was taken. The small differences that are present have no significant effect on the cross-section calculation. Additionally, lepton universality will allow us to apply the scale factor and uncertainty across all HNL samples, regardless of which lepton flavor(s) they couple with.

The resulting LO cross-section for $W \to \ell\ \bar{\nu}$ ($\ell = e\ ,\ \mu\ ,\ \tau$) is 56500 pb. The recommended NNLO value is $61526.7^{+497.1}_{-264.6} \pm 2312.7$ pb where the quoted uncertainties are respectively scale and PDF uncertainties. Assuming uncorrelated uncertainties and taking the maximum of the two asymmetric errors, the combined uncertainty is 61526.7 ± 2365.5 pb, an effect of 3.86%. This gives a final scale factor of 1.089 ± 0.042.

5.4 Data sets

For each CMS analysis according to the final states we select, a specific type of primary datasets (PDs) is used.

The definition of the primary datasets is intrinsically connected to the HLT trigger paths (2.2.2.6). The PD design is centered around particles reconstructed in the event by the HLT, and follows one simple principle: grouping together events with similar physics content; for instance, there are single-lepton datasets and double-leptons datasets. Since an event can pass more than one HLT path, it can enter more than one primary dataset. At a practical level, possible overlaps among different datasets are removed by checking run, lumi-section, and event numbers in order to not have twice the same event coming from different PDs.

The analysis presented in Chapter 6 includes `SingleElectron`, `SingleMuon`, `DoubleEG`, `DoubleMuon` and `MuonEG` primary datasets; the choice was driven by the multiple trigger requests, both single lepton trigger and dilepton triggers in order to maximize the trigger efficiency.

The analysis presented in Chapter 7 includes only `SingleElectron` and `SingleMuon` for signal search, while `DoubleEG` and `DoubleMuon` primary datasets are used for background measurements. For this specific case, the choice was made considering the limitations due to the presence of displaced leptons in the final states. Since (most of) the CMS leptonic triggers are optimized for prompt lepton identification, it was decided to use single-electron and single-muon triggers for the signal selection.

The first analysis presented in the following chapters used only *pp* collision data collected by the CMS experiment at a center-of-mass energy of 13 TeV in 2016, corresponding to an integrated luminosity of 35.92 fb^{-1}.

The long-lived HNL analysis uses three sets of *pp* collision data corresponding to three years of data-taking at a center-of-mass energy of 13 TeV, corresponding to integrated luminosities of 35.92 fb^{-1} (2016), 41.53 fb^{-1} (2017), and 59.97 fb^{-1} (2018).

5.5 Summary

In this chapter an overview of the simulated signal and main background samples and the data sets samples is presented.
We first introduced the different "ingredients" that compose the background of the analyses presented in Chapters 6 and 7. We tried to explain which SM processes can contribute and contaminate the signal region accidentally passing the object and event selection criteria. Taking into account the three prompt leptons final state scenario, we listed the processes that better mimic the signal signatures while having a sizable branching ratio and large production cross-sections.

We described the HNL model adopted in the context of this thesis. The main features were presented with a large focus on long-lived HNL case. In this framework the re-weighting procedure was introduced, which is going to be a key point for the interpretation of the results in both the prompt and displaced heavy neutral lepton analyses of Chapters 6 and 7.

Finally, details about data taking, data campaigns, and primary datasets were presented.

Chapter 6

Search for HNL in events with three charged prompt leptons

The first search [151] on HNLs using a multilepton final state at the CMS experiment is presented here. The targeted signature comprises three prompt charged leptons in any flavor combination of electrons and muons.

6.1 Introduction

The search probes direct heavy neutrino production in the decay of W bosons, in which the SM neutrino oscillates into a HNL. The focus lies on events in which the HNL decays either into a Z boson and a neutrino, or into a W boson and a charged lepton. The resulting electroweak gauge boson can then decay leptonically, leading to a final state with three charged leptons and a neutrino. The Feynman diagrams corresponding to the described processes are shown in Figure 6.1. Further, a Majorana HNL can decay into a lepton with either same-sign (Figure 6.1 left) or opposite-sign (Figure 6.1 right) with respect to the lepton, ℓ, coming directly from W boson.

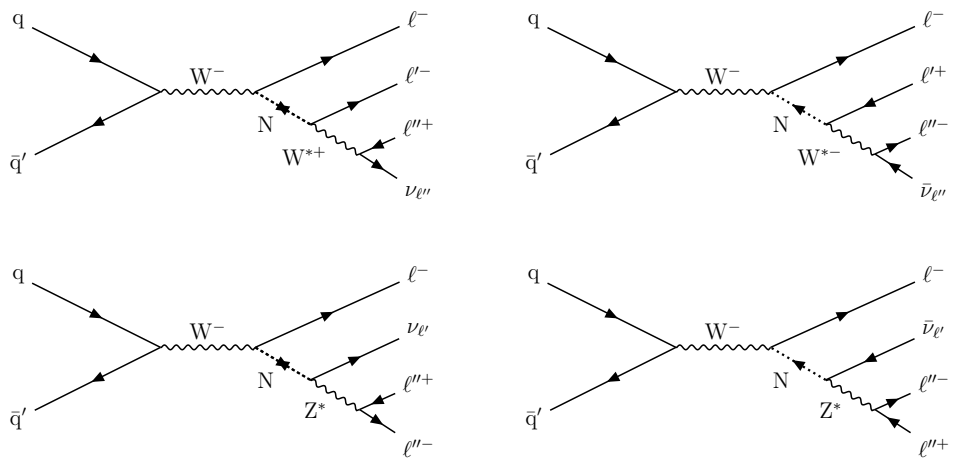

FIGURE 6.1: Typical diagrams for the production of a HNL (N) at the LHC through its mixing with a SM neutrino, leading to a final state with three charged leptons and a neutrino.

The final results of this analysis will be presented as sensitivity curve as a function of both the mass and the mixing parameter, $|V_{\ell N}|^2$ of the HNLs.

6.2 Analysis setup

6.2.1 Data and simulation samples

The current analysis uses the set of pp collision data collected during the 2016 run at a center-of-mass energy of 13 TeV corresponding to an integrated luminosity of 35.9 fb^{-1}.

A number of signal models, as described in the previous chapter, Section 5.3.1, were simulated with NLO precision in perturbative QCD.

The luminosity scenario has a 25 ns bunch crossing separation with an average of about 23 pileup interactions per bunch crossing, for details, refer to Section 2.1.

6.2.2 Signal compression and trigger strategy

A challenging aspect of the signal under consideration is that except for very high masses, the p_T spectra of the resulting leptons are in general very soft and they are all collected in the same low p_T region; we can say that the p_T spectra are compressed. The degree of this compression, and which leptons are affected, depends on the mass of the produced HNL. The p_T spectrum of the three highest p_T generator-level charged leptons is shown in figure 6.2 for different HNL mass scenarios, ranging from 5 to 200 GeV.

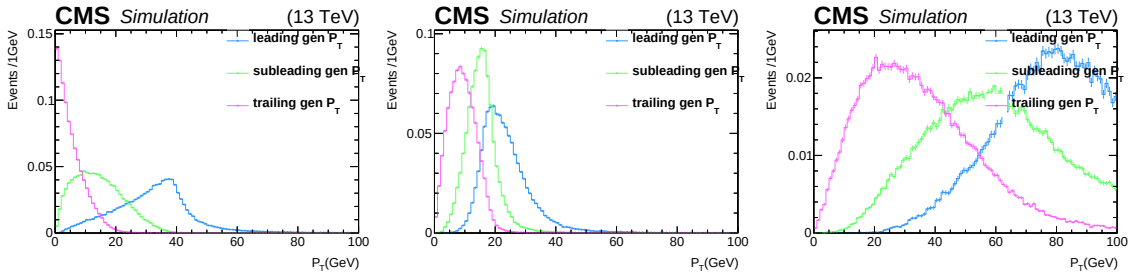

(A) (B) (C)

FIGURE 6.2: p_T spectrum of the three highest generator-level leptons in the signal simulation of several HNL masses. From top left to bottom right the HNL mass scenarios for which the spectrum is shown are 5 GeV (A), 60 GeV (B), and 200 GeV (C). Courtesy of W. Verbeke.

It can be seen that for every mass scenario below the W-mass, one or more leptons have a tendency to have very low p_T values. For low mass samples, both the trailing and subleading leptons are soft because of the small mass of the decaying HNL. For HNL masses close to the mass of the W, very little phase space is left for the emission of the lepton in the W's decay since all of the W's mass has to go into the production of the HNL. For high masses, on the other hand, the compression is not as pronounced even though the trailing lepton can still be seen to prefer relatively low momenta because of the high off-shell W-boson required for the production of very heavy HNL's. Furthermore, the cross-section for off-shell W-boson production drops rapidly with increasing mass, and as such the lepton with the smallest p_T also tends to have very little phase space available for its production in very high mass scenarios.

We can clearly notice in Figure 6.2 different lepton p_T spectra according to the M_{N} and the correlation between the distributions and the M_W. For this reason the analysis strategy has been divided in two main phase spaces:

- *low mass search:* soft leptons, $M_{\mathrm{N}} < M_W$;
- *high mass search:* hard leptons, $M_{\mathrm{N}} > M_W$;

6.2.2.1 Trigger strategy

Due to the low p_T spectra of the leptons in the HNL signals, designing a trigger strategy is a challenging task. For high HNL masses, the leading lepton p_T is generally on the efficiency plateau of the single-lepton triggers. For low HNL masses, we need to add double- and triple-lepton triggers to obtain optimal signal efficiency. The triggers used in this analysis are listed in table 6.1.

TABLE 6.1: Overview of the lepton p_T thresholds imposed in the analysis and the p_T regime in which each trigger path provides sensitivity.

search region	lepton flavors	selected p_T range (GeV)			sensitive trigger paths
	ℓ^{leading} $\ell^{\text{subleading}}$ ℓ^{trailing}	p_T^{leading}	$p_T^{\text{subleading}}$	p_T^{trailing}	
low mass	$ee\mu$	30–55	> 15	> 5	$1e$
		15–30	> 15	> 8	$2e1\mu$
		23–30	10–15	> 8	$1e1\mu$
		25–30	> 15	5–8	$2e$
	$e\mu e$, μee	30–55	> 15	> 10	$1e$ or 1μ
		15–30	> 15	> 15	$2e1\mu$
		23–30	> 10	10–15	$1e1\mu$
	$\mu\mu e$	30–55	> 15	> 10	1μ
		15–30	> 10	> 10	$1e2\mu$
	$\mu e\mu$, $e\mu\mu$	30–55	> 10	> 10	$1e$ or 1μ
		15–30	> 10	> 9	$1e2\mu$
		23–30	> 10	5–9	$1e1\mu$
high mass	all flavors	> 55	> 15	> 10	all paths

The overall approach to selecting the offline thresholds in the analysis is the following: .

- Each trigger path could select one or more leptons (refer to table 6.1 for all the used trigger paths); furthermore for each lepton a specific efficiency can be individually measured, it will be referred to as lepton-specific efficiency. Then data/MC scale factors (SF) are calculated for each used lepton-specific trigger and determine values where these SFs are constant. Typical SF values are 98% for a muon-specific and 99% for an electron-specific.
- determine total efficiency of trigger combinations (not anymore lepton-specific) in MC simulation, and choose p_T thresholds leading to the highest overall efficiency and being not lower than the values determined in the first step;
- check the overall data/MC SF in an orthogonal and unbiased dataset which was selected by triggering on p_T^{miss} or on the hadronic activity of the event;
- determine systematics from the SF values obtained in the first step and validate its choice in the previous step:
  - use 5% systematics for events with leading lepton $p_T < 30$ GeV (max. SF value for $ee\mu$ and $e\mu\mu$ case),

  - and 2% for events with leading lepton $p_T > 30$ GeV (max. SF value of a muon leg).

- require trigger information in MC samples when deriving the yields, but not apply any additional correction.

The overall $1\ell+2\ell+3\ell$ trigger efficiency was measured in WZ MC samples after selecting 3 leptons with relevant flavor combinations which pass the offline analysis identification selection. The efficiency is typically close to 100% and always above 92%, for events with leading lepton $p_T > 30$ GeV. For events in which the leading lepton p_T is < 30 GeV, the efficiency falls down reaching the value of 70% in the worst case scenario. Hence we assign a 5% uncertainty on the trigger efficiency for leading lepton $p_T < 30$ GeV and for $p_T > 30$ GeV we assigned a 2% uncertainty.

6.2.3 Object selection

For the rigorous explanation of the single object reconstruction in CMS see Chapter 3, section 3.1.

6.2.3.1 Leptons

The base objects of this analysis are electrons and muons. Both electrons and muons have three selection working points, called LOOSE, FAKEABLE OBJECT (FO) and TIGHT [1] which are specifically delineated for this analysis. The LOOSE working point is used when cleaning electrons from overlap with muons, to be specific, electrons are not considered for selection if they fall within a cone of $\Delta R = 0.05$ around a LOOSE muon. The FO working point is slightly tighter than the LOOSE one and is extensively used for the estimation of the background due to nonprompt and fake leptons as described further in this text. The ideal feature of a typical FO working point is that after applying it the probability that a selected nonprompt lepton also passes the TIGHT working point should be independent of the flavor of its origin parton. This property will prove essential for the nonprompt lepton background estimation as further specified. The full definitions of each selection working point, for respectively muons and electrons are shown in tables 6.2 and 6.3.

Signal leptons are required to be isolated (refer to Section 3.3) from any hadronic activity in the event. LOOSE and FO leptons are required to have $I_{\text{rel}} < 0.6$. TIGHT leptons must satisfy $I_{\text{rel}} < 0.1$.

A notable difference between the muon and electron selection criteria is the p_T thresholds that are being used. Considering the earlier discussion on the compressed p_T spectra of the low HNL mass scenario, it is clear that we want to apply p_T thresholds as low as feasible in order to gain the maximum signal efficiency. So ideally we would want low p_T thresholds on both muons and electrons, but for low mass search, the triggers are a limiting factor in how low we can realistically go. The higher electron trigger thresholds make going lower than 10 GeV in electron p_T unfeasible, even though our trigger strategy is optimized for maximum efficiency and thresholds as low as possible, as described in the previous section. The relatively high p_T thresholds forced upon us by the available triggers leave us with

[1] N.B. these working points do not necessarily coincide with the ones defined in Sections 3.1.3.2 and 3.1.4.2. For these latter, the italic style is used.

TABLE 6.2: All the variables used in the table are introduced in Chapter 3 in Sections 3.1, 3.1.3.2 and 3.3. Requirements to pass each definition of the muon selection.

Selection criteria	LOOSE	FO	TIGHT
$\|\eta\| < 2.4$	✓	✓	✓
p_T	> 5	> 5	> 5
$\|d_{xy}\| < 0.05$ (cm)	✓	✓	✓
$\|d_z\| < 0.1$ (cm)	✓	✓	✓
$\text{SIP}_{3D} < 4$	–	✓	✓
I_{rel}	< 0.6	< 0.6	< 0.1
is PF Muon	✓	✓	✓
is Global or Tracker Muon	✓	✓	✓
is *Medium* Muon	–	✓	✓

TABLE 6.3: All the variables used in the table are introduced in Chapter 3 in Sections 3.1, 3.1.4.2 and 3.3.

Selection criteria	LOOSE	FO	TIGHT
$\|\eta\| < 2.5$	✓	✓	✓
p_T	> 10	> 10	> 10
$\|d_{xy}\| < 0.05$ (cm)	✓	✓	✓
$\|d_z\| < 0.1$ (cm)	✓	✓	✓
$\text{SIP}_{3D} < 4$	–	✓	✓
I_{rel}	< 0.6	< 0.6	< 0.1
MVA ID ($p_T < 15$ GeV)	–	$> (-0.02, -0.52, -0.52)$	$> (0.77, 0.56, 0.48)$
MVA ID ($p_T > 25$ GeV)	–	$> (-0.02, -0.52, -0.52)$	$> (0.52, 0.11, -0.01)$
$\sigma_{i\eta i\eta} < (0.011, 0.011, 0.030)$	–	✓	✓
$\text{H/E} < (0.10, 0.10, 0.07)$	–	✓	✓
$\Delta\eta_{\text{in}} < (0.01, 0.01, 0.008)$	–	✓	✓
$\Delta\phi_{\text{in}} < (0.04, 0.04, 0.07)$	–	✓	✓
$-0.05 < 1/E - 1/p < (0.010, 0.010, 0.005)$	–	✓	✓
conversion rejection	✓	✓	✓
Number of missing hits	< 2	$== 0$	$== 0$

relatively low signal efficiencies, as the often very soft trailing, and subleading signal leptons do not manage to pass the thresholds of the baseline object selection. Aside from this, harsher p_T thresholds of 15 and 10 GeV are applied to the leading and subleading leptons in order to pass the employed triggers.

6.3 Analysis strategy

All events entering the signal regions are required to have three light leptons passing the TIGHT requirements as described in the section above (6.2.3). The events with three leptons of the same sign are not retained in the analysis. Events with three leptons in which one or several leptons fail the TIGHT criteria, but pass the FO selection entered the sideband region to estimate the nonprompt lepton background. The presence of a fourth FO lepton was vetoed in order to suppress the contribution of processes yielding four leptons such as ZZ, while having only a sub-percent effect on the predicted signal yields.

Events in which a jet with $p_T > 25$ GeV is found, passing the loose working point of the CSV b-tagging algorithm, are rejected in order to substantially decrease the background from the $t\bar{t}$ process.

The baseline p_T cuts applied in the analysis are driven by the trigger thresholds of the available triggers as described in Table 6.1.

Aside from kinematic criteria, the events are categorized according to the sign and flavor of the three leptons; events with an OSSF (Opposite Sign Same Flavor) pair and events without an OSSF pair. This categorization helps to discriminate between different backgrounds and it consistently reduces the background yields from SM processes.

As described in Section 6.2.2, the analysis strategy is spilt into two main phase spaces, the *low mass search* ($M_{\mathrm{N}} < M_W$) and the *high mass search* ($M_{\mathrm{N}} > M_W$).

6.3.1 Low mass search

As the name suggests the low mass region focuses on the search for HNLs of low mass, in particular those below the mass of the W boson. These low mass HNL events are characterized by relatively low values for p_T^{miss} and for the trilepton invariant mass $M_{3\ell}$. Thus, upper bounds are applied on p_T^{miss} and $M_{3\ell}$, namely: $p_T^{miss} < 75$ GeV and $M_{3\ell} < 80$ GeV. The latter requirement contributes to suppress the background from asymmetric external- and internal conversions (a detailed explanation of this background contribution is given in Section 7.4.2.3). In such events, a lepton might radiate a real or virtual photon converting into a lepton pair where one lepton takes away most of the photon's energy, and the second lepton ends up failing basic selection requirements. A large contribution of such events is expected from the Z + γ process, mainly having $M_{3\ell}$ values close to the Z boson mass. The p_T^{miss} threshold is applied since almost all low mass HNL production events fall below this value, whereas several major backgrounds such as $t\bar{t}$ and WZ often have larger p_T^{miss} values.

The low mass HNL search is split into two distinct categories. Events are categorized according to the p_T of the leading lepton as anticipated earlier. The first category consists of events with leading lepton p_T values between 30 and 55 GeV. This category mainly targets HNL scenarios in which the difference between the W mass and the HNL is large, in other words very low HNL masses, in which the leading lepton is expected to be hard. The second category is characterized by leading lepton p_T values below 30 GeV and is mainly used for inquiring about the existence of HNLs with masses close to that of the W boson. In such cases, the limited phase space available for the production of the charged lepton in the W decay, and the other in the HNL decay leads to three relatively soft leptons. Dedicated studies were performed in order to select the optimal value of the upper p_T cut on the leading lepton p_T. The implementation of this upper p_T cut can be seen to help reduce the background significantly while only minimally affecting the signal efficiency.

The low mass category of this analysis only considers events without an OSSF pair due to the massive contribution of Drell-Yan + jets, asymmetric conversion and WZ backgrounds in events with an OSSF pair. Though it is combinatorially more likely for the signal to contain an OSSF pair, the background is multiple orders of magnitude larger for such events, and the sensitivity was negligible compared to events without an OSSF pair. Attempts were made to define search regions for such events, which ended up being roughly two orders of magnitude less sensitive than those without an OSSF pair. Thus, these events are not further considered for low mass search.

The summary of the *low mass* search event selection is listed in Table 6.4.

In the selected events without an OSSF pair, the best discrimination between the signal and the background came from the minimal invariant mass, $min(M_{OS})$, out of all possible

TABLE 6.4: Baseline selection requirements applied to all data sets for the *low mass* search.

Variable	Requirement
N. b jets	$= 0$
4th ℓ veto	✓
p_T^{leading}	< 55 GeV
$M_{3\ell}$	< 80 GeV
p_T^{miss}	< 75 GeV

pairs of opposite sign leptons in the event. The distribution of this variable is shown for the signal and the background in Figure 6.3 (left) before the low/mass categorization. In Figure 6.3 (middle/right) the $min(M_{OS})$ distribution is shown for the signal and the background for both the low and high leading p_T categories of the low mass search.

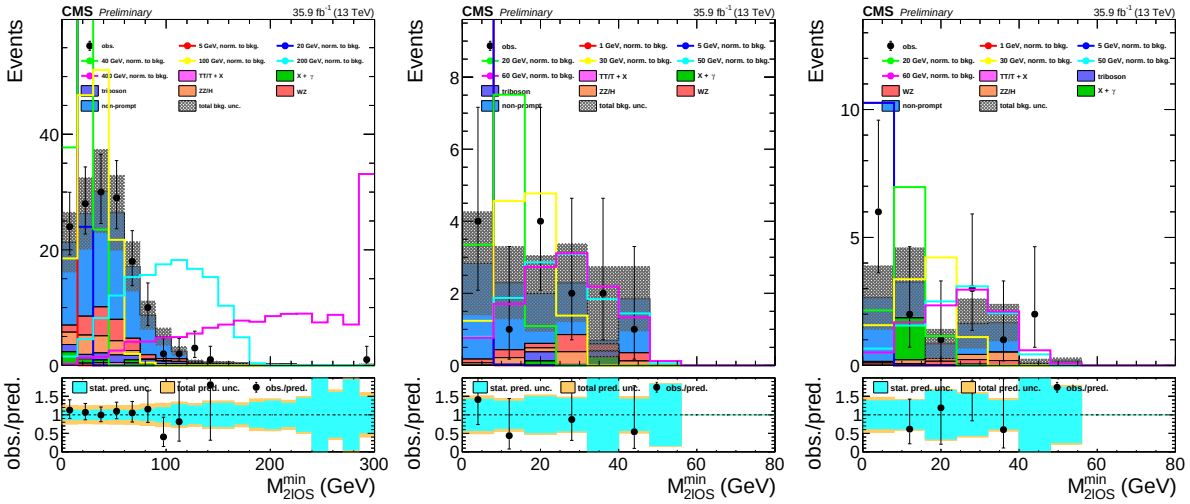

FIGURE 6.3: Expected background yields and signal yields normalized to the total background as a function of $min(M_{OS})$ for the high leading p_T category of the low mass search (middle) and the low leading p_T category (right). Courtesy of W. Verbeke.

The definitions of the low mass search regions, using this variable, are shown in Table 6.5. The expected yields in each of these search regions, compared to the predicted yields of several HNL mass scenarios, with $|V_{\ell N}|^2 = 10^{-5}$ can be found in Section 6.6.

TABLE 6.5: Search regions in the low mass category.

p_T^{leading} (GeV)	$min(M_{OS})$ (GeV)			
	< 10	$10 - 20$	$20 - 30$	> 30
< 30	SR A1	SR A2	SR A3	SR A4
$30 - 55$	SR B1	SR B2	SR B3	SR B4

6.3.2 High mass search

To facilitate the simultaneous interpretation of the low- and high mass searches, the selection of events entering each search category should be orthogonal. In the low mass search, the following upper limits are applied to several kinematic quantities: $p_T^{miss} < 75$ GeV, p_T of

leading lepton < 55 GeV and $M_{3\ell} < 80$ GeV. Applying a threshold in p_T^{miss} to guarantee orthogonality will cut away a significant portion of the signal, so we opted for using either the p_T of the leading lepton or $M_{3\ell}$ to require orthogonality. By testing both orthogonality requirements separately, and computing expected exclusion limits using the search regions defined further, it was established that requiring the p_T of the leading lepton to be larger than 55 GeV gave the best performances.

In addition to this, the subleading lepton is required to pass a p_T threshold of 15 GeV and the trailing lepton is required to be above 10 GeV in p_T. This selection requirement somewhat lower the signal acceptance, but drastically reduce the background from non-prompt leptons which is especially large for very low trailing lepton p_T values. Events in which an OSSF pair is present are rejected if $M_{\ell\ell}$, defined as the OSSF pair mass closest to the Z mass, falls within a range of 15 GeV around the Z boson mass, in order to reject the bulk of the WZ background. The same off-Z requirement is applied to $M_{3\ell}$ in order to suppress the contribution from the earlier mentioned asymmetric external and internal conversions.

The summary of the *high mass* search event selection is listed in Table 6.6.

Table 6.6: Baseline selection requirements applied to all data sets for the *high mass* search.

Variable	Requirement
N. b jets	$= 0$
4th ℓ vetoe	✓
p_T^{leading}	> 55 GeV
$p_T^{\text{subleading}}$	> 15 GeV
p_T^{trailing}	> 10 GeV
$\lvert M_{3\ell} - 91\rvert$	> 15 GeV
$\lvert M_{\ell\ell} - 91\rvert$	> 15 GeV
$min(M_{OS})$	> 5 GeV

In order to minimize the expected exclusion limits on the HNL mixing parameter, we started by checking a plethora of variables for discriminating power between the signal and the background. The shapes of the background and of the signal were compared in all of those variables, and the most promising variables, giving large and obvious shape differences were picked out by eye. All the variables displaying shape differences were then used to design multiple sets of preliminary search region definitions used for binning the events. The expected signal exclusion limits were computed for each set of search regions by performing a simultaneous fit and compared among the several preliminary search region definitions. Two variables were found to be more optimal than the others: the earlier mentioned $min(M_{OS})$ and the transverse mass of the lepton not belonging to the pair forming this minimum mass referred to as M_T^{other}. The expected yields are shown in Figure 6.4 for events with- and without an OSSF pair, compared to several HNL mass scenarios with yields normalized to those of the background.

The selection of the search regions was done by defining, in bins of M_T^{other} and $min(M_{OS})$, a very large number of search regions that were iteratively collapsed in order to retain about one background event in each search region, facilitating correct limit setting and a reliable background prediction. Events with low $M_{3\ell}$ bin ($M_{3\ell} < 100$ GeV) are expected to significantly contribute to the sensitivity for HNL masses below the W mass. For events with

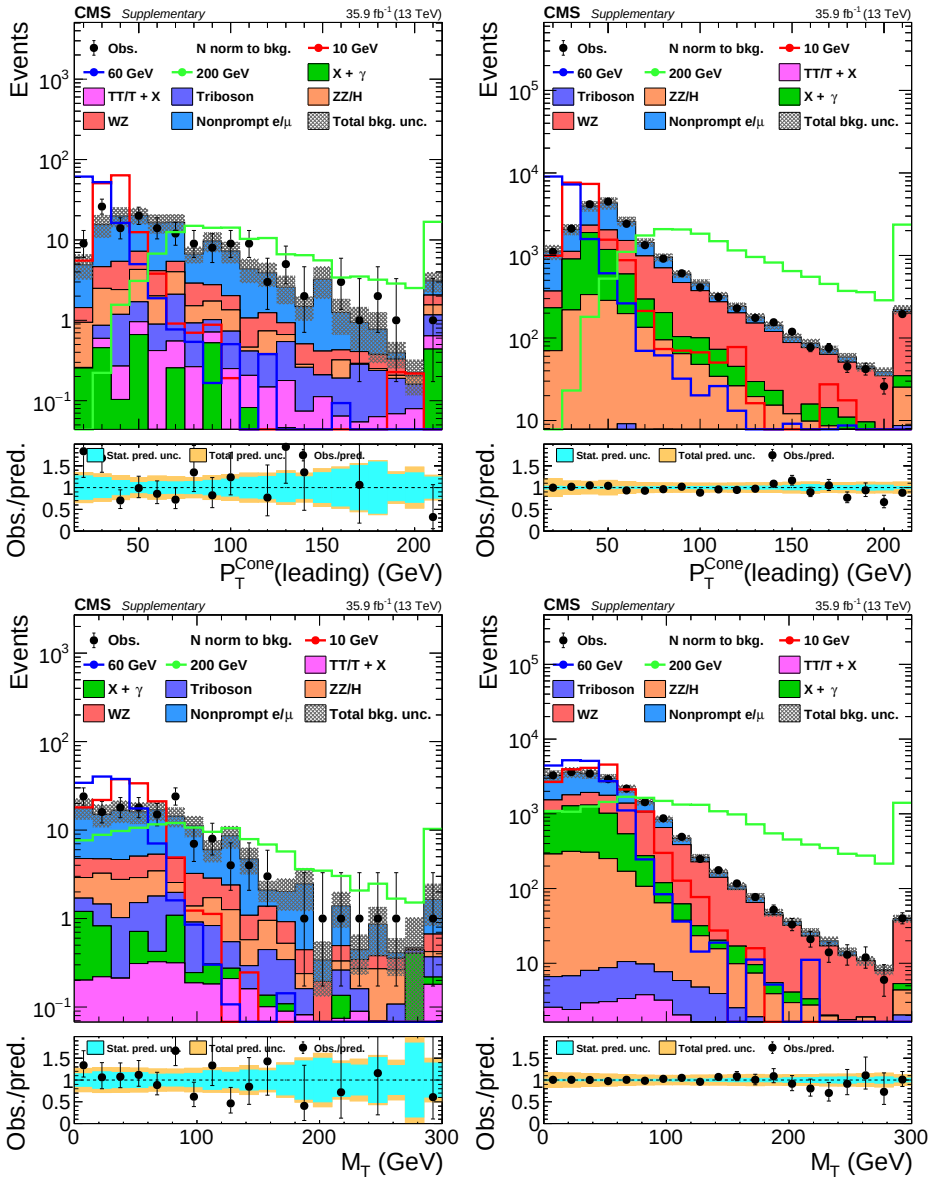

FIGURE 6.4: The distributions of p_T^{cone} and M_T^{other} for events without an OSSF pair (left) and with an OSSF pair (right). Courtesy of W. Verbeke.

an OSSF pair, events with a lepton pair forming a mass below 5 GeV are vetoed in order to purify the low $M_{3\ell}$ bin from a very large conversion and Wγ^* backgrounds. The search region definitions are shown in tables 6.7 and 6.8. The expected background yields as a function of the search region, together with signal yields for several HNL masses at $|V_{\ell N}|^2 = 10^{-2}$ can be found in Section 6.6.

TABLE 6.7: Search regions for events with an OSSF pair in the high mass category.

$M_{3\ell}$ (GeV)	M_T^{other} (GeV)	$min(M_{OS})$ (GeV)		
		< 100	$100 - 200$	> 200
$0 - 100$	< 100	SR C1		
	$100 - 200$	SR C2		
	> 200	SR C3		
> 100	< 100	SR C4	SR C9	SR C13
	$100 - 200$	SR C5	SR C10	SR C14
	$200 - 300$	SR C6	SR C11	SR C15
	$300 - 400$	SR C7	SR C12	SR C16
	> 400	SR C8		

TABLE 6.8: Search regions for events without an OSSF pair in the high mass category.

$M_{3\ell}$ (GeV)	M_T^{other} (GeV)	$min(M_{OS})$ (GeV)		
		< 100	$100 - 200$	> 200
$0 - 100$	< 100	SR D1		
	> 100	SR D2		
> 100	< 100	SR D3	SR D7	SR D9
	$100 - 150$	SR D4	SR D8	
	$150 - 250$	SR D5		
	> 250	SR D6		

6.4 Background estimation

An overview of the principal background contributions is shown in Figure 6.5. The main sources of backgrounds (refer to Section 5.2 for an extensive overview) present in the final search regions can be divided into the following categories:

- **WZ production:** when both W and Z bosons decay leptonically, these events produce the same signature as the new physics scenarios targeted by this analysis: three energetic and isolated leptons and a sizable p_T^{miss} due to a neutrino from the W boson decay. This is the dominant background by large in the searches with three e or μ forming an OSSF dilepton pair. Further details in Section 6.4.3.2.
- **Nonprompt e and μ:** nonprompt leptons are leptons from heavy-flavor decays, misidentified hadrons, muons from light-mesons that decay in flight, or electrons from unidentified conversions of photons in jets. This background is dominated by the $t\bar{t}$ and Drell-Yan processes. This category provides the largest background contribution in the trilepton search regions without an OSSF pair. Further details in Section 6.4.1.
- **External and internal conversions:** events in which a virtual photon decays (internal conversion) or in which a real photon converts into leptons by interacting with the detector material (external conversion). In these cases, this photon undergoes an asymmetric internal or external conversion in which one of the leptons has very low p_T. This soft lepton has a high probability of failing the selection criteria of the analysis, leading to a reconstructed two- (in case of a W boson) or three-lepton (in case of a Z boson) final state. This background mostly contributes to categories with an OSSF pair. Further details in Section 7.4.2.3.
- Rare SM processes with multiple prompt leptons: rare standard model processes that yield three or more leptons include multi-boson production (W, Z, H), single boson production in association with a $t\bar{t}$ pair, and double-parton scattering. Such processes

generally have very small production rates and in some cases are further suppressed by the b-jet veto.

The background from nonprompt light leptons is estimated by using the TIGHT-TO-LOOSE ratio method. The probability for a loosely defined light lepton to pass the full set of selection criteria are measured in a multi-jet sample in data enriched in nonprompt leptons, called the measurement region, refer to Section 6.4.1 for details. Once measured, this probability is applied in a sample of events which pass the full kinematic selection, but where at least one of the leptons fails the nominal selection but passes the FO requirements (refer to Tables 6.2- 6.3), in order to predict the number of events from nonprompt leptons entering each search region. The residual contribution from prompt leptons in the measurement and application regions is subtracted using MC simulation. It is verified in both MC simulation and $t\bar{t}$- or DY-enriched data control regions that this method describes the background from the nonprompt leptons entering the different search regions within a systematic uncertainty of 30%.

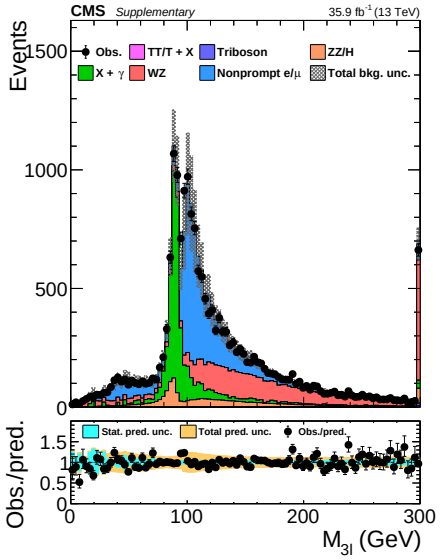

FIGURE 6.5: Observed and expected yields as a function of $M_{3\ell}$ for events with an OSSF lepton pair. Courtesy of W. Verbeke.

The modeling of the conversion background is verified in a data control region enriched in both external and internal conversions. The rate of $Z \to 3\ell$ events where one lepton from $\gamma^{(*)} \to \ell\ell$ is out of acceptance is compared with the full prediction derived from the MC simulation and the nonprompt leptons estimation method, in an off-Z control region defined by $|M_{\ell\ell} - M_Z| < 15$ GeV, $|M_{3\ell} - M_Z| < 15$ GeV, and $p_T^{miss} < 50$ GeV.

The WZ background is normalized to data in a control region obtained requiring an on-Z OSSF pair to be present. An additional requirement applied for events to enter the control region is $p_T^{miss} > 50$ GeV.

The predicted background yields are found to agree with the simulation within the statistical uncertainties.

Figure 6.5 shows the background composition at the first stage of the analysis selection.

6.4.1 Background from nonprompt and fake leptons

The contribution from nonprompt leptons is derived with the TIGHT-TO-LOOSE method by using event yields with three leptons where at least one lepton fails to satisfy TIGHT selection criteria (refer to Tables 6.2- 6.3) but passes FO [2] ones (*application region*), and by applying to them a TIGHT-TO-LOOSE ratio or a FAKE-RATE (FR or f) which is the probability for a nonprompt lepton to pass the TIGHT and isolation selection.
This ratio is constructed in such a way that eliminates the mother parton p_T and flavor

[2] We all agree that TIGHT-TO-LOOSE naming is not optimal when the ratio happens between TIGHT and FO leptons. For "historical" and "traditional" reasons we use TIGHT-TO-LOOSE name keeping in mind that the selection in the denominator is the FO one.

dependence. Hence, while measured in the dijet events, it allows to reliably estimate nonprompt lepton background arising both from $t\bar{t}$ and DY+jets processes.
To mitigate FAKE-RATE dependence on the mother parton p_T, the FAKE-RATE is defined as a function of a quantity which serves as a proxy for mother parton p_T for non-isolated leptons, and which is equal to a lepton p_T for isolated leptons. This quantity is constructed as lepton p_T plus the activity in the isolation cone around the lepton, and is thus referred to as p_T^{cone}:

$$p_T^{cone} = p_T^{\ell} \times \Big(1 + \min\big(0., I_{\text{rel}} - I_{\text{rel}}^{\text{tight}}\big)\Big) \tag{6.1}$$

where the I_{rel} is the relative isolation of the lepton calculated in a cone with size $\Delta R = 0.3$, while the $I_{\text{rel}}^{\text{tight}}$ is the TIGHT working point defined in tables 6.2 and 6.3. In the application region, p_T^{cone} is used to compute all lepton-related kinematic variables such as $M_{\ell\ell}$, M_{T}, etc., as well as is used instead of the lepton p_T when applying search regions p_T thresholds.

Flavor dependence of the FAKE-RATE is important in the estimation of nonprompt electrons. While the nonprompt muons are mainly real muons coming from semileptonic b-decays, the nonprompt electrons are often misidentified light-flavor jets. The contribution of this source of misidentified light-flavor jets varies significantly between the FR measurement multijet region and between the various signal regions used in this analysis. Minimize the dependency of the results of the method to the composition of nonprompt electrons is then necessary; hence the definition of FO electron is tuned in such a way that FR for real electrons from semileptonic b-decays is close to the FR for misidentified jets in the kinematic region of interest to the analysis. This tuning is performed by using $t\bar{t}$ and QCD MC samples and is done by finding a working point of electron MVA classifier which leads to the desired effect.

6.4.1.1 FAKE-RATE measurement

We measure the FAKE-RATE maps in data.
The control region we use to measure is enriched in QCD jet events and it is defined:

- one FO (defined in Tables 6.2 and 6.3);
- at least one jet with ΔR (jet,FO) > 1;
- $p_T^{miss} <$ 20 GeV and $M_{\text{T}} <$ 20 GeV;
- pass a specific single leptons trigger with p_T thresholds: 3,8,17 GeV for μ and 8,12 GeV for electrons.

While measuring the FAKE-RATE in data in lepton+jet events we should take into account the contamination from prompt leptons, mostly from W and Z production in association with jets. To discriminate between QCD events and W/Z events we can use the transverse mass of the lepton and the missing transverse energy; requiring p_T^{miss} and M_{T} upper limits we strongly reduce the contribution from prompt leptons in the measurement region.
The residual contamination is subtracted both from the numerator and from the denominator transverse momentum bins using the simulated $W + jets$, DY, and $t\bar{t}$ events from MC samples. The simulation is normalized in the control region dominated by $W + jets$, DY processes, with $p_T^{miss} >$ 20 GeV and 70 $< M_{\text{T}} <$ 120 GeV. Due to different trigger pre-scales of the single lepton triggers, the MC normalization and the prompt leptons contribution subtraction are performed separately for all triggers in the corresponding lepton p_T ranges.

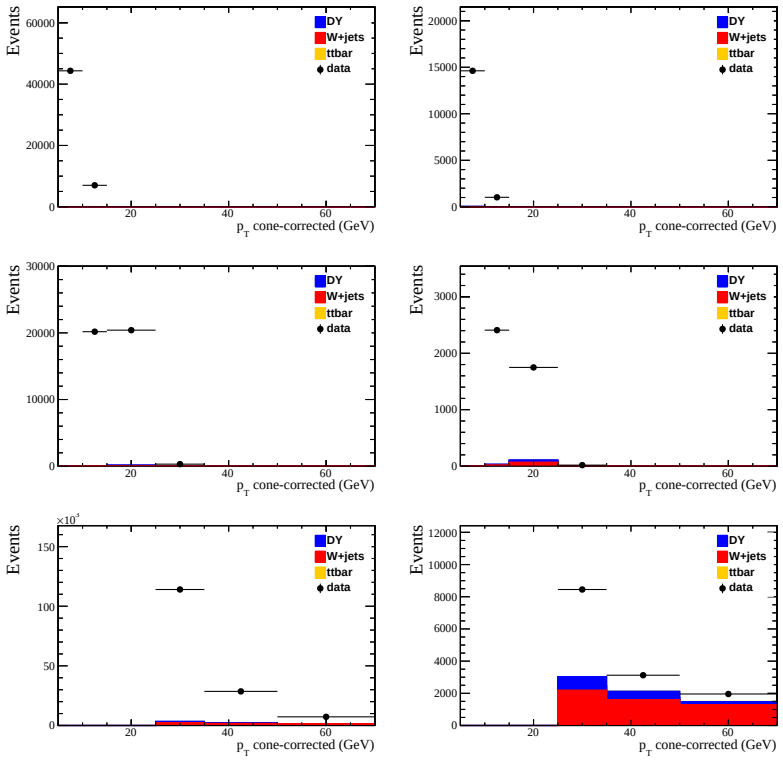

FIGURE 6.6: p_T^{cone} distributions, here labeled p_T^{cone}-corrected, for muons. In the left column there are p_T^{cone} distributions for FO (denominator) while in the right one for TIGHT leptons (numerator). Three rows for the three muon triggers: Mu3, $p_T^{cone} \in [5, 12]$ GeV, Mu8 $p_T^{cone} \in [12, 25.5]$ GeV and Mu17 $p_T^{cone} > 25.5$ GeV.

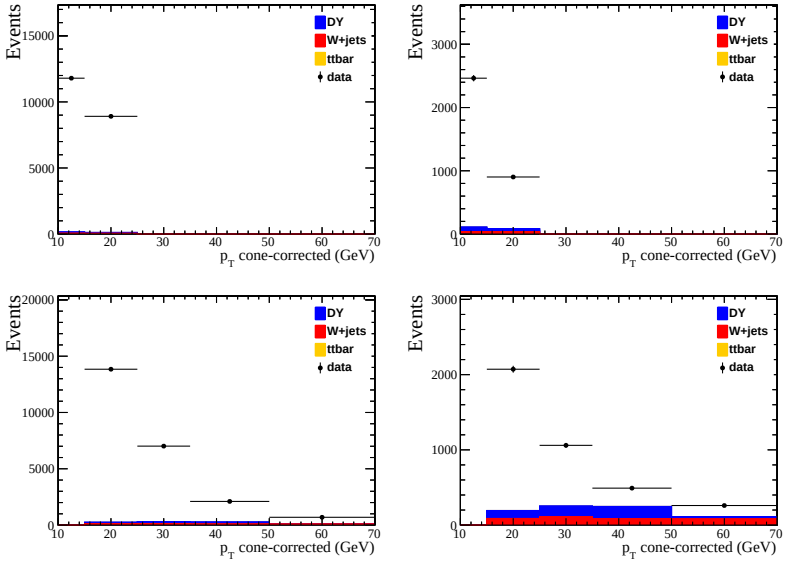

FIGURE 6.7: p_T^{cone} distributions, here labeled p_T^{cone}-corrected, for electron. In the left column there are p_T^{cone} distributions for FO (denominator) while in the right one for TIGHT leptons (numerator). Two rows for the two electron triggers: Ele8 $p_T^{cone} \in [10, 18]$ GeV and Ele12 $p_T^{cone} > 18$ GeV.

In Figures 6.6 and 6.7 the contribution of the prompt leptons in the measurement region is shown, after the normalization. As we expected the majority of leptons from W and Z production in association with a jet is located in the region with high p_T leptons. This is reflected in the calculation of the FAKE-RATE map.

FAKE-RATE measured in MC We also measure the FAKE-RATE in MC QCD di-jets and MC $t\bar{t}$ by finding a nonprompt lepton by means of MC truth-matching. In Figure 6.8 the comparisons between the fake rate measured in data and in MC (QCD di-jets and $t\bar{t}$) are presented.
The data-MC comparison offers the possibility to verify and cross-check the measurement done in data. The usage of the MC truth-information guarantees the proper identification of the nonprompt leptons among the leptons selected with the FO and TIGHT IDs. Hence the contamination from prompt leptons in the denominator failing the TIGHT selection is none. Thus the discrepancies in Figure. 6.8 in the bins at high p_T are due to the large EWK contamination. Then the last bin is not used due to the sizable EWK contamination, leptons with p_T larger than 40 GeV are predicted with FAKE-RATE measured with leptons with p_T $[35-50]$ GeV.
It is essential to point out that for this analysis the softest lepton (trailing) is typically the one that fails the TIGHT selection and it is predicted using the FAKE-RATE ratio measured in data. Thus, the fact that the last bin of the FR shown in Figure 6.8 is not used does not affect the analysis because there are no fake leptons at high p_T.

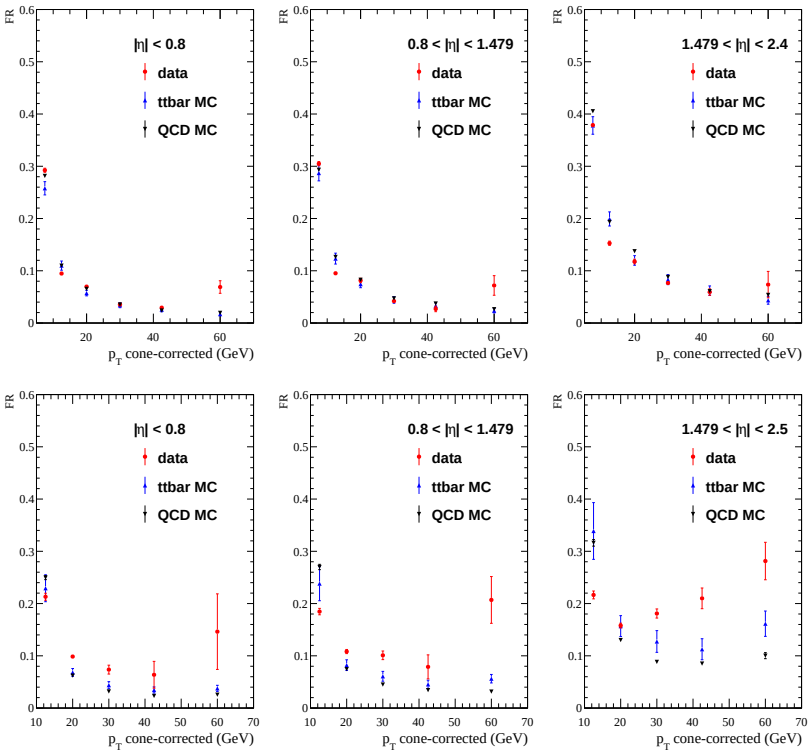

FIGURE 6.8: FAKE-RATE values for muons (top) and electron (bottom), calculated in data (red), QCD MC (black) and $t\bar{t}$ MC(blue).The last bin is not used due to the large EWK contamination, leptons with p_T larger than 40 GeV are predicted with FR at the bin $[35-50]$ GeV.

6.4.1.2 FAKE-RATE application

We define the application region requiring at least one of the three selected leptons to fail the TIGHT lepton definition. In the signal region, we estimate the contribution by expressing the yields of events where l leptons pass the full selection, and $n - l$ fail it. In this way the background prediction is obtained by weighting the events in the application region according to:

- if the event is $T_1T_2L_3$, i.e. only one fails, it is weighted by $f_3/(1-f_3)$
- if the event is $T_1L_2L_3$, i.e. two fail, it is weighted by $-(f_2\ f_3)/(1-f_2)(1-f_3)$
- if the event is $L_1L_2L_3$, i.e. all fail, it is weighted by $(f_1\ f_2\ f_3)/(1-f_1)(1-f_2)(1-f_3)$

where f_i is the FAKE-RATE evaluated on the p_T^{cone} and η of the failing lepton.

6.4.1.3 Validation of the TIGHT-TO-LOOSE method in simulation, $t\bar{t}$ MC

Closure tests are necessary in order to test if we are able to predict the nonprompt background after the event selection requirements.

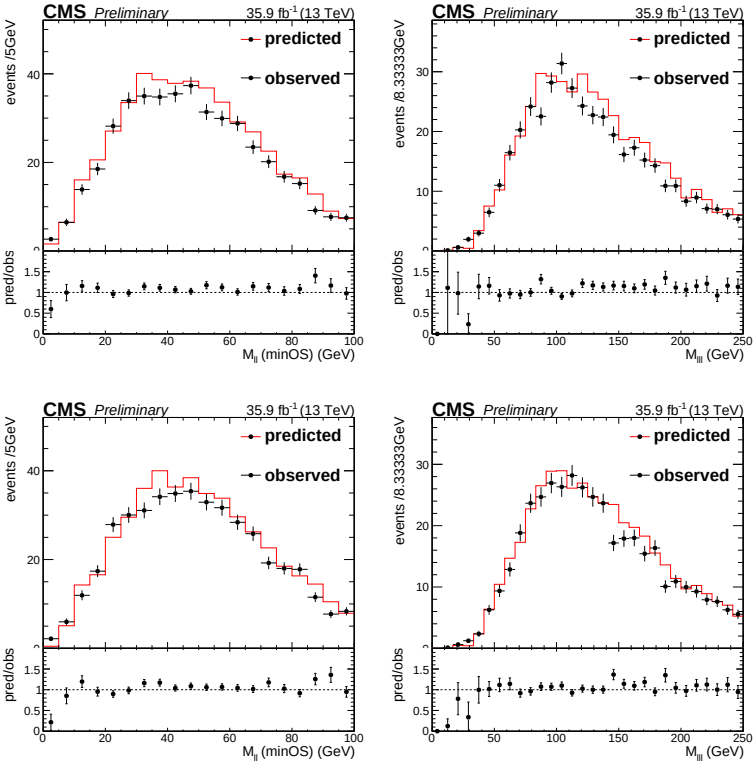

FIGURE 6.9: Closure test on $t\bar{t}$ for electrons (top) and for muons (bottom) with the FAKE-RATE extracted from nonprompt leptons in QCD MC. Red lines are the predicted nonprompt $t\bar{t}$ events, black dots the observed number of nonprompt $t\bar{t}$ events using MC-truth information.

The FAKE-RATE extracted from nonprompt leptons in QCD MC events is used in the application region to estimate the nonprompt $t\bar{t}$ events in the signal region. Then we compare the observed number of nonprompt $t\bar{t}$ events using MC-truth information. The results

of these tests in 3 lepton events are shown in the following Figure 6.9. The two variables which are shown are the $min(M_{OS})$ and $M_{3\ell}$ already described and motivated in Section 6.3. As previously explained, the events are selected and divided in categories according to the values of $min(M_{OS})$ and $M_{3\ell}$; thus it is mandatory having good understanding and control on the predictions for these specific distributions which are used for the final results.
The plots in Figure 6.9 present excellent agreement between predictions and observations with discrepancies smaller than 30%.

6.4.2 Nonprompt background validation

In addition to the validation done with MC closure tests, we also want to test it in data in two specific control regions: Drell-Yan enriched and $t\bar{t}$ enriched CR.

Drell-Yan enriched control region: The major background contribution in the low mass region comes from Drell-Yan events in which a third lepton is a nonprompt lepton. Thus, we define a control region requiring an OSSF pair with a mass within 15 GeV of that of the Z boson, and with $p_T^{miss} < 30$ GeV and $M_{\mathrm{T}} < 30$ GeV. The latter cuts largely remove the contamination from WZ in this control region. The background prediction is then compared with data, and an excellent match is found, as shown in Figure 6.10.

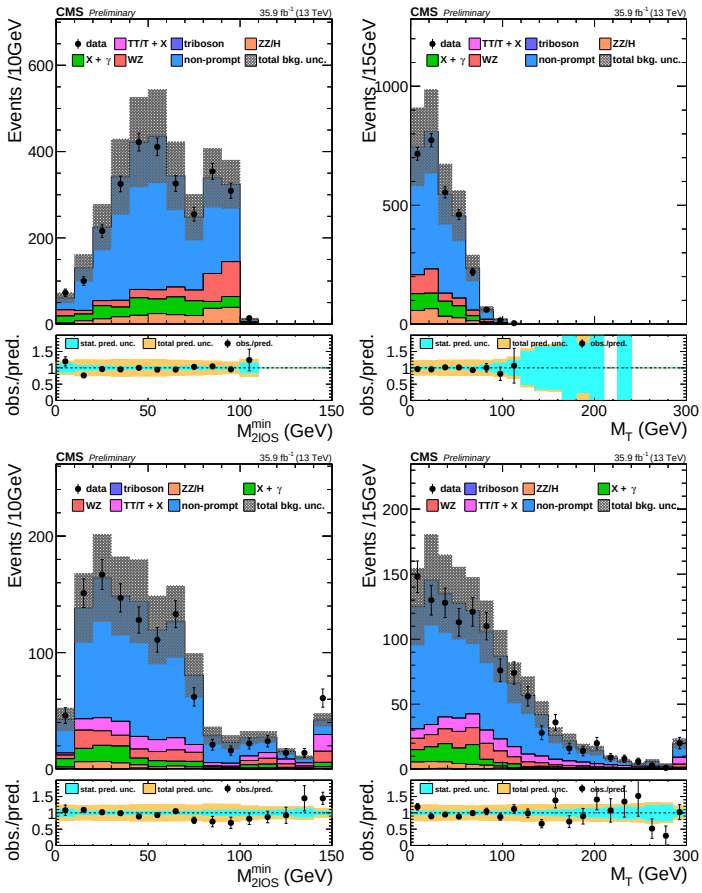

FIGURE 6.10: Comparison of data to background prediction in the Drell-Yan (top) and $t\bar{t}$ (bottom) enriched control region, for $min(M_{OS})$ and M_T^{other}. Courtesy of W. Verbeke.

$t\bar{t}$ enriched control region: The FAKE-RATE for light-flavor and heavy-flavor jets is expected to be different because of their different structure, and possibilities to nonprompt leptons. In particular beauty quarks might decay semi-leptonically, resulting in harder leptons. As discussed earlier, the FO working point used in this analysis is tuned in such a way that the FAKE-RATE is expected to be nearly identical for light- and heavy-flavor jets. If this is the case, the FAKE-RATE should also predict the background due to $t\bar{t}$ in a control region enriched in this process. For this purpose, we select events with at least one loosely b-tagged jet. For events with an OSSF pair, we exclude events within a 15 GeV window around the Z-mass for both $M_{3\ell}$ and the best Z-candidate mass. Additionally, these events are vetoed if they contain an OSSF pair with mass below 12 GeV in order to suppress the contamination from Wγ^* and conversions. Good closure is observed in Figure 6.10, further strengthening our confidence in the data-driven prediction of the nonprompt background.

Considering the results in both the $t\bar{t}$ and Drell-Yan enriched control regions, we assign a flat 30% uncertainty to this background prediction.

6.4.3 Background from prompt leptons

As described in Section 5.2, sizable background contributions come from ZZ production and from associated production of W and Z bosons.

The predictions of those backgrounds with prompt leptons are obtained from simulations. First, three specific control regions enriched respectively with either ZZ or WZ or conversions processes are defined. Thus, the normalization weights are extracted and the MC predictions are validated in specific kinematic distributions.
To measure the normalization factors, a simultaneous fit of the three control regions has been performed on the data yields and simulation yields. The ratios are then applied to scale the predicted yields.
In addition, it was checked the contamination of possible signal events in the control regions and was found negligible considering as $|V_{\ell N}|^2$ the ones close to the sensitivity of the analysis.
The control regions and the results from the validations are discussed in the following paragraphs.

6.4.3.1 ZZ background validation and normalization

Due to the fourth lepton veto, we can define a 4ℓ control region, fully orthogonal to any of the search regions in which we can normalize the ZZ cross-section to data. We define a control region with 4 TIGHT leptons, with two OSSF pairs, both having a mass on-Z; events with a loose b-tagged jet are vetoed. With the above requirements, this control region is extremely pure in ZZ, with other processes being almost negligible. In the given control region, we measure the ZZ normalization by doing a maximum likelihood fit of the ZZ signal hypothesis, including the same treatment of systematic uncertainties as done for the interpretation of the HNL exclusion limits shown later in this text. This procedure yields the following scale factor: $\text{data}_{ZZ}/\text{MC}_{ZZ} = 1.03^{+0.11}_{-0.10}$

Then, we check the prediction of the kinematic shapes in data and MC, a few examples of which can be found in Figure 6.11. Overall data and MC predictions match well; in the top-right plot in Figure 6.11 at low m_T the predictions from MC are within the experimental and theoretical uncertainties, at large m_T values there are still remaining discrepancies.

Thus we add 25% systematic uncertainty for events with $m_T > 75$ GeV, larger than the normalization uncertainty.

6.4.3.2 WZ background normalization and validation

As described earlier, events in which the OSSF pair with the mass closest to that of the Z boson fell within 15 GeV of the Z mass were vetoed in order to suppress the WZ background. Because of this veto, we can employ this region to validate and normalize the WZ background. We select 3 TIGHT leptons and require $p_T^{miss} > 50$ GeV. The sample used here has a large, known, overestimation of the cross-section, making it necessary to perform a cross-section measurement in our control region. This is done in the same way as for the previously mentioned ZZ background, and the following scale factor is obtained: $\text{data}_{WZ}/\text{MC}_{WZ} = 0.652^{+0.061}_{-0.058}$.

Figure 6.11 shows the distribution of the three important analysis variables. An extremely good match is seen in the $min(M_{OS})$ and M_T^{other} distributions, which are used to bin the high mass search regions in which WZ is the dominant background.

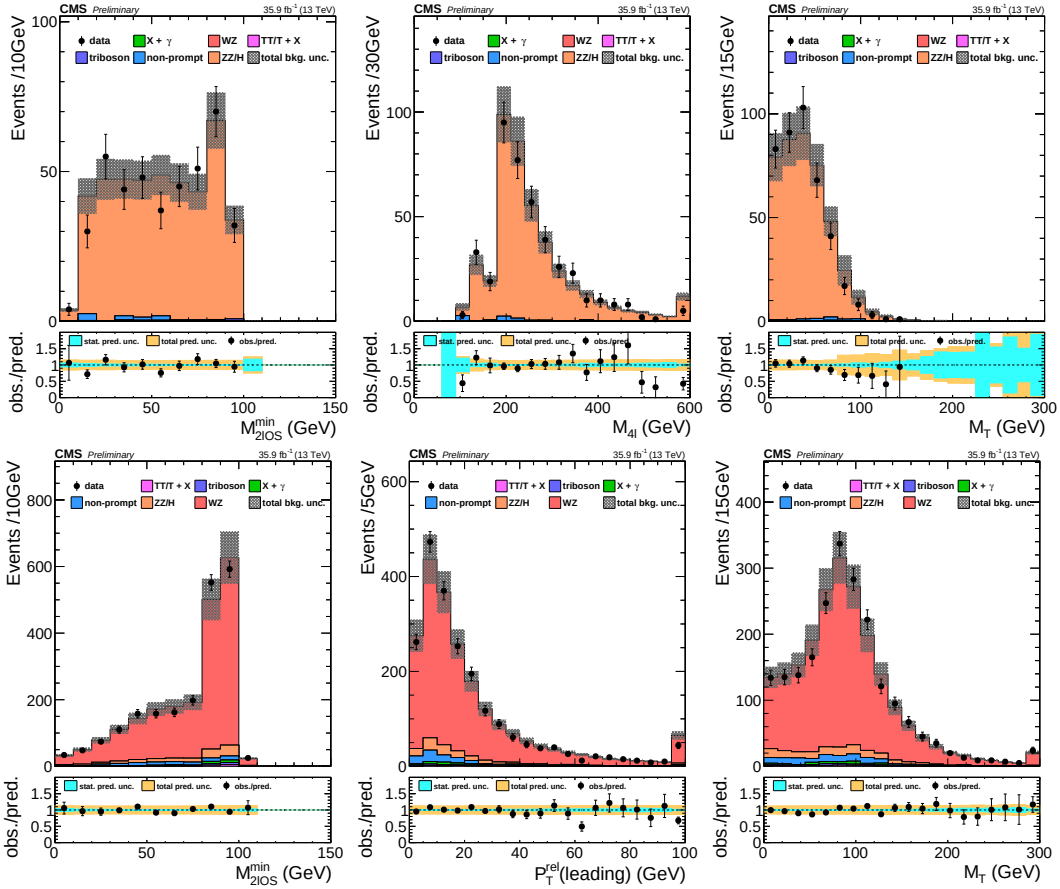

FIGURE 6.11: Comparison of data and MC in the ZZ control region (top) and in the WZ control region (bottom) for several kinematic variables, after normalization of the ZZ/WZ cross section. Courtesy of W. Verbeke.

6.4.4 Background from internal and external γ conversion

Events in which a virtual photon decays (internal conversion) or in which a real photon converts into electron-positron pair by interacting with the detector material (external conversion) constitute one of the main backgrounds in the low mass search bins, and in the low $min(M_{OS})$ and $M_{3\ell}$ regions of the high mass search. The main contribution comes from asymmetric conversions. Wγ^* does not constitute a large contribution since the probability of both conversion decay products passing the analysis p_T requirements is rather small. Nonetheless, it is important at very low masses, and vetoed in the low $M_{3\ell}$ part of the high mass search regions with OSSF pairs by removing events where an OSSF pair has a mass below 5 GeV.

In order to normalize and validate this background, we use a control region defined requiring the presence of an OSSF pair and $M_{3\ell}$ to be compatible with the Z mass within a 15 GeV window. Additionally, the OSSF pair with the mass closest to that of Z is required to have a mass below 75 GeV in order to remove the contribution of Drell-Yan and WZ to this control region. The Zγ cross-section is normalized with respect to the data in this control region. The obtained scale factor is: $\text{data}_{Z\gamma}/\text{MC}_{Z\gamma} = 0.95^{+0.08}_{-0.08}$

The validation of the internal-external conversion background is shown in Figure 6.12. It is observed a good agreement between data and MC, but considering the small discrepancies at large $p_T^{leading}$ we apply an additional 15% systematic uncertainty to the modeling of conversions.

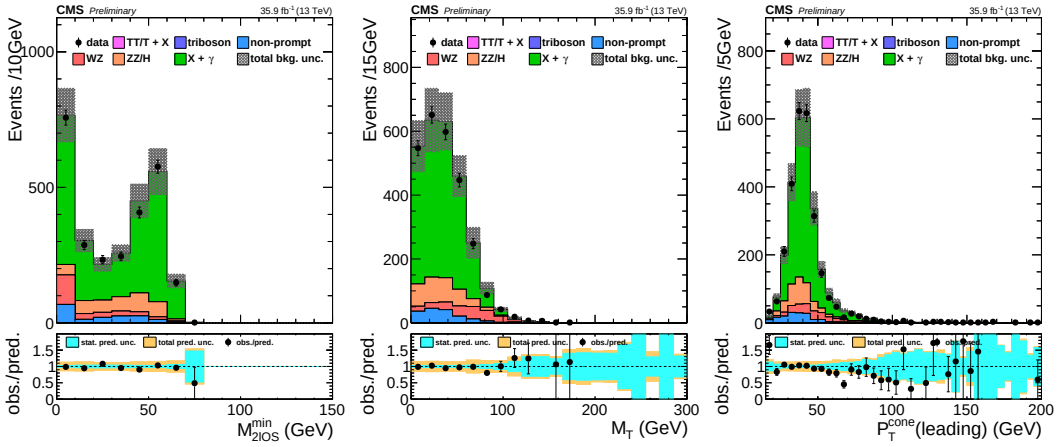

FIGURE 6.12: Comparison of data and MC in the conversion control region for the most important kinematic variables, after normalization of the Zγ and Wγ cross sections. Courtesy of W. Verbeke.

6.5 Systematic uncertainties

The analysis is prone to several sources of systematic uncertainties which are listed below in table 6.9.

The jet energy scale uncertainty varies between 0 and 3%, depending on the search region. This uncertainty affects other event quantities such as the b tag veto, p_T^{miss}, and M_T^{other}, and is computed by shifting the energies of all jets coherently and propagating the variation to all these kinematic variables [152]. Correlation effects due to the migration of events from one search region to another are taken into account. Similarly, the b jet veto efficiency is corrected for the differences between data and simulation, and associated uncertainty in this correction is derived to be 1–5% [153]. The uncertainty in the modeling of pileup is computed by modifying the minimum bias cross-section by 5% [154], and it is measured to be 1–5%, depending on the search region. The uncertainty in the integrated luminosity is 2.5% [155].

All sources of systematics that are labeled as "shape" are computed by varying the yields across the search regions bin-by-bin using the recommended procedures to assess the listed sources of systematic uncertainty.

The dominant uncertainty in the total background prediction is the statistical uncertainty in the nonprompt leptons background estimation, which comes from the limited number of events in the application region. The systematic uncertainty on the nonprompt prediction has a subleading value.

In the high-mass search regions with the OSSF pair present the dominant background is from WZ and external/internal conversion process, hence the uncertainties on this process, as well as MC-modeling uncertainties, become more important.

TABLE 6.9: Summary of systematic uncertainties in the event yields in the search regions and their treatment. Uncertainties are allowed to vary only the normalization of all the bins at once, or both the shape and the normalization (allowing for different correlations across the bins). The upper group lists uncertainties related to experimental effects for all processes whose yield is estimated from simulation; the middle group lists uncertainties in these yields related to the event simulation process itself. The third group lists uncertainties for background processes whose yield or normalization is estimated from data.

Source	typical uncertainty value (%)	Treatment
e/μ selection	3 (per ℓ)	normalization
Trigger efficiency	2–5	normalization
Jet energy scale	0–3	shape
b tag veto	1–5	shape
Pileup	1–5	shape
Integrated luminosity	2.5	normalization
Scale variations	1-15	shape & normalization
PDF variations	0.1-1	shape
Other backgrounds	50	normalization
MC samples statistical precision	1–30	normalization
Nonprompt leptons	30	normalization
Nonprompt leptons (W, Z bkg. subtraction)	5–20	shape
$X\gamma$ normalization	15	normalization
WZ normalization	8.5	normalization
ZZ normalization	25	normalization

6.6 Results

In the left part of Figure 6.13(top) the expected and observed yields in each of the *low mass search* regions are shown, compared to the predicted yields of several HNL masses, with $|V_{\ell N}|^2 = 10^{-5}$. These yields, together with their statistical and systematic uncertainties can also be found in Table 6.10.
The expected and observed yields in the *high mass search regions*, compared to several HNL mass scenarios at $|V_{\ell N}|^2 = 10^{-2}$, for events with and without an OSSF pair are shown in Figure 6.13. All search region yields, with their separate statistical and systematic uncertainties are listed in Tables 6.11 and 6.12.
We see no evidence of an excess in data beyond the SM background.

TABLE 6.10: Observed (expected) event yields in the low-mass search region. The uncertainties contain both the statistical and systematic components.

Flavor	p_T^{leading} (GeV)	$M_{2\ell OS}^{\text{min}}$ (GeV)							
		< 10		10–20		20–30		> 30	
$e^{\pm}e^{\pm}\mu^{\mp}$	< 30	1	(0.61±0.44)	0	(0.45±0.48)	0	$(0.14^{+0.25}_{-0.14})$	3	$(0.27^{+0.50}_{-0.27})$
	30–55	1	(1.05±0.82)	1	(0.28±0.25)	2	(0.53±0.47)	0	(1.7±1.1)
$e^{\pm}\mu^{\mp}\mu^{\mp}$	< 30	5	(3.0±1.4)	3	(2.6±1.3)	3	(1.38±0.77)	0	(1.71±0.83)
	30–55	3	(2.5±1.2)	2	(2.4±1.2)	2	(2.6±1.2)	3	$(1.0^{+1.9}_{-1.0})$

TABLE 6.11: Observed (expected) event yields in the high-mass search region for events with no OSSF lepton pair. The uncertainties contain both the statistical and systematic components.

Flavor	$M_{3\ell}$ (GeV)	M_T (GeV)	$M_{2\ell OS}^{\text{min}}$ (GeV)					
			< 100		100–200		> 200	
$e^{\pm}e^{\pm}\mu^{\mp}$	< 100	< 100			1	(1.45±0.63)		
		> 100			0	(0.43±0.20)		
	> 100	< 100	16	(12.4±2.7)	2	(1.31±0.34)		
		100–150	4	(4.1±10)				
		150–250	2	(1.99±0.55)	1	(1.16±0.29)	1	(0.54±0.16)
		> 250	1	(0.70±0.43)				
$e^{\pm}\mu^{\mp}\mu^{\mp}$	< 100	< 100			2	(0.88±0.32)		
		> 100			1	(0.54±0.29)		
	> 100	< 100	12	(10.9±2.3)	1	(1.93±0.60)		
		100–150	5	(4.1±1.1)				
		150–250	2	(2.72±0.73)	0	(0.64±0.24)	0	(0.160±0.093)
		> 250	0	(0.44±0.19)				

TABLE 6.12: Observed (expected) event yields in the high-mass search region for events with an OSSF lepton pair. The uncertainties contain both the statistical and systematic components.

Flavor	$M_{3\ell}$ (GeV)	M_T (GeV)	$M_{2\ell OS}^{\text{min}}$ (GeV)					
			< 100		100–200		> 200	
$\geq 2e$	< 100	< 100			10	(12.3±1.7)		
		100–200			3	(1.67±0.35)		
		> 200			0	(0.226±0.064)		
	> 100	< 100	127	(131±14)	31	(38.2±4.3)	6	(4.56±0.94)
		100–200	34	(40.9±4.9)	8	(12.7±1.8)	0	(2.37±0.50)
		200–300	3	(5.28±0.78)	1	(1.81±0.29)	0	(0.57±0.13)
		300–400	1	(1.20±0.24)	0	(0.86±0.17)	0	(0.61±0.14)
		> 400	1	(0.87±0.24)				
$\geq 2\mu$	< 100	< 100			30	(24.4±2.9)		
		100–200			3	(3.64±0.56)		
		> 200			1	(0.63±0.22)		
	> 100	< 100	220	(217±22)	63	(65.6±6.6)	8	(6.6±1.4)
		100–200	77	(61.3±6.9)	23	(17.6±2.3)	7	(3.50±0.63)
		200–300	8	(9.1±1.2)	1	(3.08±0.54)	0	(1.64±0.73)
		300–400	1	(2.10±0.44)	1	(1.34±0.24)	0	(0.62±0.59)
		> 400	2	(1.54±0.30)				

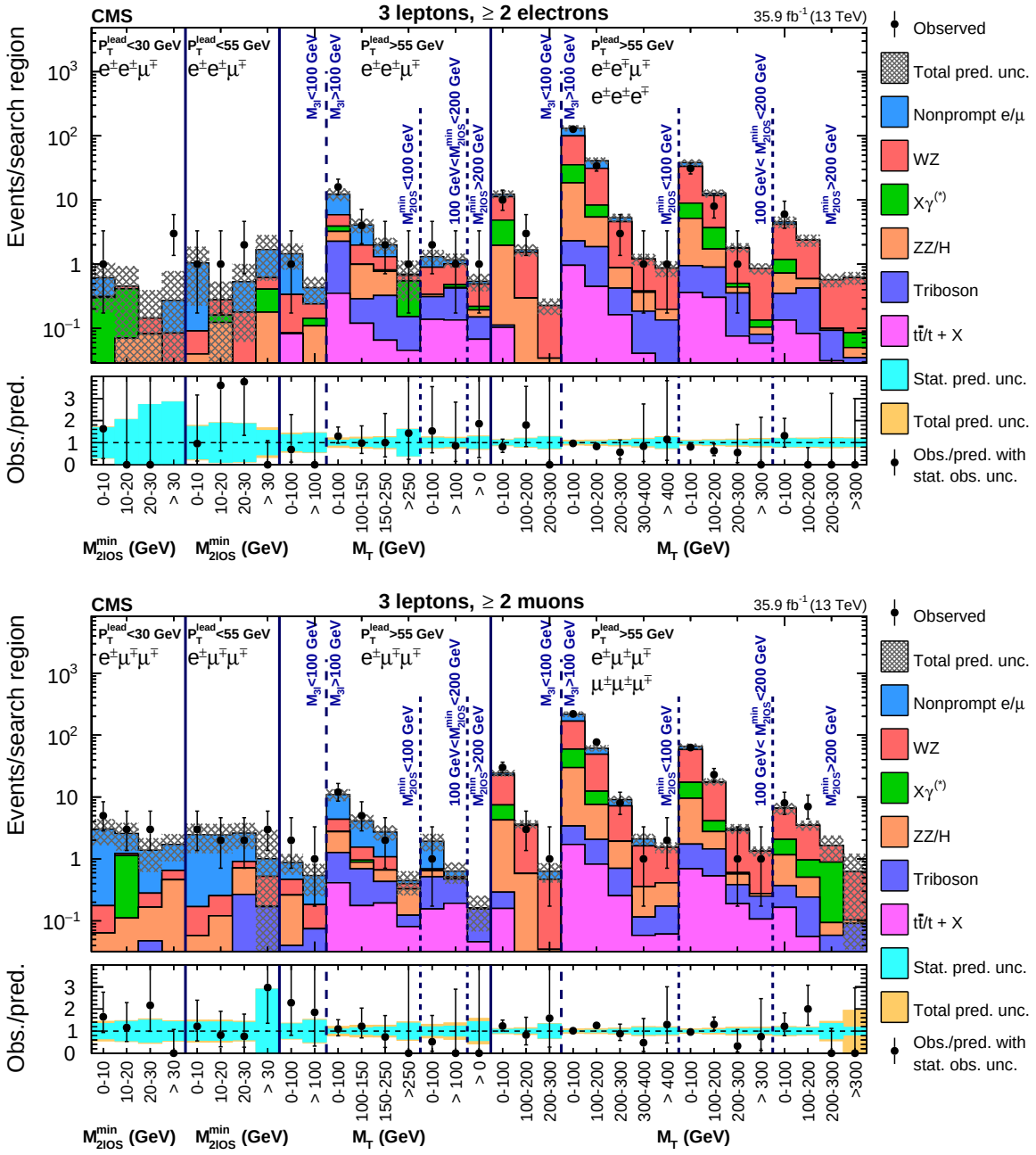

FIGURE 6.13: Observed and expected event yields as a function of $min(M_{OS})$ and M_T^{other} for events with at least two electrons (upper), and with at least two muons (lower). The contribution of each background source is shown. The first 8 bins of each figure correspond to the low-mass region, while the rest display the high-mass region. Courtesy of W. Verbeke.

6.6.1 Interpretation

The expected signal exclusion limits are calculated for several mass points using a simultaneous fit to every search region bin, together with the observed limit. This fit is done in the Asymptotic approximation. The upper limit set on the signal strength for each mass point can then be interpreted as a limit on the effective couplings of the HNL to SM neutrinos, $|V_{eN}|^2$, and $|V_{\mu N}|^2$. Limits were explicitly calculated for HNL masses of 1, 2, 5, 10, 20, 30, 40, 50, 60, 80, 100, 130, 150, 200, 400, 600, 800 and 1000 GeV. Using linear interpolation between the mass points and assuming only coupling to either ν_μ or ν_e, we obtain the exclusion limits shown in Figure 6.14. It can be seen that the expected and observed limits agree well, within less than one standard deviation for almost every point, indicating that no significant excess beyond the SM expectations has been observed.

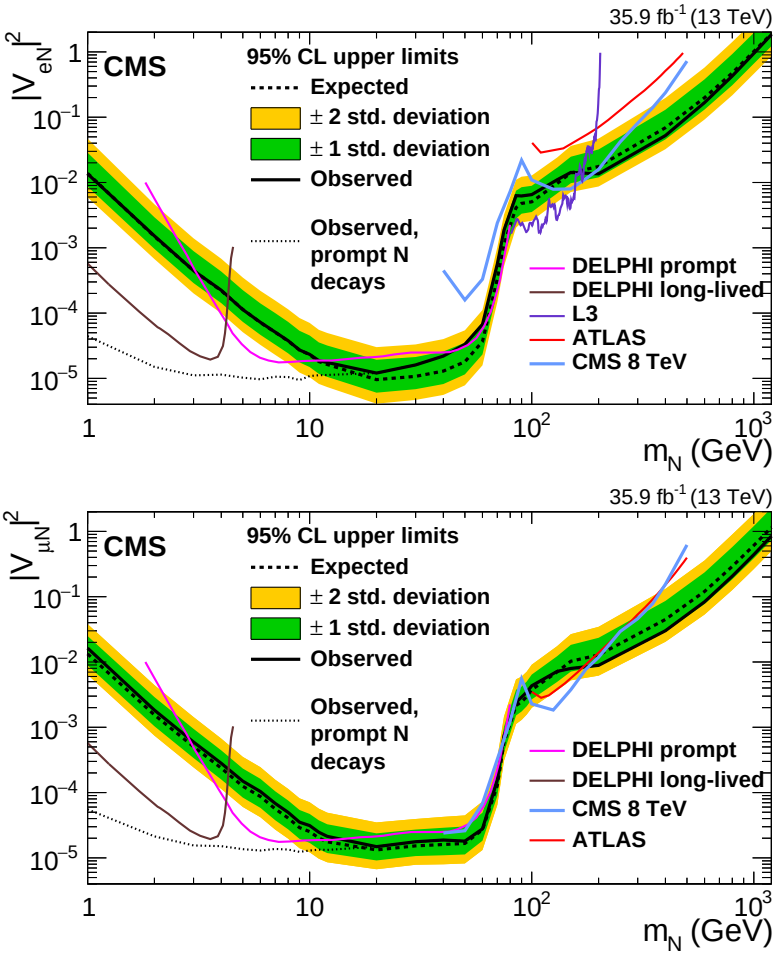

FIGURE 6.14: Exclusion region at 95% CL in the $|V_{eN}|^2$ vs. m_N (top) and $|V_{\mu N}|^2$ vs. m_N (bottom) planes. The dashed black curve is the expected upper limit, with one and two standard-deviation bands shown in dark green and light yellow, respectively. The solid black curve is the observed upper limit, while the dotted black curve is the observed limit in the approximation of prompt N decays. Also shown are the best upper limits at 95% CL from other collider searches in L3 [156], DELPHI [121], ATLAS [157], and CMS [123]. Courtesy of W. Verbeke.

6.7 Summary

In this chapter, the search for heavy neutral leptons in events with three prompt charged leptons is presented. The analysis results were published in Physical Review Letters in early 2018 [151].

The signature consists of three prompt charged leptons in any flavor combination of electrons and muons. No statistically significant excess of signal events over the expected SM background was observed. At 95% confidence level, upper limits were set on the mixing parameters $|V_{eN}|^2$ and $|V_{\mu N}|^2$. The excluded values are in the range between 1.2×10^{-5} and 1.8 for masses between 1 GeV and 1.2 TeV.

The results were positively received by the community and highly appreciated for the big effort that was put into extending the mass range and improving the existing sensitivity at the time of the publication. These were the first direct limits for HNL masses above 500 GeV and the first limits obtained at hadron colliders for HNL masses below 40 GeV. At large HNL masses, the results improved those previously published by the ATLAS [157] and CMS [123, 158] experiments. In particular, with respect to the ATLAS search the mass range was substantially extended towards values below the W boson mass. The previous CMS searches were carried out with the data collected in 2012 at $\sqrt{s} = 8$ TeV, which corresponds to an integrated luminosity of 19.7 fb^{-1}. For the first time at hadron colliders, this search focuses on low HNL mass ranges ($m_N < 40$ GeV) increasing the sensitivity reached by the L3 [156] and DELPHI [121] Collaborations in the prompt case scenario.

The specification for the promptly decaying HNL scenario is necessary when taking into account what is known about the correlation between $|V_{\ell N}|^2$, m_N and N lifetime, which is: $c\,\tau_N \propto m_N^{-5}|V_{\ell N}|^{-2}$ (for references and details see Section 4.2.3). This implies that a HNL with mass and mixing parameter small enough has a lifetime that is not inconsequential with respect to reconstruction limitations and analysis acceptance. The presented search expressly targets prompt HNL decays through the selection of light leptons with limited impact parameters. Keeping in mind that displaced leptons occur as decay products of long-lived HNLs, it is appropriate to quantify the impact of the prompt selection on the displaced lepton selection efficiency. For example considering the scenario $m_N = 3$ GeV and $|V_{\mu N}|^2 = 1.0 \times 10^{-5}$, the N travels a distance of about 3 m. By requiring d_{xy} and d_z to be smaller than 0.05 cm and 0.1 cm respectively, we indirectly reduce the selection acceptance. If HNLs with $m_N = 3$ GeV would be created with coupling $|V_{\mu N}|^2 = 1.0 \times 10^{-5}$, the analysis as it is designed would not select them and hence probe them. This led to the conviction that the final exclusion limits have to be adjusted for the HNL lifetime. This was discussed and fixed with the re-weighting procedure as presented in Chapter 5. The corrected observed upper limits were computed for masses from 1 GeV to 20 GeV, above which the lifetime becomes so small that corrections do not have to be applied.
From there on, it was very natural to start thinking about a dedicated analysis specifically designed to be optimal for moderately displaced scenarios. It was the premise for the considerable leap towards the challenging long-lived HNL search. We wanted to span all the low mass phase spaces while aspiring to be competitive with the DELPHI long-lived results [121] and touching upon the domain of fixed-target experiments. With this drive, the analysis presented in the next chapter began and it became the main topic of my PhD project.

An extra pending point of the presented results is the lacking of upper limits on $|V_{\tau N}|^2$. At the moment of the drafting of this thesis, only the DELPHI Collaboration [121] provided exclusion limits on the mixing parameter between HNL and ν_τ (Figure 4.7) in the studied phase space. Considering the main process to be $W \to \tau N \to \tau\tau\ell\nu_\ell$, the tau channel could be probed either via leptonic or hadronic τ decays. Both cases presented quite considerable challenges. Tau leptons decay $\sim 65\%$ of the cases hadronically [9]; thus the exploitation of the easier leptonic decay channels – $2 \times 17.8\%$ decays – is greatly limited. Regarding the abundant hadronic-tau events, the main test comes from large p_T trigger thresholds for tau objects. To give the reference point, the *singleTau* trigger has a p_T threshold of about 120 GeV and *diTau* triggers start from ~ 40 GeV. The tau-HNL analysis is absolutely demanding and therefore it constitutes an analysis of its own which is currently carried out by my colleague Liam Wezenbeek. More details on the relevance of $|V_{\tau N}|^2$ limits and on its framework and context will be given in the conclusion Chapter 8.

Several people were involved in the completion of the HNL prompt analysis.
In the context of the CMS collaboration, this HNL search was led by the members of the UGent team.
Willem Verbeke was the main analyzer.
I have designed the search strategy for low HNL mass region, and performed the measurement of the lepton fake-rate and its validations in MC. Additionally, I gave the CMS pre-approval presentation of the analysis which is an important scrutiny moment for the results on their way to be submitted to a journal.

Conference talks and posters

On behalf of CMS Collaboration, I have presented these results at various conferences:

- "(YSF talk) Search for heavy neutral leptons (sterile neutrinos) with the CMS detector", plenary at La Thuile 2018, 25 Feb-3 Mar 2018 (Italy);
- "Sterile neutrino searches at LHC and CMS", talk at WP5 meeting, 26 November 2018, Antwerp (Belgium);
- "Search for Heavy Neutral Leptons with CMS detector", poster at EPS-HEP2019, 10-17 Jul 2019 (Belgium);
- "Search for Heavy Neutral Leptons with CMS detector", poster at LP2019, 5-10 Aug 2019, University of Toronto (Canada);
- "HNL experimental overview", plenary at EOS Winter Solstice meeting, 19 Dec 2019, Brussels (Belgium);
- "Search for heavy neutral leptons at CMS", parallel at ICHEP2020, 28 Jul-6 Aug 2020 (Virtual World).

The poster presented at EPS-HEP2019 was awarded "poster prize of the EPS High Energy and Particle Physics Division and the EPS HEP 2019 Conference".
As outreach activity, the results were presented during the talk "Search for exotic particles at the CMS experiment" at the webinar Fisica y Microsistemas which virtually took place at the Galileo Universidad, Guatemala, on the 10th of November 2020.

Chapter 7

Search for long-lived HNL in final states with three leptons and displaced vertices

7.1 Change of scenario

So far an explicit signal of new physics from either direct or indirect searches at the LHC, or direct detection of DM is missing. Furthermore, the theory presents no clear direction on the new physics scale. This forces refining and widening of the experimental effort investigating into BSM scenarios. We should explore various ranges of interaction strengths and masses in addition with respect to what is already probed by the current experimental settings and analyses.

Among the plethora of possible new physics theories, quite eccentric possibilities could be the introduction of long-lived particles (LLPs) decaying in the detector or long-lived detector-stable particles that decay outside the detector volume. These hypotheses call for a change of scenario with respect to the usual new physics signals probed until some years ago, and they prompt the need to search for unconventional experimental signatures.
Long-lived particles are predicted by several models as a result of:

- *small coupling constants* – e.g. HNLs, R-parity violating SUSY, etc;
- *very off-shell intermediate decay products* – e.g. split SUSY where heavy intermediate squarks enhance the gluino lifetime [159, 160];
- *limited decay phase space* — e.g. anomaly-mediated SUSY-breaking models where the lightest neutralino and chargino are nearly degenerate [161, 162].

CMS and ATLAS were originally designed to identify prompt particles, thus integrating displaced signatures into the CMS framework we have to face several challenges:

- *triggers*: timing information at trigger level is not always available and the majority of current triggers use primary vertex constraints to identify particle tracks;
- *particle reconstruction*: we need to develop algorithms to fit possible secondary vertices and integrate such information in the particle reconstruction procedure;
- *background*: additional sources of background have to be considered, such as noise from the detector (instrumental background), cosmic rays traveling through CMS, in-time and out-of-time pileup, and long-lived SM hadrons that could mimic the BSM particle under investigation.

7.1.1 Displaced signature at CMS

In Figure 7.1 several examples of displaced signatures are shown.
If the LLP decays into charged objects (leptons or jets), we have observable secondary vertices that can be fit from the displaced particles' tracks. In case the LLP decays into photons, then we can rely on the capability of the CMS ECAL to measure γ arrival times with enough precision to discriminate delayed signals produced at displaced vertices [161]. A charged LLP decaying within the volume of the silicon tracker could produce an isolated track that "disappears", i.e. without hits in the outermost layers of the silicon tracker, with little energy deposited in the calorimeters, and with no hits in the muon detectors [163].

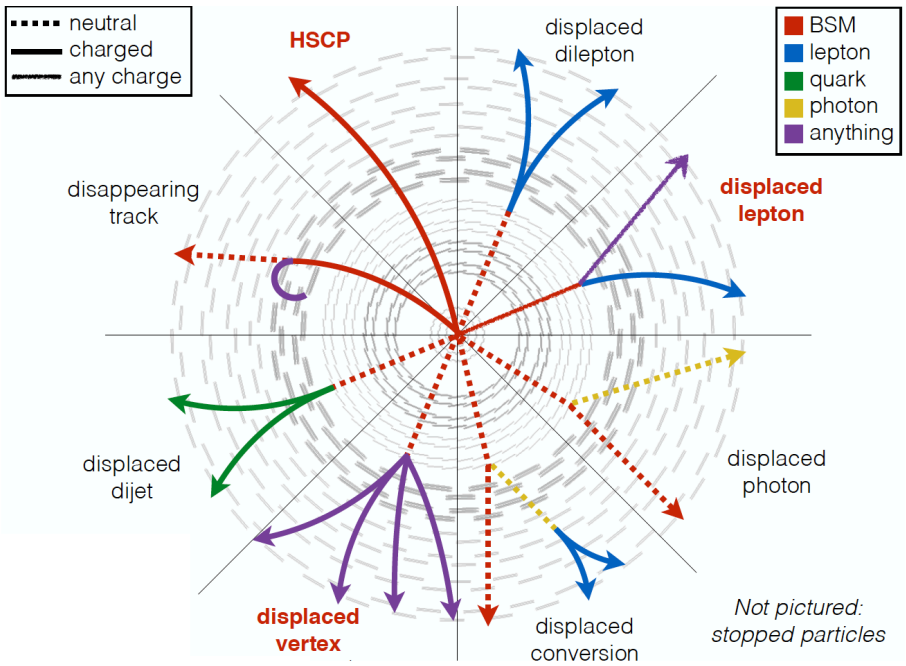

FIGURE 7.1: Didactic sketch, by J. Antonelli, showing the numerous experimental signatures in the CMS tracker from various hypothetical particles proposed in long-lived models.

These are just a few examples of the almost endless configurations that can be studied, including some of the long-lived particle signatures investigated by current searches.

7.1.1.1 HNL with long lifetime

Along these lines, extending the HNL search described in Chapter 6 including the long-lived HNL decays it feels like a logical continuation.

Recalling the considerations illustrated in Section 4.2.3, the lifetime of a HNL is strongly dependent on M_N and $|V_{\ell N}|^2$, and it increases rapidly at small masses and low values of the mixing parameter (see Figure 4.4): $\tau_N \propto M_N^{-5}|V_{N\ell}|^{-2}$. As a result, the kinematics and the acceptance of HNLs with masses below about 20 GeV are significantly affected by their long lifetimes, and must be accounted for in the signal simulation and in the results' interpretation. If N has a long lifetime, then a secondary vertex formed by the decay products of the HNL ($\ell^{\pm\prime}$, $\ell^{\mp\prime\prime}$, $\nu_{\ell''}$ or $\nu_{\ell'}$, $\ell^{\pm\prime\prime}$, $\ell^{\mp\prime\prime}$) can be experimentally identified.

We present here the search of long-lived heavy neutral leptons in final states with three charged leptons and displaced vertices.
The analysis strategy we follow here shares some similarities with the prompt HNL search (Ref. [151], Chapter 6) and uses the lessons learned from that analysis. The main objective of the current search is to extend the sensitivity to low HNL masses and mixing parameters, namely HNL masses below 20 GeV. This is obtained by optimizing the identification of leptons produced in the decay of long-lived HNLs and by fitting their displaced decay vertices. More precisely, the search is performed by designing search regions on the basis of the displacement of the HNL vertex and the invariant mass of the displaced leptons. The maximum sensitivity is reached by simultaneously fitting these search regions in each lepton flavor channel. The mixing of HNLs to electron neutrinos, $|V_{eN}|^2$, is probed using the leptonic final states eee, $e^{\pm}e^{\mp}\mu$, and $e^{\pm}e^{\pm}\mu$ (collectively called eeX), while the $\mu\mu\mu$, $\mu^{\pm}\mu^{\mp}e$, and $\mu^{\pm}\mu^{\pm}e$ final states (collectively called $\mu\mu$X) are used to probe the coupling to muon neutrinos, $|V_{\mu N}|^2$. With these lepton flavor/charge categories, the search is sensitive to both LNV and LNC scenarios. The search uses the full Run2 data set with an integrated luminosity of 137 fb^{-1}, and the major backgrounds are estimated using a data-driven technique.

7.2 Analysis setup

7.2.1 Data and simulation samples

The current analysis uses three sets of pp collision data at a center-of-mass energy of 13 TeV, corresponding to integrated luminosities of 35.92 fb^{-1} (2016), 41.53 fb^{-1} (2017), and 59.97 fb^{-1} (2018).
A number of signal samples were used for the optimization of the selection and the interpretation of the results, using the modeling described in Section 5.3. Signal samples include HNL final states with three charged leptons and a neutrino, coming from both the $N \to W(\ell\nu)\ell$ and $N \to Z(\ell\ell)\nu$ decay modes of N (refer to Section 5.3).

7.2.2 Trigger strategy

Every HNL signal event contains one prompt lepton and two (generally) displaced leptons. Since most of the CMS leptonic triggers are optimized for prompt lepton identification, we opted for the use of single-electron and single-muon triggers for the signal selection, as listed in Table 7.1.

Table 7.1: List of triggers used for the signal selection in the three data-taking periods.

Primary data set	Trigger name		
	2016	2017	2018
SingleElectron	`Electron > 27`	`Electron > 32`	—
EGamma	—	—	`Electron > 32`
SingleMuon	`Muon > 24`	`Muon > 24` `Muon > 27`	`Muon > 24`

The trigger efficiency in Monte Carlo samples is corrected according to the efficiency observed in data, by using the per-event scale factors (SFs) as a function of the prompt lepton p_T and η. In order to make this correction possible, the prompt lepton identified in each event is matched geometrically to the relevant "trigger lepton" (i.e., the lepton reconstructed by the CMS high-level trigger software) that fired the event. Prompt electrons (muons) must be matched to the trigger electron (muon) that fired one of the single-electron (-muon) triggers in Table 7.1. The matching is ensured by requiring that the angular distance ΔR between the reconstructed trigger lepton and offline lepton be less than 0.3.

7.2.3 Object selection

For a detailed description of particle reconstruction in CMS, see Section 3.1.
In Sections 3.1.3.2 and 3.1.4.2 the prompt lepton identification criteria are presented.
For displaced leptons and SV, detailed explanations can be found in Sections 3.1.3.3 (displaced muons), 3.1.4.3 (displaced electrons), and 3.2 (displaced SV reconstruction).

In the following sections, only the additional selections targeting this specific scenario are described and motivated.

7.2.3.1 Electrons

The electron selection criteria are summarized in Table 7.2. Different criteria are applied to identify prompt and displaced electrons.

Prompt electrons. Prompt electrons are identified using a multi-variate discriminator with identification efficiency above 90% (90% working point MVA ID). Prompt electrons must have p_T greater than 30 (32, 32) GeV in 2016 (2017, 2018) data set. The offline p_T threshold is driven by the trigger p_T threshold in each data set, such that the offline criteria always falls in the plateau of the trigger efficiency curve. Prompt electrons passing this selection will be referred to as TIGHT PROMPT electrons[1] hereafter.

Displaced electrons. Displaced electrons passing their selection will be referred to as TIGHT DISPLACED electrons. They must have p_T greater than 7 GeV. Samples enriched in fake electrons are selected with identification criteria looser than those used for TIGHT DISPLACED electrons. These loosely selected electrons referred to as "fakeable objects" or FO electrons, are employed to determine the rate of fake electrons misidentified as signal electrons (FAKE-RATE or FR).

7.2.3.2 Muons

Muons are required to have $|\eta| < 2.4$ to fall inside the geometric acceptance of the muon detector. All muons considered for analysis must pass the *Loose ID* (as defined in Section 3.1.3.2), in addition to a number of loose criteria on isolation and track impact parameters with respect to the PV.
Muon selection criteria are summarized in Table 7.3. Different selections are applied to prompt and displaced muons.

[1] These working points do not necessarily coincide with the ones defined in Sections 3.1.3.2 and 3.1.4.2. For the latter, the italic style is used.

TABLE 7.2: Requirements for an electron to pass each of the defined selection working points. Variables defined in Section 3.3.

Selection name	TIGHT PROMPT	TIGHT DISPLACED	FO
$\|\eta\|$	< 2.5	< 2.5	< 2.5
p_T	$>$ 30–32 GeV	$>$ 7 GeV	$>$ 7 GeV
$\|d_{xy}\|$	< 0.05 cm	> 0.01 cm	> 0.01 cm
$\|d_z\|$	< 0.1 cm	—	—
I_{rel}	< 0.1	< 0.2	< 2.0
$\sigma_{i\eta i\eta}$	—	$<$ (0.011, 0.011, 0.030)	$<$ (0.011, 0.011, 0.030)
H/E	—	$<$ (0.10, 0.10, 0.07)	$<$ (0.10, 0.10, 0.07)
$\Delta\eta_{\text{in}}$	—	$<$ (0.01, 0.01, 0.008)	$<$ (0.01, 0.01, 0.008)
$\Delta\phi_{\text{in}}$	—	$<$ (0.04, 0.04, 0.07)	$<$ (0.04, 0.04, 0.07)
$1/E - 1/p$	—	$<$ (0.010, 0.010, 0.005)	$<$ (0.010, 0.010, 0.005)
MVA estimator	$> f(\eta, p_T)$	—	—

Prompt muons. Prompt muons must pass *Medium ID* (refer to Section 3.1.3.2) criteria. They must have p_T greater than 25 (28, 25) GeV in the 2016 (2017, 2018) data set. Prompt muons passing this selection will be referred to as TIGHT PROMPT[2] muons hereafter.

Displaced muons. Displaced muons that pass the displaced ID criteria (3.1.3.3) will be referred to as TIGHT DISPLACED muons. The displaced muons are required to have p_T greater than 5 GeV.

In addition, loosely defined muons, referred to as FO muons, are selected with identification criteria looser than those used for TIGHT DISPLACED muons and are employed to determine the muon FR.

TABLE 7.3: Requirements for a muon to pass each of the defined selection working points. Variables defined in Section 3.3.

Selection name		TIGHT PROMPT	TIGHT DISPLACED	FO
$\|\eta\|$		< 2.4	< 2.4	< 2.4
p_T		$>$ 25–28 GeV	$>$ 5 GeV	$>$ 5 GeV
$\|d_{xy}\|$		< 0.05 cm	> 0.01 cm	> 0.01 cm
$\|d_z\|$		< 0.1 cm	< 10 cm	< 10 cm
I_{rel}		< 0.1	< 0.2	< 2.0
Loose ID		True	True	True
Fraction of valid tracker hits		> 0.8	—	—
Global muon	Global muon fit	True	True	True
	Global track χ^2/dof	< 3	—	—
	Track–muon matching χ^2/dof	< 12	< 12	< 12
	"Kink finder" estimator	< 20	< 20	< 20
	Segment-compatibility estimator	> 0.303	> 0.303	> 0.303
Tracker muon	Segment-compatibility estimator	> 0.451	> 0.451	> 0.451

[2] These working points do not necessarily coincide with the ones defined in Sections 3.1.3.2 and 3.1.4.2. For the latter the italic style is used.

7.3 Analysis strategy

Signal events are characterized by the presence of a prompt lepton (in the following often referred to as ℓ_1, or "ℓ from W" in some of the figures presented in this thesis), two displaced leptons (ℓ_2 and ℓ_3, or "ℓ from N" and "ℓ from N $\to W^{*}$" in some figures), and a neutrino, see Figure 7.2. In the following sections, events are split into categories in which ℓ_1 and at least one of ℓ_2 or ℓ_3 are electrons (eeX) or muons ($\mu\mu$X).

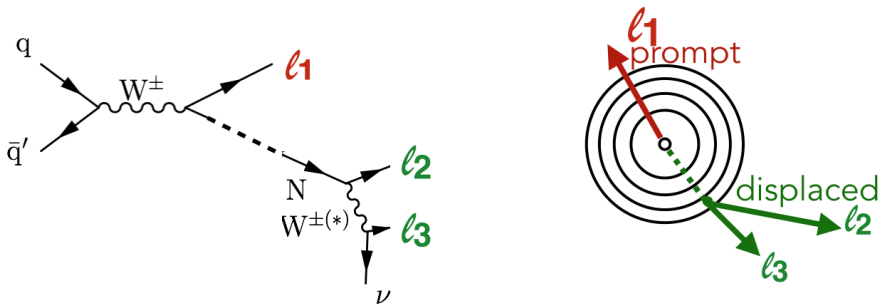

FIGURE 7.2: Diagram for the production of a long-lived HNL (left) with colors underlining the nomenclature adopted in the following sections. Prompt lepton referred to as ℓ_1 and two displaced leptons (ℓ_2 and ℓ_3). Didactic sketch on the right showing the usual signature with ℓ_1 back-to-back with respect to ℓ_2 and ℓ_3 which form a SV.

Figure 7.3 illustrates some kinematic properties of the leptons in signal events, both at the generator and reconstruction levels.
Given the low HNL masses considered in this analysis ($M_{\mathrm{N}} < 20$ GeV), ℓ_1 has the typical p_T spectrum expected for W decays, with a Jacobian peak around 40 GeV, while ℓ_2 and ℓ_3 have very soft p_T spectra (Figure 7.3 (top-left)), invariant mass smaller than M_{N} (Figure 7.3 (top-right)), and a small opening angle (Figure 7.3 (bottom-left)). In the absence of significant hadronic activity, ℓ_1 and N are typically separated by a large azimuthal angle (Figure 7.3 (bottom-right)). These features, along with the possible displacement of ℓ_2 and ℓ_3 can be used to identify the two leptons coming from the HNL decay.

7.3.1 HNL candidate selection

As shown in Tables 7.2 and 7.3, the displacement of ℓ_2 and ℓ_3 is requested by imposing a minimum $|d_{\mathrm{xy}}|$ cut of 0.1 mm to the reconstructed leptons. Given the rapid variation of the N displacement with M_{N} and $|\mathrm{V}_{\ell\mathrm{N}}|^2$, this preliminary displacement requirement must be rather mild, and does not resolve completely possible ambiguities between prompt and displaced reconstructed leptons.

Other than the two leptons from the HNL decay, additional leptons—real or misidentified—may satisfy the $|d_{\mathrm{xy}}|$ requirements and pass the displaced-lepton selection. In this case, criteria must be put in place to resolve the ambiguities and correctly identify the two leptons from the HNL decay. To this purpose, variables such as the invariant mass of ℓ_2 and ℓ_3, $M(\ell_2, \ell_3)$, and the ΔR separation between ℓ_2 and ℓ_3, $\Delta R(\ell_2, \ell_3)$, are found to be effective, and with similar performances. Therefore, the three leptons from HNL decay are identified as follows. Among all the leptons that pass the prompt selection of Tables 7.2 and 7.3, the one with highest p_T is chosen as ℓ_1 and it is not considered anymore for the selection of ℓ_2

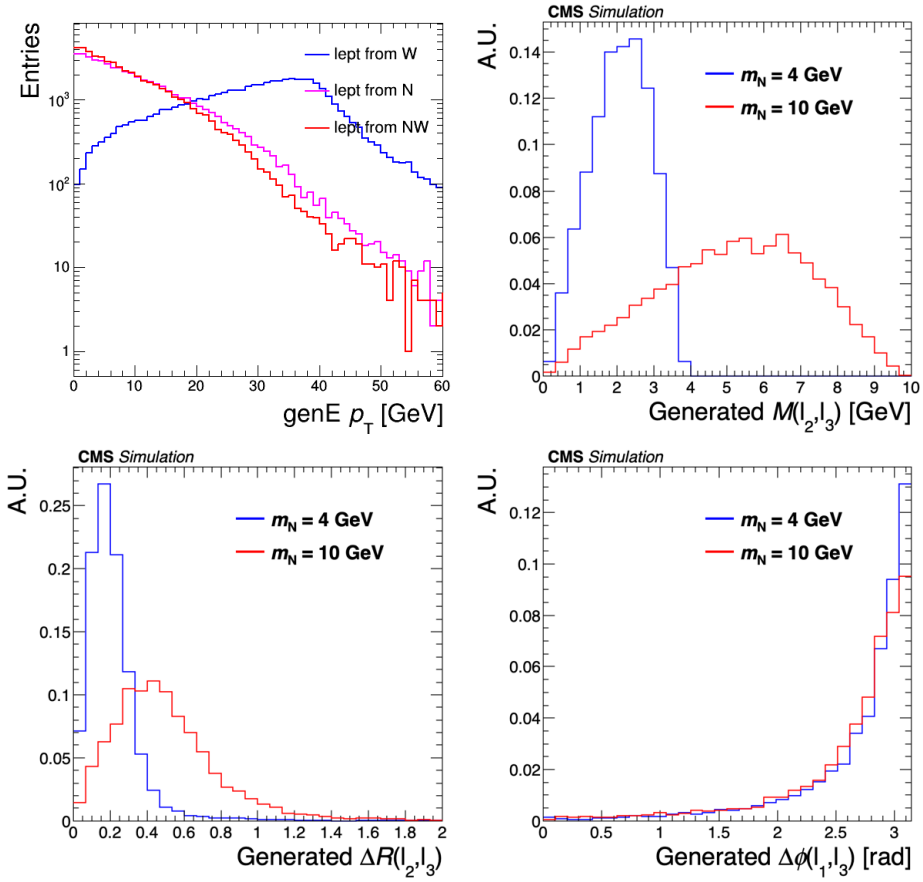

FIGURE 7.3: For the HNL scenario: HNL of mass $M_N = 4$ GeV and $|V_{\ell N}|^2 = 10^{-4}$. Top left, generated lepton p_T, separately for ℓ_1 ("from W"), ℓ_2 ("from N"), and ℓ_3 ("from NW"). Top right, the invariant mass of ℓ_2 and ℓ_3 at generator level. Bottom left, ΔR between ℓ_2 and ℓ_3. Bottom right, $\Delta\phi$ between ℓ_1 and ℓ_3. Courtesy of D. Trocino.

and ℓ_3. Among all the selected displaced leptons, the two leptons of any flavor with the largest di-lepton p_T (vectorial sum of $p_{T_{\ell_2}}$ and $p_{T_{\ell_3}}$) and opposite charge are selected as ℓ_2 and ℓ_3, ($e^{\pm}e^{\mp}$, $e^{\pm}\mu^{\mp}$, $\mu^{\pm}\mu^{\mp}$). If there is no opposite-charge displaced lepton pair, the event is rejected. This reduces background processes with misidentified leptons while retaining almost full efficiency for the signal. In the following, we will label the lepton in the pair with higher (lower) p_T as ℓ_2 (ℓ_3).
This selection strategy correctly identifies the one prompt and two displaced leptons in more than 99% of signal events (99.9% of signal events that pass the full analysis selection, described in Section 7.3.2).

7.3.1.1 Secondary vertex fit

Once ℓ_2 and ℓ_3 have been identified, we can reconstruct their common vertex of origin, i.e. the decay vertex of the HNL.
For the SV reconstruction, the procedure described in Section 3.2 is used. The fitted SV estimates the production vertex of ℓ_2 and ℓ_3.

7.3.2 Event kinematics and baseline selection

Starting from all events with one prompt lepton and two displaced leptons forming an SV, the kinematic properties and particle content of typical HNL signal events are used to suppress the background contributions (more details in the following Section 7.4).

The baseline selection includes the following requirements, summarized in Table 7.4. Please consider Figure 7.2 as a reference for the lepton nomenclature. The distributions of all the variables used for the selection are shown in Figure 7.5.

TABLE 7.4: Baseline selection requirements applied to all data sets.

Variable	Requirement
$\Delta R(\ell_2, \ell_3)$	< 1
$\min \Delta\phi(\ell_1, \ell_{2/3})$	> 1 rad
$M_{3\ell}$	$\in [50, 80]$ GeV
N. b jets	$= 0$
p_T $(\ell_2 + \ell_3)$	> 15 GeV
$\cos\theta_{\mathrm{SV,\,N}}$	> 0.99
p_{SV}	> 0.001
$S(\Delta_{2D})$	> 20
resonance vetoes	✓

As explained above, ℓ_2 and ℓ_3 are expected to have small opening angle, given the small mass and relatively large momentum of the HNL. As can be seen in Figure 7.5 (top-left), the variable $\Delta R(\ell_2, \ell_3)$ discriminates the signal from all background processes. To retain high signal efficiency and reduce backgrounds where two leptons are relatively separated from each other, we select events with $\boldsymbol{\Delta R(\ell_2, \ell_3) < 1}$.

In the absence of energetic jets in signal events, ℓ_1 is expected to recoil at a large angle in the transverse plane from the HNL, and thus from ℓ_2 and ℓ_3. Since both $\Delta\phi(\ell_1, \ell_2)$ and $\Delta\phi(\ell_1, \ell_3)$ are large and close in value (which may not be true for other processes with two uncorrelated nonprompt leptons), we apply a cut on the smaller of the two angles, $\boldsymbol{\min \Delta\phi(\ell_1, \ell_{2/3}) > 1\,\mathrm{rad}}$.

The invariant mass of the three charged leptons $M_{3\ell}$, $M(\ell_1, \ell_2, \ell_3)$, is limited by the mass of the on-shell W boson. Given the relatively low momentum carried away by the neutrino, $M_{3\ell}$ tends to peak just below the W mass, with a steep fall above 80 GeV and a larger tail at lower masses. We select events with $\boldsymbol{M_{3\ell}}$ values **between 50 and 80 GeV**. This requirement proves particularly effective against the $\mathrm{Z}\gamma^{(*)}$ background, where the photon radiated by one of the leptons from the Z decay undergoes an asymmetric conversion: one of the leptons receives most of the γ momentum, while the other is too soft to be detected or identified. Such events manifest themselves as a peak at about 91 GeV in the $M(\ell_1, \ell_2, \ell_3)$ spectrum.

Events with a b jet (see Section 6.2.3) with p_T greater than 25 GeV are rejected, in order to substantially reduce the background from the top processes.

The vector sum of the momenta of ℓ_2, ℓ_3, and the neutrino corresponds to the momentum of the HNL and points back exactly to the PV. Unfortunately, the total momentum

of the neutrino is unknown, and its transverse momentum, estimated by p_T^{miss}, has limited resolution. The decay products of the HNL, however, are emitted at small opening angles with respect to the HNL direction. We can thus expect the vector sum of the ℓ_2 and ℓ_3 momenta to follow closely, though not exactly, the direction of the HNL. Figure 7.5 shows a distribution of the cosine of the angle between the SV position, which estimates the direction of flight of the HNL before decaying, and the vector sum of the ℓ_2 and ℓ_3 momenta ("back-pointing angle"): $\cos\theta_{\mathrm{SV,N}} = \vec{r}_{\mathrm{SV}} \cdot \vec{p}_{\ell_{2/3}} / \left(|\vec{r}_{\mathrm{SV}}||\vec{p}_{\ell_{2/3}}|\right)$. As expected, the signal events peak at values very close to 1, $\mathbf{\cos\theta_{SV,N} > 0.99}$. Processes with two uncorrelated nonprompt leptons should exhibit a flat $\cos\theta_{\mathrm{SV,N}}$ distribution. The requirement on $\Delta R(\ell_2, \ell_3)$, however, selects events with two relatively close-by leptons, therefore the vector sum of the p_T of the two displaced leptons makes a small angle with the vector drawn from the PV to SV. In principle this is a genuine property of the boosted displaced HNL, however, the angular cuts on the two leptons bias the background to have a small angle as well. For this reason, all background processes exhibit a peaking structure, randomly at -1 or $+1$.

The quality of the secondary vertex ($\boldsymbol{p_{SV}}$) necessarily correlates with the precision of the trajectories from ℓ_2 and ℓ_3, as well as to how close they are at the intersection point. It is represented as a probability based on the maximum likelihood fit from the kinematic vertex fitter. One can observe that for low probability values, the background dominates. This motivates a requirement for the **probability to be larger than 0.001**.

The quality of the SV fit is also used as a discriminating variable against random vertices. The significance of the distance between PV and SV, $\boldsymbol{S(\Delta_{2D})}$ is shown in Figure 7.5. A requirement on the **significance to be larger than 20** is applied.

The dilepton (ℓ_2, ℓ_3) transverse momentum is required to be larger than 15 GeV, since the low-p_T region is heavily dominated by the nonprompt lepton background. The dilepton mass $M(\ell_2, \ell_3)$ distribution has an upper threshold that corresponds to the largest mass among all the considered signal samples. Due to the presence of the neutrino in the final state, the mass is always lower than the HNL mass.

In addition to the selections mentioned above, numerous dilepton resonances (see Figure 7.4) within the search region are removed. In case of ℓ_2 and ℓ_3 having the same flavor and opposite charges and with the transverse position of the dilepton vertex $\Delta_{\mathrm{2D}} < 1.5$ cm, the following resonance masses ($M(\ell_2, \ell_3)$) are removed: J/Ψ (3.10 ± 0.08 GeV), Ψ (3.69 ± 0.08 GeV), ω (0.78 ± 0.08 GeV), and ϕ (1.02 ± 0.08 GeV). In case ℓ_1 and ℓ_2/ℓ_3 have the same flavor and opposite charges, events are removed if $M(\ell_1, \ell_2)$ or $M(\ell_1, \ell_3)$ are in the ranges listed above, or consistent with other higher-mass resonances, including Υ ($1S$) (9.46 ± 0.08 GeV), Υ ($2S$) (10.02 ± 0.08 GeV), Υ ($3S$) (10.36 ± 0.08 GeV), and Z (91.19 ± 10.00 GeV).

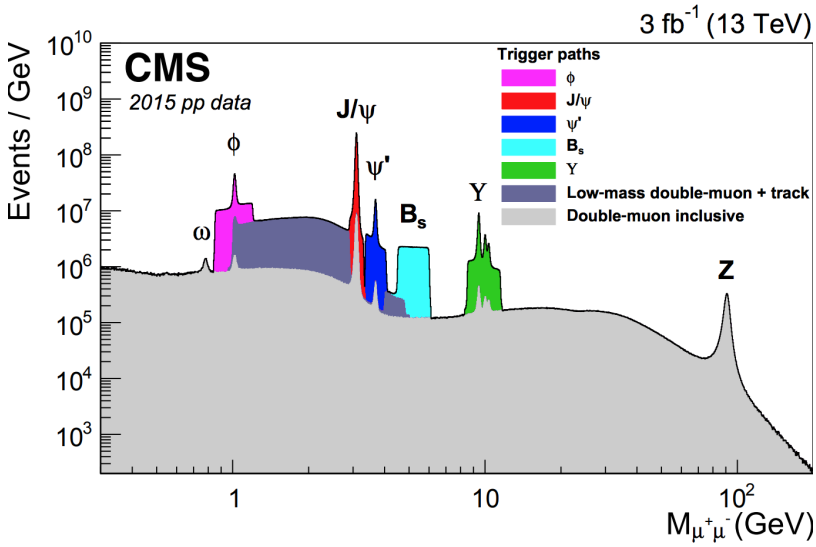

FIGURE 7.4: The dimuon invariant mass distribution showing dilepton resonances [81].

The convention for the legends in all following plots in Chapter 7 backgrounds will be grouped into macro-categories of histograms as follows. When there are only MC predictions:

- MC nonprompt DF: processes that give rise to two nonprompt leptons, such as W + jets, $t\bar{t}$ + jets, single-top. To be defined as DF it has to be defined "double-fake" according to the definition in Section 7.4;
- MC nonprompt SF: processes that give rise to one or two nonprompt leptons, such as W + jets, $t\bar{t}$ + jets, single-top and DY+ jets. To be defined as SF it has to be defined "single-fake" according to the definition in Section 7.4;
- Conversions: processes with photon conversions, such as Zγ and Wγ;
- $Z\gamma^*$: it includes DY events with additional prompt lepton(s) from a virtual photon conversion;
- Other: processes like diboson and triboson.

When there are both MC and data-driven predictions:

- Nonprompt DF/SF: data-driven predictions that are explained in Section 7.4;
- Conversions: processes with photon conversion, like Zγ and Wγ, and DY;
- Other: processes like diboson and triboson.

Figures 7.6 and 7.7 are a summary view of the entire selection, step by step, in the form of "cutflow" histograms. The first set, Figure 7.6, shows the event yields for all processes at each step of the selection: each bin displays the number of remaining events after each analysis cut, sequentially. The second set, Figure 7.7, shows the event yields for "$N-1$" analysis cuts: each bin corresponds to the number of events after the full selection is applied, with the exception of the particular cut in question; this way it is possible to appreciate the real impact of each selection, regardless of the order of the cuts in the selection sequence. As can be seen in Figure 7.7, the most effective background rejection is achieved with the $M(\ell_1, \ell_2, \ell_3)$ selection. In particular, it is effective in eeX final states as it rejects DY events where at least one electron comes from conversions. In such events, $M(\ell_1, \ell_2, \ell_3)$ typically lies in the proximity of M_Z, which is outside the [50-80] GeV signal region.

Figure 7.8 shows the transverse distance of the SV from the PV, Δ_{2D}, for events passing the full baseline selection. Δ_{2D} is the most important experimental observable to discriminate signal from background.

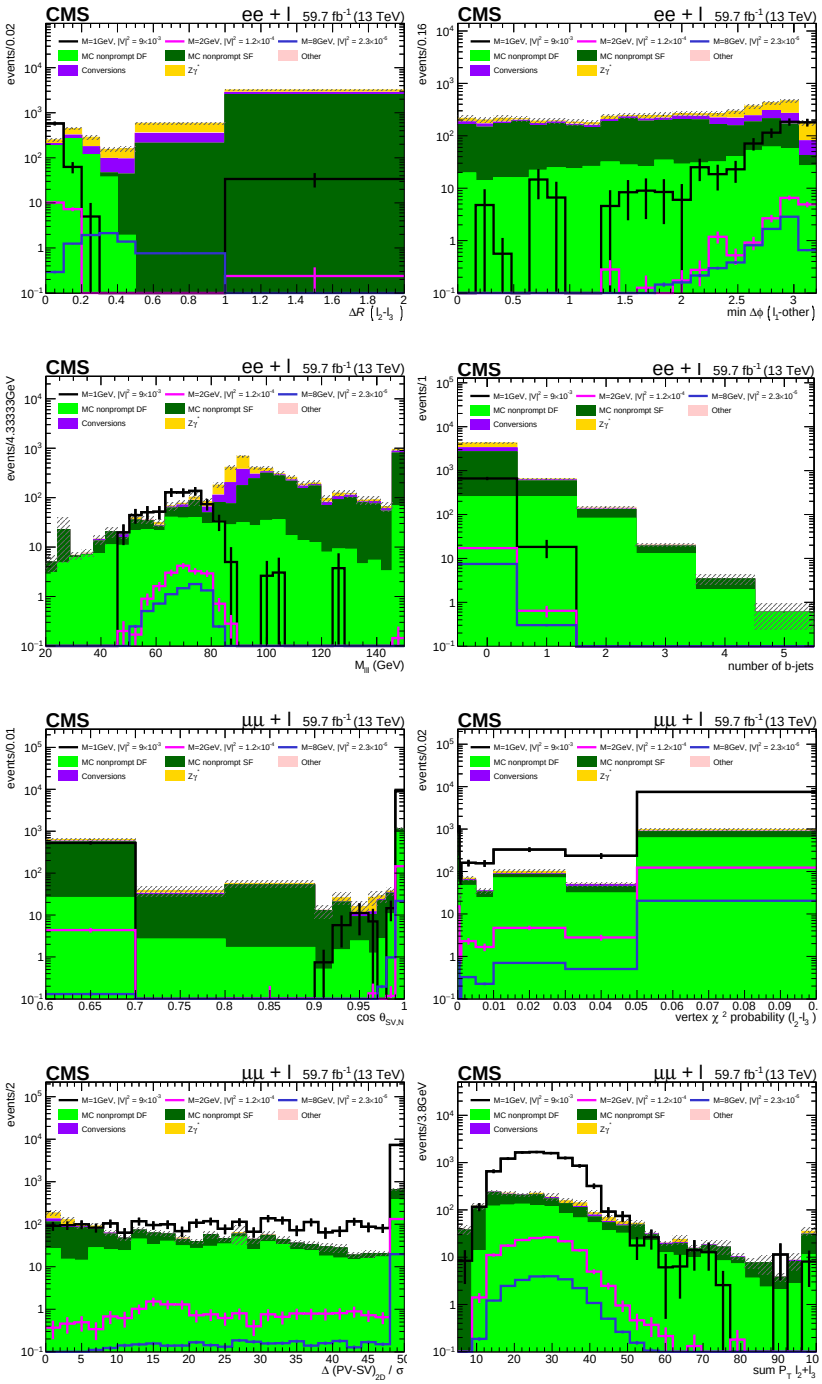

FIGURE 7.5: Distributions of the event selection's variables listed in Table 7.4. Simulated backgrounds (shaded histograms, stacked), using the 2018 MC samples, after the selection of the three leptons ℓ_1, ℓ_2, and ℓ_3, in eeX final states for the top 4 plots and $\mu\mu$X final states for the 4 bottom plots. Signal models for different values of M_N and $|V_{\ell N}|^2$ are shown as empty histograms.

In the region of large displacement, the sensitivity of the analysis greatly increases, with a relatively low abundance of nonprompt lepton background and being virtually free of

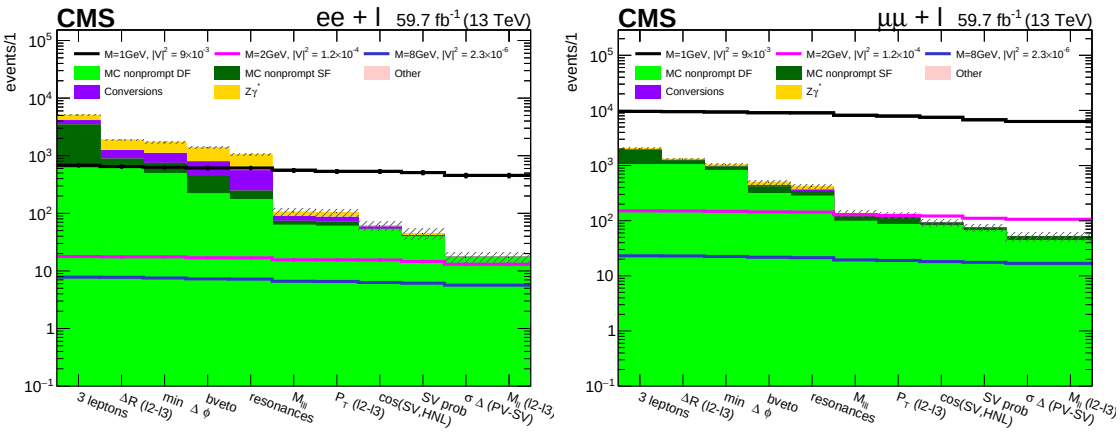

FIGURE 7.6: Cutflow plots showing the full selection applied in simulated backgrounds using the 2018 MC samples, in eeX (left) and $\mu\mu$X (right) final states. Signal models for different values of M_{N} and $|\mathrm{V}_{\ell\mathrm{N}}|^2$ are shown as empty histograms. For illustration purposes, we show only the predictions corresponding to 2018 data-taking and luminosity.

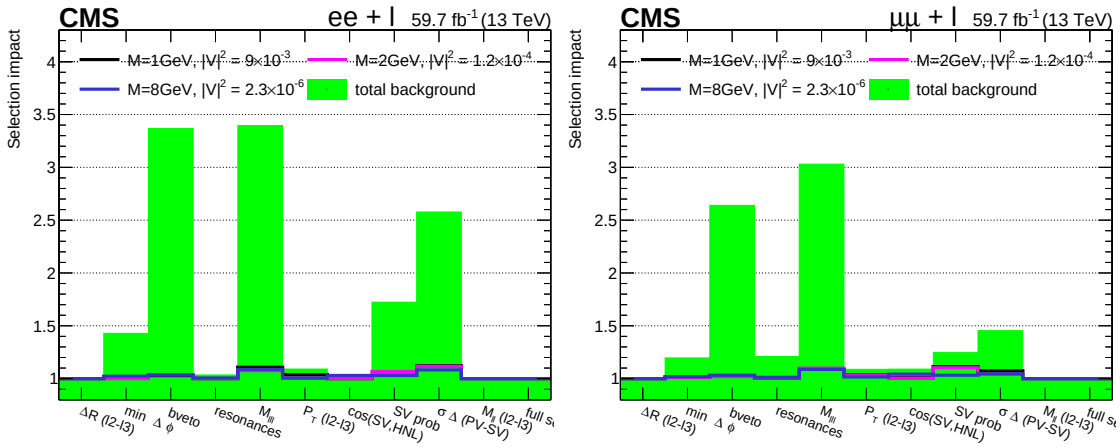

FIGURE 7.7: $N-1$ plots but showing the impact in percentage of the single cut (each bin is $yield_{bin}/yield_{full\ selection}$). Signal models for different values of M_{N} and $|\mathrm{V}_{\ell\mathrm{N}}|^2$ are shown as empty histograms. For illustration purposes we show only the predictions corresponding to 2018 data-taking and luminosity.

prompt lepton background contributions. This represents the key feature of the analysis. On the contrary, HNL signals with higher masses are short-lived and they decay in low displacement regions, where both the prompt and nonprompt lepton contributions are large, similarly to the previous CMS search presented in Chapter 6. Although the sensitivity of the analysis strongly depends on the secondary vertex displacement, no selection is applied on this variable. This is due to the fact that both small and large displacement regimes are interesting for the search. The small displacement region represents the domain of the previous CMS search and can be used to cross-check its results, while the large displacement region provides the highest sensitivity to long-lived HNLs. Thus, the selected events will be divided into different $\Delta_{2\mathrm{D}}$ categories, as well as different $M(\ell_2, \ell_3)$ categories (Figure 7.8).

The residual background, dominated by $X\gamma$, Z/γ^*+jets, and top processes, accumulates at low displacement. The HNL signal models populate higher Δ_{2D} bins, depending on M_N and $|V_{\ell N}|^2$. In particular, Δ_{2D} is found to provide the best discrimination between signal and background, and among different signal models. Therefore we select four event categories, based on the value of Δ_{2D}, with different sensitivities for different signal scenarios: $\Delta_{2D} < 0.5$ cm (fully background dominated), $0.5 < \Delta_{2D} < 1.5$ cm, $1.5 < \Delta_{2D} < 4$ cm and $\Delta_{2D} > 4$ cm.
In addition, the events are split into three different categories according to lepton flavors. When the muon coupling is being probed, the three final states $\mu\mu\mu$, $\mu^{\mp}\mu^{\pm}e$, and $\mu^{\pm}\mu^{\pm}e$ are considered; when the electron coupling is concerned, the three final states are eee, $e^{\mp}e^{\pm}\mu$, and $e^{\pm}e^{\pm}\mu$. This categorization is necessary to provide separate limits for LNC and LNV scenarios (see Section 4.2.2.2). The different categories are also characterized by different background levels and composition, thus providing different sensitivities.

Finally, we notice that the top background processes, where ℓ_2 and ℓ_3 are typically produced in the semi-leptonic decay of B hadrons, populate a region of $M(\ell_2, \ell_3) < 4$ GeV and are basically absent at higher dilepton masses. Therefore we further split the data into two categories: $M(\ell_2, \ell_3) < 4$ GeV and $M(\ell_2, \ell_3) > 4$ GeV.

Since the background yields are extremely low in large displacement bins for the high-mass category, we opted for a lower number of bins, as follows:

- for $M(\ell_2, \ell_3) < 4$ GeV
  - $\Delta_{2D} < 0.5$ cm
  - $0.5 < \Delta_{2D} < 1.5$ cm
  - $1.5 < \Delta_{2D} < 4$ cm
  - $\Delta_{2D} > 4$ cm
- for $M(\ell_2, \ell_3) > 4$ GeV
  - $\Delta_{2D} < 0.5$ cm
  - $\Delta_{2D} > 0.5$ cm

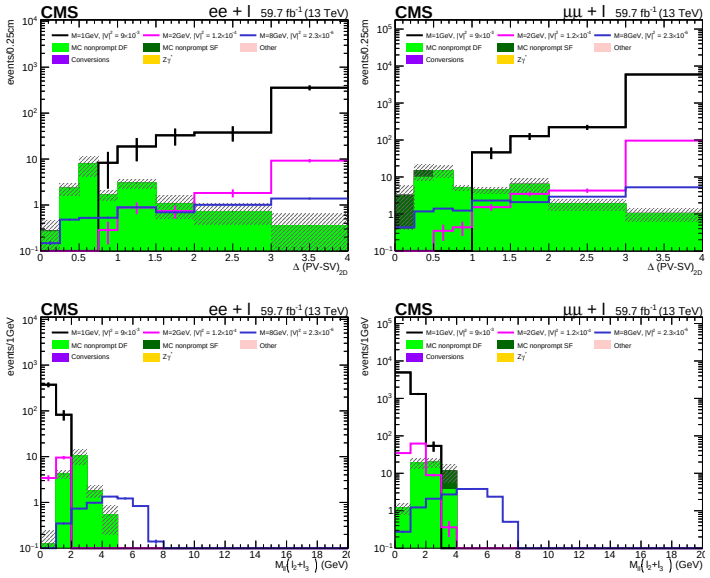

FIGURE 7.8: Δ_{2D} (left), and $M_{\ell_2\ell_3}$ (right) in events passing the baseline selection of Table 7.4. For illustration purposes we show only the predictions corresponding to 2018 data-taking and luminosity.

7.4 Background estimation

7.4.1 Background composition

The main SM background processes mimicking the signal final states can be classified as follows.

- **"Fake" nonprompt leptons (e or μ):** muons from light-flavor mesons that decay in flight, or electrons from unidentified conversions of photons in jets can mimic the displaced leptons from the HNL decay, ℓ_2 and ℓ_3. This background is dominated by top–quark and Drell–Yan processes, and is measured with the data-driven method described in Section 7.4.2.
  In most analyses—such as the one presented in Chapter 6—this background consists of events where one lepton is fake. The specific selection used in this search, however, leads to a majority of background events with two fake displaced leptons. Therefore, the measurement of this background needs to be carried out with particular care. To this purpose, fake nonprompt lepton backgrounds are split into two categories:
  - **single fake nonprompt leptons**: a single reconstructed lepton produced via one of the above mechanisms, e.g. the (semi-)leptonic decay of a meson. Multiple single-fake leptons can be found in an event, produced in the independent decays of different mesons. In this case, the probabilities to select different fake nonprompt leptons for the analysis can be treated as uncorrelated.
  - **double fake nonprompt leptons**: a pair of reconstructed leptons produced in the decay chain of the same hadron, typically a B meson (e.g. via $b \to \ell^- \bar{\nu}_\ell c \to \ell^- \bar{\nu}_\ell \ell'^+ \nu_{\ell'} s$) or a quarkonium state (e.g. $J/\Psi \to \ell^- \ell^+$). In such decays the two leptons are manifestly not independent and their selection probabilities are strongly correlated. Therefore, the lepton pair must be treated as a single system.
- **Photon conversions:** this background was extensively introduced in Sections 5.2 and 6.4.
  It is estimated from simulation and verified in control regions with three leptons with an invariant mass close to the Z mass (Section 7.4.2.3). Such conversions are considered as a source of background, as well as an excellent probe for nonprompt lepton efficiency measurement, in many searches for displaced vertices.

7.4.2 Fake-lepton background

The fake-lepton background is estimated using the TIGHT-TO-LOOSE method. A general description of the fake-rate method can be found in Section 6.4.1.
For this search, the probability for a fake lepton to pass the TIGHT DISPLACED (Tables 7.2 and 7.3) and isolation requirements is estimated by using event yields where at least one lepton fails to satisfy TIGHT DISPLACED selection criteria, but passes the FO ones[3].

The main difference with respect to the prompt HNL analysis (Chapter 6) comes from the different sources of fake leptons: here both fake leptons are typically found in the

[3]The "TIGHT-TO-LOOSE" naming is not very accurate when the ratio is calculated between TIGHT DISPLACED and FO leptons. For "historical" reasons, however, we will use TIGHT-TO-LOOSE, keeping in mind that the selection in the denominator is the FO one.

proximity of a jet—the same for ℓ_2 and ℓ_3—and their properties are correlated. Each FO lepton is therefore associated with the jet of $p_T > 10$ GeV closest in ΔR, if $\Delta R < 0.4$. If two FO leptons are either associated with the same jet or have $\Delta R < 0.45$, they are considered double-fake candidates and treated as a single dilepton system. In all other cases—i.e., if the two FO leptons are associated to different jets and $\Delta R > 0.45$—, the FO leptons are considered as single fakes and (if more than one) treated independently.

An important clarification has to be made regarding the estimation of the fake-lepton background. This prediction only accounts for fake "displaced" ($\ell_{2/3}$) leptons. The contribution from fake prompt (i.e. ℓ_1) leptons is expected to be very small, on account of the much higher probability for fake ℓ_2 and ℓ_3 to pass the tight displaced selection. This assumption has been verified in MC using the information at generated level (MC truth); at the beginning of the selection, only 1‰ of background events have fake nonprompt ℓ_1, at the end of the selection all ℓ_1 leptons are prompt leptons, which ensures that the contribution from pure QCD processes is negligible. For this reason, the contribution from fake ℓ_1 is neglected.

7.4.2.1 Estimation of double-fake background

Events in the application region are classified as double-fake background if the two fake leptons are either associated to the same jet or the distance between them is $\Delta R < 0.45$, and at least one of them is FO. In the first case (same associated jet), the p_T of the mother parton, p_T^{mom}, from which both fake leptons originate, is estimated using the p_T of the associated jet, $p_T^{\text{mom}} = p_T^{\text{jet}}$, calibrated using jet energy corrections (JEC, see Section 3.1.2.1) after subtracting the p_T of the two leptons:

$$p_T^{\text{mom}} = p_T^{\text{jet}} = \left(p_T^{\text{raw jet}} - p_T^{\ell_2} - p_T^{\ell_3}\right) \times \text{JEC} \; + \; p_T^{\ell_2} \; + \; p_T^{\ell_3}. \tag{7.1}$$

In this formula, all the p_T are 4-vectors. Similar is the case when the distance between them is $\Delta R < 0.45$:

$$p_T^{\text{mom}} = p_T^{\text{jet}} = p_T^{jet,2} + p_T^{jet,3} \tag{7.2}$$

where the $p^{jet,i}$ is the jet associated to the lepton i and then corrected using the JEC right correction:

$$p_T^{jet,i} = \left(p_T^{\text{raw jet}_\text{i}} - p_T^{\ell_i}\right) \times \text{JEC} \; + \; p_T^{\ell_i}. \tag{7.3}$$

DOUBLE-FAKE-RATE (f_D) is parametrized and applied as a function of the p_T of the associated jet: $f_\text{D} = f_\text{D}(p_T^{\text{jet}})$. The definition of the measurement region is similar to that of the signal region, with the following differences:

- the two fake leptons, ℓ_2, and ℓ_3, are selected with the FO identification criteria (see Tables 7.2 and 7.3) and must be either associated to the same jet or have $\Delta R < 0.45$;
- a b-tagged jet with $p_T > 25$ GeV must be present (not necessarily the same that ℓ_2 and ℓ_3 are associated to).

The requirement of a b jets enriches the sample in top-quark backgrounds, which are the main source of double-fake leptons, see Table 7.5. Events in this measurement region have two FO leptons, of which zero, one, or both can be TIGHT DISPLACED.

The DOUBLE-FAKE-RATE, f_D, is defined as the fraction of events in this region where both FO leptons pass TIGHT DISPLACED selection. Figure 7.9 (top) shows the measured values

TABLE 7.5: Measurement region selection requirements for double fake.

Variable	Requirement
N. b jets	≥ 1
$M(\ell_2, \ell_3)$ in eee	> 0.5 GeV
resonance vetoes	✓
$M(\ell_1, \ell_2, \ell_3)$ in eee and $\mu\mu e$ OS	< 80 GeV or > 101 GeV
$M(\ell_2, \ell_3)$ in eee	> 0.5 GeV

of f_{D} for events with two electrons, an electron and a muon, and two muons, respectively, as a function of p_T^{jet}. Figure 7.9 (bottom) shows the measured values of f_{D} for events with two electrons, an electron and a muon, and two muons, respectively, as a function of $\Delta_{2\mathrm{D}}$. The $\Delta_{2\mathrm{D}}$ bins are the four bins chosen for the SR, in order to evaluate the f_{D} dependence on the displacement of the SV of the N decay.

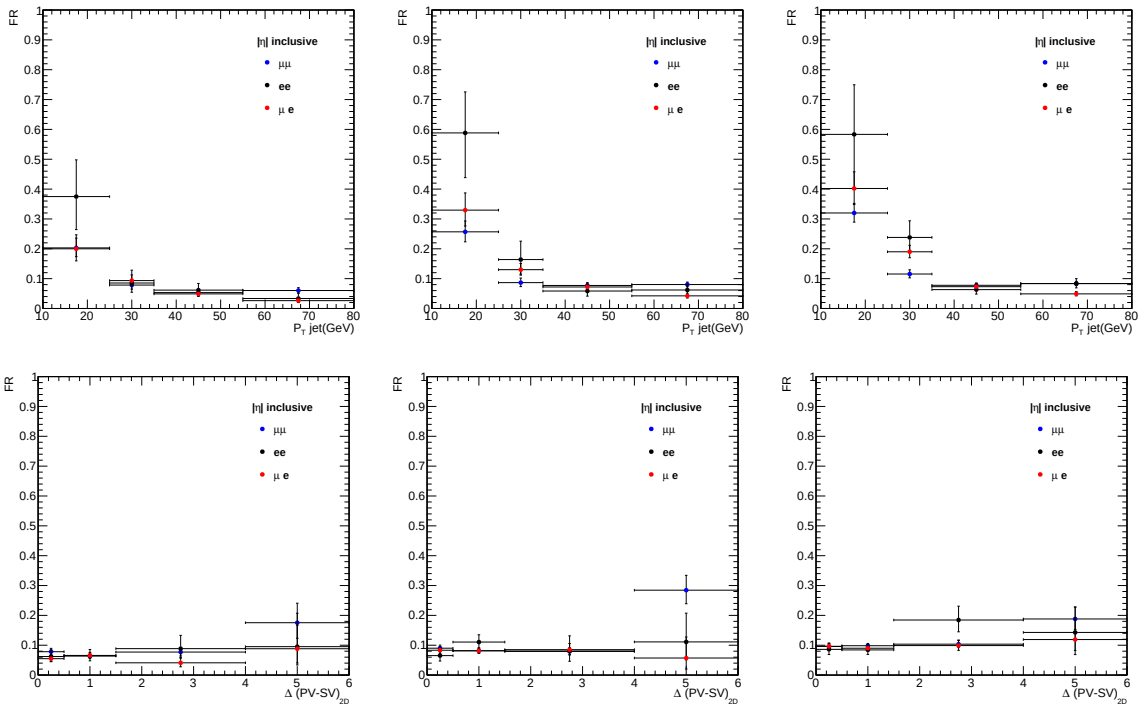

FIGURE 7.9: DOUBLE-FAKE-RATE (f_{D}) measured in 2016/17/18 (left, middle, right) data as a function of p_T^{jet} (top) and $\Delta_{2\mathrm{D}}$ (bottom), for events with two electrons (black), with an electron and a muon (red), and with two muons (blue).

The application region for double-fake lepton backgrounds is defined using the same selection as the signal region (see Table 7.4), but with one or two FO-non-TIGHT DISPLACED leptons that are either associated to the same jet or have $\Delta R < 0.45$. The background from double-fake leptons in the signal region is estimated from the event yields in the application region using the formula

$$N^{\mathrm{sig}}_{\mathrm{double\ fakes}} = \sum_i \frac{f_{\mathrm{D}}(p^{\mathrm{jet}}_{\mathrm{T},i})}{1 - f_{\mathrm{D}}(p^{\mathrm{jet}}_{\mathrm{T},i})}\,, \tag{7.4}$$

where the sum runs over all the events in the application region, with jet transverse momentum $p_{\mathrm{T},i}^{\mathrm{jet}}$.

7.4.2.2 Estimation of single-fake background

The measurement of the single-FAKE-RATE (f_{S}) background follows the exact same procedure as the one explained in Section 6.4.1.1. Thus, to avoid repetitions, only the final measured FAKE-RATE are presented here.

Figure 7.10 shows the measured values of f_{S} for electrons and muons in simulation and in data, respectively, as a function of p_T^{cone} and in different $|\eta|$ bins.

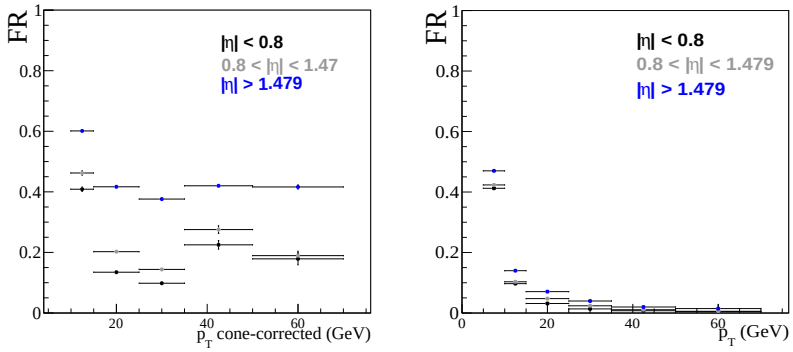

FIGURE 7.10: FAKE-RATE (f_{S}) measured in 2016 data for electrons (left) and muons (right) as a function of p_T^{cone}, for $|\eta|$ ranges $[0, 0.8]$, $[0.8, 1.479]$, and $[1.479, 2.5]$.

Several studies in simulation are performed to ensure that different origins of fake leptons lead to similar FAKE-RATE values (refer to Section 6.4.1 for all the detailed motivations). To a good extent, no strong dependence on d_{xy} is observed, nor on the different origins of fake leptons. Thus, f_{S} is parametrized to only depend on p_T^{cone} and $|\eta|$, while the dependence on d_{xy} is ignored. Figure 7.11 shows that f_{S} values are fairly independent of the lepton d_{xy}, which is used as a proxy for the displacement.

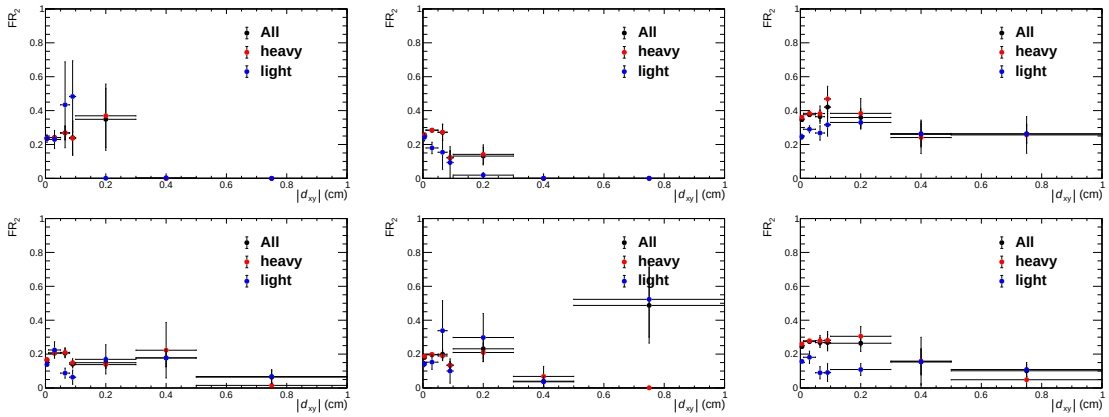

FIGURE 7.11: Single fake rates obtained in 2016 simulation for electrons (top) and muons (bottom) as a function of d_{xy}, for $|\eta|$ ranges $[0, 0.8]$ (left), $[0.8, 1.479]$ (middle), and $[1.479, 2.5]$ (right). The different origins of the mother parton is shown, light (u,d,s quarks or gluons) and heavy (b, c quarks).

7.4.2.3 Application of the TIGHT-TO-LOOSE methods

To check the accuracy of the background estimates obtained with the TIGHT-TO-LOOSE method (both FAKE-RATE and DOUBLE-FAKE-RATE), *closure tests* are performed in simulation, as well as in control data samples. The prediction of the fake background is obtained as the combination of the two contributions described above. The total fake background is thus estimated as follows:

$$N_{\text{fake}}^{\text{sig}} = \sum_i \frac{f_{\text{S}}(\eta_i,\, p_{\text{T},i}^{\text{cone}})}{1 - f_{\text{S}}(\eta_i,\, p_{\text{T},i}^{\text{cone}})} + \sum_i \frac{f_{\text{D}}(\eta_i^{\text{jet}},\, p_{\text{T},i}^{\text{jet}})}{1 - f_{\text{D}}(\eta_i^{\text{jet}},\, p_{\text{T},i}^{\text{jet}})} \,,$$

Closure test in simulation This test is performed using $t\bar{t}$ MC samples, with the following selection: one prompt lepton and two OS displaced leptons and no b jets.
The results are shown in Figure 7.12 for 2016. The MC events are classified based on the presence of one or two single-fake leptons (dark-green histogram) or a double-fake lepton pair (green histogram), according to the definitions given in the introduction to Section 7.4.1. MC events are compared with the estimates obtained from the FAKE-RATE methods described in Section 7.4.2.2 and 7.4.2.1, combined in the red histogram. We notice that the double-fake background contributes mostly to the large-Δ_{2D} and low-$M(\ell_2, \ell_3)$ regions. We can conclude that the fake-rate background estimations correctly reproduce the expected single- and double-fake lepton backgrounds, both the overall yields and the kinematic spectra. Although in some places, e.g. in the $M(\ell_2, \ell_3)$ distribution (middle plot in Figure 7.12) around 4 GeV, the transition region between single- and double-fake lepton background shows some discrepancies, in the actual SR bins (right plot of Figure 7.12) the agreement is reasonable. Nevertheless, we value the validation tests in data control regions more than that in simulation, which is prone to mis-modeling from various sources.

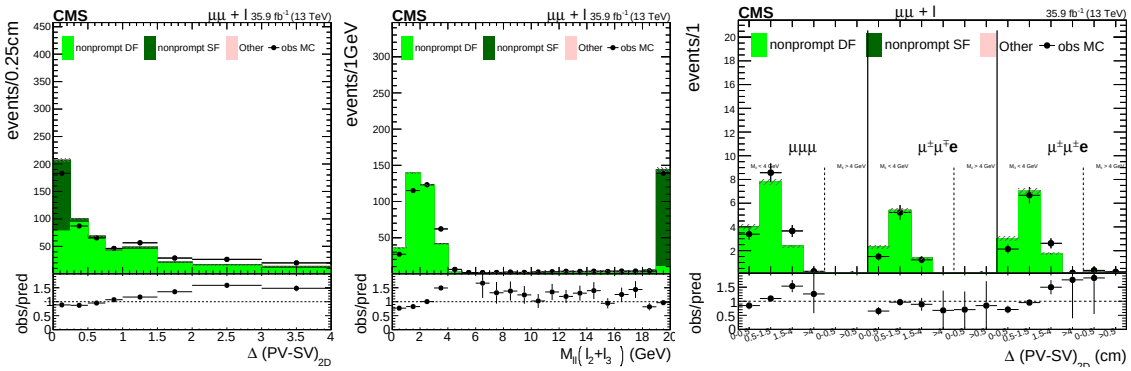

FIGURE 7.12: Distributions of Δ_{2D} (left), $M(\ell_2, \ell_3)$ (middle) 2016 $t\bar{t}$ MC samples, comparing the MC events containing SF leptons and DF leptons with the prediction, for the sum of all final states. The right plot shows the signal-region yields after all the event selection, 7.4, has been applied.

In the following, we present data control regions orthogonal to the defined search region, to test the predictive power of the method.

Closure test in data sample: sideband control region This control region is defined in Table 7.6. Data in this region are compared to our data-driven (nonprompt DF and SF) and MC-based (the other) background estimates.

Results for Run2 data are shown in Figure 7.13.

TABLE 7.6: Control region selection requirements applied to all data sets.

Variable	Requirement
$\Delta R(\ell_2, \ell_3)$	< 1
$\min \Delta\phi(\ell_1, \ell_{2/3})$	> 1 rad
$M_{3\ell}$	< 50 OR > 80 GeV
N. b jets	$= 0$
$(\ell_2 + \ell_3)$ p_T	> 15 GeV
$\cos\theta_{\mathrm{SV,\,N}}$	> 0.99
$M(\ell_2, \ell_3)$	< 20 GeV
p_{SV}	> 0.001
$S(\Delta_{2D})$	> 20
resonance vetoes	✓
$M(\ell_1, \ell_2, \ell_3)$ in eee and $\mu\mu e$ OS	< 50 GeV or > 101 GeV

Closure test in data sample: b jets control region This control region is defined in Table 7.7. Data in this region are compared to our data-driven (nonprompt DF and SF) and MC-based (the other) background estimates.
Results for Run2 data are shown in Figure 7.14.

TABLE 7.7: b jets control region selection requirements applied to all data sets.

Variable	Requirement
$\Delta R(\ell_2, \ell_3)$	< 1
$\min \Delta\phi(\ell_1, \ell_{2/3})$	> 1 rad
N. b jets	$\neq 0$
$(\ell_2 + \ell_3)$ p_T	> 15 GeV
$\cos\theta_{\mathrm{SV,\,N}}$	> 0.99
$M(\ell_2, \ell_3)$	< 20 GeV
p_{SV}	> 0.001
$S(\Delta_{2D})$	> 20
resonance vetoes	✓
$M_{3\ell}$ in eee and $\mu\mu e$ OS	< 50 GeV or > 101 GeV

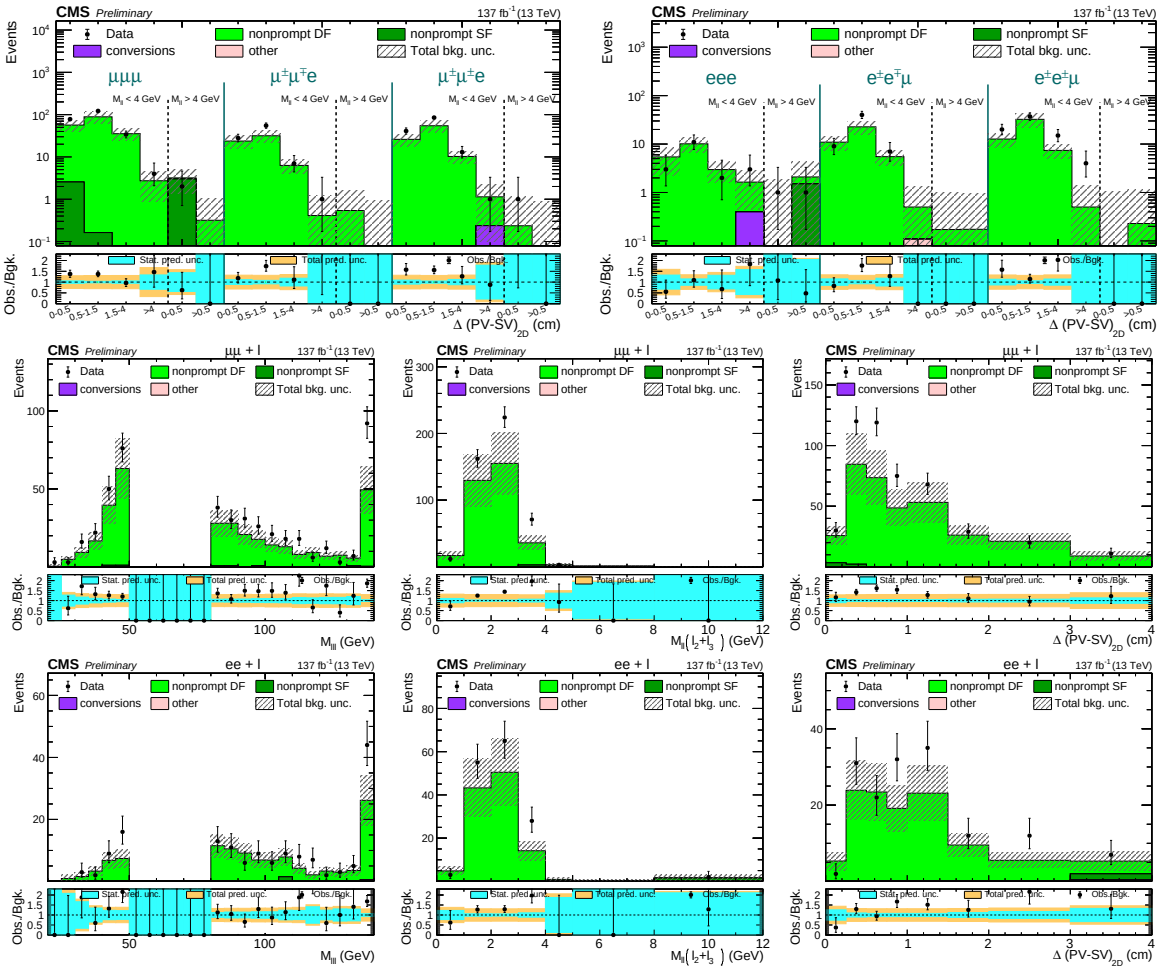

FIGURE 7.13: At the top, search region-like distributions with the selection of the sideband control region, in data and background predictions, in final states with more than two muons (left) and more than two electrons (right). In the middle and at the bottom, distributions of three-lepton invariant mass (left), $M(\ell_2, \ell_3)$ (middle), and Δ_{2D} (right) in the combined Run2 sideband control region, for the sum of all final states with muon couplings (middle) and electron couplings (bottom).

Closure test in data sample: sideband plus b jet control region Taking into account the complementarity of the two control regions just presented, and considering the low statistical power exhibited in Figure 7.13, a new CR was defined.

This control region combines the b jet and the sideband control regions and it is defined by the criteria listed in Table 7.8. The combination of these two control regions is still fully orthogonal to the signal region.

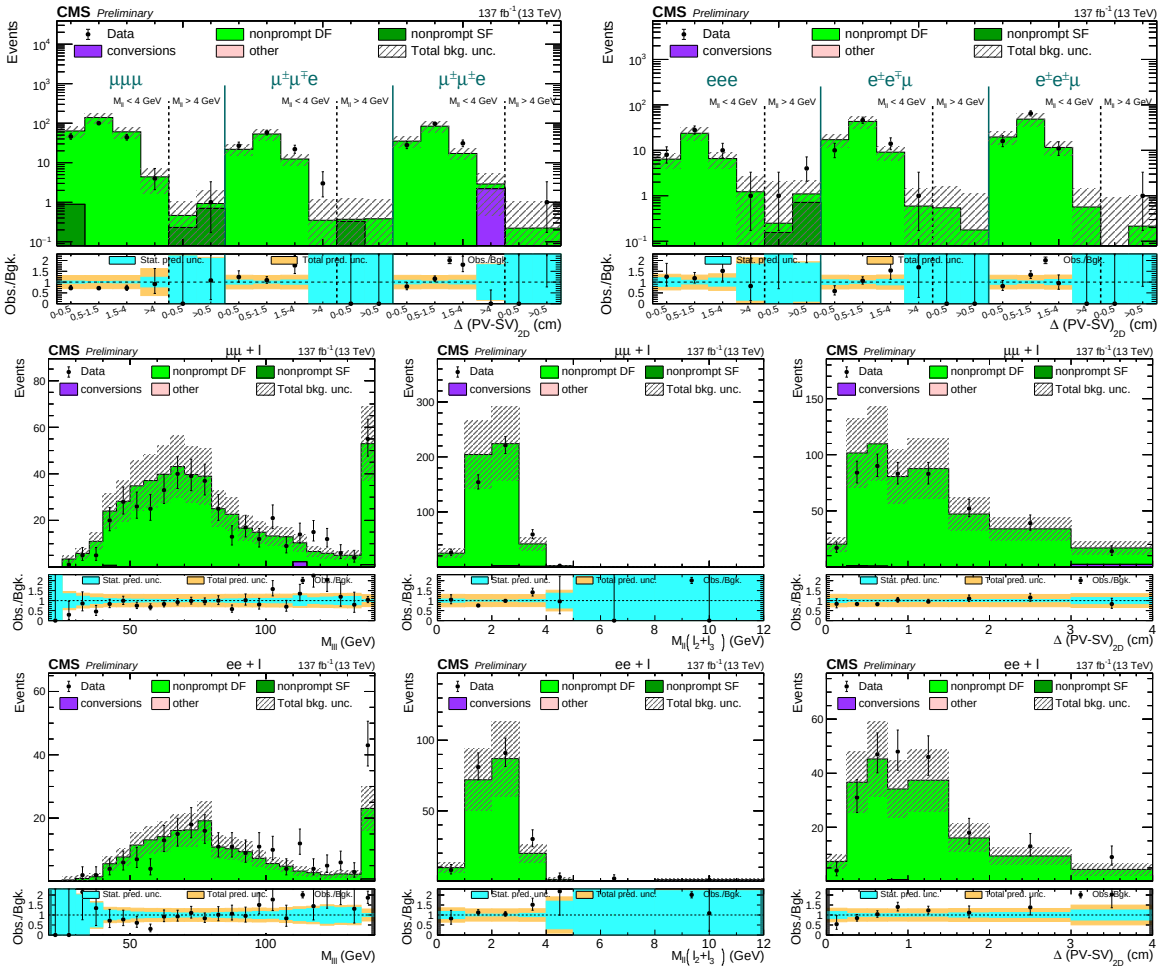

FIGURE 7.14: Search region-like distributions with the selection of the b jets control region, in data and background predictions, in final states with more than two muons (left) and more than two electrons (right). In the middle and at the bottom, distributions of three-lepton invariant mass (left), $M(\ell_2, \ell_3)$ (middle), and Δ_{2D} (right) in the combined Run2 sideband control region, for the sum of all final states with muon couplings (middle) and electron couplings (bottom).

TABLE 7.8: Control region selection requirements applied to all data sets.

Variable	Requirement
$\Delta R(\ell_2, \ell_3)$	< 1
$\min \Delta\phi(\ell_1, \ell_{2/3})$	> 1 rad
$(\ell_2 + \ell_3)$ p_T	> 15 GeV
$\cos\theta_{\mathrm{SV,\,N}}$	> 0.99
$M(\ell_2, \ell_3)$	< 20 GeV
p_{SV}	> 0.001
$S(\Delta_{2D})$	> 20
resonance vetoes	✓
$M(\ell_1, \ell_2, \ell_3)$ and N. b jets	(< 50 GeV or > 80 GeV and N.b jets $= 0$) OR (N.b jets $\neq 0$)
$M(\ell_1, \ell_2, \ell_3)$ in eee and $\mu\mu e$ OS	< 50 GeV or > 101 GeV

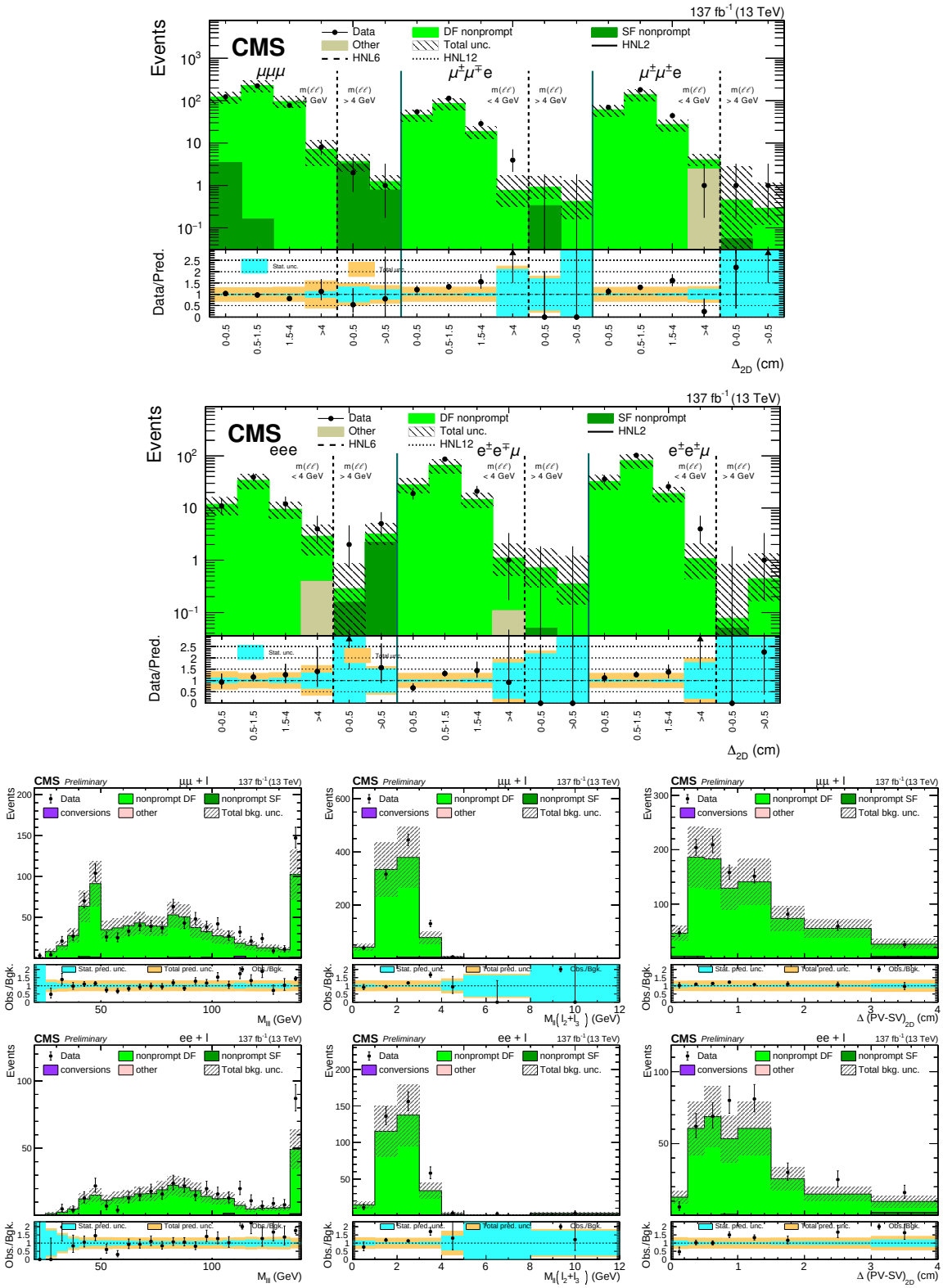

FIGURE 7.15: Distributions of three-lepton invariant mass (left), $M(\ell_2, \ell_3)$ (middle), and Δ_{2D} (right) in the combined Run2 control region in table 7.8, for the sum of all final states with muon couplings (top) and electron couplings (bottom).

Closure test in data sample: validation of internal and external conversions
The photon conversion background is modeled using simulated events, but its overall normalization is checked in a $Z \to \ell^-\ell^+\gamma^{(*)}$ control region in data, as defined in Table 7.9.

TABLE 7.9: Conversion control region selection requirements applied to all data sets.

Variable	Requirement
$\Delta R(\ell_2, \ell_3)$	< 1
$\min \Delta\phi(\ell_1, \ell_{2/3})$	> 1 rad
$M(\ell_1, \ell_2, \ell_3)$	between 81 and 101 GeV, i.e. consistent with an on-shell Z boson
N. b jets	$= 0$
$(\ell_2 + \ell_3)$ p_T	> 15 GeV
$\cos\theta_{\mathrm{SV,\,N}}$	> 0.99
$M(\ell_2, \ell_3)$	< 20 GeV
p_{SV}	> 0.001
$S(\Delta_{2D})$	> 20
resonance vetoes	✓

This region is dominated by $Z \to \ell^-\ell^+\gamma \to \ell^-\ell^+e$ events, with an asymmetric conversion of the real photon. The $M(\ell_1, \ell_2, \ell_3)$ and $M(\ell_2, \ell_3)$ spectra of such events are shown in Figures 7.16. A fair agreement is found between data and simulation, with no corrections required.

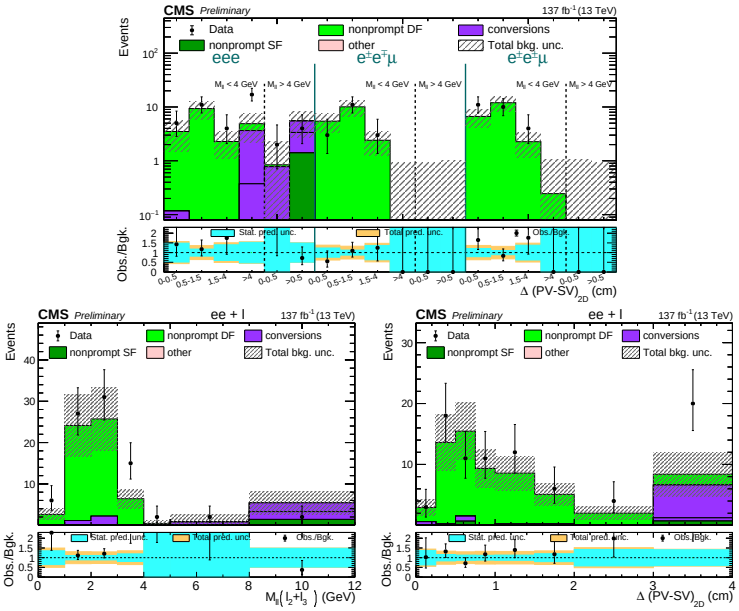

FIGURE 7.16: Distribution of SR-like bins, the two-lepton invariant masses, $M(\ell_2, \ell_3)$, and Δ_{2D} in the photon-conversion control region with events with at least 2 electrons in the final state. Run2.

7.5 Signal efficiency validation

7.5.1 Prompt lepton efficiency

Prompt electron and muon identification and isolation efficiencies are measured in data and simulation using a tag-and-probe method, applied to samples of inclusive Z boson events. The data-to-MC ratios of efficiencies ("scale factors") measured centrally by the CMS *muon physics object group* as a function of the lepton p_T and η are used to correct the simulated events. Additionally, the scale factors are measured for the isolation requirement and the impact parameter cuts. The results are presented in Figure 7.17.

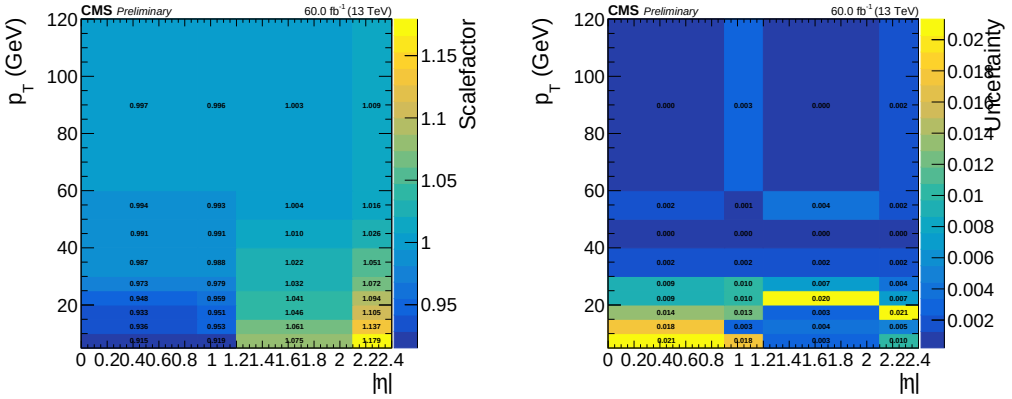

FIGURE 7.17: Data/MC efficiency scale factors (left) and associated systematic uncertainty (right) for impact parameter and isolation requirement efficiency for prompt muons.

For prompt electrons, the SFs are obtained following the CMS *electron-photon physics object group* prescriptions, using the same tag-and-probe techniques as the ones for the muons. The results as a function of transverse momentum and pseudorapidity are shown in Figure 7.18.

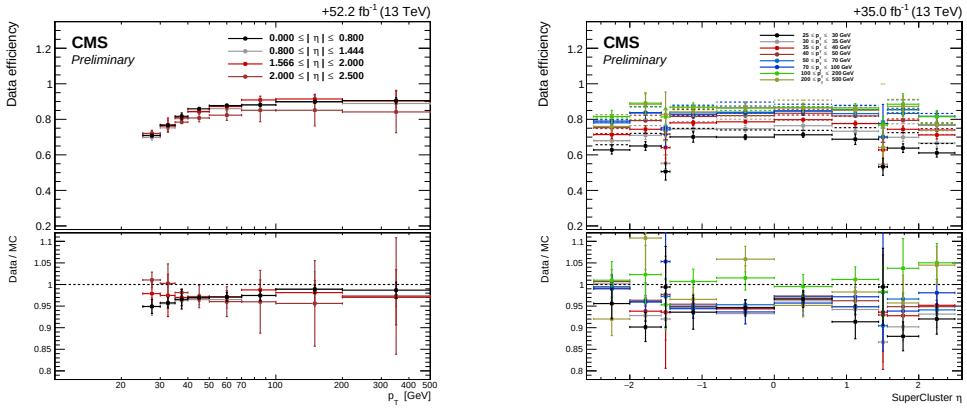

FIGURE 7.18: Prompt electron efficiencies and data-MC scaling factors as a function of transverse momentum (left) or pseudorapidity (right).

7.5.2 Trigger efficiency

Events for this analysis are selected by means of single-electron and single-muon triggers, geometrically matched to the prompt lepton ℓ_1 (see Section 7.2.2). Similar to the prompt-lepton identification and isolation, trigger efficiencies are also measured in data and simulation with a tag-and-probe technique. The resulting data-MC scaling factors are used to correct the simulated event yields.

Trigger efficiencies and data-MC scaling factors for electrons are shown in Figure 7.19. They include both statistical and systematic uncertainties.

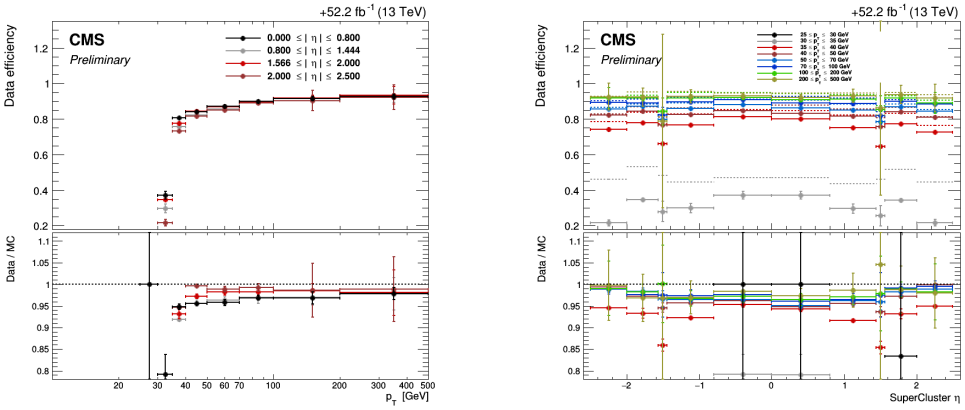

FIGURE 7.19: Trigger efficiencies and data-MC scaling factors as a function of transverse momentum (left) or pseudorapidity (right) for HLT_Ele32 in 2018 data.

7.5.3 Displaced-lepton reconstruction and selection efficiency

Muons The identification and isolation requirement selection efficiency corrections for displaced muons are measured using $Z \to \mu^-\mu^+$ events. The results are presented in Figure 7.20.

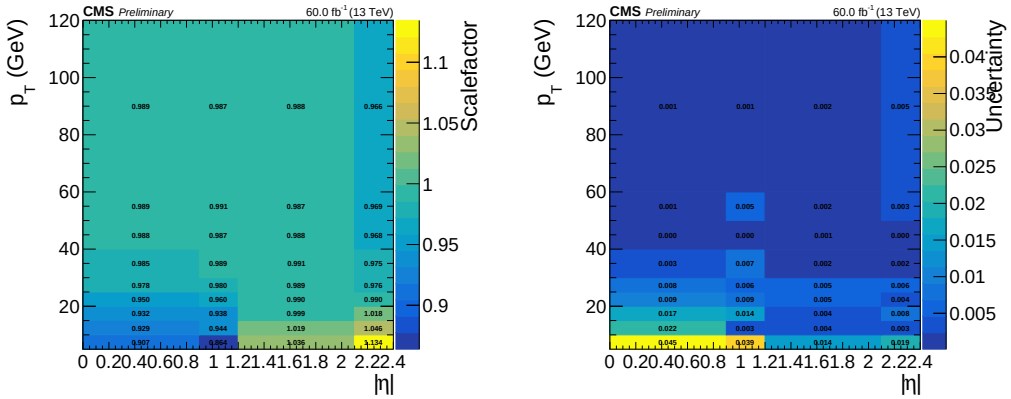

FIGURE 7.20: Data/MC efficiency scale factors (left) and associated systematic uncertainty (right) for ID selection and isolation requirement efficiency for nonprompt muons.

Additional validation is performed in a sample enriched with moderately displaced muons. Displaced muon identification efficiencies without isolation requirements are validated using $B^\pm \to J/\psi K^\pm \to \mu^+\mu^- K^\pm$ events, where the two muons from the J/ψ meson

decay originate from an SV. The estimated efficiencies are found to be very close to 100% and the data-MC agreement is within the statistical uncertainties.

These two complementary measurements give us confidence in our understanding and in the validity of the displaced muon identification strategy.

Electrons Different reference processes are identified which could mimic—to some extent—the main characteristics of displaced electrons stemming from HNL decays, such as photon conversions in the detector material.

We select asymmetric photon conversions in events $Z \to \ell^-\ell^+\gamma \to \ell^-\ell^+e^\pm(e^\mp)$. The reconstructed three leptons, therefore, have invariant mass $m(\ell^-\ell^+e^\pm)$ close to that of the Z boson. The events are selected as follows:

- a pair of oppositely-charged prompt electrons (muons) is selected with $p_T > 35$ (28) GeV and 10 (10) GeV requirements applied on the leading and sub-leading lepton transverse momenta, respectively. Electrons (muons) are reconstructed and selected with the identification criteria listed in Tables 7.2 and 7.3. The higher-p_T threshold is driven by trigger constraints, while the lower-p_T threshold is chosen to improve the statistical power of the sample;
- the higher-p_T prompt lepton must be matched geometrically to a trigger object and fire the single-electron or single-muon trigger;
- a displaced tight electron (see Table 7.2) with $p_T > 7$ GeV, to match the selection on displaced electrons in the analysis;
- the invariant mass of the three leptons must lie within 10 GeV of the Z boson mass.

By comparing the rates in data and simulation, we can deduce the level of disagreement in displaced electron reconstruction and identification efficiencies. As explained above, it is not straightforward to disentangle different contributions to this discrepancy, therefore any data-MC difference is to be taken as a maximum possible difference in the efficiency of displaced electrons.

Since the position of the displaced electron production vertex is unknown, as a proxy for its displacement we use the following variable [164]:

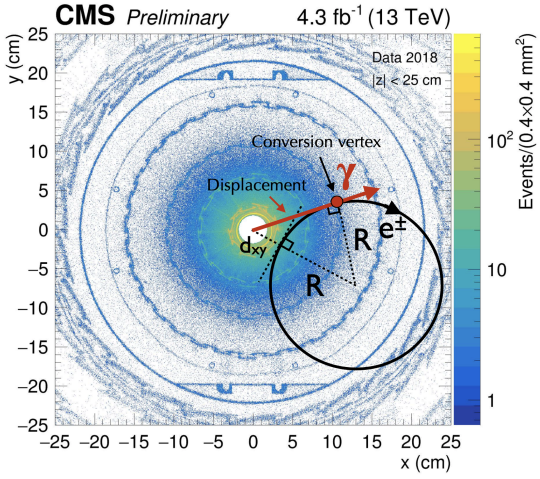

$$\mathrm{d} = \sqrt{2\mathrm{R}\mathrm{d}_{\mathrm{xy}} + \mathrm{d}_{\mathrm{xy}}^2}; \qquad \mathrm{R[m]} = \frac{\mathrm{p_T[GeV]}}{0.3 \cdot \mathrm{B[T]}}, \tag{7.5}$$

where R is the radius of curvature of the trajectory of a charged particle in a magnetic field, d_{xy} is the transverse impact parameter of the trajectory, and B is the magnitude of the magnetic field. The resulting data/MC ratio measured in bins of displacement (Figure 7.21) is used as a per-electron correction factor applied to signal events. Half of the difference of the scaling factor with respect to unity is considered as an uncertainty.

We obtained similar results in an independent study, where we used K^0_s mesons to measure displaced muon reconstruction efficiencies (see Section 7.5.4). The details of how the scale factors and the systematic uncertainties from each of these studies are implemented in the analysis can be found in Section 7.6.1.

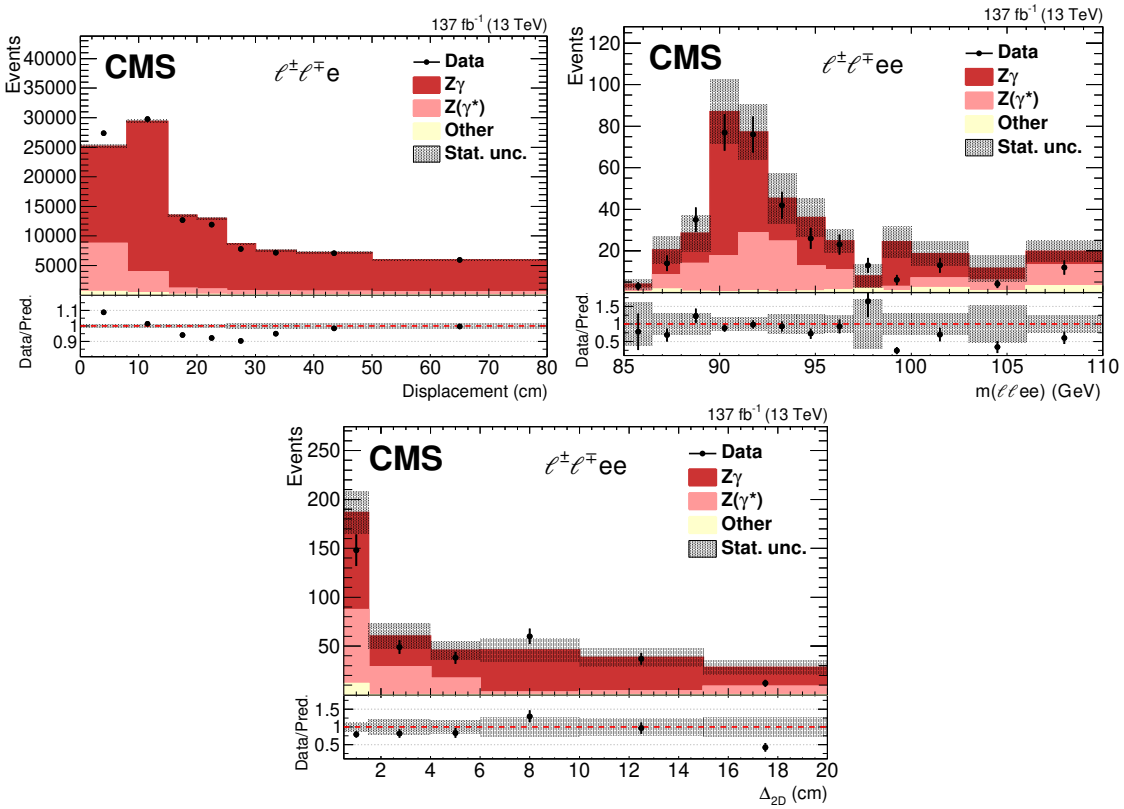

FIGURE 7.21: Comparison between the observed number of events in data and simulation for converted photons. Events are selected in the final states with three (upper left) or four (upper right, lower) leptons, with one (or two) of the leptons identified as nonprompt electron(s). The distributions are shown for the nonprompt electron displacement (upper left) and reconstructed invariant mass of four leptons (upper right). Additionally, the distance between the reconstructed PV and fitted SV is presented (lower). The simulated events correspond to the processes with external conversions, $Z\gamma^{(*)}$; internally converted photons, $Z(\gamma^*)$; and other processes with the production of vector bosons and top quarks. The hashed band represents the statistical uncertainty in the simulation. Courtesy of K. Skovpen.

7.5.4 Displaced tracking and vertexing efficiency

In this subsection, we investigate the discrepancy between simulation and data for strongly displaced tracks and vertices. The method is based on the displaced decay of the neutral hadrons K_S^0 to two charged particles (see Figure 7.22), producing a signature of two displaced tracks originating from a common vertex.
We will briefly discuss the methodology and the most important results. More information can be found at [165].
The events in the selected data and simulated sets must pass the requirements listed below:

- exactly 2 muons in the event;
- the leading muon must have a p_T of at least 30 GeV, the trailing muon of at least 25 GeV;
- the selected muon invariant mass is required to be within 10 GeV of the Z-boson mass;
- events containing one or more loosely tagged b-jet are vetoed.

The vertex reconstruction algorithm developed for this study closely resembles the built-in V^0-vertex fitter in the CMS software (where V^0 is used to refer to K_S^0 vertex), for details refer to
Sections 3.1.1 and 3.2. Furthermore, we re-optimized some of the cut values in order to retain more V^0 candidates at small radial displacements from the primary vertex, at the cost of a slightly larger overall background. This design choice was inspired by the need for a large number of candidates close to the primary vertex, as these will be used for normalization (see further on).
The number of K_S^0 mesons in data and simulation are estimated by a template fit to the invariant mass distribution of the $\pi^{\pm}\pi^{\mp}$ pairs; the combinatorial background is subtracted. The results of this validation are presented in four Δ_{2D} ranges from "almost prompt" to very displaced in Figure 7.23.

A normalization factor to correct the event yield in simulation to the corresponding yield in data is extracted at very small radial distances (0–0.5 cm). It represents an overall normalization correction for possible MC mis-modeling of the K_S^0 production in Z boson events. This approach allows us to correct for overall mis-modeling effects of V^0-particles and to isolate the effect under consideration, i.e. a systematic difference in vertex reconstruction efficiency due to its being displaced.

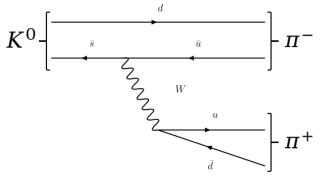

FIGURE 7.22: Diagrams for the decays of K_S^0 studied in this method.

As a first remark, we plot the yield of K_S^0 particles using a relatively fine binning in Figure 7.24 (left). Notice how the pixel detector layout has a clear structural influence on the yield, both in simulation and data.
Scale factors for SV efficiencies are measured in Δ_{2D} bins, as well as in lepton p_T bins for each data-taking period.
In Figure 7.24 (right), the comparison of data to simulation in all p_T ranges is shown as a function of Δ_{2D}. In events with either two displaced muons or one displaced muon, these results are used to extract correction factors for MC signal event acceptances in bins of displacement, as well as the corresponding systematic uncertainties for displaced track and vertex reconstruction.

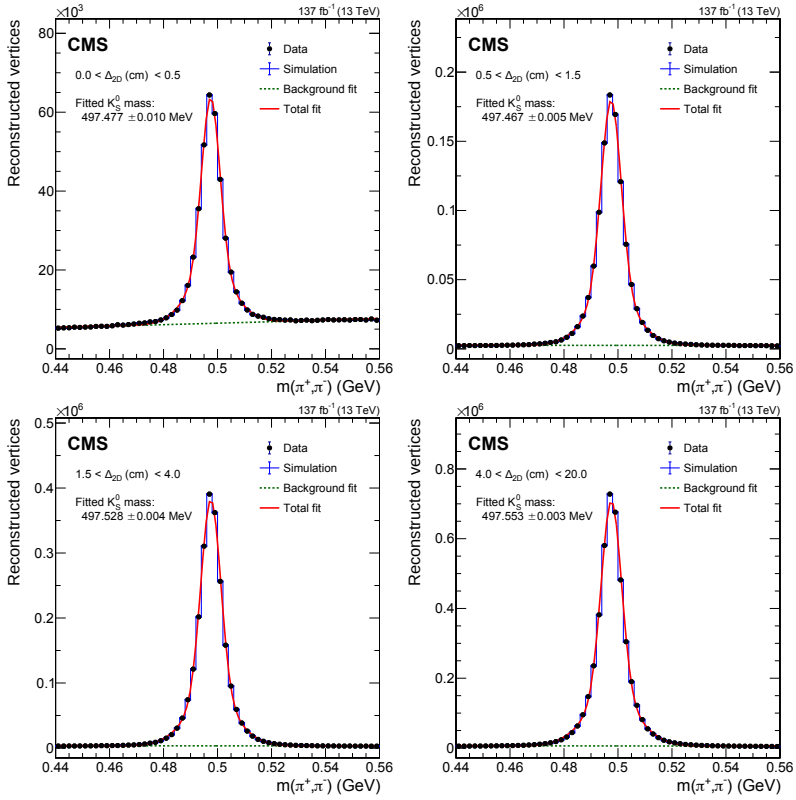

FIGURE 7.23: The invariant mass distribution of the K_S^0 candidates was reconstructed using the $\pi^{\pm}\pi^{\mp}$ tracks for various displacement regions. The fitted K_S^0 candidate mass in data in each region is also shown. Courtesy of L. Lambrecht.

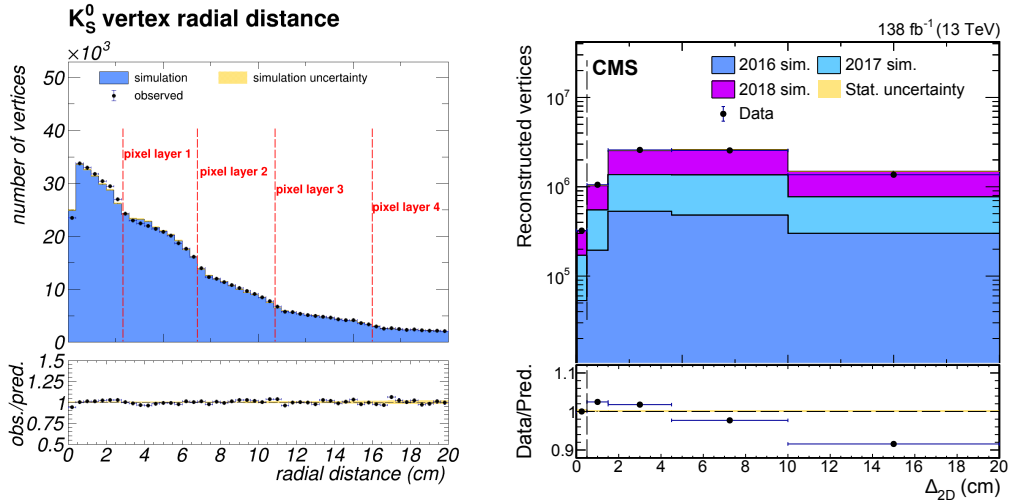

FIGURE 7.24: Results for K_S^0 particles using a fine binning and linear y-axis scale with the radial distances of the pixel detector layers superimposed. Note that in this plot, the total number of K_S^0 particles in simulation was normalized to that in data as we merely wanted to perform a shape comparison. The right plot shows the K_S^0 candidate yield after subtracting the background in data and in simulation, as well as their ratio, as a function of radial distance of the K_S^0 vertex to the PV. Courtesy of L. Lambrecht.

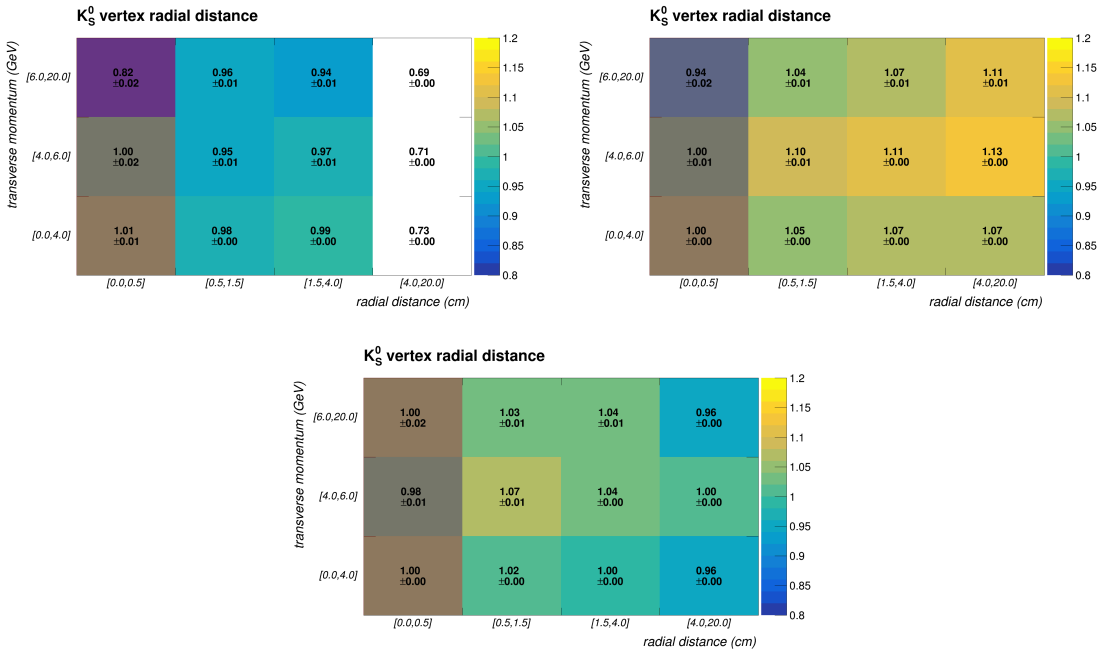

FIGURE 7.25: Uncertainty factors per bin in radial distance and transverse momentum. The red-colored band overlaying the figure shows the normalization range, i.e. 0 - 0.5 cm. Note that an error of ±0.00 indicates that the (statistical) error is smaller than 0.005. Courtesy of L. Lambrecht.

In Figure 7.25, we extend these results by performing a two-dimensional binning: the x-axis again represents the radial distance from the primary vertex, while the y-axis now holds the reconstructed transverse momentum of the particle. Note that the discrepancy is very large in the last bin for 2016 data. This can be explained by a reduced tracking performance during part of the 2016 data taking, caused by a saturation effect in the silicon tracker electronics [166]. This issue was fixed for the second half of the 2016 data taking, as can be observed in the detailed studies reported in [165].

7.6 Systematic uncertainties

Several sources of systematic uncertainty affect the expected signal and background yields in different search regions. The effect of the main uncertainties on the signal yields in each search region and lepton channels are summarized in Figure 7.26. Most of the experimental uncertainties are relatively small (less than a few %). In some search regions, the uncertainties are dominated by the signal modeling, because of the limited size of the signal MC samples.

7.6.1 Uncertainties on the signal yields

All uncertainties summarized in this section are evaluated per search region and per lepton channel, and considered as shape uncertainties in the final fit, with the exception of those that only affect the overall normalization, such as the signal cross-section and luminosity.

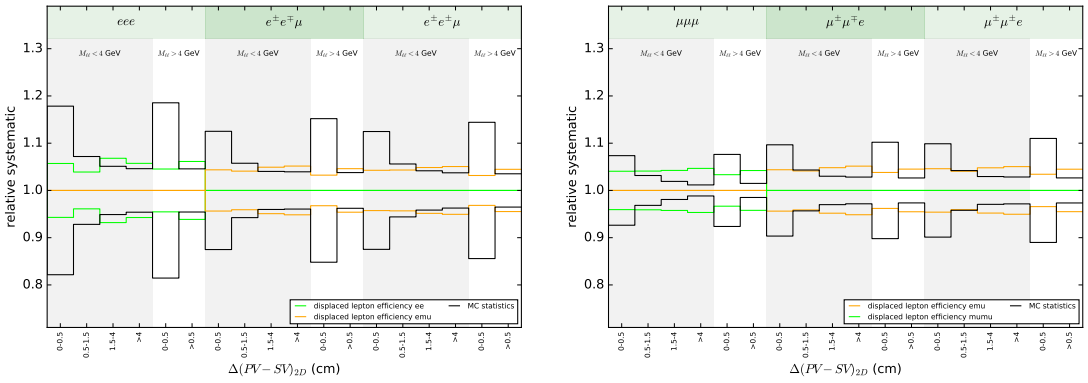

FIGURE 7.26: Relative up and down variation from the nominal yields for the signal sample with $M_{\mathrm{N}} = 6$ GeV and $|\mathrm{V}_{\ell\mathrm{N}}|^2 = 4 \times 10^{-6}$. The variation is shown for each of the search regions for electrons (left) and muons (right), for the 2018 data taking year.

Integrated luminosity The uncertainties on the measurements of the LHC integrated luminosities are 2.5% (2016) [155,167], 2.3% (2017) [168], and 2.5% (2018) [169]. They affect the yields of the signal and of the MC-based background estimations in a fully correlated way (within the same data-taking period).

Pileup The uncertainty in the modeling of the pileup is evaluated by decreasing and increasing the minimum bias cross-section by 5% [170], resulting in an uncertainty of 1–4% for most search regions, with some larger deviations for statistically limited search regions.

Trigger efficiency Trigger scale factors are used to correct the simulated event yields (see Section 7.5.2), and the uncertainties from the tag-and-probe fits are used to assess systematic uncertainties. These are found to be less than 1% for electron triggers and less than 1% for muon triggers.

Prompt lepton reconstruction and identification efficiency To find the uncertainties associated with the prompt-lepton identification and isolation efficiency scale factors (see Section 7.5.1), the total yields in each search region are recomputed with the scale factors varied up and down by the tag-and-probe fit uncertainties, treating all bins as correlated. Uncertainties of 2–5% on the signal yields are found for events with a prompt electron, while the uncertainty on prompt muons stays consistently below 1% for all search regions.

Displaced lepton identification efficiency and displaced vertex efficiency Data events with Z bosons decaying into lepton pairs provide an excellent testing ground for the prompt lepton reconstruction and identification efficiencies in simulation. The main source of the systematic uncertainty in our analysis is the displaced track and vertex reconstruction modeling. We make use of two types of processes to estimate this uncertainty. Converted photons in Z events (described in section 7.5.3) are used to assess the modeling of displaced

electron reconstruction, and long-lived K^0_S mesons are used to scrutinize the displaced track and vertex reconstruction in simulation.

Both studies show consistent results in terms of data/MC agreement across the data-taking periods. In both cases, we observe larger data/MC scale factors in 2016 data, which is caused by a known tracking inefficiency in data that is not simulated in MC (see Section 7.5.4). In this data set the discrepancy between can reach up to 30% (see Figures 7.21–7.25). Based on these studies, we apply data/MC scale factors per displaced lepton in simulation, and half of the difference between 1 and the SF is considered as a systematic uncertainty. In channels with displaced ee or $\mu\mu$, the scale factors are derived from conversions (K^0_S). In events with displaced $e\mu$ instead, scale factors from conversions are used for the electron, while the corrections for the muon are taken from the K^0_S study. The displaced-muon reconstruction and ID efficiency (Section 7.5.3) is added per muon in $\mu\mu$ and $e\mu$ events on top of the corrections for the displaced track and vertex reconstruction.

The uncertainties in the final yields in the different search regions and data-taking periods are calculated by varying the MC event weights by half of these scale factors for each displaced lepton (i.e. two per event). The resulting uncertainties in each signal region/year and lepton channel can be seen in Figure 7.26.

Displaced muon momentum scale and resolution The study of K^0_S decays (Section 7.5.4) also provides useful information about the momentum scale and resolution of the displaced-muon tracks. For p_T below 200 GeV, the muon momentum estimate is fully dominated by the tracker-only fit. It is easy to prove that the muon momentum resolution $\sigma(p_T)/p_T$ is approximately equal to the dimuon mass resolution $\sigma(M_{2\ell})/M_{2\ell}$. The Gaussian

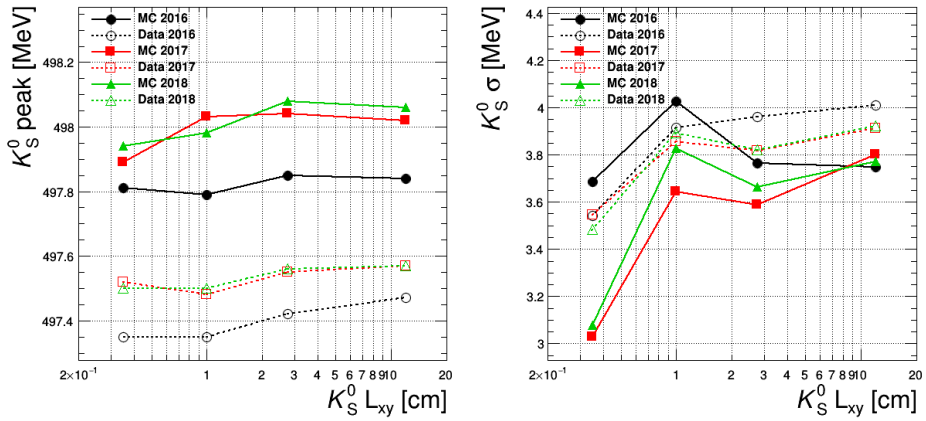

FIGURE 7.27: Values of the K^0_S mass peak (left) and width (right) as a function of the transverse displacement Δ_{2D}, in data and simulation, for the three data taking years. The mass peak and width are estimated, respectively, by the μ and smaller σ parameters of the double-Gaussian fit to the K^0_S mass profile (e.g., see Figure 7.23). Courtesy of D. Trocino.

fits to the K^0_S mass profiles, such as Figure 7.23, can thus be used to estimate the momentum scale and resolution through the fit parameters μ and σ/μ, respectively. The width of the central mass peak is estimated by the smaller of σ_1 and σ_2, whereas the larger σ represents the mass tails. Figure 7.27 shows the values of the K^0_S mass peak and width as a function of the transverse displacement Δ_{2D}, in data and simulation, for the three data taking years.

TABLE 7.10

(A) Relative difference in mass (or momentum) scale between data and simulation, estimated as $(\mu_{\text{data}} - \mu_{\text{sim}})/\mu_{\text{sim}}$.

Δ_{2D} [cm]	Data-MC scale difference [%] 2016	2017	2018
< 0.5	−0.092	−0.074	−0.088
0.5–1.5	−0.088	−0.110	−0.096
1.5–4.0	−0.086	−0.098	−0.104
> 4.0	−0.074	−0.090	−0.098

(B) Difference in quadrature in mass (or momentum) resolution between data and simulation, where the resolution is estimated as σ/μ.

Δ_{2D} [cm]	Data-MC resolution difference [%] 2016	2017	2018
< 0.5	0.20	0.37	0.33
0.5–1.5	0.19	0.26	0.15
1.5–4.0	0.25	0.26	0.22
> 4.0	0.29	0.19	0.22

As can be seen, the differences between data and simulation are relatively small. Table 7.10a reports the relative data-MC differences in the scale parameter (μ). The differences are at the per-mil level, thus negligible. Table 7.10b reports the differences (in quadrature) in resolution between data and simulation, where the resolution is estimated as σ/μ. The mass (or momentum) resolution is below 1% in both data and simulation, and the differences in quadrature are 0.15–0.40%. No corrections and no uncertainties are applied.

Statistical uncertainty due to limited MC sample For the processes estimated from simulation, the available number of events in the MC samples limits the precision of the modeling. The statistical uncertainty on the event yield in each search bin, corresponding to the sum in quadrature of the MC event weights is taken into account for the final limit computation.

Other minor systematic uncertainties

JEC and JER The uncertainty in the calibration of the jet energy scale, as well as the jet energy resolution in simulation, affect directly the veto on b jets with $p_T > 25$ GeV. The uncertainties on jet energy scale and resolution are estimated by scaling independently the energy of jets up and down by one standard deviation; this results in uncertainties on the final signal yields of about 0–5% for the energy scale and 0–3% for the energy resolution, mostly around the lower side of these ranges, but occasionally larger deviations happen in lower statistics search regions. This includes the effect of the migration of events from one search region to another.

b tagging The efficiency of the b jet veto is corrected for the difference between data and simulation. The resulting uncertainty is found to be below 1% for all search regions.

7.6.2 Uncertainties on the background data-driven predictions

The background consisting of fake leptons is estimated using data-driven techniques as described in Section 7.4.2. The general features of the method were validated in simulation (Figure 7.12) as a function of the search variables. A very detailed validation is performed in each lepton channel and in each search category separately, using four data control samples. Although the limited number of events in the high displacement regions does not allow for a precise validation, we find that in regions where enough events are available the method checks out fairly well. Based on the agreement between predictions and observations in these data control samples and simulation, we assessed the uncertainties as follows:

- 30% for all channels flat;
- additional 50% uncorrelated nuisance for the highest displacement bin and the $M(\ell_2, \ell_3) >$ 4 GeV bins;
- 3 additional uncorrelated nuisances ($\mu\mu$, $e\mu$ and ee) to account for the differences in sources and statistics between the 3 channels in the DOUBLE-FAKE-RATE measurement region.

The 30% covers all the discrepancies we observe in our control region closure and 50% is motivated by the lack of statistics in the control regions for the closure test. The closure tests in simulation and data in each data-taking period show no particular dependence on the different data-taking periods, as such we consider the 30% and 50% systematic uncertainties correlated overall data-taking period and lepton channels, while the additional 3 flavor systematics are taken uncorrelated among the channels and the years. ($\mu\mu$, $e\mu$ and ee. For 2016 17, 20, 40 %, for 2017 14, 14, 33 % and for 2018 10, 11, 25 %).

Concerning the eee and $\mu\mu e$ channels, where we observe a large discrepancy in the largest displacement region in the data control region, we performed convincing studies to prove that the origin of it is not the nonprompt lepton background, but rather the photon conversion background. The main evidence is that the excess in data only appears in channels with at least one displaced electron (from $\gamma \to ee$). In these events, the three leptons form a mass peak in the proximity of the Z boson mass. The contribution from conversions in the signal region, however, is expected to be very small, because of the $M_{3\ell}$ upper bound at 80 GeV.

The statistical uncertainty in the predicted fake lepton background in the majority of search regions is driven by the limited amount of data in the application region. This uncertainty is propagated to the signal region and modeled using Gamma distributions, with a shape parameter $\alpha = 1 +$ the number of events in the application region, and a scale parameter θ equal to the average FR for each bin. If no events are observed in the application region, the uncertainty is set to the standard deviation of a Gamma distribution with $\alpha = 1$ and θ equal to the maximum measured fake rate in the corresponding channel.

7.7 Results

The two variables which are used to classify the selected events are Δ_{2D} and $M(\ell_2, \ell_3)$. In Figure. 7.28, the comparison between the number of observed data events and their background predictions is shown.

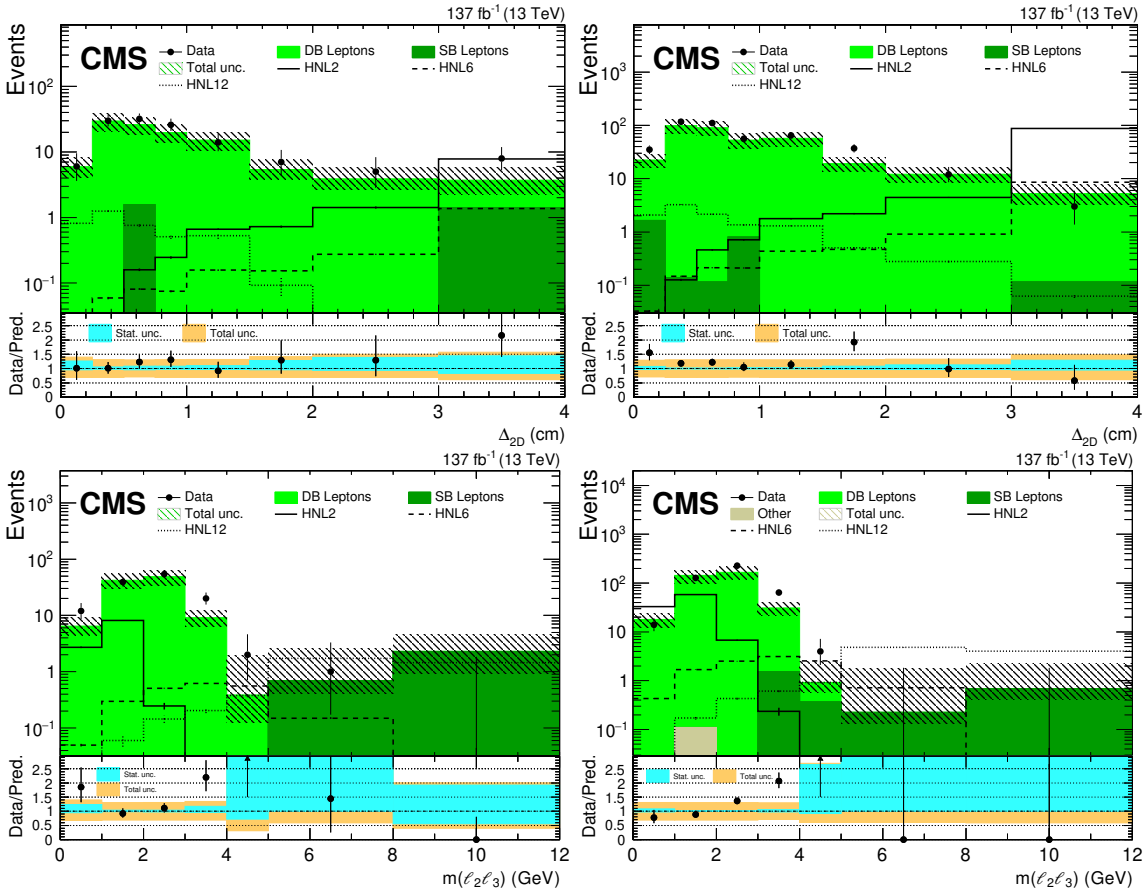

FIGURE 7.28: Comparison between the number of observed events in data and their background predictions (shaded histograms, stacked) for the Δ_{2D} variable in eeX (top-left) and $\mu\mu$X (top-right) final states and for the $M(\ell_2, \ell_3)$ variable in eeX (bottom-left) and $\mu\mu$X (bottom-right) final states. Predictions for signal events are shown for several benchmark hypotheses for Majorana HNL: $M_N = 2$ GeV and $|V_{\ell N}|^2 = 0.8\times10^{-4}$ (HNL2), $M_N = 6$ GeV and $|V_{\ell N}|^2 = 1.3\times10^{-6}$ (HNL6), $M_N = 12$ GeV and $|V_{\ell N}|^2 = 1.0\times10^{-6}$ (HNL12). Events in the overflow bin are included in the last bin.

The predictions and observations in each of the search regions are shown in Figure 7.29. Only cases where the HNL mixes with a SM neutrino flavor per time are considered in this scenario, i.e., only one of $|V_{eN}|^2$ and $|V_{\mu N}|^2$ is nonzero (see Section 5.3). Thus, the eeX channels (eee, $e^{\pm}e^{\mp}\mu^{\pm}$, and $e^{\pm}e^{\pm}\mu^{\mp}$) are sensitive to the $|V_{eN}|^2$ mixing parameter, while the $\mu\mu$X channels ($\mu\mu\mu$, $\mu^{\pm}\mu^{\mp}e^{\pm}$, and $\mu^{\pm}\mu^{\pm}e^{\mp}$) are sensitive to $|V_{\mu N}|^2$.

The yields of the observed events in data show a good agreement with the SM background expectations. The agreement is within the statistical and systematic uncertainties and no significant excess with respect to the SM background predictions is found. The number of events for both observed data and background yields is shown in Tables 7.11 and 7.12. The

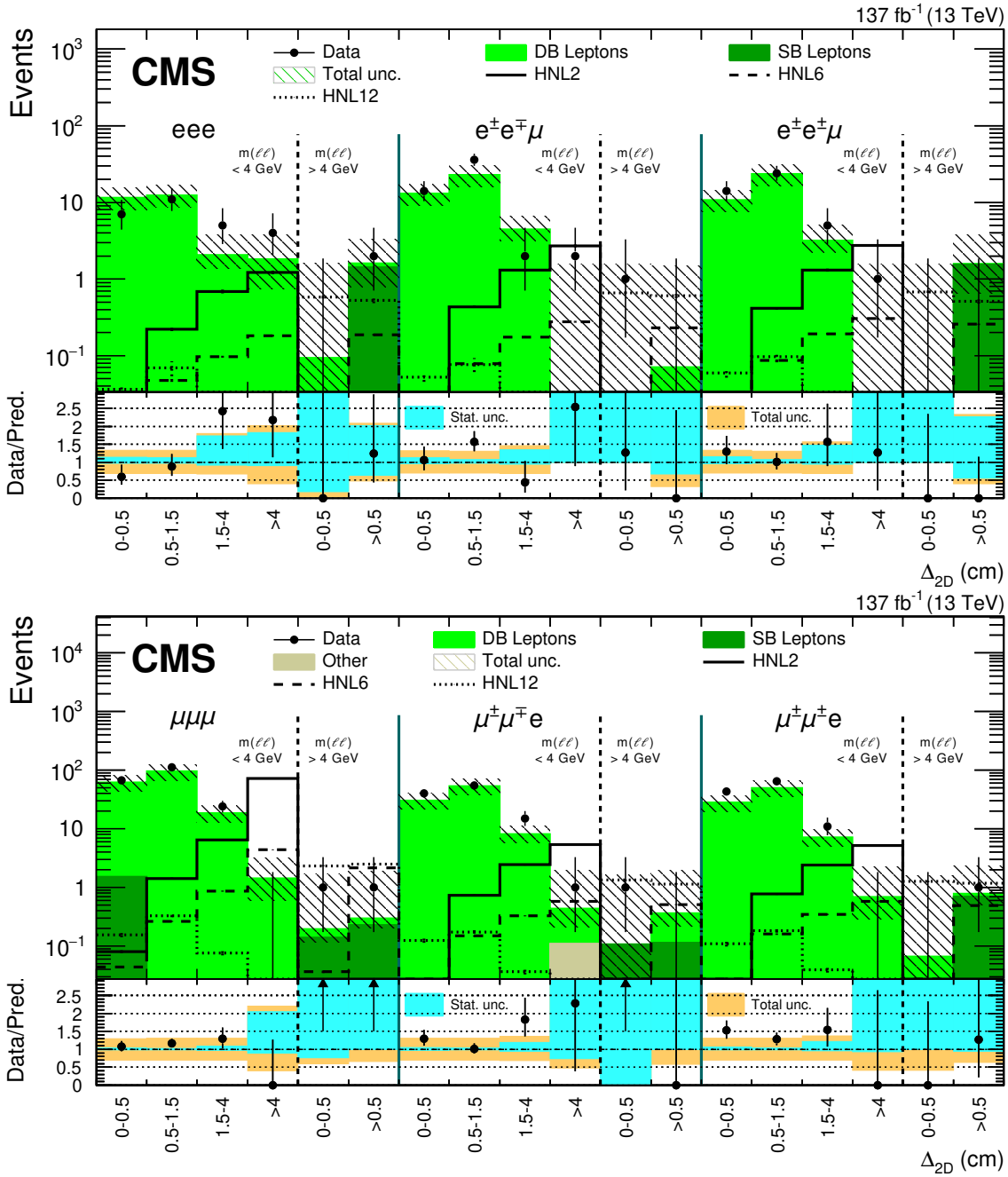

FIGURE 7.29: Predicted and observed yields in the different search regions for (upper) eeX and (lower) $\mu\mu$X final states, compared to one HNL signal scenario with nonzero $|V_{eN}|^2$ and $|V_{\mu N}|^2$ parameter, respectively. The predictions for signal process are obtained assuming Majorana HNL. Predictions for signal events are shown for several benchmark hypotheses: $M_N = 2$ GeV and $|V_{\ell N}|^2 = 0.8\times10^{-4}$ (HNL2), $M_N = 6$ GeV and $|V_{\ell N}|^2 = 1.3\times10^{-6}$ (HNL6), $M_N = 12$ GeV and $|V_{\ell N}|^2 = 1.0\times10^{-6}$ (HNL12). The uncertainty band assigned to the background prediction includes statistical and systematic contributions.

quoted uncertainties include statistical and systematic uncertainties.

TABLE 7.11: Number of predicted and observed events in the eeX final states.

$M(\ell_2,\ell_3)$ (GeV)		<4			>4		
Δ_{2D} (cm)		<0.5	0.5–1.5	1.5–4	>4	<0.5	>0.5
eee	Data	7	11	5	4	0	2
	Background	$11.6^{+3.9}_{-3.6}$	$12.5^{+4.2}_{-3.9}$	$2.1^{+1.7}_{-0.7}$	$1.8^{+1.9}_{-1.1}$	$0.1^{+1.5}_{-0.1}$	$1.6^{+1.7}_{-0.8}$
$e^{\pm}e^{\mp}\mu^{\pm}$	Data	14	36	2	2	1	0
	Background	$13.1^{+4.3}_{-4.0}$	$23.0^{+7.2}_{-7.0}$	$4.5^{+2.1}_{-1.4}$	$0^{+1.6}_{-0.0}$	$0^{+1.6}_{-0.0}$	$0.1^{+1.5}_{-0.0}$
$e^{\pm}e^{\pm}\mu^{\mp}$	Data	14	24	5	1	0	0
	Background	$10.8^{+3.6}_{-3.3}$	$23.8^{+7.4}_{-7.3}$	$3.2^{+1.8}_{-1.0}$	$0^{+1.6}_{-0.0}$	$0^{+1.6}_{-0.0}$	$1.6^{+2.1}_{-0.9}$

TABLE 7.12: Number of predicted and observed events in the $\mu\mu$X final states.

$M(\ell_2,\ell_3)$ (GeV)		<4			>4		
Δ_{2D} (cm)		<0.5	0.5–1.5	1.5–4	>4	<0.5	>0.5
$\mu\mu\mu$	Data	67	112	24	0	1	1
	Background	$62.1^{+18.5}_{-18.4}$	$95.7^{+29.0}_{-29.0}$	$18.6^{+5.9}_{-5.6}$	$1.4^{+1.7}_{-0.9}$	$0.2^{+1.5}_{-0.1}$	$0.3^{+1.6}_{-0.1}$
$\mu^{\pm}\mu^{\mp}e^{\pm}$	Data	40	55	15	1	1	0
	Background	$30.8^{+9.5}_{-9.3}$	$54.1^{+16.4}_{-16.4}$	$8.2^{+3.0}_{-2.6}$	$0.4^{+1.5}_{-0.2}$	$0.1^{+1.6}_{-0.1}$	$0.4^{+1.6}_{-0.2}$
$\mu^{\pm}\mu^{\pm}e^{\mp}$	Data	43	64	11	0	0	1
	Background	$28.2^{+8.7}_{-8.5}$	$50.1^{+15.3}_{-15.2}$	$7.2^{+2.7}_{-2.2}$	$0.7^{+1.6}_{-0.4}$	$0.1^{+1.6}_{-0.0}$	$0.8^{+1.5}_{-0.3}$

The yields of expected HNL signal events for a set of benchmark signal models are listed in Table 7.13. The quoted uncertainties include statistical and systematic uncertainties.

TABLE 7.13: The number of predicted signal events in the eeX and $\mu\mu$X final states. The results are presented for several benchmark signal hypotheses for Majorana HNL: $M_N = 2$ GeV and $|V_{\ell N}|^2 = 0.8\times10^{-4}$ (HNL2), $M_N = 6$ GeV and $|V_{\ell N}|^2 = 1.3\times10^{-6}$ (HNL6), $M_N = 12$ GeV and $|V_{\ell N}|^2 = 1.0\times10^{-6}$ (HNL12).

$M(\ell_2,\ell_3)$ (GeV)		<4			>4		
Δ_{2D} (cm)		<0.5	0.5–1.5	1.5–4	>4	<0.5	>0.5
HNL2	eee	0	0.22 ± 0.02	0.69 ± 0.06	1.20 ± 0.12	0	0
	$e^{\pm}e^{\mp}\mu^{\pm}$	0.01 ± 0.00	0.43 ± 0.03	1.30 ± 0.10	2.70 ± 0.25	0	0
	$e^{\pm}e^{\pm}\mu^{\mp}$	0.01 ± 0.00	0.41 ± 0.03	1.30 ± 0.10	2.70 ± 0.26	0	0
HNL6	eee	0	0.05 ± 0.00	0.10 ± 0.01	0.18 ± 0.01	0	0.19 ± 0.01
	$e^{\pm}e^{\mp}\mu^{\pm}$	0.01 ± 0.00	0.08 ± 0.01	0.17 ± 0.01	0.28 ± 0.02	0	0.23 ± 0.02
	$e^{\pm}e^{\pm}\mu^{\mp}$	0.02 ± 0.00	0.09 ± 0.01	0.19 ± 0.01	0.30 ± 0.03	0.01 ± 0.00	0.26 ± 0.02
HNL12	eee	0.04 ± 0.01	0.07 ± 0.01	0	0	0.58 ± 0.04	0.53 ± 0.06
	$e^{\pm}e^{\mp}\mu^{\pm}$	0.05 ± 0.01	0.08 ± 0.02	0	0	0.66 ± 0.05	0.60 ± 0.06
	$e^{\pm}e^{\pm}\mu^{\mp}$	0.06 ± 0.01	0.10 ± 0.02	0	0	0.68 ± 0.05	0.51 ± 0.05

$M(\ell_2,\ell_3)$ (GeV)		<4			>4		
Δ_{2D} (cm)		<0.5	0.5–1.5	1.5–4	>4	<0.5	>0.5
HNL2	$\mu\mu\mu$	0.08 ± 0.01	1.40 ± 0.09	6.50 ± 0.41	73.00 ± 7.40	0	0
	$\mu^{\pm}\mu^{\mp}e^{\pm}$	0.02 ± 0.00	0.73 ± 0.05	2.50 ± 0.17	5.40 ± 0.47	0	0
	$\mu^{\pm}\mu^{\pm}e^{\mp}$	0.02 ± 0.00	0.78 ± 0.05	2.40 ± 0.16	5.20 ± 0.46	0	0
HNL6	$\mu\mu\mu$	0.04 ± 0.00	0.27 ± 0.02	0.87 ± 0.05	4.40 ± 0.45	0.04 ± 0.00	2.20 ± 0.19
	$\mu^{\pm}\mu^{\mp}e^{\pm}$	0.03 ± 0.00	0.15 ± 0.01	0.33 ± 0.02	0.58 ± 0.05	0.02 ± 0.00	0.51 ± 0.03
	$\mu^{\pm}\mu^{\pm}e^{\mp}$	0.03 ± 0.00	0.16 ± 0.01	0.35 ± 0.02	0.58 ± 0.04	0.02 ± 0.00	0.50 ± 0.03
HNL12	$\mu\mu\mu$	0.15 ± 0.02	0.33 ± 0.02	0.08 ± 0.01	0	2.30 ± 0.17	2.50 ± 0.14
	$\mu^{\pm}\mu^{\mp}e^{\pm}$	0.13 ± 0.01	0.18 ± 0.02	0.04 ± 0.00	0	1.30 ± 0.08	1.10 ± 0.07
	$\mu^{\pm}\mu^{\pm}e^{\mp}$	0.11 ± 0.01	0.18 ± 0.02	0.04 ± 0.01	0	1.30 ± 0.08	1.20 ± 0.07

7.7.1 Interpretation

At this stage, it is relevant to recall the distinction between Majorana and Dirac particles explained in Section 4.2.2.1. An important difference between the two HNL natures concerns the decay widths (as explained in Section 4.2.2.3):
$\Gamma_{\mathrm{N}}^{Tot,\,Majorana} = 2 \times \Gamma_{\mathrm{N}}^{Tot,\,Dirac}$, and then consequently $c\,\tau_{\mathrm{N}}^{Tot,\,Majorana} = \frac{1}{2} \times c\,\tau_{\mathrm{N}}^{Tot,\,Dirac}$.
This last difference has a direct impact on the final signal yields in two unambiguous ways; first, in Dirac scenarios LNV categories ($\mu^{\pm}\mu^{\pm}e$ and $e^{\pm}e^{\pm}\mu$) have zero signal events, while LNC categories ($\mu^{\pm}\mu^{\mp}e$ and $e^{\pm}e^{\mp}\mu$) have twice the number of signal events than Majorana scenarios. Furthermore, Dirac HNLs have longer lifetimes and the decay SVs are more displaced. This, on the one hand, leads to a smaller acceptance, due to a lower reconstruction efficiency. On the other hand, it also leads to a shift of signal events from small displacement bins to larger displacement bins, increasing the S/B ratio.

Distinct treatments for Majorana and Dirac interpretations are then necessary.

7.7.1.1 Statistical analysis

Given the expected background yields and the observed yields in all search regions, we can test the exclusion of different HNL signal scenarios by computing the excluded cross-section for each $(M_{\mathrm{N}}, |\mathrm{V}_{\ell\mathrm{N}}|^2)$ hypothesis. In order to obtain the correct excluded regions in the $(M_{\mathrm{N}}, |\mathrm{V}_{\ell\mathrm{N}}|^2)$ parameter space, however, we need to extrapolate the calculated limits across different points in the $|\mathrm{V}_{\ell\mathrm{N}}|^2$ axis. As explained in Section 5.3.1.1, varying the mass and mixing probability of the HNL does not only change its production cross section, but also its kinematics and acceptance. Therefore, the excluded signal strength computed for a given $(M_{\mathrm{N}}, |\mathrm{V}_{\ell\mathrm{N}}|^2)$ value ($\mu = \sigma_{\mathrm{excl}}/\sigma_{\mathrm{theor}}$) only tells us whether that specific point is excluded ($\mu \leq 1$) or not ($\mu > 1$), but it cannot be interpreted as an excluded cross-section. Instead, we need to employ the event-by-event re-weighting method described in Section 5.3.1.1 to emulate HNLs of the same mass and different $|\mathrm{V}_{\ell\mathrm{N}}|^2$, until we find the exact $|\mathrm{V}_{\ell\mathrm{N}}|^2$ value for which $\mu = 1$.

Limits are calculated with the modified frequentist construction $\mathrm{CL_S}$ with a binned profile likelihood test statistic, using the bins of Figures 7.29. This fit is performed in the asymptotic approximation [171]. The likelihood is constructed using the observed data yields and the signal and background expectations obtained from simulation or from data-driven methods, along with nuisance parameters that encode the effect of the systematic uncertainties associated with the estimated yields, including possible effects on the shapes of the kinematic distributions.

Limits on V_{Nl}: Majorana HNL. Limits on $|\mathrm{V}_{\mathrm{eN}}|^2$ and $|\mathrm{V}_{\mu\mathrm{N}}|^2$ as a function of M_{N} for a Majorana HNL are shown in Figure 7.30 for the Run2 data set.

Limits on V_{Nl}: Dirac HNL. Limits on $|\mathrm{V}_{\mathrm{eN}}|^2$ and $|\mathrm{V}_{\mu\mathrm{N}}|^2$ as a function of M_{N} for a Dirac HNL are shown in Figure 7.31 for the Run2 data set.

The simulation of Dirac HNL scenarios is obtained from the samples used for the Majorana HNL interpretation, by applying appropriate lifetime corrections, as explained in Section 5.3.1.2. As a result, the Majorana and Dirac HNL simulations used for the limit

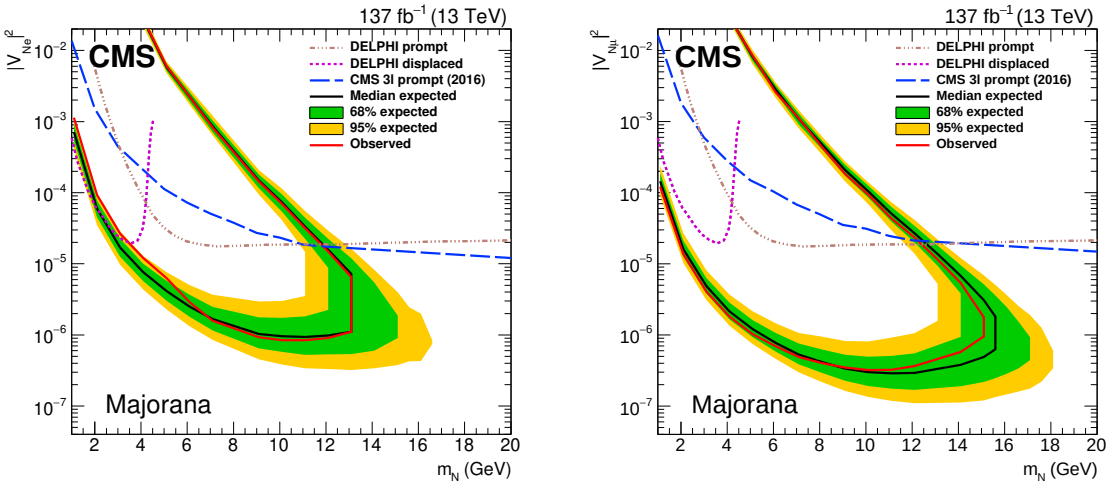

FIGURE 7.30: Limits on $|V_{eN}|^2$ (left) and $|V_{\mu N}|^2$ (right) as functions of M_N for a Majorana HNL. Results from the DELPHI [121] and the CMS [151] Collaborations are shown for reference.

computation are statistically correlated, which may lead to similar statistical fluctuations in the exclusion curves in the two interpretations.

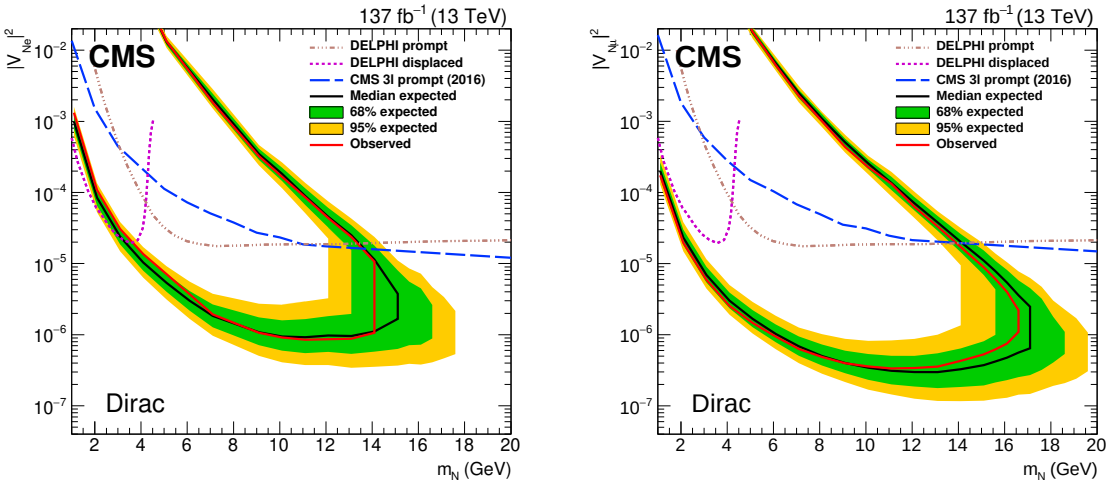

FIGURE 7.31: Limits on $|V_{eN}|^2$ (left) and $|V_{\mu N}|^2$ (right) as functions of M_N for a Dirac HNL. Results from the DELPHI [121] and the CMS [151] Collaborations are shown for reference.

In the Dirac HNL scenario, we exclude electron (muon) couplings of 1.0×10^{-4} (2.0×10^{-5}) and higher for a HNL mass of 2 GeV, and of 0.7×10^{-7} (2.5×10^{-8}) for a HNL mass of 12 GeV.

In the Majorana HNL scenario, the exclusion limits are slightly less stringent. For the case of muon couplings, the limits in both scenarios improve significantly with respect to the results of the DELPHI [121] and CMS [151] Collaborations. For the case of electron couplings, the limits improve with respect to the DELPHI results for masses above about 3.5 GeV.

7.8 Summary

In this chapter, the search for long-lived heavy neutral leptons with displaced vertices is presented. The analysis is completed using data collected from the CMS experiment in the years 2016 – 18 corresponding to an integrated luminosity of 137 fb^{-1}.
At the moment of this thesis drafting, the results have been made public by the CMS collaboration after passing a series of scrutiny processes and the publication is going to be submitted soon to Journal of High Energy Physics (JHEP). The public results can be accessed in Ref. [172].

The experimental signature consists of one prompt charged lepton and two displaced charged leptons in any flavor combination of electrons and muons. Two interpretations are proposed considering on one hand uniquely the Dirac HNL nature, on the other hand, the Majorana HNL nature. No statistically significant deviation from the expected SM background was observed. At 95% confidence level limits were set on the mixing parameters $|V_{eN}|^2$ and $|V_{\mu N}|^2$. The excluded values are in the ranges between 3×10^{-7} and 1×10^{-3} for masses included between 1 GeV $< m_N <$ 15 GeV.

The analysis makes use of dedicated techniques to select leptons associated with long-lived HNL decays. Great effort was given to quantify the reconstruction efficiency and the acceptance phase space for displaced leptons and secondary vertices. Several innovative methods were exploited to get proper predictions of the significant background processes from control samples in data. Background estimation undeniably represents one of the decisive challenges in this type of search at the hadron collider.
Cases with LNV and LNC events are handled in separate ways in order to compute the final limits in Majorana and Dirac scenarios. By applying appropriate lifetime corrections, the simulated samples of the Dirac HNL scenarios are fetched from the samples adopted for the Majorana HNL interpretation.

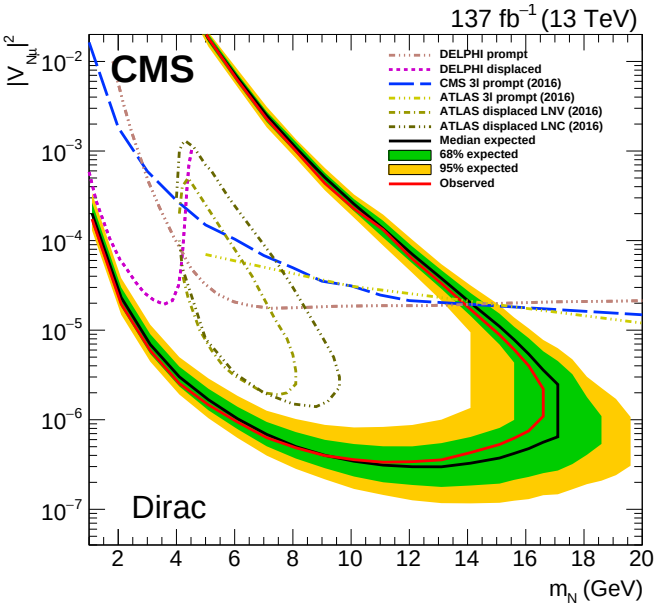

FIGURE 7.32: Limits on $|V_{\mu N}|^2$ as functions of M_N for a Dirac HNL. Results from the DELPHI [121], the CMS [151] and ATLAS [173] Collaborations are shown for reference.

At the time of the writing, these current results are the most stringent limits on this type of process in the explored parameter space of the HNL production. The two direct comparisons are the DELPHI [121] and ATLAS [173] results.
DELPHI Collaboration performed HNL searches using the data corresponding to 3.3×10^6 hadronic Z_0 decays at LEP1, see Section 4.3.1. This set of results includes both the short-lived HNL and the long-lived HNL and all three lepton flavor couplings. For the long-lived HNL case, it was looked

for detectable secondary vertices or calorimeter clusters. Upper limits were set for the branching ratio $BR(Z_0 \to \mathrm{N})$ of about 1.3×10^{-6} at 95% C.L. for N masses between 1 and 15 GeV for a mean decay length of 100 cm for a $m_{\mathrm{N}} = 3$ GeV.

The second comparison is made with the relatively recent ATLAS results [173] which are marked in chartreuse in Figure 7.32 for an easier juxtaposition. The search used data corresponding to an integrated luminosity of 32.9 fb^{-1} ([4]); it looked for HNLs produced through mixing with muon neutrinos only. The desired signature consists of one prompt muon and SVs with either $\mu\mu$ or μe pairs. The considered displacements are located in the transverse plane by 4-300 mm from the PV. The results set limits on the $|\mathrm{V}_{\mu\mathrm{N}}|^2$ for HNL masses 4.5-10 GeV.
Some techniques of the ATLAS's analysis gave us several useful insights regarding the displaced tracking and vertexing efficiency. The use of $K^0_S \to \pi\pi$ events was also adopted by CMS analysis to model of displaced tracks and SV reconstruction, see Section 7.5.4.

Several people were involved in the completion of the long-lived HNL analysis.
The analysis presented in this chapter was performed in the context of CMS collaboration, with leading contributions from the several members of the UGent CMS team.
I was the main analyzer responsible for designing the entire analysis from the beginning to the writing of the journal publication. I performed the measurement of the lepton FAKE-RATE and DOUBLE-FAKE-RATE and their validation in both MC and data. I produced the final results in the search regions and control regions. I also gave most of the internal CMS presentations on the topic, including the so-called pre-approval and approval talks.

Conference talks and workshops

I have presented the results in different various occasions:

- "Sterile neutrino searches at LHC and CMS", talk at WP5 meeting, 26 November 2018, Antwerp (Belgium);
- "HNL experimental overview", talks Searching for long-lived particles at the LHC: firth workshop of the LHC LLP Community, 27-29 May 2019, CERN (Switzerland);
- "Neutral Long-Lived Particle Search", plenary at DM LHC 2019, 13-16 Aug 2019, University of Washington (United States);
- "HNL experimental overview", plenary at EOS winter Solstice meeting, 19 Dec 2019, Brussels (Belgium);

I have actively participated in five *LHC LLP Community* workshops. My contribution was specifically in the HNL search working group. As result of the great discussions and consultations, a white paper came out "Searching for long-lived particles beyond the Standard Model at the Large Hadron Collider" [174] of which I am an author. In November 2019 we hosted and organized the winter edition of the workshop at UGent university.

[4] Novel with respect to standard ATLAS analyses is the employment of a dedicated algorithm called Large-radius tracking, LRT, which is run on a smaller dataset of pre-selected events. So the 32.9 fb^{-1} with respect to the 35.9 fb^{-1} of the standard analyses.

Chapter 8

Conclusions

Searches for heavy neutral leptons in events with three charged leptons, either from a common vertex or with two leptons forming a displaced secondary vertex are presented. The published results can be found in Ref. [151] and [172], respectively.

8.1 Summary

The observation of neutrino flavor oscillations was one of the first definite experimental indications of the presence of new physics not described by the SM theory. Thus, the comprehension of the mechanism behind the neutrino masses would be an essential guide for the development of new BSM physics models. Therefore, it is crucial for the LHC experiments to investigate the signatures of all possible neutrino mass models to try spotting the mysterious new physics.
The two results presented in this thesis cooperate in the arduous attempt of confronting exotic BSM models with the experimental data. The aspiration is to experimentally observe new particles able to describe the unexplained physics observations not covered by the SM.

Our studies focus on the concept of right-handed (RH) neutrinos as implemented in heavy neutral lepton (HNL) models. The introduction of massive RH neutrinos provides an answer to the problem of the neutrino masses via the seesaw mechanism. In Chapters 1 and 4, we illustrated the relevance and the interest for the ongoing HNL search program, describing first the theory setting and then mentioning the various experiments and results focusing on HNL signatures.
When we hypothesize new particles as RH neutrinos, N, we are interested in their properties like the mass m_{N} and their mixing parameter, $|V_{\alpha \mathrm{N}}|^2$, with the SM neutrino of flavor α, related to the Yukawa coupling $F_{\alpha \mathrm{N}}$. The values of $|V_{\alpha \mathrm{N}}|^2$ are unknown. The measured experimental sensitivities are expressed in terms of the coupling $|V_{\alpha \mathrm{N}}|^2$ as a function of m_{N} for a given flavor α.

Furthermore, we introduced a list of direct HNL search results; we give an overview of the past and current experimental landscape describing the different decay modes and mass ranges that are targeted by single measurements. The strategies adopted in direct HNL searches vary greatly with the mass range under investigation. For $m_{\mathrm{N}} > 5$ GeV, N can be produced uniquely at high-energy particle colliders like the LHC, via different possible mechanisms (vector boson fusion, s-channel exchange of virtual W-bosons or in real gauge boson decays) according to the production energy and N mass. For $m_{\mathrm{N}} < 5$ GeV, we recur to b-factories or fixed-target experiments.

Special attention is paid to lepton and hadron collider searches. The LEP results from DELPHI provide the best results at low mass from collider experiments up to the publication of the results of this dissertation. The outstanding sensitivity at low mass from e^+e^- data was surely a good motivation to invest into extending the low mass sensitivity of the CMS experiment as well.

Chronologically, we have focused first on the moderate and high mass search and then migrated to the very low mass search which necessarily requires the inclusion of scenarios with displaced decays.

During my first PhD year, I worked on the "search for heavy neutral leptons in events with three charged leptons in proton-proton collisions at $\sqrt{s} = 13$ TeV" [151]. No statistically significant excess of signal events over the expected SM background was observed. At 95% confidence level, upper limits were set on the mixing parameters $|V_{eN}|^2$ and $|V_{\mu N}|^2$. The excluded values are in the ranges between 1.2×10^{-5} and 1.8 for masses between 1 GeV $< m_N <$ 1.2 TeV. These were the first direct limits for HNL masses above 500 GeV and the first limits obtained at hadron colliders for HNL masses below 40 GeV. At large HNL masses, the results improved with respect to those previously published by the ATLAS [157] and CMS [123, 158] experiments.

The remaining time of my PhD was dedicated to the "Search for long-lived heavy neutral leptons with displaced vertices in pp collisions at $\sqrt{s} = 13$ TeV" [172]. The signature consists of one prompt charged lepton and two displaced charged leptons in any flavor combination of electrons and muons. Two interpretations are proposed, considering on the one hand uniquely the N with Dirac nature, and on the other hand the N with Majorana nature. No statistically significant deviation from the expected SM background was observed. At 95% confidence level, limits were set on the mixing parameters $|V_{eN}|^2$ and $|V_{\mu N}|^2$. The excluded values are in the ranges between 3×10^{-7} and 1×10^{-3} for masses included between 1 GeV $< m_N <$ 15 GeV.

The opportunity to work on such complementary analyses allowed me to gain over the years considerable expertise in HNL searches with multi-lepton final states at CMS.
The highlights were the LL-HNL workshops (in 2017 at CERN, in 2018 at CERN and Amsterdam, in 2019 CERN and Ghent) where I had the pleasure of actively participating. They gave me the chance to explore the state-of-the-art of HNL models and results in particular with LLP signatures [174]. Furthermore, we identified new open questions, emphasized the priority of complementary and synergetic searches, and formulated new search strategies and new opportunities for discovery. The results of our discussions were published in a white paper [174].

Before introducing the exciting prospects for future HNL searches, some suggestions can be brought up for the forthcoming editions of long-lived N searches at CMS.
The results discussed in Chapter 7 are the best that could be obtained taking into account the limitations encountered. Nevertheless, a few improvements can be implemented and additional features included in future analysis strategies. The first compelling and straightforward revision would be on the limited available MC statistics for both signal and background samples. The number of events in the MC samples limits the precision of the modeling and the statistical uncertainty taken as a systematic uncertainty plays a major role

in the final results. Moreover, a larger number of background MC events would help in the low mass region to properly represent the contribution from photon conversion background. Furthermore, an advantageous upgrade comes from the new reconstruction algorithms that have been introduced during Run2 including displaced muons among the PF elements. The most important feature is the removal of constraints on the interaction point in muon reconstruction. The deployment of the two new algorithms, *Displaced Standalone Muon* and *Displaced Global Muon* [79], could increase the total reconstruction efficiency for displaced dimuon events by one order of magnitude. Taking into account the limited analysis acceptance at very low HNL mass, this integration will result in a sizable change in the final sensitivity.
Finally, the DOUBLE-FAKE-RATE (f_{D}) measurement can be improved further. Low statistics and numerous f_{D} dependencies pose a few challenges to the conventional tight-to-loose method: for n f_{D} parameters, an n-dimensional quotient histogram is created dividing the tight selection by the FO selection. In order to deal with these shortcomings, a possibility could be a new background estimation developed by reformulating the f_{D} measurement as a classification problem for a deep neural network.
These examples give a feeling of the possible improvements that could be added to the long-lived HNL analysis.

In the next section, the latest sensitivity estimations and expected experimental results in the near future are presented. Finally, an overview of possible future experiments and detector upgrades is given.

8.2 Outlook

It is abundantly clear that HNLs are one of the most exciting and well-motivated potential solutions for some of the outstanding problems of the SM. However, if they happen to exist, their Majorana/Dirac natures, their masses, and their coupling with the SM neutrinos are far from obvious and clear. Thus, we need to adopt a comprehensive and vast approach in searches for HNL probing heavy neutral leptons with MeV- and TeV-scale masses.

For HNLs in the GeV-TeV mass range, we enter the domain of particle colliders and we are looking for promptly decaying HNLs. In this phase space, we find several new results with promising new search strategies.

Recently, at CMS a search for right-handed bosons (W_R) and RH neutrinos in the left-right symmetric model extension of the SM [175] has been carried out using pp collision data collected at $\sqrt{s} = 13$ TeV and corresponding to 137 fb^{-1} integrated luminosity. The signature consists of events with two same-flavor light leptons and two quarks. For $m_{\mathrm{N}} = m_{W_R}/2$ ($m_{\mathrm{N}} = 200$ GeV), the mass of the W_R is excluded at 95% CL up to 4.7 (4.8) and 5.0 (5.4) TeV for the electron and muon channel, respectively.

At the time of the publication of the analysis presented in Chapter 6, the results were positively received by the community and highly appreciated for the big effort that was put into widening the mass range and improving the sensitivity previously obtained. The data correspond to an integrated luminosity of 35.9 fb^{-1} collected in 2016. Thus, it is desirable to perform the same search on the full available dataset which corresponds to an integrated

luminosity of 137 fb^{-1}.
The analysis is being carried out by a UGent colleague (L. Wezenbeek) who plans not only to integrate the larger data set but to also improve some selection strategy aspects to increase the quality of the final results. In particular, if we recall well one of the largest background of the 2016 analysis [151] is the contribution with nonprompt leptons. The updated lepton selection makes use of a new machine learning based lepton identification algorithm which was developed to be optimal at rejecting nonprompt leptons [1]. The algorithm exploits the characteristics of the jet containing the lepton, and puts together all variables that discriminate between prompt and nonprompt leptons with a machine learning algorithm. It results in an increase in efficiency per lepton of 20% and for the same signal efficiency a reduction of the nonprompt background by factor 10%, when compared to standard algorithms. Although the rest of the analysis workflow is going to be very similar to what was published in 2018, the advancements done in reducing the major background, possible progress in signal categorization and the triple amount of data will bring sizable change in the final sensitivity.

In the same analysis framework and timeline, a new exciting addition is going to be included. For the first time at CMS, the mixing between HNL and tau neutrinos is going to be probed. In Figure 4.7, the necessity to dedicate some effort in searches sensitive to tau neutrino-HNL couplings, $|V_{\tau N}|^2$, is indisputable. The ongoing analysis effort will include events with one or two hadronically decaying tau leptons in the HNL search. The probed mass range is between 20 GeV and 1 TeV. The main difficulties of these final states are on one hand trying to reduce the considerable nonprompt tau background and improve the S/B ratio; on the other hand, dealing with quite large tau p_T thresholds which automatically exclude a part of the phase space reducing the selection acceptance.
Despite the numerous challenges, estimating the limits for $|V_{\tau N}|^2$ is one of the most important pieces of the big HNL puzzle and a result long-awaited by the theory community.

For future very high HNL mass searches, an interesting suggestion comes from the work presented in Ref. [124]. The final state $N\ell + X \to 3\ell + p_T^{miss} + X$ considered. The authors use as major discriminant techniques a dynamic jet veto (i.e. it depends on the p_T of the highest p_T lepton) and a requirement on the scalar sum of three leptons p_T. At 14 TeV, it appears that the proposed analysis strategy can improve sensitivity by an order of magnitude for $m_N > 150$ GeV at $\mathcal{L} = 300$ fb^{-1} and 3 ab^{-1} when compared to a conventional search for prompt signatures.

Figures 4.5 and 4.6 show that the HNL mass range between 1 GeV and 20 GeV is one the most contend phase space by so many different present and future experiments. This results in quite vigorous competition as well as in a very driving experimental environment. The analysis presented in Chapter 7 sits exactly there.
Along these lines, it makes sense to explore almost one by one the other players with great attention paid to future results and experiments.

In the long-lived HNL scenario, the channel with hadronic W decay can also be probed, i.e. $N\ell \to \ell\ell qq$. The analysis is being carried out by a UGent colleague (B. Vermassen). A search for HNLs is performed using the pp collision data collected by the CMS detector during Run 2. The search targets final states with a prompt lepton, a displaced lepton, a

[1] This machine learning based lepton identification algorithm was originally proposed in the context of the $t\bar{t}H$ analysis [176] and further improved at UGent by Willem Verbeke and deployed later in several outstanding analysis [177, 178].

displaced jet, and a secondary displaced vertex. A machine learning technique called Particle Flow Network (PFN) [179] is deployed to improve the separation between signal and background. The output of the PFN classifier is used together with the displacement of the SV and its mass to categorize the search regions. The estimation of the SM background appears to be challenging for reasons similar to the ones explored in this dissertation. The analyzers are going to estimate the background contribution using a data-driven technique and then validate it in data control regions. The final sensitivity will be presented in the two-dimensional $|V_{\ell N}|^2$– m_N plane as for the three lepton final state analyses.

The next groundbreaking moment will happen with the start of **High-Luminosity** LHC, HL-LHC [180]. The project objective is to ramp up the instantaneous luminosity by a factor of 10 further than the LHC's design value (refer to Figure 2.2). Starting from the end of 2027, the HL-LHC will accumulate ten times more data than the LHC is expected to collect until the end of 2024. It will help to detect extremely rare processes and improve the SM precision measurements. Additionally, to fully profit from the increased quantity of data, CMS and the other LHC experiments have launched ambitious detector upgrades.

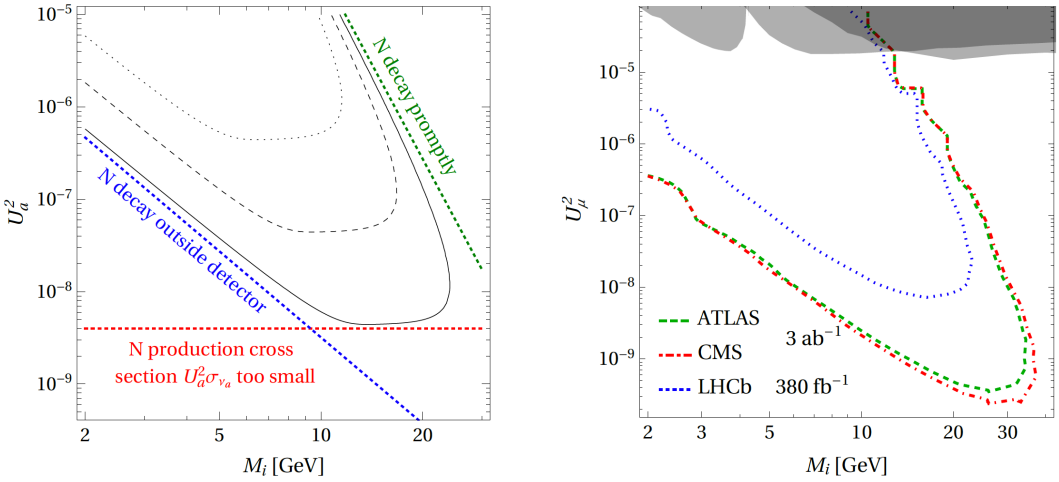

FIGURE 8.1: Left, a scheme illustrating the three main challenges in improving the sensitivity in a displaced analisys. Right, exclusion limits of ATLAS, CMS (3 ab^{-1}) and LHCb (380 fb^{-1}) for the HL-LHC for $|V_{\mu N}|^2$. Both plots are from Ref. [141].

There has been a great number of studies estimating HNL future projections with $\mathcal{L} = 3$ ab^{-1}.
In the research in Ref. [141], the authors inspect the sensitivity of long-lived HNLs produced in ATLAS, CMS, and LHCb detectors at HL-LHC. Furthermore, a new analysis strategy is proposed. To extent the analysis acceptance, the reconstruction using the muon system to identify tracks from the SV is introduced. Even the HNLs decaying outside the tracker volume are considered and included. It was found (Figure 8.1) that the exclusion reach that can be obtained at ATLAS or CMS during HL-LHC surpasses DELPHI's limits [121] by three orders of magnitude for $|V_{\mu N}|^2$ and $|V_{eN}|^2$.

The displaced vertices searches will profit from the programmed ATLAS and CMS detector upgrades for the HL-LHC. They will increase coverage in the forward regions, they will contribute to have better timing and spatial resolutions, and they will add novel features

like track triggers [174].
The subsequent brief descriptions can be extended further in Ref. [181–185].

At the HL-LHC the instantaneous luminosity will be a factor ∼5 higher than the LHC one, with 140-200 pp collisions in each bunch crossing. This harsh environment will make object reconstruction and particle identification more difficult due to tracks coming from nearby vertices making the planned detector upgrades essential. Thus, better coverage in $|\eta|$ and timing and spatial resolution become crucial to separate distinct events from each other.

The CMS inner tracker will have four additional cylindrical layers covering the region with $|z| < 200$ mm with the first layer positioned at 28 mm, and up to twelve endcap disks, which will improve the $|\eta|$ coverage going from the current value of 2.4 to almost 4 (Figure 8.3, left).

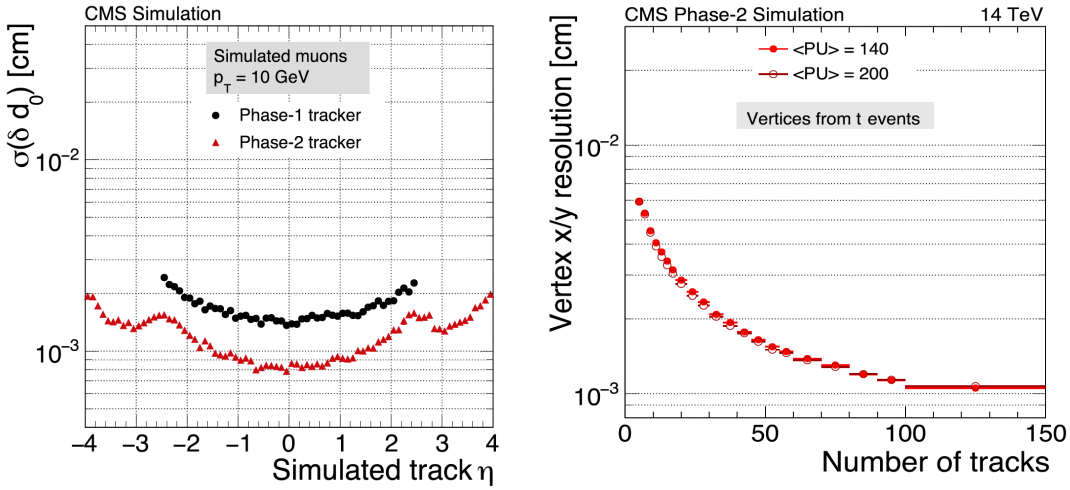

FIGURE 8.2: Left, relative resolution of the transverse impact parameter as a function of the η for the Run2 (black dots) and the HL-LHC (red triangles) CMS tracker, using single isolated muons with p_T of 10 GeV. Right, x and y position resolution of the vertex as a function of the number of tracks associated to the vertex, with two pile-up scenarios [174].

Extra modules will be installed in the CMS outer tracker. Correlating the signals from their sensors, the modules called p_T will be able to identify the hit pairs (named 'stubs') consistent with particles above $p_T = 2$ GeV. Furthermore, these stubs are given as input to the L1 trigger, which enables the L1 trigger to make use of track-finding.

Additional muon chambers will be set up in the endcaps. They will be included in the muon trigger at L1. The supplementary hits in the endcap, with improved algorithms, will allow high trigger efficiency on displaced muon tracks regardless of the high occupancy environment of the HL-LHC.

The CMS MIP timing detector (MTD) will consist in a barrel and an endcap parts formed by a single layer module placed between the tracker and calorimeters covering $|\eta|$ up to ∼3. MTD will improve reconstruction by collecting timing information on charged particles and by combining tracking with timing. The design will provide a timing resolution at the start of HL-LHC of ∼ 30–40 ps for p_T threshold of 0.7 GeV, the timing resolution in

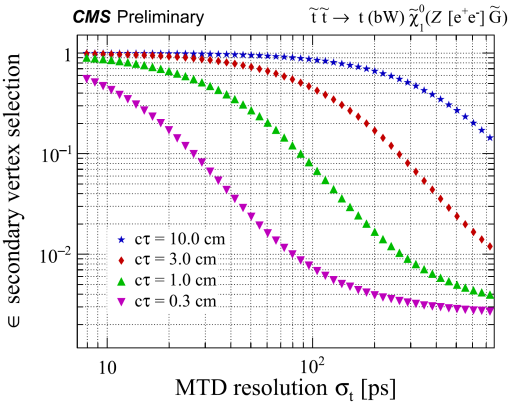

FIGURE 8.3: Efficiency as a function of the timing resolution of the MTD for reconstruction of a specific Supersymmetry model considering events with a separation of PV and SV by more than 3σ in both space and time [174].

the barrel will degrade to 50–60 ps at end of HL-LHC [186]. The introduction of a timing detector will help for the mitigation of pile-up effects.

The CMS detector upgrades for the HL-LHC will globally improve the lepton reconstruction acceptance and efficiency thanks to the wider coverage in the forward regions and the new timing and trigger features. The long-lived HNL search will greatly profit from these developments. Moreover, the timing information can be used as an additional discriminating variable between the HNL signals and backgrounds. Considering the projected time resolution of about 40 ps, the MTD detector would in principle be able to detect the delayed leptons originated from long-lived HNL decays [2].

After exploring the CMS outlook for the next 20 years, we have to satisfy our curiosity and look at the forthcoming experimental landscape. We focus only on the research program for long-lived particles at the LHC, in the specific cases designed to probe HNLs.

The **MATHUSLA** (MAssive Timing Hodoscope for Ultra-Stable neutraL pArticles) experiment will look for long-lived particle with $c\tau \gg 100$ m. MATHUSLA is a

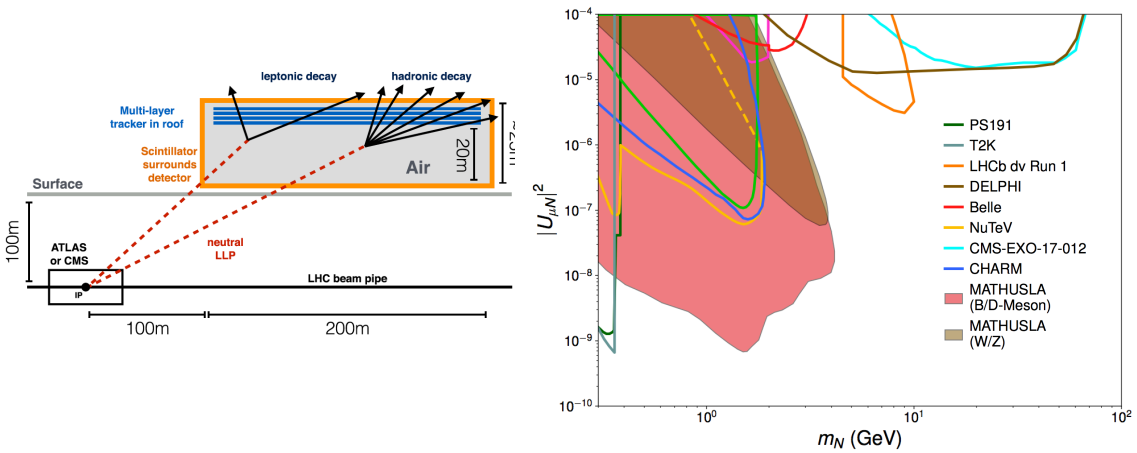

FIGURE 8.4: Left, simplified MATHUSLA detector layout [174]. Right, projected sensitivity in $|V_{\mu N}|^2$- m_N plane for N produced in W/Z decays (brown regions) and in B/D-meson decays (light red region) [187].

large, simple surface detector (see Figure 8.4) able to reconstruct SVs with proper timing resolution. The main part is a tracker array located on top of a 200 m $\times$ 200 m $\times$ 20 m air-filled decay volume.

[2] Flight distance of about 3 m, flight time of $\sim$10 ns for $m_N = 3$ GeV)

The great potential of such experiment comes from the dual geometric and timing requirements. The trajectories of particles coming from displaced vertices are fitted to reconstruct SVs. These SVs must satisfy the rigorous condition that all tracks coincide in time at the SV. These demanding geometric and timing requirements make sure it is very unlikely for backgrounds to mimic the long-lived signals.

MATHUSLA can excellently probe HNLs in a region of phase space close to that reachable with present and future fixed-target experiments like SHiP or DUNE. The derived sensitivity is shown in Figure 8.4 under the plausible assumption of zero background. Compared with CMS and ATLAS projections, it is foreseen that MATHUSLA results will have rather better sensitivity than the main LHC detectors for those HNL mass regimes that suffer from triggering and reconstruction restrictions.

In the central regions of Figures 4.5 and 4.6, there are striking exclusion curves labelled "SHiP". They are obtained by taking into account the reach of the general-purpose fixed target experiment projected at the CERN SPS accelerator, **SHiP** (Search for Hidden Particles) [188,189]. Although it has been decided to conclude the preparation and terminate the project of the facility, it is interesting to give a brief description of the possible contributions it could have given to the HNL hunt.

The principal physics objectives consist of probing SM extensions which include very weakly and long-lived particles by directly detecting their decays to SM particles. In the forward

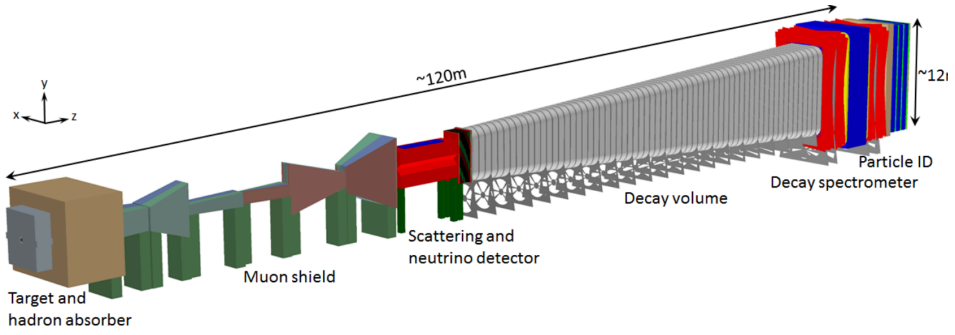

FIGURE 8.5: Schematic overview of the SHiP experiment [190].

region of the SHiP detector, a big and powerful magnetic shield is located conceived to remove all charged particles coming from the beam-target collision. Two complementary parts follow: the "Scattering and Neutrino Detector (SND)", and the "Hidden Sector (HS) spectrometer" [190]. The HS is designed to measure the decays of long-lived particles by reconstructing the SVs. The decays happen in a 50 m long empty decay volume located between SND and HS. The HS is equipped with tracker, timing, calorimeter, and muon detectors.

For HNL mass scenarios < 2 GeV, SHiP would have improved the sensitivity with respect to previous searches [188]. The projections are done considering $|V_{\mu N}|^2$, assuming HNL decays $N \to \mu^- \pi^+$ and using $D \to \mu^+ N X$ as production mechanism. The calculations led to the conclusion that for a $m_N = 1$ GeV SHiP would record 120 reconstructed $N \to \mu^- \pi^+$ using as parameters $|V_{\mu N}|^2 = 10^{-8}$, $c\tau = 1.8 \times 10^{-4}$ [188].

In the CERN North-Area in Prevessin, we find not only SHiP but also the **NA62** [191] experiment which significantly contributes in the HNL hunt. Using data collected during the

first physics data-taking in 2015, the NA62 Collaboration published a search for $K^+ \to N\ell^+$ decays for $170 < m_N < 448$ MeV/c^2 [192] (the results are shown in Figure 8.6). The analyzed events were collected by NA62 in 2015 at ∼1% of the nominal designed beam intensity. During Run3, NA62 is planning to run in beam dump mode with nominal beam intensity of 10^{18} pot (proton on target). With these conditions the final exclusion sensitivity will be improved with respect to CHARM limits (Figures 4.5 and 4.6) by about one order of magnitude in a similar phase space [193]. The projections are done assuming zero background and correspond to the 90% CL for N decaying into at least two charged tracks. The full study can be found in Ref. [193] and the estimated limits in Figures 4.5 and 4.6. The authors consider NA62 to be one of the world's best experiment to look for HNLs with masses in the range delimitated by those of kaons and D-mesons [193].

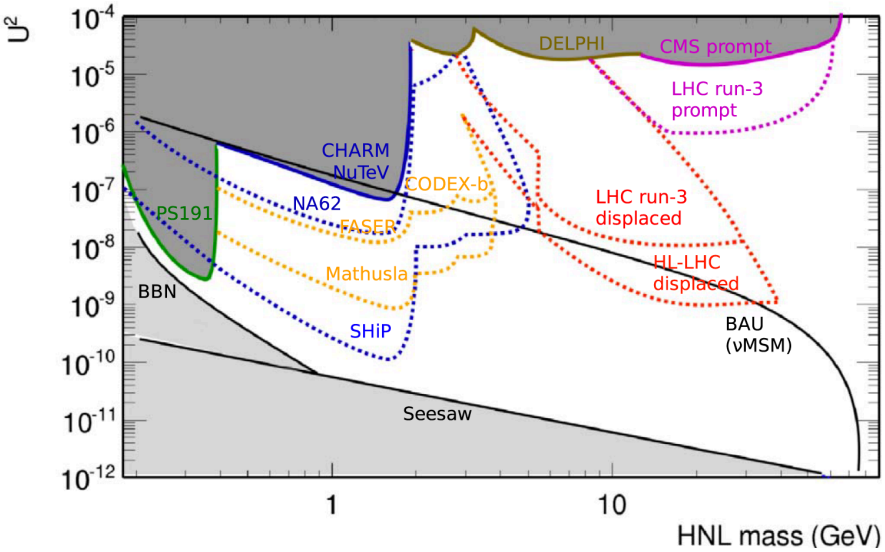

FIGURE 8.6: "Summary of projected experimental sensitivities to HNLs in various experiments, in the coupling strength $|V_{\ell N}|^2$ versus mass plane. The projections labelled "LHC Run 3" and "HL-LHC" are for HNLs in W decays in general-purpose experiments, and the one labelled "Mathusla" assumes the full HL-LHC MATHUSLA dataset. The estimated sensitivity will reach the upper theoretical constraint (labeled "BAU") in the Neutrino Minimal Standard Model for accounting for baryon asymmetry in the Universe while the lightest HNL is a dark-matter candidate" [174].

Before wrapping up, it is worth mentioning the projections for HL-LHC. In Figure 8.6 the exclusion reach using Run3 and 3 ab^{-1} (HL-LHC) data is shown for long-lived HNL analysis performed at CMS or ATLAS.

Quite far in the future, the next breakthrough moment will happen with the dedicated searches at high energy electron-positron circular collider, FCC-ee. A first exploratory study about HNL sensitivities shows exclusion limits down to $|V_{\ell N}|^2 \simeq 10^{-12}$ covering N masses between 10 and 80 GeV /c^2 [194]. The estimations are obtained considering $Z \to \nu N$ decays with N further decaying into $N \to \mu^+ W^- \to \mu^+ q\bar{q}$. Long-lived HNL scenarios are examined with decay length going from 0.01 cm up to 500 cm [194].

This final chapter is not expected to cover all the existing projections and all the new experiments. Instead, the outlook tries to give a feeling of the vast landscape where the two CMS HNL searches sit. The idea is to give a sense of the context and of the perspective

from which one should look at these results.
We have briefly seen the potential of the planned CMS detector upgrades, of the new triggers, of the improved reconstruction algorithms and analysis strategies that have been further developed.
The very wide range of masses, energies, and models necessitates to explore the complementary reach of the current and future experiments.
During the five years of my PhD, it has become so clear that collaborations among the LHC experiments, the theorists and the next generation of facilities are essential to a comprehensive understanding of the heavy neutral lepton frontier and to not missing new physics potential in the upcoming era of the HL-LHC.

Acknowledgements

"Si stava così bene tutti insieme, così bene, che qualcosa di straordinario doveva pur accadere. Bastò che a un certo momento lei dicesse: -Ragazzi, avessi un po' di spazio, come mi piacerebbe farvi le tagliatelle!- E in quel momento tutti pensammo allo spazio che avrebbero occupato le tonde braccia di lei muovendosi avanti e indietro con il mattarello sulla sfoglia di pasta, il petto di lei calando sul gran mucchio di farina e uova che ingombrava il largo tagliere mentre le sue braccia impastavano impastavano, bianche e unte d'olio fin sopra al gomito; pensammo allo spazio che avrebbero occupato la farina, e il grano per fare la farina, e i campi per coltivare il grano, e le montagne da cui scendeva l'acqua per irrigare i campi, e i pascoli per le mandrie di vitelli che avrebbero dato la carne per il sugo; allo spazio che ci sarebbe voluto perché il Sole arrivasse con i suoi raggi a maturare il grano; allo spazio perché dalle nubi di gas stellari il Sole si condensasse e bruciasse; alle quantità di stelle e galassie e ammassi galattici in fuga nello spazio che ci sarebbero volute per tener sospesa ogni galassia ogni nebula ogni sole ogni pianeta, e nello stesso tempo del pensarlo questo spazio inarrestabilmente si formava, nello stesso tempo in cui la signora Ph(i)Nko pronunciava quelle parole: -...le tagliatelle, ve', ragazzi!- il punto che conteneva lei e noi tutti s'espandeva in una raggiera di distanze d'anni-luce e secoli-luce e miliardi di millenniluce, e noi sbattuti ai quattro angoli dell'universo (il signor Pbert Pberd fino a Pavia), e lei dissolta in non so quale specie d'energia luce calore, lei signora Ph(i)Nko, quella che in mezzo al chiuso nostro mondo meschino era stata capace d'uno slancio generoso, il primo, "Ragazzi, che tagliatelle vi farei mangiare!", un vero slancio d'amore generale, dando inizio nello stesso momento al concetto di spazio, e allo spazio propriamente detto, e al tempo, e alla gravitazione universale, e all'universo gravitante, rendendo possibili miliardi di miliardi di soli, e di pianeti, e di campi di grano, e di signore Ph(i)Nko sparse per i continenti dei pianeti che impastano con le braccia unte e generose infarinate, e lei da quel momento perduta, e noi a rimpiangerla."

"*We got along so well all together, so well that something extraordinary was bound to happen. It was enough for her to say, at a certain moment: "Oh, if I only had some room, how I'd like to make some noodles for you boys!" And in that moment we all thought of the space that her round arms would occupy, moving backward and forward with the rolling pin over the dough, her bosom leaning over the great mound of flour and eggs which cluttered the wide board while her arms kneaded and kneaded, white and shiny with oil up to the elbows; we thought of the space that the flour would occupy, and the wheat for the flour, and the fields to raise the wheat, and the mountains from which the water would flow to irrigate the fields, and the grazing lands for the herds of calves that would give their meat for the sauce; of the space it would take for the Sun to arrive with its rays, to ripen the wheat; of the space for the Sun to condense from the clouds of stellar gases and bum; of the quantities of stars and galaxies and galactic masses in flight through space which would be needed to hold suspended every galaxy, every nebula, every sun, every planet, and at the same time we thought of it, this space was inevitably being formed, at the same time that Mrs. Ph(i)Nk 0 was uttering those words: "... ah, what noodles, boys!" the point that contained her and all of us was expanding in a halo of distance in light-years and light-centuries and billions of light-millennia, and we were being hurled to the four corners of the universe (Mr. Pber* Pber d all the way to Pavia), and she, dissolved into I don't know what kind of energy-light-heat, she, Mrs. Ph(i)Nk 0 , she who in the midst of our closed, petty world had been capable of a generous impulse, "Boys, the noodles I would make for you!," a tme outburst of general love, initiating at the same moment the concept of space and, properly speaking, space itself, and time, and universal gravitation, and the gravitating universe, making possible billions and billions of suns, and of planets, and fields of wheat, and Mrs. Ph(i)Nk 0 s, scattered through the continents of the planets, kneading with floury, oil-shiny, generous amis, and she lost at that very moment, and we, mourning her loss. "*

Italo Calvino "Le Cosmicomiche", 1965.

Bibliography

[1] Sean Carroll. *The big picture: on the origins of life, meaning, and the universe itself.* 2016.

[2] S. Abachi and et al. Observation of the Top Quark. *Physical Review Letters*, 74(14):2632–2637, Apr 1995.

[3] ATLAS Collaboration. Observation of a new particle in the search for the Standard Model Higgs boson with the ATLAS detector at the LHC. *Physics Letters B*, 716(1):1–29, 2012.

[4] CMS Collaboration. Observation of a new boson at a mass of 125 GeV with the CMS experiment at the LHC. *Physics Letters B*, 716(1):30–61, 2012.

[5] M. Gell-Mann. A schematic model of baryons and mesons. *Physics Letters*, 8(3):214–215, 1964.

[6] G Zweig. An SU_3 model for strong interaction symmetry and its breaking; Version 2. page 80 p, Feb 1964.

[7] A. Pais and S. B. Treiman. How Many Charm Quantum Numbers Are There? *Phys. Rev. Lett.*, 35:1556, 1975.

[8] G. Branco, R. N. Mohapatra, T. Hagiwara, and D. P. Sidhu. Weak nonleptonic decays of charmed hadrons in models with right-handed currents. *Phys. Rev. D*, 13:680–687, Feb 1976.

[9] P.A. Zyla et al. (Particle Data Group). The Review of Particle Physics (2020). *Progress of Theoretical and Experimental Physics*, 2020, 2020.

[10] P.A. Zyla et al. (Particle Data Group). The Review of Particle Physics (2020). *Progress of Theoretical and Experimental Physics*, 2020, 2020.

[11] Ziro Maki, Masami Nakagawa, and Shoichi Sakata. Remarks on the Unified Model of Elementary Particles. *Progress of Theoretical Physics*, 28(5):870–880, 11 1962.

[12] F. Englert and R. Brout. Broken Symmetry and the Mass of Gauge Vector Mesons. *Phys. Rev. Lett.*, 13:321–323, Aug 1964.

[13] Peter W. Higgs. Broken Symmetries and the Masses of Gauge Bosons. *Phys. Rev. Lett.*, 13:508–509, Oct 1964.

[14] Dmitri Yu. Bardin and G. Passarino. *The standard model in the making: Precision study of the electroweak interactions.* 1999.

[15] Mark Thomson. *Modern Particle Physics*. Cambridge University Press, 2013.

[16] N. Aghanim and et al. Planck 2018 results. *Astronomy and Astrophysics*, 641:A6, Sep 2020.

[17] X ray: NASA/CXC/CfA/M.Markevitch et al.; Optical: NASA/STScI; Magellan/U.Arizona/D.Clowe et al.; Lensing Map: NASA/STScI; ESO WFI; Magellan/U.Arizona/D.Clowe et al. 1E 065756:NASA Finds Direct Proof of Dark Matter. https://chandra.harvard.edu/photo/2006/1e0657/index.html.

[18] Douglas Clowe, Anthony Gonzalez, and Maxim Markevitch. Weak-Lensing Mass Reconstruction of the Interacting Cluster 1E 0657558: Direct Evidence for the Existence of Dark Matter. *The Astrophysical Journal*, 604(2):596–603, Apr 2004.

[19] Douglas Clowe, Maruša Bradač, Anthony H. Gonzalez, Maxim Markevitch, Scott W. Randall, Christine Jones, and Dennis Zaritsky. A Direct Empirical Proof of the Existence of Dark Matter. *The Astrophysical Journal*, 648(2):L109–L113, Aug 2006.

[20] Steven Lowette. Search for Dark Matter at CMS. *Nuclear and Particle Physics Proceedings*, 273-275:503–508, 2016. 37th International Conference on High Energy Physics (ICHEP).

[21] Bhawna Gomber. Dark Matter Searches at the CMS Experiment. *Springer Proceedings in Physics*, 248, 2020. Workshop on Frontiers in High Energy Physics 2019.

[22] Marco Drewes and Björn Garbrecht. Combining experimental and cosmological constraints on heavy neutrinos. *Nuclear Physics B*, 921:250–315, 2017.

[23] James Cline, Matteo Puel, and Takashi Toma. A little theory of everything, with heavy neutral leptons. *Journal of High Energy Physics*, 2020(5), May 2020.

[24] Sacha Davidson, Enrico Nardi, and Yosef Nir. Leptogenesis. *Physics Reports*, 466(4-5):105–177, Sep 2008.

[25] Scott Dodelson and Lawrence M. Widrow. Sterile neutrinos as dark matter. *Phys. Rev. Lett.*, 72:17–20, Jan 1994.

[26] Kevork Abazajian, George M. Fuller, and Mitesh Patel. Sterile neutrino hot, warm, and cold dark matter. *Phys. Rev. D*, 64:023501, May 2001.

[27] Alexander Kusenko. Sterile neutrinos: The dark side of the light fermions. *Physics Reports*, 481(1):1–28, 2009.

[28] A.D. Dolgov and S.H. Hansen. Massive sterile neutrinos as warm dark matter. *Astroparticle Physics*, 16(3):339–344, 2002.

[29] A. D. Sakharov. Violation of CP Invariance, C asymmetry, and baryon asymmetry of the universe. *Pisma Zh. Eksp. Teor. Fiz.*, 5:32–35, 1967.

[30] J. H. Christenson, J. W. Cronin, V. L. Fitch, and R. Turlay. Evidence for the 2π Decay of the K_2^0 Meson. *Phys. Rev. Lett.*, 13:138–140, Jul 1964.

[31] A. Alavi-Harati and et al. Observation of Direct CP Violation in $K_{S,L} \to \pi\pi$ Decays. *Physical Review Letters*, 83(1):22–27, Jul 1999.

[32] V. Fanti and et al. A new measurement of direct CP violation in two pion decays of the neutral kaon. *Physics Letters B*, 465(1-4):335–348, Oct 1999.

[33] R. Aaij and all. Observation of CP Violation in Charm Decays. *Phys. Rev. Lett.*, 122:211803, May 2019.

[34] Raj Gandhi, Boris Kayser, Mehedi Masud, and Suprabh Prakash. The impact of sterile neutrinos on CP measurements at long baselines. *Journal of High Energy Physics*, 2015(11), Nov 2015.

[35] N. Klop and A. Palazzo. Imprints ofCPviolation induced by sterile neutrinos in T2K data. *Physical Review D*, 91(7), Apr 2015.

[36] A Palazzo. Sterile neutrinos as a source of CP violation. *Journal of Physics: Conference Series*, 1586:012021, aug 2020.

[37] Raymond Davis, Don S. Harmer, and Kenneth C. Hoffman. Search for Neutrinos from the Sun. *Phys. Rev. Lett.*, 20:1205–1209, May 1968.

[38] Radioactivity.eu.com. Solar Neutrinos. https://www.radioactivity.eu.com/site/pages/Solar_Neutrinos.htm.

[39] B Pontecorvo. MESONIUM AND ANTIMESONIUM. *Zhur. Eksptl'. i Teoret. Fiz.*

[40] Y. Fukuda, T. Hayakawa, E. Ichihara, K. Inoue, K. Ishihara, H. Ishino, Y. Itow, T. Kajita, J. Kameda, S. Kasuga, and et al. Evidence for Oscillation of Atmospheric Neutrinos. *Physical Review Letters*, 81(8):1562–1567, Aug 1998.

[41] Q. R. Ahmad and et al. Measurement of the Rate of ν_e+d→p+p+e Interactions Produced byB8Solar Neutrinos at the Sudbury Neutrino Observatory. *Physical Review Letters*, 87(7), Jul 2001.

[42] O. Brüning, P. Collier, P. Lebrun, S. Myers, R. Ostojić, J. Poole, and P. Proudlock. LHC Design Report Vol.1: The LHC Main Ring. 2004.

[43] *LEP design report.* CERN, Geneva, 1984. Copies shelved as reports in LEP, PS and SPS libraries.

[44] Forthommel. The CERN accelerator complex. Jul 2016.

[45] The ALICE Collaboration. The ALICE experiment at the CERN LHC. 3(08):S08002–S08002, aug 2008.

[46] ATLAS Collaboration. The ATLAS experiment at the CERN large hadron collider. *Journal of Instrumentation*, 3(08):S08003–S08003, aug 2008.

[47] CMS Collaboration. The CMS experiment at the CERN LHC. *Journal of Instrumentation*, 3(08):S08004–S08004, aug 2008.

[48] The LHCb Collaboration. The LHCb detector at the LHC. *Journal of Instrumentation*, 3(08):S08005–S08005, aug 2008.

[49] CMS Collaboration. Public CMS luminosity information. https://twiki.cern.ch/twiki/bin/view/CMSPublic/LumiPublicResults.

[50] LHC commisioning. Schedule HL-LHC plots. https://lhc-commissioning.web.cern.ch/schedule/HL-LHC-plots.htm.

[51] CMS Coordinates system. https://wiki.physik.uzh.ch/cms/_detail/latex:cms_coordinate_system.png?id=latex3Aexample_spherical_coordinates.

[52] CMS detector. https://cms.cern/detector.

[53] CMS Collaboration. Particle-flow reconstruction and global event description with the CMS detector. *JINST*, 12(10):P10003, 2017.

[54] W. Adam and al. Alignment of the CMS Silicon Strip Tracker during stand-alone Commissioning. *JINST*, 4:T07001. 41 p, Apr 2009. Comments: 41 pages, 63 postscript figures, submitted to JINST.

[55] CMSPublic Web. CMS Tracker Detector Performance Results. https://twiki.cern.ch/twiki/bin/view/CMSPublic/DPGResultsTRK.

[56] A Dominguez and et al. CMS Technical Design Report for the Pixel Detector Upgrade. Technical report, Sep 2012.

[57] A Benaglia. The CMS ECAL performance with examples. *Journal of Instrumentation*, 9(02):C02008–C02008, feb 2014.

[58] Cristina Biino. The CMS electromagnetic calorimeter: overview, lessons learned during run 1 and future projections. *Journal of Physics: Conference Series*, 587:012001, feb 2015.

[59] CMSPublic Web. Performance of the CMS Muon Detectors in early 2016 collision runs. https://twiki.cern.ch/twiki/bin/view/CMSPublic/MuonDPGPublic160729.

[60] CMS Collaboration. The CMS trigger system. *Journal of Instrumentation*, 12(01):P01020–P01020, jan 2017.

[61] David Barney. CMS Detector Slice. CMS Collection., Jan 2016.

[62] CMS Collaboration. Description and performance of track and primary-vertex reconstruction with the CMS tracker. *Journal of Instrumentation*, 9(10):P10009–P10009, Oct 2014.

[63] P. Billoir and S. Qian. Simultaneous pattern recognition and track fitting by the Kalman filtering method. *Nuclear Instruments and Methods in Physics Research Section A: Accelerators, Spectrometers, Detectors and Associated Equipment*, 294(1):219–228, 1990.

[64] Wolfgang Waltenberger, Rudolf Frühwirth, and Pascal Vanlaer. Adaptive vertex fitting. *Journal of Physics G: Nuclear and Particle Physics*, 34(12):N343–N356, nov 2007.

[65] Giovanni Petrucciani. Particle Flow reconstruction in the CMS Level-1 trigger for the HL-LHC. Particle Flow reconstruction in the Level-1 trigger at CMS for the HL-LHC. Technical report, CERN, Geneva, Nov 2018.

[66] Matteo Cacciari, Gavin P Salam, and Gregory Soyez. The anti-ktjet clustering algorithm. *Journal of High Energy Physics*, 2008(04):063–063, apr 2008.

[67] Matteo Cacciari, Gavin P. Salam, and Gregory Soyez. FastJet user manual. *The European Physical Journal C*, 72(3), Mar 2012.

[68] CMS Collaboration. Jet algorithms performance in 13 tev data. CMS Physics Analysis Summary CMS-PAS-JME-16-003, 2010.

[69] CMS Collaboration. Pileup Removal Algorithms. Technical report, CERN, Geneva, 2014.

[70] Matteo Cacciari and Gavin P. Salam. Pileup subtraction using jet areas. *Physics Letters B*, 659(1):119–126, 2008.

[71] Matteo Cacciari, Gavin P Salam, and Gregory Soyez. The catchment area of jets. *Journal of High Energy Physics*, 2008(04):005–005, apr 2008.

[72] CMS Collaboration. Pileup mitigation at CMS in 13 TeV data. *JINST*, 15(09):P09018, 2020.

[73] CMS Collaboration. Jet energy scale and resolution in the CMS experiment in pp collisions at 8 TeV. *Journal of Instrumentation*, 12(02):P02014–P02014, feb 2017.

[74] CMS Collaboration. Identification of heavy-flavour jets with the CMS detector in pp collisions at 13 TeV. *Journal of Instrumentation*, 13(05):P05011–P05011, May 2018.

[75] CMS Collaboration. Identification of heavy-flavour jets with the CMS detector in pp collisions at 13 TeV. *Journal of Instrumentation*, 13(05):P05011–P05011, May 2018.

[76] CMS Collaboration. CMS Phase 1 heavy flavour identification performance and developments. May 2017.

[77] CMS Collaboration. Identification of heavy-flavour jets with the CMS detector in pp collisions at 13 TeV. *Journal of Instrumentation*, 13(05):P05011–P05011, may 2018.

[78] Verzetti, Mauro. Machine learning techniques for jet flavour identification at CMS. *EPJ Web Conf.*, 214:06010, 2019.

[79] CMS Collaboration. Muon Reconstruction and Identification Improvements for Run-2 and First Results with 2015 Run Data. Jul 2015.

[80] CMS Collaboration. The performance of the CMS muon detector in proton-proton collisions at $\sqrt{s}$= 7 TeV at the LHC. *Journal of Instrumentation*, 8(11):P11002–P11002, nov 2013.

[81] CMS Collaboration. Performance of the CMS muon detector and muon reconstruction with proton-proton collisions at $\sqrt{s}$=13 TeV. *Journal of Instrumentation*, 13(06):P06015–P06015, Jun 2018.

[82] Giovanni Petrucciani and Cristina Botta. CMS internal: Proposal of a new "Medium" Muon ID. Technical report, CERN, Dec 2014.

[83] CMS Collaboration. Muon Identification and Isolation efficiency on full 2016 dataset. Mar 2017.

[84] CMS Collaboration. Muon identification and isolation efficiencies with 2017 and 2018 data. Jul 2018.

[85] CMS Collaboration. Search for long-lived particles decaying in the CMS endcap muon detectors in proton-proton collisions at $\sqrt{s} = 13$ TeV, 2021.

[86] CMS Collaboration. Search for long-lived particles using delayed photons in proton-proton collisions at $\sqrt{s} = 13$ TeV. *Physical Review D*, 100(11), Dec 2019.

[87] CMS Collaboration. Search for long-lived particles using nonprompt jets and missing transverse momentum with proton-proton collisions at $\sqrt{s} = 13$ TeV. *Physics Letters B*, 797:134876, Oct 2019.

[88] CMS Collaboration. Search for disappearing tracks in proton-proton collisions at $\sqrt{s} =$ 13 TeV. *Physics Letters B*, 806:135502, Jul 2020.

[89] CMS Collaboration. Search for long-lived particles using displaced jets in proton-proton collisions at $\sqrt{s} = 13$ TeV. *Physical Review D*, 104(1), Jul 2021.

[90] CMS Collaboration. Search for long-lived particles decaying to jets with displaced vertices in proton-proton collisions at $\sqrt{s} = 13$ TeV. 4 2021.

[91] Steven Lowette. CMS LLP Search Snapshot (3^{rd} LHC LLP Workshop), May 2018.

[92] W Adam, R Frühwirth, A Strandlie, and T Todorov. Reconstruction of electrons with the gaussian-sum filter in the CMS tracker at the LHC. *Journal of Physics G: Nuclear and Particle Physics*, 31(9):N9–N20, jul 2005.

[93] Internal CMS documentation: Multivariate Electron Identification for Run2. https://twiki.cern.ch/twiki/bin/viewauth/CMS/MultivariateElectronIdentificationRun2.

[94] Internal CMS documentation: Cut Based Electron ID for Run 2. https://twiki.cern.ch/twiki/bin/view/CMS/CutBasedElectronIdentificationRun2.

[95] CMS Collaboration. Performance of missing energy reconstruction in 13 TeV pp collision data using the CMS detector. Technical Report CMS-PAS-JME-16-004, CERN, Geneva, 2016.

[96] Peter Minkowski. $\mu \to e\gamma$ at a rate of one out of 109 muon decays? *Physics Letters B*, 67(4):421–428, 1977.

[97] Murray Gell-Mann, Pierre Ramond, and Richard Slansky. Complex Spinors and Unified Theories, 2013.

[98] Rabindra N. Mohapatra and Goran Senjanović. Neutrino Mass and Spontaneous Parity Nonconservation. *Phys. Rev. Lett.*, 44:912–915, Apr 1980.

[99] J. Schechter and J. W. F. Valle. Neutrino masses in SU(2) $\bigotimes$ U(1) theories. *Phys. Rev. D*, 22:2227–2235, Nov 1980.

[100] Laurent Canetti, Marco Drewes, and Mikhail Shaposhnikov. Matter and antimatter in the universe. *New Journal of Physics*, 14(9):095012, sep 2012.

[101] V.A. Kuzmin, V.A. Rubakov, and M.E. Shaposhnikov. On anomalous electroweak baryon-number non-conservation in the early universe. *Physics Letters B*, 155(1):36–42, 1985.

[102] Sergey Alekhin and all. A facility to search for hidden particles at the CERN SPS: the SHiP physics case. *Reports on Progress in Physics*, 79(12):124201, oct 2016.

[103] Anupama Atre, Tao Han, Silvia Pascoli, and Bin Zhang. The search for heavy Majorana neutrinos. *Journal of High Energy Physics*, 2009(05):030–030, may 2009.

[104] Frank F Deppisch, P S Bhupal Dev, and Apostolos Pilaftsis. Neutrinos and collider physics. *New Journal of Physics*, 17(7):075019, aug 2015.

[105] Robert Foot, H. Lew, X. G. He, and Girish C. Joshi. Seesaw Neutrino Masses Induced by a Triplet of Leptons. *Z. Phys. C*, 44:441, 1989.

[106] Rabindra N. Mohapatra and Goran Senjanovic. Neutrino Mass and Spontaneous Parity Nonconservation. *Phys. Rev. Lett.*, 44:912, 1980.

[107] Tsutomu Yanagida. Horizontal gauge symmetry and masses of neutrinos. *Conf. Proc. C*, 7902131:95–99, 1979.

[108] Matthew R. Francis. Neutrinos on a seesaw, 2016. https://www.symmetrymagazine.org/article/neutrinos-on-a-seesaw.

[109] Robert D. Klauber. The Seesaw Mechanism. http://www.quantumfieldtheory.info/TheSeesawMechanism.htmZEqnNum165557.

[110] Yi Cai, Tao Han, Tong Li, and Richard Ruiz. Lepton Number Violation: Seesaw Models and Their Collider Tests. *Frontiers in Physics*, 6:40, 2018.

[111] F. del Aguila, J. de Blas, and M. Pérez-Victoria. Effects of new leptons in electroweak precision data. *Phys. Rev. D*, 78:013010, Jul 2008.

[112] Marco Drewes, Björn Garbrecht, Dario Gueter, and Juraj Klarić. Testing the low scale seesaw and leptogenesis. *Journal of High Energy Physics*, 2017(8), Aug 2017.

[113] Stefan Antusch and Oliver Fischer. Non-unitarity of the leptonic mixing matrix: present bounds and future sensitivities. *Journal of High Energy Physics*, 2014(10), Oct 2014.

[114] André de Gouvêa. Seesaw energy scale and the LSND anomaly. *Physical Review D*, 72(3), Aug 2005.

[115] Belle Collaboration. Search for heavy neutrinos at Belle. *Physical Review D*, 87(7), Apr 2013.

[116] J. Dorenbosch and et al. A search for decays of heavy neutrinos in the mass range 0.5–2.8 GeV. *Physics Letters B*, 166(4):473–478, 1986.

[117] Oleg Ruchayskiy and Artem Ivashko. Restrictions on the lifetime of sterile neutrinos from primordial nucleosynthesis. *Journal of Cosmology and Astroparticle Physics*, 2012(10):014–014, Oct 2012.

[118] Stefan Antusch and Oliver Fischer. Testing sterile neutrino extensions of the Standard Model at future lepton colliders. *Journal of High Energy Physics*, 2015(5), May 2015.

[119] G. Bernardi, G. Carugno, J. Chauveau, F. Dicarlo, M. Dris, J. Dumarchez, M. Ferro-Luzzi, J.-M. Levy, D. Lukas, J.-M. Perreau, Y. Pons, A.-M. Touchard, and F. Vannucci. Further limits on heavy neutrino couplings. *Physics Letters B*, 203(3):332–334, 1988.

[120] F. Vannucci. DECAYS AND OSCILLATIONS OF NEUTRINOS IN THE PS-191 EXPERIMENT. In *20th Rencontres de Moriond: Electroweak Interactions*, 1985.

[121] DELPHI Collaboration. Search for neutral heavy leptons produced in Z decays. *Z. Phys. C*, 74:57–71, 1997. [Erratum: Z.Phys.C 75, 580 (1997)].

[122] ATLAS Collaboration. Search for displaced vertices of oppositely charged leptons from decays of long-lived particles in pp collisions at $\sqrt{s} = 13$ TeV with the ATLAS detector. arXiv:1907.10037v1, 23 Jul 2019.

[123] CMS Collaboration. Search for heavy Majorana neutrinos in same-sign dilepton channels in proton-proton collisions at $\sqrt{s} = 13$ TeV. *JHEP*, 01:122, 2019.

[124] Silvia Pascoli, Richard Ruiz, and Cedric Weiland. Heavy neutrinos with dynamic jet vetoes: multilepton searches at $\sqrt{s} = 14$, 27, and 100 TeV. *Journal of High Energy Physics*, 2019(6), Jun 2019.

[125] N. Aghanim et al. Planck 2018 results. VI. Cosmological parameters. *Astron. Astrophys.*, 641:A6, 2020.

[126] Marco Drewes. Theoretical Status of Neutrino Physics, 2015.

[127] Laurent Canetti and Mikhail Shaposhnikov. Baryon asymmetry of the Universe in the vMSM. *Journal of Cosmology and Astroparticle Physics*, 2010(09):001–001, sep 2010.

[128] Nicholas Metropolis and S. Ulam. The Monte Carlo Method. *Journal of the American Statistical Association*, 44(247):335–341, 1949. PMID: 18139350.

[129] J. Alwall, R. Frederix, S. Frixione, V. Hirschi, F. Maltoni, O. Mattelaer, H.-S. Shao, T. Stelzer, P. Torrielli, and M. Zaro. The automated computation of tree-level and next-to-leading order differential cross sections, and their matching to parton shower simulations. *Journal of High Energy Physics*, 2014(7), Jul 2014.

[130] Simone Alioli, Paolo Nason, Carlo Oleari, and Emanuele Re. A general framework for implementing NLO calculations in shower Monte Carlo programs: the POWHEG BOX. *Journal of High Energy Physics*, 2010(6), Jun 2010.

[131] Richard D. Ball, Valerio Bertone, Stefano Carrazza, Christopher S. Deans, Luigi Del Debbio, Stefano Forte, Alberto Guffanti, Nathan P. Hartland, José I. Latorre, and et al. Parton distributions for the LHC run II. *Journal of High Energy Physics*, 2015(4), Apr 2015.

[132] Richard D. Ball and et al. Parton distributions from high-precision collider data. *The European Physical Journal C*, 77(10), Oct 2017.

[133] Torbjörn Sjöstrand, Stephen Mrenna, and Peter Skands. A brief introduction to PYTHIA 8.1. *Computer Physics Communications*, 178(11):852–867, Jun 2008.

[134] Torbjörn Sjöstrand, Stefan Ask, Jesper R. Christiansen, Richard Corke, Nishita Desai, Philip Ilten, Stephen Mrenna, Stefan Prestel, Christine O. Rasmussen, and Peter Z. Skands. An introduction to PYTHIA 8.2. *Computer Physics Communications*, 191:159–177, Jun 2015.

[135] P. Skands, S. Carrazza, and J. Rojo. Tuning PYTHIA 8.1: the Monash 2013 tune. *The European Physical Journal C*, 74(8), Aug 2014.

[136] CMS Collaboration. Event generator tunes obtained from underlying event and multiparton scattering measurements. *The European Physical Journal C*, 76(3), Mar 2016.

[137] CMS Collaboration. Extraction and validation of a new set of CMS pythia8 tunes from underlying-event measurements. *The European Physical Journal C*, 80(1), Jan 2020.

[138] S. Agostinelli et al. (GEANT4 Collaboration). Geant4—a simulation toolkit. *Nuclear Instruments and Methods in Physics Research Section A: Accelerators, Spectrometers, Detectors and Associated Equipment*, 506(3):250–303, 2003.

[139] CMS Collaboration. Summaries of CMS cross section measurements. https://twiki.cern.ch/twiki/bin/view/CMSPublic/PhysicsResultsCombined.

[140] University of Zurich Physics Institute. List of Diagrams. https://www.physik.uzh.ch/~che/FeynDiag/Listing.php#id0.

[141] Marco Drewes and Jan Hajer. Heavy neutrinos in displaced vertex searches at the LHC and HL-LHC. *Journal of High Energy Physics*, 2020(2), Feb 2020.

[142] Anupama Atre, Tao Han, Silvia Pascoli, and Bin Zhang. The Search for Heavy Majorana Neutrinos. *JHEP*, 05:030, 2009.

[143] Daniel Alva, Tao Han, and Richard Ruiz. Heavy Majorana neutrinos from $W\gamma$ fusion at hadron colliders. *JHEP*, 02:072, 2015.

[144] Céline Degrande, Olivier Mattelaer, Richard Ruiz, and Jessica Turner. Fully automated precision predictions for heavy neutrino production mechanisms at hadron colliders. *Physical Review D*, 94(5), Sep 2016.

[145] SM + Heavy N at NLO in QCD FeynRules page. http://feynrules.irmp.ucl.ac.be/wiki/HeavyN.

[146] P. S. Bhupal Dev, Apostolos Pilaftsis, and Un-ki Yang. New Production Mechanism for Heavy Neutrinos at the LHC. *Phys. Rev. Lett.*, 112:081801, Feb 2014.

[147] Duane A. Dicus and Probir Roy. Supercollider signatures and correlations of heavy neutrinos. *Phys. Rev. D*, 44:1593–1596, Sep 1991.

[148] Scott S.D. Willenbrock and Duane A. Dicus. Production of heavy leptons from gluon fusion. *Physics Letters B*, 156(5):429–433, 1985.

[149] Richard Ruiz, Michael Spannowsky, and Philip Waite. Heavy neutrinos from gluon fusion. *Phys. Rev. D*, 96:055042, Sep 2017.

[150] Aneesh Manohar, Paolo Nason, Gavin P. Salam, and Giulia Zanderighi. How Bright is the Proton? A Precise Determination of the Photon Parton Distribution Function. *Phys. Rev. Lett.*, 117:242002, Dec 2016.

[151] CMS Collaboration. Search for heavy neutral leptons in events with three charged leptons in proton-proton collisions at $\sqrt{s} = 13$ TeV. *Phys. Rev. Lett.*, 120(22):221801, 2018.

[152] Ia Iashvili. Recommended Jet Energy Corrections and Uncertainties For Data and MC, March 2017. https://twiki.cern.ch/twiki/bin/view/CMS/JECDataMC.

[153] Caroline Collard. Usage of b/c Tag Objects for 13 TeV Data in 2016 and 80X MC, March 2017. https://twiki.cern.ch/twiki/bin/viewauth/CMS/BtagRecommendation80XReReco.

[154] Andrea Giammanco et al. Utilities for Accessing Pileup Information for Data, March 2017. https://twiki.cern.ch/twiki/bin/view/CMS/PileupJSONFileforData.

[155] CMS Luminosity Measurement for the 2016 Data Taking Period. CMS Physics Analysis Summary CMS-PAS-LUM-17-001, 2017.

[156] L3 Collaboration. Search for heavy isosinglet neutrino in ee annihilation at LEP. *Physics Letters B*, 517(1):67–74, 2001.

[157] ATLAS Collaboration. Search for heavy Majorana neutrinos with the ATLAS detector in pp collisions at $\sqrt{s} = 8$ TeV. *Journal of High Energy Physics*, 2015(7), Jul 2015.

[158] CMS Collaboration. Search for heavy Majorana neutrinos in $\mu^{\pm}\mu^{\mp}$ + jets events in proton–proton collisions at s=8 TeV. *Physics Letters B*, 748:144–166, Sep 2015.

[159] ATLAS Collaboration. Search for long-lived, massive particles in events with a displaced vertex and a displaced muon in *pp* collisions at $\sqrt{s} = 13$ TeV with the ATLAS detector. Technical Report ATLAS-CONF-2019-006, CERN, Geneva, Mar 2019.

[160] ATLAS Collaboration. Search for displaced vertices of oppositely charged leptons from decays of long-lived particles in pp collisions at s=13 TeV with the ATLAS detector. *Physics Letters B*, 801:135114, 2020.

[161] CMS Collaboration. Search for long-lived particles using delayed photons in proton-proton collisions at $\sqrt{s} = 13$ TeV. *Phys. Rev. D*, 100(11):112003, 2019.

[162] CMS Collaboration. Search for long-lived particles using nonprompt jets and missing transverse momentum with proton-proton collisions at $\sqrt{s} = 13$ TeV. *Phys. Lett. B*, 797:134876, 2019.

[163] CMS Collaboration. Search for disappearing tracks in proton-proton collisions at s=13TeV. *Physics Letters B*, 806:135502, Jul 2020.

[164] CMS Internal documentation. Study of displaced photon conversions. *CMS Physics Analysis Note*, AN-2021/021, 2021.

[165] CMS Internal documentation. Study of displaced vertex reconstruction using light neutral hadrons in Drell-Yan events. *CMS Physics Analysis Note*, AN-2020/111, 2020.

[166] H. Delannoy. Performance of the silicon tracker of the CMS experiment during 2016 LHC data taking. TIPP2017, 23 May 2017.

[167] CMS Collaboration. Precision luminosity measurement in proton-proton collisions at $\sqrt{s} = 13$ TeV in 2015 and 2016 at CMS. Technical report, CERN, Geneva, Apr 2021.

[168] CMS luminosity measurement for the 2017 data-taking period at $\sqrt{s} = 13$ TeV. Technical Report CMS-PAS-LUM-17-004, CERN, Geneva, 2018.

[169] CMS luminosity measurement for the 2018 data-taking period at $\sqrt{s} = 13$ TeV. Technical Report CMS-PAS-LUM-18-002, CERN, Geneva, 2019.

[170] CMS Collaboration. Measurement of the inelastic proton-proton cross section at $\sqrt{s} = 13$ TeV. *Journal of High Energy Physics*, 2018(7):161, Jul 2018.

[171] G Cowan, K Cranmer, E Gross, and O Vitells. Asymptotic formulae for likelihood-based tests of new physics. *Eur. Phys. J.*, C71:1554, 2011.

[172] CMS Collaboration. Search for long-lived heavy neutral leptons with displaced vertices in pp collisions at $\sqrt{s} = 13\,\text{TeV}$ with the CMS detector. Technical report, CERN, Geneva, 2021. https://cds.cern.ch/record/2777047.

[173] ATLAS Collaboration. Search for heavy neutral leptons in decays of W bosons produced in 13 TeV pp collisions using prompt and displaced signatures with the ATLAS detector. *Journal of High Energy Physics*, 2019(10), Oct 2019.

[174] Juliette Alimena and et al. Searching for long-lived particles beyond the Standard Model at the Large Hadron Collider. *Journal of Physics G: Nuclear and Particle Physics*, 47(9):090501, Sep 2020.

[175] CMS Collaboration. Search for a right-handed W boson and heavy neutrino in proton-proton collisions at $\sqrt{s} = 13$ TeV. Technical report, CERN, Geneva, 2021.

[176] CMS Collaboration. Observation of $t\bar{t}H$ Production. *Physical Review Letters*, 120(23), Jun 2018.

[177] CMS Collaboration. Observation of Single Top Quark Production in Association with a Z Boson in Proton-Proton Collisions at $\sqrt{s}$ =13 TeV. *Phys. Rev. Lett.*, 122(13):132003, 2019.

[178] CMS Collaboration. Evidence for Higgs boson decay to a pair of muons. *Journal of High Energy Physics*, 2021(1), Jan 2021.

[179] Patrick T. Komiske, Eric M. Metodiev, and Jesse Thaler. Energy flow networks: deep sets for particle jets. *Journal of High Energy Physics*, 2019(1), Jan 2019.

[180] I. Zurbano Fernandez and et. al. High-Luminosity Large Hadron Collider (HL-LHC): Technical design report. 10/2020, 12 2020.

[181] CMS Collaboration. The Phase-2 Upgrade of the CMS Tracker. Technical report, CERN, Geneva, Jun 2017.

[182] CMS Collaboration. The Phase-2 Upgrade of the CMS Barrel Calorimeters. Technical report, CERN, Geneva, Sep 2017. This is the final version, approved by the LHCC.

[183] CMS Collaboration. The Phase-2 Upgrade of the CMS Muon Detectors. Technical report, CERN, Geneva, Sep 2017. This is the final version, approved by the LHCC.

[184] CMS Collaboration. Technical proposal for a MIP timing detector in the CMS experiment Phase 2 upgrade. Technical report, CERN, Geneva, Dec 2017.

[185] CMS Collaboration. The Phase-2 Upgrade of the CMS L1 Trigger Interim Technical Design Report. Technical report, CERN, Geneva, Sep 2017. This is the CMS Interim TDR devoted to the upgrade of the CMS L1 trigger in view of the HL-LHC running, as approved by the LHCC.

[186] Marta Tornago. The CMS MTD Endcap Timing Layer: Precision Timing with Low Gain Avalanche Diode Sensors. Technical report, Sep 2021. 22nd Particles and Nuclei International Conference.

[187] David Curtin and et al. Long-lived particles at the energy frontier: the MATHUSLA physics case. *Reports on Progress in Physics*, 82(11):116201, Oct 2019.

[188] W. Bonivento, A. Boyarsky, H. Dijkstra, U. Egede, M. Ferro-Luzzi, B. Goddard, A. Golutvin, D. Gorbunov, R. Jacobsson, J. Panman, M. Patel, O. Ruchayskiy, T. Ruf, N. Serra, M. Shaposhnikov, and D. Treille. Proposal to Search for Heavy Neutral Leptons at the SPS, 2013.

[189] SHiP Collaboration. A facility to Search for Hidden Particles (SHiP) at the CERN SPS, 2015.

[190] SHiP Collaboration. SHiP Experiment - Progress Report. Jan 2019.

[191] NA62 collaboration. The beam and detector of the NA62 experiment at CERN. *Journal of Instrumentation*, 12(05):P05025–P05025, may 2017.

[192] NA62 collaboration. Search for heavy neutral lepton production in K+ decays. *Physics Letters B*, 778:137–145, Mar 2018.

[193] Marco Drewes, Jan Hajer, Juraj Klaric, and Gaia Lanfranchi. NA62 sensitivity to heavy neutral leptons in the low scale seesaw model. *Journal of High Energy Physics*, 2018(7), Jul 2018.

[194] Alain Blondel, E. Graverini, N. Serra, and M. Shaposhnikov. Search for Heavy Right Handed Neutrinos at the FCC-ee, 2014.